University of Southampton

Power scaling and nonlinear frequency conversion of single-frequency lasers based on Nd:YLF

By

Timothy Martin James Kendall

A thesis submitted for the degree of Doctor of Philosophy
Faculty of Science
Department of Physics
Optoelectronics research Centre
March 2004

Abstract

Faculty of science

Department of Physics

University of Southampton

Doctor of Philosophy

Powers scaling and nonlinear frequency conversion of single-frequency lasers based on Nd:YLF

By Timothy Martin James Kendall

This thesis presents a strategy for power-scaling diode-end-pumped solid-state lasers based on Nd:YLF operating on the 1.053µm line whilst retaining, efficient, single-frequency, diffraction limited output, the characteristics of low power operation. This strategy reduces the effects of energy transfer up-conversion (ETU), which can decrease the lifetime of the upper lasing level and increase the heat generated per unit volume within the laser rod, increasing the effects of detrimental thermally related problems such as thermal lensing, stress-induced birefringence and stress induced laser rod fracture. Also a passive technique for mode-hopping-suppression is described, allowing the oscillating frequency within the laser cavity to tune over many axial mode spacings before a mode-hop occurs. In order to de-couple the problems of laser resonator power scaling from the maintenance of robust and reliable single-frequency operation, the Nd:YLF laser oscillator output is amplified via Nd:YLF based amplifier stages. A model is presented of the effects of ETU on thermal lensing and small signal gain within the amplifiers along with projected results for further power-scaling prospects.

Using the master oscillator design strategy, in a ring-cavity configuration, we demonstrate 4.5W of single-frequency output (for 20W incident pump power), in a diffraction limited beam ($M^2<1.1$) throughout the entire incident pump range. The passive technique for mode hopping suppression allowed the oscillating frequency to be tuned over 8GHz (~14 axial mode spacings) before mode hopping occurred. The amplifier stages power-scaled the output from the master oscillator to ~20W whilst maintaining diffraction limited beam quality ($M^2<1.1$). In a pulse regime the amplifiers demonstrated a small signal gain of ~2000 giving 1.2kW peak power in a 100ns pulse.

In order to increase the frequency tuning capabilities of the master-oscillator-power-amplifier (MOPA), it was used to pump a series of cw singly-resonant optical parametric oscillators (SROs) based on periodically-poled lithium niobate. Although SROs are inherently single-frequency they suffer detrimentally from mode-hopping, therefore in the final stages of this thesis, we propose to utilise the novel passive technique for mode-hopping-suppression with the SRO cavities in order to achieve robust and reliable single-frequency output. Theoretical expressions and design strategy for low SRO threshold and efficient slope efficiency are expressed along with detailed analysis of the mode-hopping nature of their output. Preliminary results for cw SROs are presented and details of SRO mode-hopping-suppression are included.

Acknowledgements

Before the "big read", it is quite normal to thank a few people for all their help and support. I on the other hand have to thank a vast amount of people for telling me to "pull my finger out" and "get on with it".
Not one part of this would have been possible without the help of the Advance Solid-state Sources Group, starting with Paul (the guy pointing in the right direction), Ian (the guy pointing mathematically in the right direction), Pu, Mike, Deyuan (the guys who kept on asking me if it was finished yet) and finally Dr. Andy Clarkson (the guy that never once stopped giving me new angles to look at). Also thanks within the department has to go to Simon, Chris and Tim (the "hands-on" guys) without whose help I would probably be sobbing on the floor of the lab wondering why the "thingy does not fit in the doodaa". Also thanks to Eve and Heather for helping me sort out all and every type of paper work possible with lots of smiles.

Finally the "non-physics people" (the guys who never ask me how work is going just in case I tell them). First of all, any of the lot I still know and drink with in Ilkley (well done lads, you now have a mention in the British Library), Mum and Dad (the guys without which literally "non of this would have been possible"), Sifu and the rest of the Kung Fu club at Southampton university (the guys that helped me vent some rage – you have know idea how much that helped) and finally Bryony (the only one of the guys on the list that will hit me for calling her a guy and get away with it), without you in my life this thesis would probably be a lot longer – thank-you.

A formal acknowledgment must also go to Dr Ian Musgrave with his help of the mathematics in Chapters 3 and 4. During the course of his work with Nd:YVO_4 our research has drawn many parallels including the effects of up-conversion regarding the threshold condition of a small low power laser and the small signal gain generated within an amplifier. Numerous mathematical identities used during the analysis of these effects were found by him "within books old and new" and were graciously given to me so that I could derive the appropriate mathematical expressions for myself. All modelling explained within this thesis however was performed by T.M.J. Kendall using the computer software Mathcad.

Contents

.. 56

CHAPTER 3: SINGLE-FREQUENCY ND:YLF MASTER OSCILLATOR**.. 56**

.. 92

CHAPTER 4: HIGH-POWER SINGLE-FREQUENCY MASTER-OSCILLATOR-POWER-AMPLIFIER**.. 92**

Chapter 1: Introduction

1.1 General Introduction

Lasers appear everyday within our lives now, whether we are shopping for food or clothes, visiting the dentist or doctor or even simply listening to music, lasers can be involved in some way or another. Scaling the output powers from solid-state lasers to satisfy the needs of ever-demanding applications continues to be a very important area of research within the lasers and optics community. For many of these applications the requirements for high output power is also accompanied by the need for high efficiency and good (preferably TEM_{00}) beam quality. These operating characteristics become increasingly difficult to simultaneously achieve as pump power is increased due to heat generation in the laser medium and its degrading effects. For some (even more demanding) applications, such as the emerging fields of gravitational wave-detection and LIDAR [1-7], which require high-power, narrow linewidth single-longitudinal-mode output in a wavelength regime that is not attainable from a solid-state laser, the situation becomes rather more complicated. The standard approach is to employ a singly-resonant optical parametric oscillator

(SROPO) pumped by a solid-state laser source. The design of such a source and its implementation is complicated not only for the need for high-power and diffraction-limited beam quality from the solid-state source, but also because of the need for robust, mode-hop-free, single-frequency operation, which is very difficult to achieve at high pump powers. A further complication is mode-hopping in the SROPO caused by mechanical vibration and temperature fluctuations, which can be a very serious problem.

The research project described in this thesis had two main goals: (1) To investigate an approach for power-scaling of single-frequency operation in the 1μm wavelength regime using a novel master-oscillator-power-amplifier architecture based on Nd:YLF and employing a passive technique for suppressing mode-hopping in the master oscillator. (2) To demonstrate efficient cw SROPO's based on periodically-poled lithium niobate (PPLN), pumped by the Nd:YLF MOPA, and to investigate the application of the same passive technique for suppressing mode-hopping to a cw SROPO with the goal of achieving reliable single-frequency operation and mode-hop-free wavelength tuning.

The remainder of this opening chapter will briefly review the historical background relevant to the project and explain in more detail the motivation for the work. Finally this chapter will conclude with a short overview of the thesis contents.

1.2 Background

The need for high-power single-frequency solid-state lasers has increased dramatically over the last decade. Emerging fields of gravitational wave-detection, LIDAR, spectroscopy and others [1-7] require low noise coherent narrow linewidth sources with high output power, excellent beam quality, high efficiency and a range of operating wavelengths.

Although conventional flash-lamp pump sources have in the past allowed the development of reasonably efficient single-frequency cw and pulsed solid-state laser systems, the advent of narrower linewidth diode pump sources with emission spectra tailored to match the relevant absorption lines in various solid-state laser media, has opened the door for much more compact systems with increased efficiency. This has led to numerous demonstrations of lasers with high efficiency and reliability, as well as good frequency stability, which far exceed the capabilities of typical flash lamp pumped laser geometries albeit with lower output power. Due to the broadband output spectrum emitted by a flash lamp pump source, and the narrower width of the absorption lines in most solid-state laser materials, a large fraction of pump light is not absorbed with the result that the overall efficiencies tend to be rather low. The situation in lamp-pumped systems is further escalated by light being absorbed in high lying energy levels within the laser material, which then decay non-radiatively to the emitting level with the result that the heat loading is rather high requiring large and expensive cooling systems, hence reducing simplicity and compactness of design. A typical lifetime of a flash lamp device is currently around 500-1000 hours whereas a diode device has a lifetime of ~5000-20000 hours [8].

1.2.1 Low power diode end-pumped solid state lasers

Since 1962 when the first diode-lasers were developed [9-11], the recent surge in interest in the use of diode lasers to pump solid-state lasers has lead to the development of numerous devices both research based and commercial that have demonstrated diffraction limited beam qualities, highly efficient outputs and single-frequency operation. The first mention of the use of semi-conductor technology to pump a solid state laser, to our knowledge was by Newman et al [12], who found that radiation near 880nm from the recombination of GaAs diodes, essentially what we know today as an LED (light emitting diode), could excite fluorescence near 1.06μm in Nd:$CaWO_4$. Since then the development and understanding of such devices has leapt forwards to the point where diode-pumped solid-state lasers are now proving to be more commercially viable than their original flash-lamp pumped counterparts. The first demonstration of a diode-pumped solid-state laser was done by Keyes et al in 1964 [13], however due to short operating lifetimes and low output powers, at this point, diodes could not be considered to be practical pump sources. However, in the 1980's, improved fabrication techniques allowed the development of diode lasers with higher output powers and longer operating lifetimes and with this followed growing interest in using semiconductor lasers as pump sources for solid-state lasers [14].

As laser sources themselves, diode lasers have a number of disadvantages compared to solid-state lasers. Firstly, their short energy storage lifetimes limits the scope for producing high pulse energies by Q-switching and catastrophic facet damage limits the maximum achievable output power from a single-mode diode device (to <1W). In order to increase the output power of diode lasers it is necessary to construct a linear array of low power devices, with the result that the beam quality is degraded in the array direction. The typical dimensions of a single-mode diode emitter are ~1μm × ~5μm. A multistripe device will have dimensions of ~1μm × ~200μm, which is ~50 times (M^2 ~50) diffraction limited in the array direction. Many applications require high brightness beams. The brightness B is defined by the following equation [15]:

$$B = \frac{P}{\lambda^2 M_x^2 M_y^2}$$

Where P is the power, λ is the wavelength and $M_{x/y}^2$ are the beam quality factors (M^2 is the factor by which the far-field Gaussian beam divergence angle for a given beam waist diameter is multiplied to give the actual far-field divergence, and as such it is entirely equivalent to the number of times diffraction limited quantity [16]), in orthogonal planes x and y respectively. One of the major attractions of diode-pumped solid-state lasers therefore, is that they can allow the poor beam quality diode-laser output to be converted into diffraction limited output, hence increasing the brightness.

Further increases in diode output power are typically achieved by making longer arrays (known as diode-bars) and two dimensional stacked arrays (known as diode-stacks). The latter can produce cw output powers of several kW.

There are essentially two ways of coupling light from diode lasers into a solid-state laser crystal: side-pumping and end-pumping (Figure 1.1). The side-pumped geometry couples light into the laser medium transversely to the lasing direction and has the attraction that relatively few if any focusing optics are required. A further attraction is that the pump light is generally absorbed in a relatively uniform manner with the result that the temperature gradient and thermally induced stresses are reduced. For these reasons, side-pumped geometries are generally favoured for high-power operation. End-pumping generally requires a more complicated arrangement of optics to focus the pump beam to a small beam size and so that it propagates collinearly with, and overlaps with the laser mode. This generally allows much lower thresholds and higher slope efficiencies to be achieved at low pump powers. However, due to high pump deposition density, and high thermal loading density, thermal effects become a serious problem at high pump powers. For this reason, scaling end-pumped lasers to high power levels is quite challenging. Nevertheless, with careful selection of gain material and laser design, and with effective thermal management, end-pumping can be a very attractive and flexible route to high output power as will be shown in this thesis.

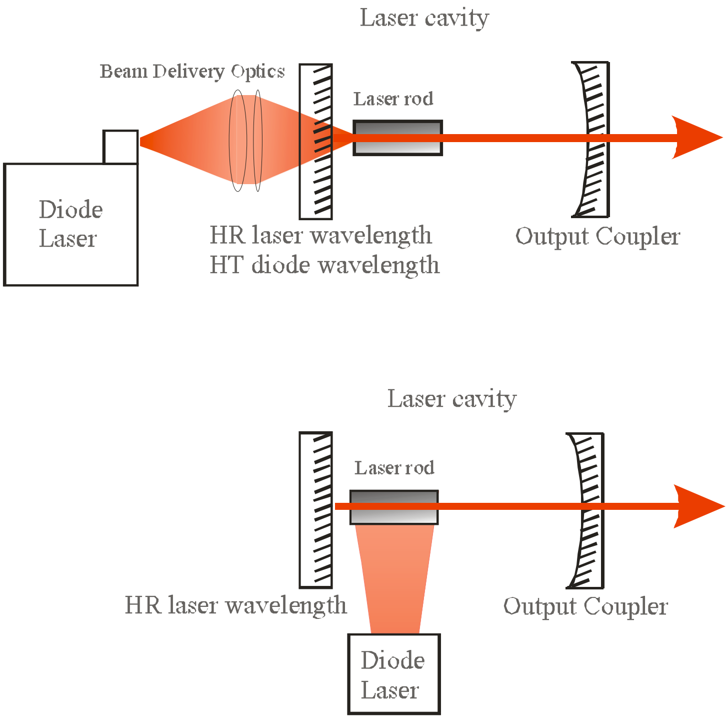

Figure 1.1 Diagram displaying two beam delivery schemes – diode-end-pumping (above) and diode-side-pumping (below).

End-pumped lasers generally consist of four elements, the diode-pump source, the beam delivery optics, the laser cavity and laser crystal. The output wavelength from diode devices can be adjusted, GaAlAs based diodes emit in the region of ~780nm-860nm, whereas InGaAs based devices emit in the region of ~910nm-

980nm. These diodes can be matched carefully in terms of choice of pump source, to material in question, for their appropriate absorption bands, and we also have the flexibility to fine tune diode devices by adjusting their temperature and by so doing, optimising pump light absorption. Diode pump light beam delivery, for low power applications (typically <1W) requires very little in terms of heat dissipation and regulation, and is normally implemented by conventional optics, however more sophisticated techniques for high power applications, where thermal effects can have catastrophically degrading effects, will be discussed later in the thesis.

The laser cavity is designed so that the laser mode matches the pump beam size allowing for efficient power extraction, and TEM_{00} operation. Furthermore, unidirectional operation can eliminate spatial-hole-burning, therefore, in conjunction with a homogeneously broadened laser material, single-frequency operation can be achieved [17].

Besides, what is generally considered to be the most common laser material dopant, Nd^{3+}, which lases at ~1μm, there are several other known rare-earth ions, each of which have been used as part of diode-pumped solid-state lasers to produce various useful output wavelengths, e.g. Ho^{3+} at 2.1μm, Tm^{3+} at 2.0μm and Er^{3+} at 2.8μm, also, by achieving higher population inversion densities by end-pumping Nd^{3+}, operation of the lower gain transitions have been achieved at 946nm and 1.3μm [18-24].

1.2.2 Optical parametric oscillators

Careful selection of laser material can provide laser output over a range of wavelengths throughout the electromagnetic spectrum. However, there are many wavelengths that are simply not directly obtainable via solid-state laser emission. Such wavelengths can be obtained however, via the use of nonlinear frequency conversion schemes. One of the most practical and efficient ways to achieve wide wavelength conversion is via the use of an optical parametric oscillator (OPO). In 1965 the first experimental demonstration of an OPO was reported by Giordmane and Miller using Lithium Niobate [25] as the nonlinear crystal. Two beams with different frequencies travelling through a nonlinear crystal will generate a travelling polarisation wave at a different frequency. Provided that the polarisation wave travels with the same velocity as the freely propagating electromagnetic wave, cumulative growth will result. The two incident waves are termed *pump* and *signal*, having the frequency ν_p and ν_s, and the resulting third wave is termed as the *idler* with frequency ν_i. Under proper conditions, the idler wave can mix with the pump beam to produce a travelling polarisation wave at the signal frequency, phased such that the growth of the signal wave results. The process continues with the signal and the idler waves both growing and the pump wave decaying as a function of distance within the crystal.

Since this first work, huge amounts of research into OPOs has been carried out with the aim of increasing efficiency and wavelength tuneability primarily, in order to provide a more practical alternative to dye based lasers for fields such as spectroscopy. Since early research in the field, a steady stream of new nonlinear crystals have been developed for use in OPOs. Significantly, in 1984 Donaldson and Tang developed an OPO based on crystalline urea, which when pumped using a UV laser produced a visible output. This was superseded by Fan *et al* [26]in 1988 who demonstrated an OPO based on β-barium borate (BBO) as the non-linear crystal with the attraction of improved resistance to damage compared to urea. The discovery of BBO and then later LiB_3O_5 (LBO) by Chen *et al* in 1989 formed the catalyst for several commercial pulsed OPO systems.

One critical design parameter in OPO research is the pump power required to reach threshold, which depends on the OPO design, cavity loss, nonlinear crystal and pump beam size. Although diode-pumped solid-state lasers seem ideal candidates for pumping such devices, for singly-resonant oscillators (SROPOs) the threshold pump power is rather high generally requiring high peak power pump sources (either mode-locked or Q-switched). A seemingly simple solution to this problem was to make the OPO resonant at both the signal and idler wavelengths. Such devices are referred to as doubly resonant oscillators (DROs). However, DRO cavities can be difficult to align and are over-constrained by their requirement to satisfy energy conservation, phase-matching and resonance of both oscillating fields leading to instabilities in the output as sub-nanometre changes in cavity length or MHz changes in the pump frequency cause mode hops in the signal and idler fields.

Hence, for practical reasons SROPOs are generally the preferred configuration for most applications. Adopting an SROPO configuration places heavy demands on the pump laser, particularly if cw oscillation is required. For ~1μm wavelength pumped SROPOs utilising birefringently phase-matched crystals, threshold pump powers typically exceed multiple watts.

1.2.3 Quasi phase-matching

The advent of new designs of nonlinear crystals such as periodically-poled lithium niobate [27] which allow high nonlinear coefficients to be exploited using quasi-phase matching have helped a great deal. The advantage of this is that any interaction within the transparency range of the material can be non-critically phase-matched at a specific temperature, even for interactions where birefringent phase-matching is not possible.

Also, interacting waves can be chosen so that coupling of fields occur through the largest $\chi^{(2)}$ tensor, meaning that the largest available non-linear coefficient can be used, increasing the gain for that interaction and lowering the threshold considerably, thus allowing the user to operate a cw SROPO with a threshold of a few Watts [28-33]. Within an SROPO, the frequency of the resonant wave corresponds with the cavity mode closest to optimum phase-matching. In a true SROPO, the required stability for the cavity length to maintain single mode output is identical to that of a conventional laser:

$$\Delta L_{stab} \approx \pm \frac{\lambda_{res}}{4}$$

where λ_{res} is the wavelength of the resonant wave. The stability requirements of the pump laser are more difficult to calculate since it depends on the phase-matching behaviour, however, assuming that the phase-matching is such that the ratio between the signal and the idler remains constant, for a small change in pump frequency, the stability requirement for the pump laser frequency is:

$$\Delta \nu_{stab} \approx \pm (FSR) \frac{\lambda_{res}}{\lambda_{nonres}}$$

where λ_{nonres} is the wavelength of the non-resonant wave and the FSR is the free spectral range of the device (the difference in frequency between two consecutive interference fringes) given by:

$$FSR = \frac{c}{d}$$

where c is the velocity of light in a vacuum and d is the total round trip distance of the optical cavity. The importance of these equations will be discussed in more detail later in this thesis. It must be noted, however, that in terms of OPO applications that require robust and stable outputs, the importance of SROPO cavity stability (thermal instabilities, pressure changes and mechanical noise with SROPO cavities mean they are very susceptible to mode hopping) and pump laser frequency stability are important in order to achieve single mode operation.

1.2 Thesis overview

The goals of this research project as stated earlier are two fold: (1) To investigate an approach for power-scaling of single-frequency operation from a diode-end-pumped solid-state laser using a novel Nd:YLF MOPA configuration. (2) To demonstrate efficient cw operation of a PPLN SROPO, with particular emphasis on investigating the use of a novel passive technique for suppressing mode-hopping in cw SROPOs to allow mode-hop-free frequency tuning. The results of this work will hopefully provide a starting point for designing more reliable and robust single-frequency SROs with broad tuneability, and hence will be of benefit to a wide range of applications. The most important application for single-frequency OPOs in spectroscopy and of wide interest is the generation of wavelengths in the mid-IR range (3-4μm), where vibrational spectroscopy of the fundamental (and hence strongest) mode of the hydrogen bond in molecules can be performed. The potential for applications is therefore very large, ranging from frequency metrology to basic molecular physics and physical chemistry to more applied studies in the fields of environmental monitoring (trace gas analysis), earth sciences (isotope spectroscopy), plant, animal and human biology (physical process monitoring via molecular gas emissions). The thesis layout is as follows:

Chapter 2 reviews the basic theory for the performance of diode-end-pumped solid-state lasers and techniques for selecting single-longitudinal mode operation. The main problems hindering power-scaling of end-pumped lasers associated with the highly asymmetric nature and beam quality of high power diode pump sources and heat generation in the laser medium are considered. Methods for alleviating the effects of heat loading in end-pumped edge-cooled laser rods are discussed including a brief overview of different laser crystals for operating at high powers.

Chapter 3 considers the design strategy for the single-frequency Nd:YLF master-oscillator, commencing with a detailed discussion of the merits and disadvantages of Nd:YLF as a gain material. The effect of energy-transfer-upconversion (ETU) on laser performance is considered and a strategy for minimising its impact is described. The Nd:YLF resonator design, which employed a passive technique for suppressing mode-hopping, is described and the results for performance are compared with theoretical expectations. Finally, issues which would need to be addressed in order to scale the oscillator power further are discussed.

Chapter 4 describes the design strategy for a first and second stage Nd:YLF amplifier beginning with a brief justification for the use of a MOPA approach for power-scaling rather than a single oscillator. The influence of amplifier design on small signal gain and power gain is discussed, and the effect of ETU and heat loading on amplifier performance and output beam quality is considered in detail. The rationale for the use of a dual rod multi-pass amplifier scheme is explained and the results for the performance are compared with theory. Finally, the prospects for further improvement in performance and the upper-limit to brightness scaling are considered.

Chapter 5 considers the influence of various parameters on OPO performance with a view to establishing a design strategy for cw, single-frequency SROPOs based on periodically-poled nonlinear crystals. This chapter briefly reviews earlier results and focuses in particular on the problem of axial-mode-hopping in SROPOs. The origin of mode-hopping in OPOs is discussed and standard techniques for preventing mode-hopping are considered. Finally, a new passive approach for suppressing mode-hopping is proposed. The rationale for this approach and its limitations are considered.

Chapter 6 describes the design and performance of various continuous-wave OPOs based on periodically-poled lithium niobate. The rationale behind the various resonator designs will be discussed and details of the alignment procedure will be described. The performance with respect to output power, wavelength tuning range and frequency spectrum is described and where possible compared with theory. Finally, prospects for achieving passive suppression of axial-mode-hopping are considered.

Chapter 7 summarises the work presented in this thesis and will discuss some possible future directions.

The work described in this thesis has been carried out whilst registered as a postgraduate student at the Optoelectronics Research Centre at the University of Southampton, England, under the supervision of Dr W. A. Clarkson.

1.3 References

1. Armstrong.M, *Development of a 25 W TEM00 diode-pumped Nd : YLF laser.* Optics Communications, 1999. **169**(1-6): p. 141-148.
2. Baer, T., *10W TEM_{00} output from a diode-pumped solid-state laser.* Conf. Lasers and Electro-Optics, OSA Technical series, 1991. **10**: p. 490.
3. Du, K., et al., *Lasers for materials processing: Specifications and trends.* Optical and Quantum Electronics, 1995. **27**(12): p. 1089-1102.
4. Judy, M.M., *Soft-Tissue Studies with 805 Nm Diode-Laser Radiation - Thermal Effects with Contact Tips and Comparison with Effects of 1064 Nm Nd-Yag Laser-Radiation.* Lasers in Surgery and Medicine, 1993. **13**(5): p. 528-536.
5. Kojima, T., S. Fujikawa, and K. Yasui, *Stabilization of a high-power diode-side-pumped intracavity- frequency-doubled CW Nd : YAG laser by compensating for thermal lensing of a KTP crystal and Nd : YAG rods.* IEEE Journal of Quantum Electronics, 1999. **35**(3): p. 377-380.
6. Kubo, T.S. and T.J. Kane, *Diode-Pumped Lasers at 5 Eye-Safe Wavelengths.* IEEE Journal of Quantum Electronics, 1992. **28**(4): p. 1033-1040.
7. Littler, C.M., *Hair removal using an Nd : YAG laser system.* Dermatologic Clinics, 1999. **17**(2): p. 401.
8. Keirstead, M., *An introduction to diode-pumped solid-state lasers*. 2000, Spectra-Physics Lasers. p. 1-4.
9. R.N.Hall, J.D Kingsley, T.J. Soltys and R.O. Carlson, *Coherent light emmissions from GaAs Junctions.* Physics Review Letters, 1962. **9**(9): p. 366-368.
10. N.Holonyak, *Coherent (visible) light emission from Ga ($As_{1-x}P_x$) Junctions.* Applied Physics Letters, 1962. **1**(4): p. 82-83.
11. T.M.Quist, R.J.Keyes, W.E.Krag , B.Lax, A.L.McWhorter, H.J.Zeigler, *Semiconductor Maser of GaAs.* Applied Physics Letters, 1962. **1**(4): p. 91-92.
12. R.Newman, *Excitation of the Nd^{3+} fluorescence in $CaWO_4$ by recombination radiation in GaAs.* Journal of Applied Physics, 1963. **34**(2): p. 437.
13. R.J.Keyes, *Injection luminescent pumping of $CaF_2:U^{3+}$ with GaAs diode lasers.* Applied Physics Letters, 1964. **4**(3): p. 50-52.

14. B.Zhou, G.J.Dixon and R.L.Byer, *Efficient, frequency-stable laser-diode-pumped Nd:YAG laser.* Optics Letters, 1985. **10**(2): p. 62-64.

15. A.C.Tropper. *Fibre and waveguide lecture notes*. in *Advances in lasers and applications*. 1998. Scottish Universitys Summer Schools in Physics.

16. Siegman, A.E., *Analysis of laser beam quality degradation caused by quatic phase aberrations.* Applied Optics, 1993. **32**: p. 5893-5901.

17. C.L.Tang., *Regular spiking and single-mode operation of ruby lasers.* Applied Physics Letters, 1963. **2**(11): p. 222-224.

18. Hardman, P.J., PhD *Power-scaling of diode-end-pumped solid-state lasers*, in *Optoelectronics Research Centre*. 1999, University of Southampton.

19. Kern, M.A., *MS Thesis*, in *Institute of Laser Physics*. 1997, University of Hamburg.

20. Koechner, W., *Solid-State Laser Engineering*. 4th ed. 1996, New York: Springer-Verlag.

21. Marshall, L. *Laser Diode-Pumped Solid-State Lasers*. in *CLEO 2001*. 2001. Baltimore.

22. Martin, PhD *High power diode pumped single frequency lasers*, in *Optoelectronics Research Centre*. 1996, University of Southampton.

23. Moore, N., *An investigation of laser oscillators and amplifiers using high intensity diode-pumping*, *Optoelectronics Research Centre*. 1998, University of Southampton.

24. Padgett, M.J., *Optical Parametric Oscillators: continuous wave operation*, University of St Andrews: Scotland. p. 209-227.

25. C.Miller, *Tunable coherent parametric oscillation in LiNbO3 at optical frequencies.* Physical Review Letters, 1965. **14**(24): p. 973-976.

26. Fan, Y.X., *Visible Bab2o4 Optical Parametric Oscillator Pumped at 355 Nm by a Single-Axial-Mode Pulsed-Source.* Applied Physics Letters, 1988. **53**(21): p. 2014-2016.

27. Myers, M.M. Fejer and R.L. Byer, *Quasi-phase-matched optical parametric oscillators in bulk periodically poled* $LiNbO_3$*.* Journal of the Optical Society of America B-Optical Physics, 1995. **12**(11): p. 2102-2116.

28. Collville, *Continuous-wave, singly resonant, intracavity parametric oscillator.* Optics Letters, 1997. **22**(2): p. 75-77.

29. D.J.M.Stothard, *Low-pump-threshold continuous-wave singly resonant optical parametric oscillator.* Optics Letters, 1998. **23**(24): p. 1895-1897.

30. I.D.Lindsay, M.H.Dunn and M.Ebrahimzadeh, *Doubly resonant continuous-wave optical parametric oscillator pumped by a single-mode diode laser.* Optics Letters, 1998. **23**(24): p. 1889-1891.

31. P.Gross, T.Walde and K.J.Boller, M.Auerbach, P.Wessels and C.Fallnich, *Fibre-laser-pumped continuous-wave singly resonant optical parametric oscillator.* Optics Letters, 2002. **27**(6): p. 418-420.

32. W.R.Bosenberg, L.E.Myers and R.L.Byer, *93% pump depletion, 3.5W continuous-wave, singly-resonant optical parametric oscillator.* Optics Letters, 1996. **21**(17): p. 1336-1338.

33. W.R.Bosenberg, L.E.Myers and R.L.Byer, *Continuos-wave singly resonant optical parametric oscillator based on periodically poled* $LiNbO_3$. Optics Letters, 1996. **21**(10): p. 713-715.

Chapter 2: Diode-end-pumped solid-state lasers

2.1 Introduction

At relatively low pump powers (typically a few watts), end-pumping is an attractive way to achieve efficient TEM_{00} operation of solid-state lasers. Moreover, end-pumping allows much more flexibility in cavity design and hence in transverse mode selection and hence the ease of achieving diffraction limited performance than is typically possible in side-pumped laser configurations. However, scaling to higher powers is hindered by two problems: Firstly, the highly asymmetric and unfriendly nature of the output beams from high-power diode pump sources, which makes matching the pump beam waist size to the resonator mode more difficult, and secondly, because of heat generation in the laser medium and its degrading effects. In this chapter we briefly review the main design criteria for efficient operation of diode-end-pumped four-level solid-state lasers in the low power regime and techniques for selecting single-longitudinal-mode operation. We then go on to discuss in more detail the main problems hindering power-scaling and ways to alleviate these problems in edge-cooled laser rods.

2.2 Design criteria for the efficient operation of diode-end-pumped four-level solid-state lasers in the low-power regime

2.2.1 Threshold and slope efficiency

Using a simplified rate equation model, approximate expressions for threshold, slope efficiency and hence output power for a four-level diode-end-pumped solid-state laser can be derived which serve as a very useful design aid.

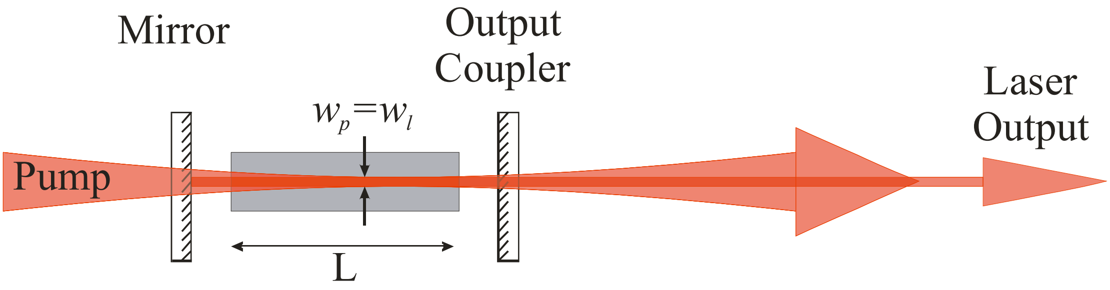

Figure 2.1 Simple plane mirror laser cavity.

For an end-pumped laser with output coupler transmission T, cavity loss (excluding output coupler transmission) L, laser mode size w_L and pump beam size w_P, the laser threshold P_{TH} and slope efficiency η_S are given by:

$$P_{TH} = \frac{\pi h \nu_P (L+T)\left(w_P^2 + w_L^2\right)}{4\sigma_{SE}\tau\eta_q\eta_{abs}}$$

[2.1]

$$\eta_S = \left(\frac{T}{T+L}\right)\left(\frac{\nu_L}{\nu_P}\right)\eta_{abs}\eta_q\eta_{PL}$$

[2.2]

where ν_P and ν_L are the pump and laser frequencies respectively, h is Planck's constant, σ_{SE} is the stimulated emission cross-section, τ is the fluorescence lifetime of the laser material, η_q is the pump quantum efficiency (that is the fraction of absorbed pump photons that lead to excitation in the upper laser level), η_{abs} is the fraction of absorbed pump power throughout the laser rod length l ($n_{abs} \sim 1-\exp[-\alpha l]$), T is the transmission of the laser output coupler and L is the residual round-trip cavity loss assuming that (L+T)<<1. η_{PL} is the effective overlap of the pump beam and the lasing mode (both assumed to have a Gaussian transverse profile) where:

$$\eta_{PL} = \frac{w_{LX} w_{LY} \left(2w_{PX}^2 + w_{LX}^2\right)^{\frac{1}{2}} \left(2w_{PY}^2 + w_{LY}^2\right)^{\frac{1}{2}}}{\left(w_{PX}^2 + w_{LX}^2\right)\left(w_{PY}^2 + w_{LY}^2\right)}$$

[2.3]

The expression threshold in equation 2.1 assumes that the laser and pump spot sizes are equal in the *x* and *y* planes respectively hence equation 2.3 can be approximated to:

$$\eta_{PL} = \frac{w_L^2 (w_L^2 + 2w_P^2)}{\left(w_L^2 + w_P^2\right)^2}$$

[2.4]

Equation 2.3 assumes asymmetric laser and mode profiles where, η_{PL} depends on the spatial overlap of the pump region and lasing mode, and also on the intracavity intensity I to the saturation intensity I_{SAT} where $I_{SAT} \sim h\nu_L/\sigma\tau_f$, in the low power regime where $I/I_{SAT} << 1$. At higher powers where $I/I_{SAT} \to 1$, $\eta_{PL} \to 1$ i.e. η_{PL} accounts for the variation in the slope efficiency with increasing pump power. Physically, this can be interpreted as being due to competition between the stimulated emission and the spontaneous emission in the wings of the pump region. At high intracavity intensities, there is an increased probability that inverted ions will be depleted by the stimulated emission and hence there will be an increase in the slope efficiency.

It can be seen from these expressions that they can be used to develop a design strategy for low power laser operation. To obtain a low threshold and increase slope efficiency, with a fixed output coupler, we need to reduce the intracavity losses (L<<T) and ensure good pump absorption. From the expression for the slope efficiency of the laser, an expression to calculate the output power P_{out} from the laser can then be shown to be:

$$P_{out} = (P_{pump} - P_{TH}) \cdot \eta_S$$

[2.5]

where P_{pump} is the incident pump power and P_{TH} is the threshold pump power. Ideally, the laser cavity design will produce a laser mode equal to or slightly larger than the pump mode preventing undepleted inversion within the gain region and eliminating the possibility of lasing on higher order transverse modes. It follows therefore, that the threshold of the laser is dictated by the minimum pump laser spot size, which in turn is governed by the beam quality M^2 (see next section) of the pump source and the absorption length of the pump light. It has been shown by Clarkson *et al* [1] that there is an optimum spot size for the pump beam, so as to minimise the volume of the Gaussian beam within the gain medium length 'l' and refractive index 'n' (reducing the laser and pump spot sizes will reduce the threshold of the laser) that can be found using the following equation:

$$w_{P\min}^2 = \frac{\lambda l M^2}{\pi n \sqrt{3}}$$

[2.6]

It can been from this expression that in order to reduce w_{pmin}, and hence the threshold of the laser, we have to reduce the '$l\ M^2$' product, that is to say, we have to use a pump source with good beam quality and/or a short laser rod which will therefore need to have a short absorption length.

2.2.2 Single-frequency operation

A four-level laser, in the steady state, with a gain profile that is homogeneously broadened, will operate on a single-frequency, and assuming that the cavity losses are independent of the laser mode frequency, the laser will lase on the axial mode with the highest stimulated emission cross-section. The essential feature of a homogeneously broadened laser is that every atom has the same atomic lineshape and frequency response so that a signal applied to the laser transition has exactly the same effect on all the atoms in the collection. This means that within the linewidth of that specific energy level, each atom has the same probability function for a transition. Homogeneously broadened lineshapes are displayed graphically as Lorentzian lineshapes (see Figure 2.2). The differences between homogeneously and inhomogeneously broadened lasers show up in the saturation behaviour of their transitions. The main feature of a homogeneously broadened transition is that it will saturate uniformly under the influence of a sufficiently strong signal applied anywhere within the atomic lineshape.

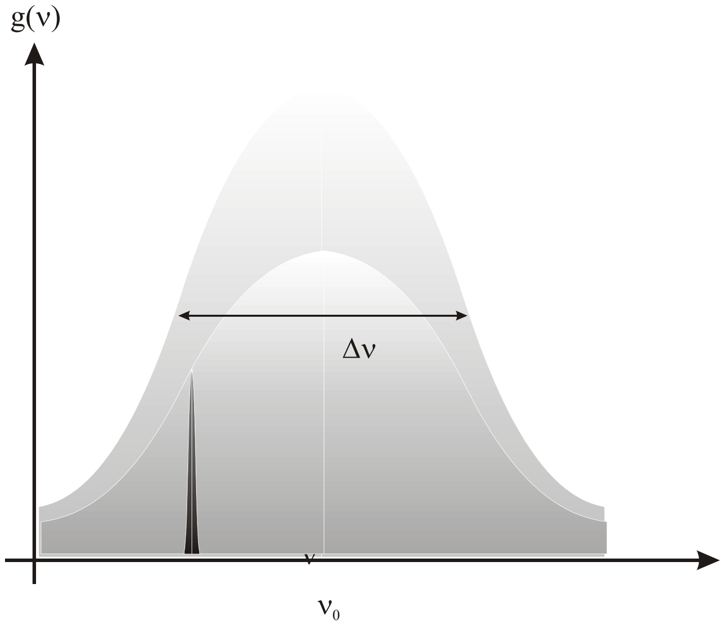

Figure 2.2 Graph showing the Lorentzian distribution of a homogeneously broadened laser gain as a function of frequency.

In the steady-state therefore, the gain of this lasing mode will equal the losses due to the laser cavity, giving it a net gain of unity and all the other axial modes will have a lower stimulated emission cross-section and therefore have gains lower than the threshold of the laser. However, due to *spatial-hole-burning*, causing a spatially inhomogeneous gain distribution, a laser can operate on many axial modes, even when the laser transition itself is homogeneously broadened. This behaviour is generally associated with standing-wave cavities with a sinusoidally varying axial intensity [2].

The mechanism behind spatial-hole-burning is that different frequencies have their standing nodes in different locations, they will access gain from different regions along the length of the laser rod and, as a result of saturation, the spectral distribution of the gain will become inhomogeneous, typically resulting in several axial modes lasing simultaneously as they independently access gain from different regions.

2.2.3 Techniques for single-frequency operation

Numerous methods have been employed to obtain single-frequency operation of a laser[3-7] which fall into two main categories: Firstly, techniques which incorporate a strong frequency discriminating element (e.g. such as an etalon) within the laser cavity in order to suppress adjacent modes from oscillating and secondly, techniques which avoid or reduce spatial-hole-burning. Whilst a frequency selective element will reduce the effect of spatial-hole-burning, it will still be present to some degree and any unused gain at the nodes of the stand-wave laser will lead to an overall reduction in efficiency of that laser. Avoiding or significantly reducing the effects of spatial-hole-burning is less straightforward, but leads to more robust and reliable single-frequency operation.

One of the most popular approaches for reducing spatial-hole-burning and hence achieving robust single-frequency operation is to employ a unidirectional ring-laser configuration. As the beam of the laser cavity is a travelling-wave, spatial-hole-burning is dramatically reduced with only a small standing wave contribution due to reflections from imperfect AR coatings. Ring-lasers have the disadvantage of adding extra complexity to cavity design and the need to introduce an optical-isolator (producing a direction dependent loss within the cavity) in order to enforce unidirectional operation. Optical isolators are generally designed to have low losses so as to not inhibit the performance of the laser (by adding to overall cavity loss), and, even with the need for a ring path within the cavity, a great deal of flexibility in cavity design can be maintained. These points can be demonstrated in monolithic ring lasers [8] and rhomb ring lasers [9]. However, in order to obtain optimised single-frequency operation, one has to ensure that the reflections for the end surfaces of any intracavity components do not overlap with the gain region within the laser rod.

An optical isolator needs to have low loss in the forward (lasing direction), and a higher loss in the backward (non-lasing direction). These isolators should not be confused with other types of optical isolator, that will attempt to reduce the reverse transmission to zero since they have a typical loss difference of <1% (100%

transmission in the forward direction to 99% transmission in the reverse). This small loss is enough to enforce uni-directional and hence single-frequency operation. The two effects that can be used in optical isolators are the acousto-optic effect [10] and the Faraday effect [11]. In acousto-optic modulators, an ultrasonic wave is launched into a block of transparent material, typically fused silica. The transparent material acts like an optical phase grating when an ultrasonic wave passes through it. This is due to the photoelastic effect, which couples the modulating strain field of the ultrasonic wave to the optical refractive index of the transparent material. The result is a travelling grating within the material with a period equal to the acoustic wavelength and an amplitude proportional to the sound amplitude. If a beam of light is incident on this grating, a portion of its intensity will be diffracted out of the beam into one or more discrete directions.

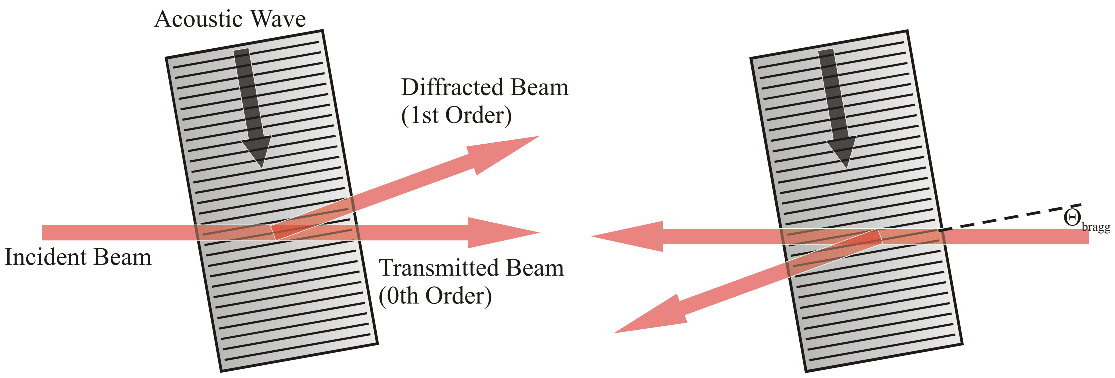

Figure 2.3 Diagram showing a laser beam scattered off the travelling acoustic waves of an acousto-optic modulator. Not to scale (acoustic wavelength is smaller than the beam diameter).

When the frequency of the acoustic wave is raised and its interaction length is increased, the higher order diffracted beams of light are eliminated and the 0th and 1st order beams become predominant (see Figure 2.3). This condition is known as Bragg scattering. For an acousto-optic modulator length l, refractive index n, with an acoustic wavelength Δ, interacting with an optical wavelength λ, the condition for Bragg scattering to occur is:

$$l\lambda \gg \Delta^2$$

[2.7]

In the Bragg regime the optical and ultrasonic beams are slightly offset from normal incidence to interact at the Bragg angle Θ (see Figure 2.3):

$$\sin\Theta = \frac{\lambda}{2\Delta}$$

[2.8]

Where it should be noted that λ, Δ and Θ are all measured inside the medium, that is $\lambda=\lambda_0/n$. An acousto-optic modulator using Bragg reflections from an acoustic travelling wave can be used within a ring laser configuration to provide non-reciprocal loss. Two independent mechanisms exist for acousto-optically induced unidirectional laser operation, namely the *intrinsic* and *feedback* mechanisms.

The intrinsic nonreciprocity of a travelling-wave acousto-optic modulator is a result of the fact that the plane of the moving acoustic wave fronts is at an angle to the optical axis of the laser beam. Looking at the incident laser beams in the forwards and backwards propagating directions (Figure 2.3) the acoustic wave is either travelling towards or away from the incident wavefront. Viewed from the system of the acoustic travelling wave, the incident light will see a small Doppler-shift i.e. in the backwards direction the acoustic wave-front appears to have a higher frequency than the forward direction and hence a smaller wavelength. This results in a small difference in the Bragg angle for the forwards and backwards propagating light beams given by:

$$\Delta\Theta_{Bragg} \approx \frac{2nv_S}{c}$$

[2.9]

When the AOM is tilted slightly away from the Bragg angle, the diffraction efficiency falls off as a sinc^2 function, which is much broader than the difference in the Bragg-angle:

$$\frac{I_1}{I_0} = \sin^2\left(\frac{\Delta\Theta}{2}\right)$$

[2.10]

Hence, since the forward and backward counter propagating beams see different diffraction efficiencies and therefore loss-differences, this intrinsic technique can be used to achieve unidirectional operation and therefore reliable single-frequency operation of a ring laser. In addition to the intrinsic mechanism, there exists a second method based around the feeding-back of the diffracted beams. Under the appropriate conditions, this feedback technique can yield much higher loss-differences than that of the intrinsic technique alone. The feedback mechanism relies on the beam frequency *v*, when diffracted, being shifted by the acoustic travelling wave frequency ν_S. the beams in the forward propagating direction (figure 2.3) are shifted down in frequency $\nu - \nu_S$, whilst in the opposite direction, the beam is shifted up $\nu + \nu_S$. A basic schematic of the feedback oscillator can be seen in figure 2.4:

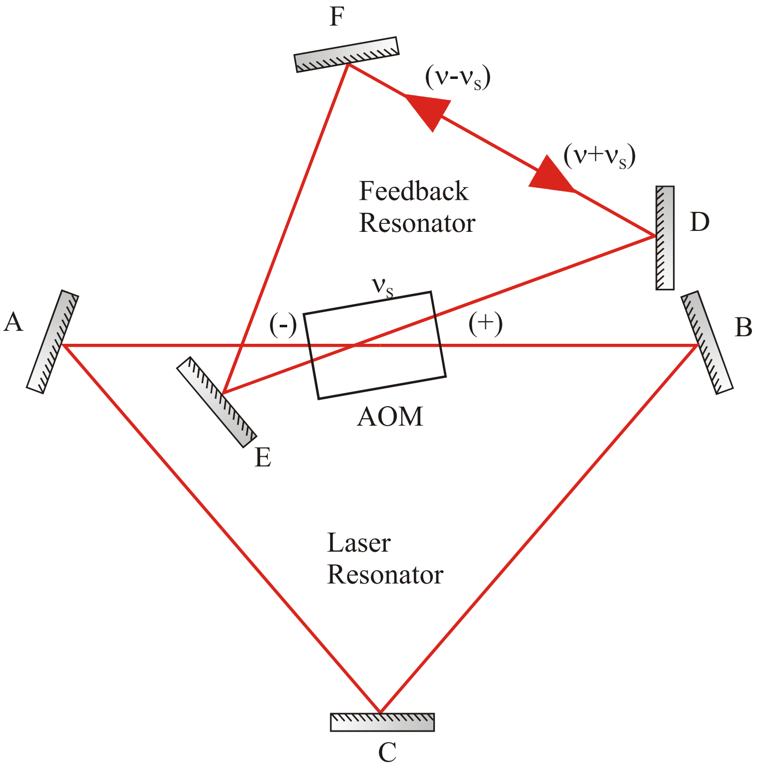

Figure 2.4 Diagram showing acousto-optic travelling wave feedback technique using external ring feedback resonator.

The laser resonator is formed using the mirrors A, B and C. The external feedback resonator is formed by mirrors D, E and F and is fed back into the acousto-optic modulator where it is partially diffracted back into the path of the laser. The path that was originally shifted down to $\nu - \nu_S$ will be shifted up to the original laser frequency so that it can interfere with the main beam. Light in the opposite direction is shifted up to $\nu + \nu_S$ and shifted down when fed back into the laser resonator. The feedback path length is practically the same in both directions, however they experience different round-trip phase shifts causing an interferometrically produced loss-difference, meaning that it can be much larger for a given diffraction efficiency within an acousto-optic modulator than for the intrinsic case[10]). Even though the feedback technique produces larger loss-differences however, the cavity alignment is unstable and complicated to implement. An attractive solution to this problem is to use the mirrors of the laser resonator itself to feedback through the diffracted light (self-feedback technique) since any given change in the cavity length will effect not only the laser but the feedback path as well. It has been observed that this approach will improve the stability of the laser to within two to three orders of magnitude compared to the external feedback resonator, however, the loss of the feedback path will be greater than that of the external resonator due to the number of round trips of each cavity, leading to a higher insertion loss and reduced loss-difference between the opposing cavity directions. There needs to be only a very small loss-difference within a laser ring cavity to ensure unidirectional operation, however, acousto-optic modulators are also especially useful if Q-switching is required. Hardman *et al* [12], demonstrated a Nd:YLF ring laser that utilized the 1^{st} order diffracted beam from the acousto-optic modulator (intrinsic technique) as the output coupling. In this case the AOM allowed Q-switched operation of the laser and also allowed optimised output coupling in a cw regime.

Optical isolators based of the Faraday effect can give a much higher loss-difference than acousto-optic devices at the expense of higher insertion losses due to absorption in the Faraday medium and any incurred anti-reflection coating losses. However, in the cases where a higher loss-difference is needed, they are essential. A typical Faraday rotator optical isolator consists of the Faraday rotator itself with an optical rotator (half-wave plate) and a polariser. In the forward direction, the Faraday rotator, rotates the polarisation of the laser mode, which is then rotated back by the optical rotator to its original position, it then passes through the polariser with the correct orientation for maximum transmission. In the reverse direction, because of the non-reciprocity of the Faraday rotator, the rotations add instead of cancelling, thus causing the light in the backwards direction to see losses at the polariser. In order to calculate the average loss per round trip, it is useful to analyse the laser cavity in question with Jones matrices to find the eigen-polarisations of the resonator (i.e. the state for which the polarisation state is conserved after one round trip).

The thermo-mechanical stresses produced due to power-scaling a uni-directional ring-oscillator leading to stress induced birefringence and mode mismatch between the laser and the pump source can lead to changes in the loss-difference within the cavity, this in turn can lead to mode-hopping due to fluctuations in the optical cavity length and higher order mode oscillation at higher pump powers. Because of this, at higher pump powers, instabilities in single-frequency operation can occur and therefore, careful design considerations must again be made in order to maintain robust and reliable operation.

2.2.4 Diode pump sources

As diode based pump source output powers have been increased over the last decade, thermal loading of laser gain materials has led to increased problems related to power scaling. In the previous section we mentioned the astigmatic output from low power diode devices that could be coupled into a laser material using conventional optics. However, at higher powers, more complex systems are needed due to the highly elliptical output beam and highly asymmetric diffraction properties of the high power diode lasers. Due to improvements in fabrication techniques in the 1980's, diode devices became both reliable and efficient with early devices (typical dimensions of 1μm × 5μm) producing output powers of up to ~200mW. Multi-stripe laser devices were then developed to reduce the risk of facet damage, producing up to a few watts of output power from a device with overall dimensions of around 1μm × ~200μm. Limited by thermal effects, the construction of even longer arrays of these low-power multi-stripe devices lead to devices that are known as *diode-bars*, with even higher output powers.

The emitting area of these devices has typical overall dimensions of ~ 1μm × 10mm, made up of an array of multi-stripe devices each ~ 1μm × 200μm. These multi-stripe devices have a typical centre to centre spacing of ~400μm. Commercial devices based on this technology are readily available with output powers of up to 80W. In the following table 2.1 are a series of example specifications of readily available Coherent diode pump sources (40 and 60W devices). Diode-bars are a very attractive pump-source for solid-state lasers, but their output beam shape is very inconvenient for end-pumped configurations. The output beam is highly elliptical due to the 1μm × 10mm emitter region, and is nearly diffraction limited in the plane orthogonal to the array but is ~2000 times diffraction limited in the array-plane.

Thus, focussing the output to the small beam sizes required for efficient end-pumping of solid-state lasers is very difficult to achieve [1].

Specification	**808nm 1024306[3]**	**808nm 1024306[3]**
Output Power (W)	40	60
Centre Wavelength (nm)	808	808
Centre Wavelength Tolerance (nm)	±2.5	±2.5
Wavelength Temperature Coefficient (nm/^{0}C)	0.28	0.28
Spectral width (FWHM) (nm)	<0.25	<0.25
Array Length (mm)	10	10
No. of emitters	19	49
Emitter Size (μm)	150×1	100×1
Emitter spacing (μm)	500	200
Slope efficiency (W/A)	1.1	1.1
Conversion Efficiency (%)	>45	>45
Threshold Current (A)	<10	<15
Operating Current (A)	45	60
Operating Voltage (V)	1.8	1.85

Table 2.1 Example specifications of Coherent diode pump sources s/n 1024306[3]

The fact that the output from a diode bar is nearly diffraction limited M^2~1 in one plane and is M^2~2000 in the other, has a serious limitations on the optimised focus spot that can be achieved in the array plane using conventional optics. Using equation 2.6 from the previous section, we can calculate that the optimal focussed spot in the array plane for a resonator with a circular mode (M^2~2000) would be ~1.3mm and ~10mm in the x and y planes respectively. Because of this the threshold from equation 2.1 would be respectively larger and poor mode matching between the laser mode and the pump would result.

2.2.5 Diode beam delivery schemes for high-power diode pump sources

Various diode-bar beam delivery systems have been demonstrated over the past few years utilizing, for example, cylindrical and aspheric lenses or multi-prism arrays [13-16], which will allow the user to focus to smaller spot-sizes at the cost of large reductions in brightness from the device.

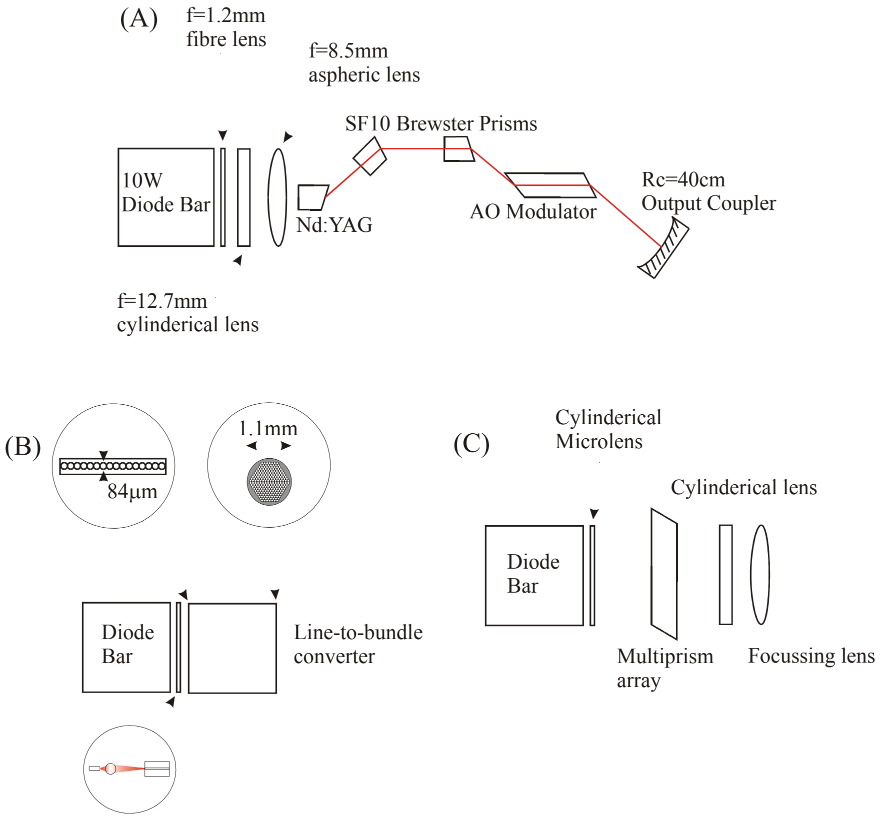

Figure 2.5 Diagram showing three examples of high-power diode coupling techniques, (A) using a cylindrical and aspheric lens [13], (B) fibre-coupled diode bar [17] and (C) multiprism array rotating output from each emitter by 90^0 [16].

The solution adopted for the purposes of this research was to use a simple beam-delivery technique that chops and stacks the output of the diode effectively equalising the beam quality of the diode-bar in both orthogonal planes with only a small decrease in brightness. This scheme, known as the two-mirror-beam-shaper [18], converts the collimated output from a diode bar into a stack of beams, one from each emitter in the diode-bar array. The outcome of this is that the diode-bars original output ($M_x^2 \sim 1$, $M_y^2 \sim 2000$), is equalised so that the beam quality M^2 in the x and y planes is ~ 70.

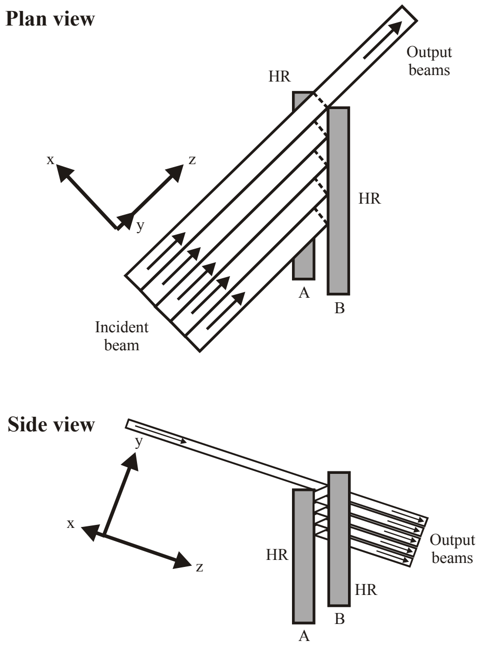

Figure 2.6 Diagram showing the two mirror beam shaper [18].

By beam-shaping the output from the diode in this way (Figure 2.6) we can focus the pump light to a smaller spot size, keeping the 'l M^2' product low. This improved beam quality allows us to focus the output from the diode bar to a relatively small beam size, with a long Rayleigh range, z_0 which is calculated using the following expression:

$$z_0 = \frac{\pi n w_{P(x,y)}^2}{M_{(x,y)}{}^2 \lambda}$$

[2.11]

The beam-shaped output from a diode bar is therefore ideal for end pumping solid-state and fibre laser systems. In addition, the shaped output also allows the light from the diode to be efficiently coupled into an undoped optical fibre with a relatively small core diameter, allowing us to efficiently couple the light from the diode to a laser system without the need for any expensive intermediate optics that would require critical alignment. In the case of these experiments, the pump delivery fibre was undoped silica fibre of 250μm diameter core, with an N.A. = 0.22 and we typically measured coupling efficiencies of up to 85%.

Based on the focussing scheme described in this section, it is possible to estimate the threshold and output power of an end-pumped solid-state laser using equations 2.1-2.5. From equation 2.6, the minimum effective pump beam size (assuming M^2 in the x/y planes is ~70) is decreased dramatically and becomes dependent on length of the laser gain medium. Hence, it can be calculated that for an Nd:YAG laser operating at 1064nm with an output coupler transmission of 10% and a roundtrip loss of 2%, the threshold is ~0.2W. By making $\eta_{PL} \sim 1$and using $w_L = w_P$ (~ 250μm), a maximum TEM_{00} output power of ~8W for 15W of incident pump power can be achieved. Due to the small threshold in relation to the maximum available pump power therefore, it could also be possible to operate the laser on much lower gain transitions, as well as many three-level transitions, proving that the beam-shaper route to diode-end-pumping offers a very attractive route to power-scaling solid-state lasers.

2.3 Thermal effects

2.3.1 Heat Generation

……

Due to the simplicity of mounting and heat sinking, copper mounted edge cooled laser rod geometries have been adopted as a means to dissipate heat from the laser rod. It is the heat extraction from a laser rod that causes a non-uniform temperature gradient across its radius under end-pumped conditions. An expression can be derived for the resulting temperature distribution for an edge cooled rod of radius r_a and length l mounted in a heatsink that is maintained at a constant temperature and end-pumped by a diode laser of incident pump power P_P ,[12] (Figure 2.7).

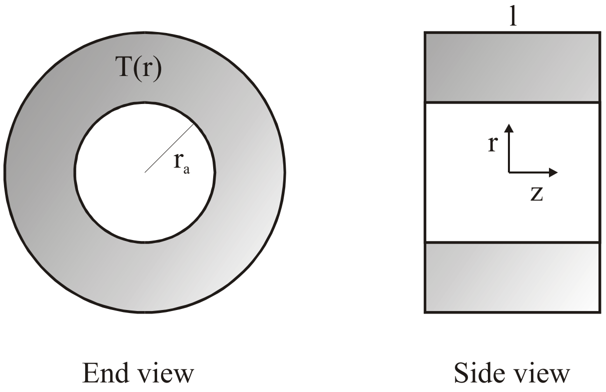

……………………………………………………………………………………………………

Figure 2.7 Simple diagram showing the edge-cooled rod of radius r_a and length l.

It can be shown that the heat flux *h(r,z)* under steady state conditions must satisfy the general equation 2.12:

$$\nabla . h(r,z) = Q(r,z)$$

[2.12]

Where *Q(r,z)* is the absorbed pump power converted to heat per unit volume.

If we now make the assumption that the temperature at the edge of the laser rod is equal to the temperature of the heatsink *T(r)*, from equation 2.12 we can show that the net radial heat flow from the thin disk of radius r and thickness Δz at axial position z [19] by

$$2\pi \Delta z h(r,z) = \int_{z}^{z+\Delta z} \int_{0}^{r} Q(r,z) 2\pi r dr dz$$

[2.13]

This expression neglects axial heat flow within the laser rod. Making further assumptions that the ground state is not significantly depleted, the pump has a transverse Gaussian intensity profile and neglecting diffraction, then *Q(r,z)* can be written as:

$$Q(r,z) = \rho \alpha_P I_P(r,z)$$

[2.14]

where

$$I_P(r,z) = \frac{2P_P}{\pi w_P} \exp\left[\frac{-2r^2}{w_P^2} - \alpha_P z \right]$$

[2.15]

is the pump intensity, ρ is the fraction of absorbed pump power converted to heat, w_P in the $1/e^2$ radius of the pump beam, α_P is the pump absorption coefficient. By substituting eq.2.14 into eq.2.13, we can obtain the expression for the radial heat flux h(r,z):

$$h(r,z)=\frac{\alpha_P\rho P_P}{2\pi}\exp(-\alpha_P z)\left[\frac{1-\exp(-2r^2/w_P^2)}{r}\right]$$

[2.16]

So, it follows that the temperature difference, *ΔT(r,z)* inside the crystal can then be calculated as follows:

$$\Delta T(r,z)=T(r,z)-T(r_a,z)=\frac{1}{K_C}\int_r^{r_a}h(r,z)dr$$

[2.17]

Where K_C is the thermal conductivity. From equation 2.17, we can therefore produce a 3-dimensional picture of the temperature distribution within a laser rod. In the following example a 3mm diameter, 15mm long Nd: YLF laser rod is used, K_c = 6.3Wm^{-1}K^{-1}, α_p = 107m^{-1}, w_p = 250µm, the incident pump power is 20W and ρ = 0.24 assuming quantum defect heating only.

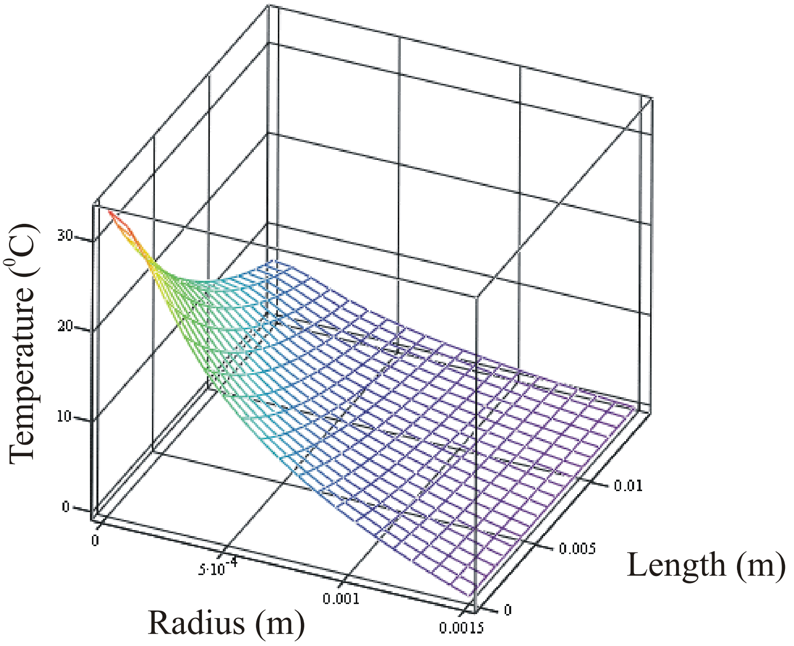

Figure 2.8 Temperature distribution in example 3x15mm Nd: YLF laser rod with K_c=6.3Wm^{-1}K^{-1}, α_p ~107m^{-1}, w_p=250µm, P_p=20W and ρ=0.24.

It can be seen from this figure 2.8 that there is a large radial variation of temperature. The temperature is highest at the centre front end and decays exponentially towards the opposite surface. It is this radial variation of temperature that leads to the main thermal problems of thermal lensing, thermally-induced birefringence and ultimately, stress-fracture.

2.3.2 Thermal Lensing

There are three contributing mechanisms to thermal lensing: Firstly, the temperature dependence of refractive index. Secondly, the mechanical stresses within the laser rod brought about by the temperature gradient within the rod as it undergoes cooling via the heatsink – leading to a stress-induced change in refractive index. Finally, the temperature distribution causes a physical distortion of the end faces of the rod (i.e. end-face bulging).

The model given in the previous section (2.3.1) can be used to derive an expression for the thermal lens power due to the temperature dependent refractive index [12, 20]. The relative importance of this contribution depends on the thermo-optical and thermo-mechanical properties of the laser material. In the case of Nd:YAG lasers, the refractive index variation with temperature accounts for 80% of the contribution to thermal lensing, however for other materials such as Nd:YLF it may be necessary to take into account the contributions to the thermal lens due to the end-face curvature of the laser rod and the stress dependence of the refractive index as well. Here we merely quote the final expression in terms for thermal lens power, where f_{th} is the thermal lens focal length:

$$f_{th}(r) = \frac{2\pi K_C r^2}{P_P \rho \eta_{abs} \frac{dn}{dT} s(r)}$$

[2.18]

where

$$s(r) = \frac{2\pi}{P_P} \int_0^r r' I_P(r') dr'$$

[2.19]

The thermal lens generated within a laser rod can hinder the power scaling of diode-end-pumped solid-state lasers in two ways. Firstly, the lens can affect the mode size of the laser within the resonator leading, at higher pump powers, to poor overlap between the laser mode and the pump mode (allowing the possible lasing of higher order transverse modes which in turn start depleting the gain, restricting single-frequency operation and degrading beam quality) so it becomes essential to have accurate knowledge of how the thermal lens varies with pump power. This leads to difficulties in maintaining TEM_{00} operation over the entire range of pump powers available. Secondly, in general, it can be seen from equation 2.18, the focal length $f_{th}(r)$ varies radially. This is a consequence of the non-uniform transverse intensity profile of the pump beam and hence the non-parabolic phase aberrations that result. Thus, a rapidly varying focal length with radial position implies a highly aberrated thermal lens which will severely degrade laser beam quality. Thus a pump beam with a relatively high on-axis intensity compared to its wings will lead to both a strong and very aberrated thermal lens. As an example we can consider the special cases of *top-hat* and Gaussian pump beam profiles. For a pump beam of radius w_p and a uniform intesity $I_p=P_p/\pi w_p^2$ for $r \leq w_p$ and $I_p = 0$ for $r > w_p$, we can obtain the following expression for thermal lens focal length:

$$f_{th}(r) = \frac{2\pi K_C w_P^2}{P_P \rho \eta_{abs} \frac{dn}{dT}} \qquad (r \leq w_P)$$

$$f_{th}(r) = \frac{2\pi K_C r^2}{P_P \rho \eta_{abs} \frac{dn}{dT}} \qquad (r \geq w_P)$$

[2.20]

From the equations in 2.20 it can be seen that the thermal lens has no high-order phase aberrations within the pumped region (i.e f_{th} a constant value independant of r) but is highly aberatted outside the pump region $r > wp$ where f_{th} is proportional to r^2. This indicates that a laser beam mode size $w_L < w_P$ will experience no degradation in beam quality.

A Gaussian pump beam profile however, with intensity $I_P(r) = \left(\frac{2P_P}{\pi w_P^2}\right)\exp\left(\frac{-2r^2}{w_P^2}\right)$,

will produce a corresponding expression for thermal lens focal length:

$$f_{th}(r) = \frac{2r^2 f_{th}(0)}{w_P^2\left[1-\exp\left(\frac{-2r^2}{w_P^2}\right)\right]}$$

$$f_{th}(0) = \frac{\pi K_C w_P^2}{P_P \rho \eta_{abs} \frac{dn}{dT}}$$

[2.21]

Where $f_{th}(0)$ is the on axis focal length (i.e. at $r = 0$). In contrast with the top-hat beam profile, it can be seen from equation 2.21 that a Gaussian pump beam leads to a much more highly aberrated thermal lens which is in fact two times stronger on axis for the same pump spot and power. Therefore, a Gaussian pump mode profile, whilst providing better mode overlap with the fundamental transverse laser mode leading to lower laser threshold and increased slope efficiency than a top-hat beam, does have the disadvantage of leading to more pronounced beam distortion and degradation in beam quality.

In practice, a typical focused beam from a high-power diode source will have a transverse intensity profile that lies somewhere between the Gaussian and top-hat examples and precise control of the pump beams transverse mode profile is difficult leading to a reduction in available pump power and brightness (sections 2.2.4 and 2.2.5). However, a limited degree of reshaping of the pump beams profile to reduce the aberrated nature of the thermal lens, and hence decreased beam distortion can be achieved by coupling the pump light into a multimode fibre (section 2.2.5).

The strength of the on-axis thermal lens contribution due to temperature dependence of the refractive index for three common laser materials Nd:YAG, Nd:YVO$_4$ and Nd:YLF, assuming a Gaussian pump beam mode profile can be calculated as a useful comparison of the various material properties. Using the same example as in section 2.3.1, where w_P=250µm, ρ=0.24, P_P=20W, the on-axis thermal lens strength can be calculated for Nd:YAG, Nd:YVO$_4$ and Nd:YLF:

	Nd:YAG	**Nd:YVO$_4$**	**Nd:YLF**
dn/dT (K^{-1})	7.3×10^{-6}	3.9×10^{-6}	-2.0×10^{-6}
K_C(Wm^{-1}K^{-1})	13	5.3	6.3
$f_{th}(0)$ (mm)	72	55	-129

Table 2.2 Table showing the calculated on axis thermal lens for Nd:YAG, Nd:YVO4 and Nd:YLF using equation 2.21 where w_p=250μm, ρ=0.24, P_P=20W.

In table 2.2 it can be seen that the Nd:YLF produces a comparatively longer negative thermal lens focal length (on the 1053nm line) due to the small negative change in refractive index. The positive contribution of the lens produced by the bulging end-faces of the laser rod in the case of Nd:YAG and Nd:YVO$_4$ will lead to the thermal lens strength increasing, whereas it must be noted that the same contribution to Nd:YLF will lead to the thermal lens becoming weaker still. This calculation therefore implies that under the same pumping conditions, Nd:YLF will experience a thermal lens that will contribute comparatively less to beam distortion and the degradation of beam quality than Nd:YAG and Nd:YVO$_4$ respectively.

An important consideration is what effect on the TEM$_{00}$ laser operation is imposed by thermally induced lens aberrations. The degradation of beam quality which results from the propagation of light through an aberrated thermal lens can be compared to the effect of quartic phase aberration in a standard spherical lens analysed by Seigman [21], in that we can determine the effect of a Gaussian beam passing through a highly aberrated thermal lens generated by a pump beam with intensity profile $I_P(r)$. According to [21], a laser beam with a Gaussian intensity profile and initial beam quality M_i^2 after propagating through a lens of focal length f will produce a phase distortion $\Delta\phi(r)$:

$$\Delta\phi(r) = \frac{2\pi}{\lambda}\left[\frac{r^2}{2f} - C_4 r^4\right]$$

[2.22]

It suffer degradation in beam quality such that the resultant beam quality factor M_f^2 is given by:

$$M_f^2 = \sqrt{\left(M_i^2\right)^2 + \left(M_q^2\right)^2}$$

[2.23]

Where M_q^2 is due to the quartic phase aberrations of the lens and is given by:

$$M_q^2 = \frac{8\pi C_4 w_L^4}{\lambda\sqrt{2}}$$

[2.24]

w_L is the beam radius and C_4 is the quartic phase aberration coefficient. In general, a thermal lens will produce a more complicated phase distortion than a standard optical lens, but restricting the consideration to situations where $w_L < w_P$, so that higher order terms than the quartic can be neglected, the resulting expression for the beam quality degradation of the thermal lens M_q^2 is given by:

$$M_q^2 = \frac{\rho\eta_{abs}\frac{dn}{dT}}{K_C\lambda}\left[\frac{\pi w_L^2 B}{2\sqrt{2}}\right]$$

where

$$B = 0.5d^2 I_P(r)/dr^2 \text{ at } r = 0$$

[2.25]

Thus from equation 2.23 and 2.25 we can estimate the degradation in beam quality which results after a passage of the laser beam through an aberrated thermal lens, generated by a pump beam with an arbitrary intensity profile.

For a top-hat pump beam $B = 0$ so there is no degradation in beam quality, however, for a Gaussian beam profile, $B = 4P_p / \pi w_P^4$ and hence

$$M_q^2 = \left(\frac{P_p\rho\eta_{abs}\frac{dn}{dt}}{\lambda K_c\sqrt{2}}\right)\cdot\left(\frac{w_L^4}{w_p^4}\right)$$

[2.26]

This expression shows that in addition to the dependence on power dissipated as heat, thermo-mechanical and thermo-optical properties of the laser material, the degradation in beam quality also depends strongly on the ratio of laser beam radius to pump beam radius. Hence, if $w_L \ll w_P$, then the beam quality is less influenced by thermally induced aberrations and the limit where $w_L/w_P \to 0$, then $M^2 \to 1$. Also, if

$w_L \geq w_P$, even a weakly aberrated thermal lens can result in a large degradation in beam quality.

The physical explanation of this phenomenon is that the degradation in beam quality is dependent on the wave front distortions introduced by non-parabolic aberrations in the generated thermal lens [22]. A laser of small beam radius, and hence small Rayleigh range, has wave fronts with a relatively large radius of curvature, because of this, any relative deviation in phase due to an aberrated thermal lens will be much smaller than in the case of a large laser beam. It must be noted at this point, however, that the presence of an aberrated thermal lens is not totally exclusive to the case of end-pumping with high-power diode bars. The ability to generate a strong lensing effect is due to the brightness of the pump sources and low power diodes are generally much brighter than their diode-bar counterparts, hence, they can produce a very aberrated thermal lens. The fact that there is generally little effect seen in beam quality degradation is due to the small spot sizes used in low power cases. So, degradation in beam quality due to thermal lensing in high power cases is due to a combination of thermally induced aberrations and the requirement for comparatively large TEM_{00} mode sizes, with Rayleigh ranges comparable or greater than the thermal lens focal length.

No matter what precautions are taken therefore, end-pumping a solid-state laser will generate a thermal lens, the magnitude of which is determined by the pump beam and the laser material. Using a Gaussian profile to the pump beam in order to reduce threshold and increase laser slope efficiency will lead to a very highly aberrated thermal lens leading to laser mode distortion and degradation in beam quality. A pump beam top-hat mode profile will distort and degrade the laser mode much less at the cost of threshold power and slope efficiency.

2.3.3 Thermally Induced Birefringence

The mechanical stresses within the laser rod, leading to changes in the refractive index via the photo-elastic effect can not only contribute to thermal lensing but can also cause thermally induced birefringence [12, 23], which can dramatically reduce the efficiency when a polariser is used to select a linearly polarised output. Therefore, when using an optically isotropic material such as Nd: YAG (cross-sectional diagram in Figure 2.9), we must force the laser to emit a linearly polarised output by inserting a polariser into the resonant cavity.

Consider point *P* in the diagram (2.9) at this point, there is a radial refractive index of component n_r and a tangential component of refractive index n_ϕ perpendicular to n_r.

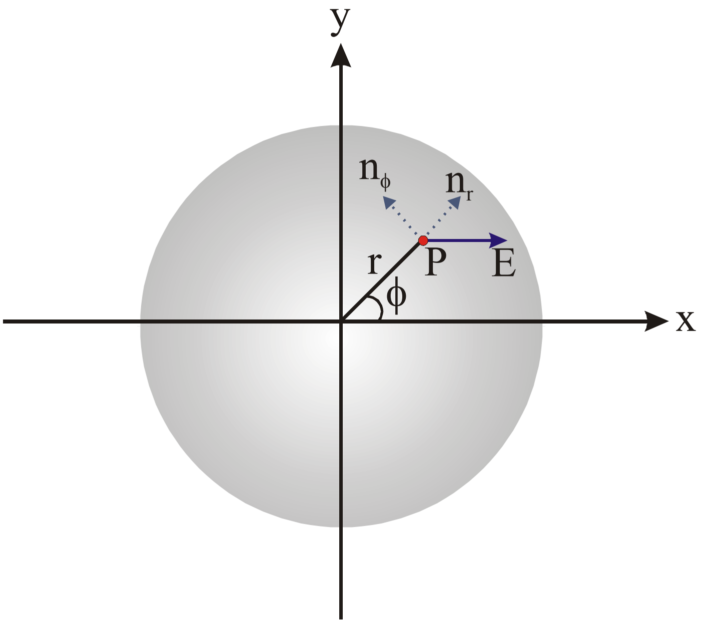

Figure 2.9 Simplified diagram of laser rod cross-section demonstrating thermally-induced birefringence

The propagating radiation in the rod has a polarisation *E*, and so at any point *P* within the cross-section of the laser rod, the polarisation can be resolved into the radial and tangential components, n_r and n_ϕ. Since $n_r \neq n_\phi$ there is a difference between these refractive index components ($\Delta n(r) = n_r(r) - n_\phi(r)$), therefore, there will be a phase difference between the two. The single-pass phase difference will be:

$$\Delta\theta(r) = \frac{2\pi l \Delta n}{\lambda}$$

[2.27]

This phase difference has the effect that any light emerging from the laser rod will be (in general) elliptically polarised and this polarisation state will depend on position P. Because of this, if there are any polarisation selective components within the laser cavity, for example a Brewster plate, there will be an additional depolarisation loss, which can significantly decrease the linearly polarised output from the laser [24].

There are a number of well-established techniques for reducing the effects of stress-induced birefringence. For example, using two laser rods with a 90^0 optical rotator between them, or, in a single rod laser cavity configuration, a Porro prism and a quarter-wave plate can be used. Both techniques can provide a high degree of compensation to the effects of stress induced birefringence but with added complexity and cost to the laser resonator cavity design, and these techniques are also difficult to implement in low-gain end-pumped solid-state lasers which employ small beam sizes.

A simple alternative to reduce the effects of stress induced birefringence is to incorporate a quarter-wave plate into the resonator between the laser rod and the mirror, with its fast or slow axis aligned parallel to the preferred direction of polarisation as defined by the intra cavity polariser [24]. With the quarter-wave plate in position and correctly aligned, any phase shift between radial and tangential polarisation components, due to stress induced birefringence after the first pass of the laser rod is cancelled by the phase shift of equal magnitude but opposite sign on the second pass, with the result that there is no change in polarisation.

2.3.4 Thermally induced fracture

The upper limit on power scaling is the thermal fracture limit of the laser material. The large tensile and compressive forces that are exerted on the laser rod can eventually exceed the maximum stress that can be tolerated by the laser material causing it to fracture or shatter. A reasonable model for this behaviour in laser rods has been derived [25] for the absorbed pump power at the thermal fracture limit in end-pumped systems assuming a "top-hat" pump distribution [2]:

$$\rho P_{abs} = \frac{8\pi S_T}{\alpha_P}$$

[2.28]

where:

$$S_T = \frac{K_C}{\alpha_T Y}\sigma_{\max}$$

[2.29]

S_T is the thermal shock parameter and is dependent on the mechanical and thermal properties of the host material, P_{abs} is the absorbed pump power, Y is the Young's modulus of elasticity of the material, α_T is the thermal coefficient of expansion and σ_{max} is the maximum surface stress at which fracture occurs.

From the equation we can see that the longer the absorption length within the material (ie. the smaller the thermal loading per unit volume), the higher the permitted thermal loading before fracture occurs. The following table (Table 2.3) is a list of typical values of S_T for a number of commonly used laser materials:

Material	**YLF**	**GSGG**	**YAG**	**Al_2O_3**
Thermal Shock Parameter S_T (W/cm)	2	9	11	~100

Table 2.3 Typical values for the thermal shock parameters of different materials.

2.3.5 Power-scaling limitations

The ultimate power-scaling limit of any laser must essentially be determined by the stress fracture limit of the material used [26]. However, numerous brightness dependent applications, such as nonlinear optics and materials processing, require the scaling of higher laser output powers without degradation to beam quality. Since there are numerous techniques for the reduction of the effects of stress induced birefringence, it is degradation due to the highly aberrated nature of the thermal lens that limits the maximum power that can be achieved. We can establish a very rough guide to power scaling limitation by saying that $M_q^2 \leq 0.46$ (corresponding to $M^2 \leq 1.1$) from equation 2.26. The net result from equation 2.26 is that the maximum pump power used P_{pmax} must satisfy the following condition for good beam quality:

$$P_{p\max} \leq \frac{0.65 K_C \lambda}{\rho_\omega^{\ 4} \gamma \eta_{abs} \dfrac{dn}{dT}} \qquad [2.30]$$

where $\rho_\omega = w_L/w_P$. It should be noted that this condition is a very rough guide since it considers only a single pass of the laser rod and is only valid for $w_L \leq w_P$. It may appear from equation 2.30 that the maximum useful pump power is independent of the actual pump beam and laser mode size and is only dependent on their ratio, insinuating that the limit is dependent on pump intensity, however the power scaling limit of the laser cannot simply be increased by using a larger pump beam size. Using a larger beam size to reduce pump intensity, and hence phase aberration necessitates the use of a larger laser mode to allow efficient extraction of the gain. A larger laser mode will have a longer Raleigh range, meaning that it would be more susceptible to beam distortion via phase aberrations, hence the net result of increasing the pump beam size would be to leave the value of M^2 approximately unchanged.

From the point of view of optimising laser efficiency therefore, it could be argued that a better approach is to use the smallest possible pump beam, and hence laser mode size, to allow efficient utilisation of the gain in the wings of the pump region.

This however, would require a high power diode pump source with good beam quality. The main disadvantage of intense pumping is that due to the very strong thermal lensing that will result, TEM_{00} operation can only be maintained over a small power range.

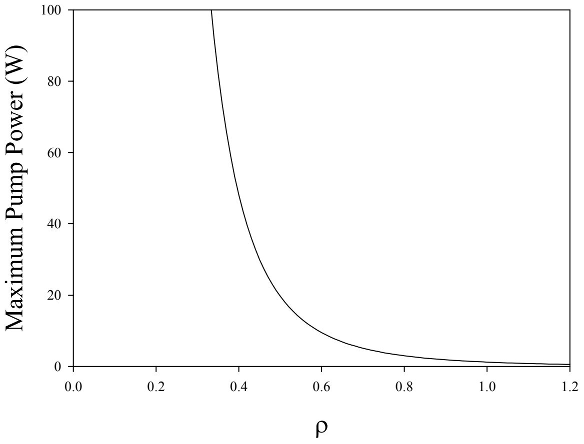

Figure 2.10 Graph showing a rough guide for maximum incident pump power for low TEM_{00} beam degradation of Nd:YAG as a function of ρ_{ω}.

Figure 2.10 suses equation 2.30 to give a rough guide to the maximum pump power that could be used for a diode-pumped Nd:YAG laser at 1064nm for different values of ρ_{ω}. The graph shows that the condition where $w_L \leq w_P$ for good beam quality at low pump powers becomes invalid for pump powers in excess of a few Watts. It follows therefore, that in order to avoid significant TEM_{00} beam distortion, when scaling to higher pump powers, progressively smaller values of ρ should be used. However, if the ratio ρ is too small, the undepleted inversion in the wings of the pump region leads to multi-transverse operation, even when using a resonator selected to satisfy the condition that the TEM_{00} mode sizes decreases with increasing thermal lens focal length. Under these conditions, an aperture is required to provide extra discrimination to prevent higher order mode oscillation. However, since the TEM_{00} intensity is very low in the wings of the pump region it is difficult to use the undepleted inversion, hence the efficiency decreases. The implication of this is that there is a very definite power-scaling limit for diffraction-limited diode-end-pumped solid-state lasers due to thermal lensing.

2.4 Summary

Thermal loading per unit volume due to heat generation within a laser rod due to some of the absorbed pump light being converted to heat leads to degrading effects: thermal lensing, stress induced birefringence and stress induced fracture. Numerous measures can be taken to reduce the likelihood of stress fracture and to reduce the effects of stress induced birefringence. However the highly aberrated nature of the generated thermal lens leads to an upper limit of power-scaling due to the beam quality requirements of a laser source used for applications involving nonlinear optics or materials processing.

One approach to power scaling, rather than resorting to a change of heat sink configuration (i.e. thin disk laser [27]) or the use of compensating components for phase aberration (i.e. phase conjugate holographic resonators [28]), is to use laser materials which have characteristics better suited to operation at high powers. A material of increasing interest in the power-scaling of diode-pumped solid-state lasers is Nd:YVO_4 (neodymium vanadate). The main attraction of Nd:YVO_4 apart from its natural birefringence, is its high $\sigma\tau_f$ product, which is a factor of two times larger than that of Nd:YAG operating on the 1064nm transition. Nd:YVO_4 also has a short absorption length meaning that a much tighter diode-pump focus can be used at 809nm. Its low saturation intensity and the ability to use a relatively small pump mode sizes allows us to better extract the gain from the wings of the laser pump region, and hence we can use resonator designs that allow the scaling of TEM_{00} output to much higher incident pump powers. The main disadvantage with Nd:YVO_4 however is that is exhibits quite a strong thermal lens, comparable with Nd:YAG making it difficult to ensure TEM_{00} operation over the full range of available pump power without the use of apertures. Although the relative merits of Nd:YAG and Nd:YVO_4 have been discussed, Nd:YLF has natural birefringence (making the effects of stress induced birefringence negligible) and more importantly its behaviour in terms of thermal lensing, whereby on the 1053nm line the small negative change in refractive index with increasing temperature, is offset by the positive thermal lens contribution of the bulging laser rod end faces leads to a very weak thermal lens overall. This makes Nd:YLF a good (although possibly unlikely) candidate for use in higher power laser sources, even though it has a much lower thermal fracture limit and a comparatively lower gain cross-section on the 1053nm line than its own 1047nm line and the 1064nm lines of Nd:YAG and Nd:YVO_4.

In order to decrease thermal loading per unit volume within a given laser rod the pump power must be absorbed over a longer length of rod, this could be achieved by temperature tuning the diode-pump-source slightly away from peak absorption or by reducing the crystal dopant concentration, however in order to achieve this, we require pump sources with good beam quality to minimise diffraction along the length of the longer laser rods used.

An added complication to power-scaling an oscillator is that the laser must remain dynamically stable throughout the power range of the incident pump light. That is to say, the change in laser mode size with change in thermal lens must remain small, throughout the entire available pump power range. The combination of the thermal effects within a laser due to the heat generation within the laser rod can not only inhibit the beam quality, TEM_{00} operation, but can also affect the output power of the laser and the robust and reliable single-frequency operation through cavity length fluctuations and changes in mode-matching conditions.

One way of separating power scaling issues from the maintenance of single-frequency operation is to adopt a master-oscillator power-amplifer design strategy. By building a small robust master laser, capable of producing a few watts of output power in a single-frequency, diffraction limited beam and amplifying this via various amplifier chains, we can effectively decouple the problem of maintaining single-frequency operation for power-scaling, also further power scaling can be achieved by the addition of more amplifiers. As long as we can compensate for degradation in beam quality due to the amplifier stages, the master-oscillator power-amplifier approach appears to be a desired design strategy.

In summary to this chapter, we have outlined the various general problems associated with power scaling of diode-pumped solid-state lasers. The development of high-power diode-bars has provided an effective pump source in terms of compact design and lower operating cost at the expense of increased thermally related problems due to the thermal gradient that is generated throughout an edge-cooled laser rod under pumped conditions. These temperature gradients cause thermo-optical and thermo-mechanical stresses throughout the laser rod leading to thermal lensing, stress-induced-birefringence and ultimately stress-induced fracture. These thermal effects can degrade laser output power, beam quality and can lead to instabilities in the maintenance of robust and reliable single-frequency operation.

Certain design strategies can be adopted to compensate for thermal effects such as careful resonator design in selection of TEM_{00} mode selection and laser material properties, however, it appears that a master-oscillator power-amplifier approach would decouple the problems associated with the maintenance of single-frequency operation from power-scaling, making it an obvious choice in terms of design flexibility and future power-scaling prospects.

2.5 References

1. Bollig, C, *2-W Ho : YAG laser intracavity pumped by a diode-pumped Tm : YAG laser.* Optics Letters, 1998. **23**(22): p. 1757-1759.
2. Koechner, W., *Solid-State Laser Engineering.* 4th ed. 1996, New York: Springer-Verlag.
3. Clarkson, W.A., *Acoustooptically Induced Unidirectional and Single-Frequency Operation of a Nd-Glass Ring Laser-Based on the Acoustooptic Effect in the Laser Medium.* Optics Letters, 1994. **19**(24): p. 2059-2061.
4. Evtuhov, V., *A twisted mode technique for obtaining axial uniform energy density in a laser cavity.* Applied Optics, 1965. **4**(1): p. 142.
5. Zayhowski, *Single frequency microchip Nd lasers.* Optics Letters, 1989. **14**(1): p. 24.
6. Hariharan, P., *Concentric etalon for single-frequency operation of high-power ion lasers.* Optics Letters, 1982. **7**(6): p. 674.
7. Kintz, *Single frequency operation in solid state lasers with short absorption depths.* IEEE Journal of quantum Electronics, 1990. **26**(9): p. 1457-1459.
8. Kane, T.J. and R.L. Byer, *Monolithic, Unidirectional Single-Mode Nd-Yag Ring Laser.* Optics Letters, 1985. **10**(2): p. 65-67.
9. Clarkson, W.A., A.B. Neilson, and D.C. Hanna, *Unidirectional operation of ring lasers via the acoustooptic effect.* IEEE Journal of Quantum Electronics, 1996. **32**(2): p. 311-325.

10. Clarkson, W.A., A.B. Neilson, and D.C. Hanna, *Acoustooptically Induced Unidirectional Operation of a Ring Laser - a Feedback Mechanism.* Optics Communications, 1992. **91**(5-6): p. 365-370.

11. Johnston, *Design and performance of a broad-band optical diode to enforce one-directional travelling-wave operation of a ring laser.* IEEE Journal of Quantum Electronics, 1980. **16**(4): p. 483.

12. Hardman, P.J., PhD *Power-scaling of diode-end-pumped solid-state lasers*, *Optoelectronics Research Centre*. 1999, University of Southampton.

13. Shannon, D.C. and R.W. Wallace, *High-Power Nd-Yag Laser End Pumped by a Cw, 10 Mm X-1 Mu-M Aperture, 10-W Laser-Diode Bar.* Optics Letters, 1991. **16**(5): p. 318-320.

14. Baer, T., *10W TEM_{00} output from a diode-pumped solid-state laser.* Conf. Lasers and Electro-Optics, OSA Technical series, 1991. **10**: p. 490.

15. Leger, L. and W.C. Goltsos, *Geometrical transformation of linear diode-laser arrays for longitudinal pumping of solid-state lasers.* Ieee Journal of Quantum Electronics, 1995. **28**: p. 1088-1100.

16. Yamaguchi, S., *Colimation of emissions from a high-power multistripe laser-diode bar with multiprism array coupling and focusing to a small spot.* Optics Letters, 1995. **20**(898-900).

17. Graf, T. and J.E. Balmer, *High-Power Nd-YLF Laser End-Pumped by a Diode-Laser Bar.* Optics Letters, 1993. **18**(16): p. 1317-1319.

18. Clarkson, W.A. and D.C. Hanna, *Two-mirror beam-shaping technique for high-power diode bars.* Optics Letters, 1996. **21**(6): p. 375-377.

19. M.E Innocenzi, H.T.Y., C.L. Fincher, R.A. Fields, *Thermal modeling of continous wave end pumped solid state lasers.* Applied Physics Letters, 1990. **56**(19): p. 1831-1833.

20. Kern, M.A., *MS Thesis*, in *Institute of Laser Physics*. 1997, University of Hamberg.

21. Siegman, A.E., *Analysis of laser beam quality degradation caused by quartic phase aberrations.* Applied Optics, 1993. **32**: p. 5893-5901.

22. Clarkson, W.A. *Resonator design considerations for efficient operation of solid-state lasers end-pumped by high-power diode-bars.* Optical Resonators - Science and engineering., R. Kossowsky (editor.). 1998, Kluwer Academic Publishers. 327-361.

23. Martin, PhD *High power diode pumped single frequency lasers*, in *Optoelectronics Research Centre*. 1996, University of Southampton.

24. Clarkson, W.A., N.S. Felgate, and D.C. Hanna, *Simple method for reducing the depolarization loss resulting from thermally induced birefringence in solid-state lasers.* Optics Letters, 1999. **24**(12): p. 820-822.

25. Chen, Y.F., *Design criteria for Concentration optimisation in Scaling Diode End-Pumped Lasers to High Powers: Influence of Thermal Fracture.* IEEE J. Quant. Electron, 1999. **35**(2): p. 234-239.

26. Clarkson, W.A., *Resonator design considerations for efficient operation of solid-state lasers end-pumped by high-power diode-bars*, in *Optical resonators- Science and Engineering*. 1998, Kluwer Academic Publishers. p. 327-361.

27. Contag, K., *Theoretical modelling and experimental investigation of the diode-pumped thin-disk Yb : YAG laser.* Quantum Electronics, 1999. **29**(11): p. 1025-1025.

28. Hendricks, J.M., PhD *Holographic laser resonators*, in *Optoelectronics Research Centre*. 2002, University of Southampton: Southampton.

Chapter 3: Single-frequency Nd:YLF master oscillator

3.1 Introduction

We established in Chapter 2 that thermal lensing, stress induced birefringence and ultimately stress induced laser rod fracture, brought about by excessive heat generation within a laser material can all contribute to poor beam quality, poor efficiency and unstable longitudinal and transverse mode output. By careful selection of laser material, proper understanding of the nature of these thermally related problems and careful design considerations, it is possible however to develop a laser with TEM_{00} multiple watt output powers, in a near diffraction limited beam that remains both robustly and reliably single-frequency over very long periods of time.

Chapter 2 also gave a brief overview of some reasonably common techniques employed to allow a laser to operate single frequency. The robust and reliable output from a single-frequency laser can be used for optical length and frequency standards, components testing and optical inspections, communications, nonlinear optical pump sources, injection locking and seeding of high-power lasers, precision interferometry and spectroscopy, fibre-optic sensing and LIDAR applications. The need for scaling output powers however, and the heat generation associated with the scaling of such lasers has led to design complications and excessive costs in order to achieve and maintain single-frequency operation. Single frequency lasers have several advantages over multi-frequency lasers e.g. the elimination of beating between axial modes giving greater amplitude stability and the elimination of the so-called “green problem” [1] seen in intra-cavity frequency doubled lasers, whereby coupling between axial modes via sum-frequency generation can cause large fluctuations in output power. As an optical pump source for nonlinear interactions such as optical parametric oscillators, single-frequency lasers have numerous advantages. The detailed spectral properties of the output from an OPO depend on the longitudinal mode structure of the pump source and on the frequency spacing of the OPO cavity. For a singly resonant oscillator, the non-resonant frequency within the OPO is free to adjust so that $\omega_3=\omega_1+\omega_2$ is satisfied. This allows singly-resonant OPOs to have improved spectral stability over doubly resonant oscillators (DROs), we will discuss in more detail these advantages later in the thesis. Also, unlike other laser sources, which can show a power loss as the bandwidth of the laser is narrowed, an SROPO is expected to remain at full efficiency even for a single longitudinal mode since it will behave like a homogeneously broadened source.

The uni-directional ring laser is generally thought to be the most flexible way to achieve a stable source of single-frequency light. Chapter 3 considers the design strategy for the single-frequency Nd:YLF master-oscillator, commencing with a detailed discussion of the merits and disadvantages of Nd:YLF as a gain material. The effect of energy-transfer-up conversion (ETU) on laser performance is considered and a strategy for minimising its impact is described. The Nd:YLF resonator design, which employed a passive technique for suppressing mode-hopping, is described and the results for performance are compared with theoretical expectations. Finally, issues which would need to be addressed in order to scale the oscillator power further are discussed.

3.1.1 Nd:YLF

An alternative laser material that has the potential for scaling up to higher powers is Nd:YLF. Yttrium lithium fluoride (YLF) has the same form as the tetragonal crystal structure scheelite ($CaWO_4$) with yttrium corresponding to calcium, lithium to tungsten and fluoride to oxygen [2, 3].

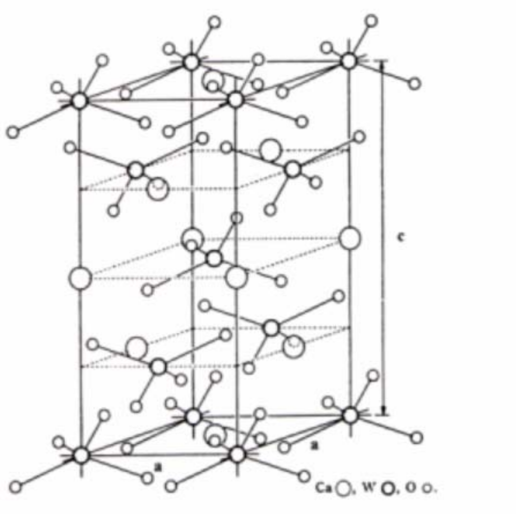

Figure 3.1 Tetragonal crystal structure scheelite ($CaWO_4$) [2].

In Nd YLF, Nd^{+3} substitutes yttrium in the lattice with a concentration of around 1.37×10^{20} cm^{-3} which is equivalent to 1% yttrium being replaced by Nd. Because of its crystal structure, Nd:YLF is naturally birefringent and many of its properties are dependent on the polarisation direction through the crystal. Table 3.1 shows the various material properties of Nd:YLF compared to another commonly used laser material Nd:YAG [4]:

Material Property	Nd:YAG	Nd:YLF
Heat Conductivity at 300K($Wm^{-1}K^{-1}$)	13	6
Expansion Coefficient α_T ($10^{-6}K^{-1}$)	8.2	c:8,a:13
Elastic Modulus (GPa)	310	75
Poisson ratio	0.3	0.33
Refractive index at ~1μm	1.82	π:1.470,σ:1.448
dn/dt at 300K ($10^{-6}K^{-1}$)	7.3	π:-4.3,σ:-2.0
Tensile strength (10^7 Nm^{-2})	21	3.3

Table 3.1 Various material properties of Nd: YAG and Nd: YLF

Nd:YLF has the attraction that on its σ-polarisation (corresponding to 1053nm operation in table 3.1) the thermal lensing is very weak. This is due to a combination of a small change in refractive index with temperature dn/dT ($\sim$-$2.0\times10^{-6}K^{-1}$) and a positive contribution to thermal lensing from end-face bulging which offsets the negative lensing. The net result is that for the same pumping conditions and hence, amount of heat generation, the thermal lens on the 1053nm transition in Nd:YLF is ~6 times weaker than in Nd:YAG. However, Nd:YLF does suffer from the problem that its has a stress-fracture limit that is ~ 5 times lower than that of Nd:YAG meaning that in previous experiments involving 1% dopant concentration Nd:YLF thermal fracture was found to occur for diode pump power in the range of ~14W of absorbed pump power [2] in a pump waist size of ~100µm. Nd:YLF also has the disadvantage to suffer largely from energy transfer up-conversion, resulting in a significant reduction in the fluorescence lifetime τ_f and a significant increase in the thermal loading which places extra constraints on the laser.

In Chapter 2, we mentioned the spectroscopic losses that are encountered within Nd: doped laser materials. Several authors [5-12] have measured the Stark-energies of various multiplet levels in Nd:YLF. Although the majority of heat generation at low powers within these materials is due to quantum defect heating, as the incident pump power is increased, other spectroscopic losses, namely energy transfer upconversion, that are present and increase non-linearly with increasing pump power dramatically increasing heat generation and its detrimental effects.

Figure 3.2 shows a simplified energy level diagram for Nd:YLF, displaying fluorescence and the various spectroscopic losses that lead to excess heat generation. Pump radiation (797nm) is absorbed from the ground state ($^4I_{9/2}$) to the pump level ($^4F_{5/2}$) from where it non-radiatively decays to the upper-laser level. Under non-lasing conditions, the upper-laser level decays via four fluorescent processes emitting at ~1830nm ($^4F_{3/2}\rightarrow{}^4I_{15/2}$), ~1330nm ($^4F_{3/2}\rightarrow{}^4I_{13/2}$), ~1050nm ($^4F_{3/2}\rightarrow{}^4I_{11/2}$) and ~900nm ($^4F_{3/2}\rightarrow{}^4I_{9/2}$) as well as via phonon decay on the transition $^4F_{3/2}\rightarrow{}^4I_{15/2}$ [2].

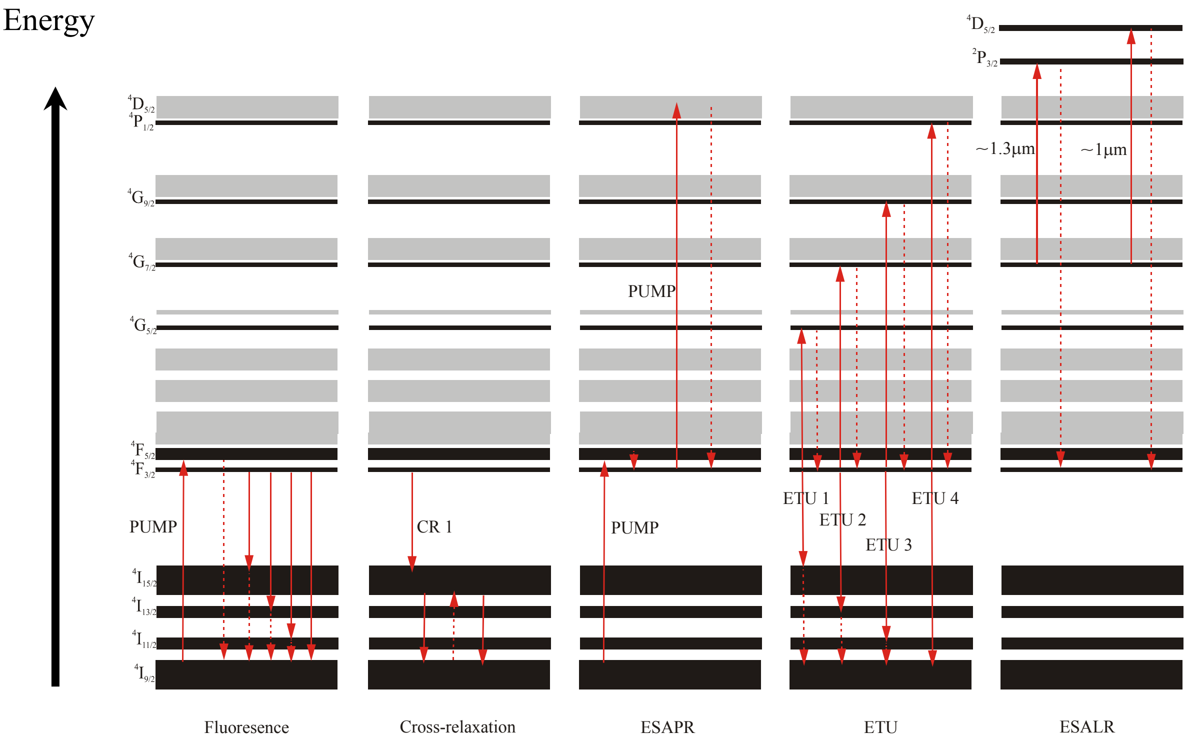

Figure 3.2 Diagram showing various energy levels for Nd^{+3}, displaying fluorescence and various spectroscopic loss mechanisms. ESA PR/LR – excited state absorption of pump radiation / laser radiation. ETU – Energy transfer up-conversion. CR – cross relaxation. All dashed lines indicate heat generating processes[2].

These processes are shown in figure 3.2 by a solid arrow and the following mulitphonon decay by a dotted arrow. In 1998, Pollnau *et al* [11], utilised the branching ratios B_{4j} from the $^4F_{3/2}$ level (including radiative and mulitphonon decay) and the fluorescence wavelengths to calculate the fraction of absorbed pump power ρ_{nl} converted to heat, under non-lasing conditions, without the effect of energy transfer up-conversion (see later in the Chapter). Assuming that all the fluorescence processes occurred from the lowest Stark level in the $^4F_{3/2}$ multiplet and using a pump wavelength of 797nm, a value of ρ_{nl} ~ 25% was obtained. This is only a small increase from the quantum defect heating, under lasing conditions, of ~24% [2].

Cross-relaxation occurs where an excited ion transfers part of its energy to an unexcited ion so that both are in the $^4I_{15/2}$ level. Excited state re-absorption of the pump (ESAPR) occurs when an excited ion in the $^4F_{3/2}$ multiplet absorbs a pump photon and is excited up to the $^2D_{5/2}$ multiplet. Excited-state absorption of the laser radiation (ESALR) is when an excited ion in the $^4G_{7/2}$ multiplet (which can be populated by ETU) absorbs a laser photon and is excited to either the $^4D_{5/2}$ or the $^2P_{3/2}$ multiplets (this is a very weak effect because the lifetime of the $^4G_{7/2}$ multiplet is very fast. One effect that has to be considered in any power-scaling approach on any Nd doped laser is that of energy transfer up-conversion (ETU) [10-16], whereby, one excited ion in the upper laser level, relaxes down to a lower lying levels and transfers its energy to a neighbouring excited ion, also in the $^4F_{3/2}$ level, which is the raised (up-converted) to a higher level.

Figure 3.3 shows the absorption spectra for a 1.15% doped Nd: YLF rod taken with a Perkin-Elmer spectrophotometer [2], in the wavelength range of interest for diode pumping. It can be seen that the two highest absorption peaks occur at 792nm and 797nm respectively, for light polarised parallel to the c-axis of the crystal. It must be noted that since a diode pump source has a finite bandwidth (typically ~3nm) that there will be a distribution of absorption coefficients within the laser rod itself. If the diode pump source were to be temperature tuned away from the material absorption peaks, most of the pump light will be absorbed along a longer length of crystal, however the light closer to the absorption peak will be absorbed over a much smaller distance. This in itself can have important consequences when designing a laser with the aim of reducing up-conversion, thermal lensing and the chance of thermal fracture.

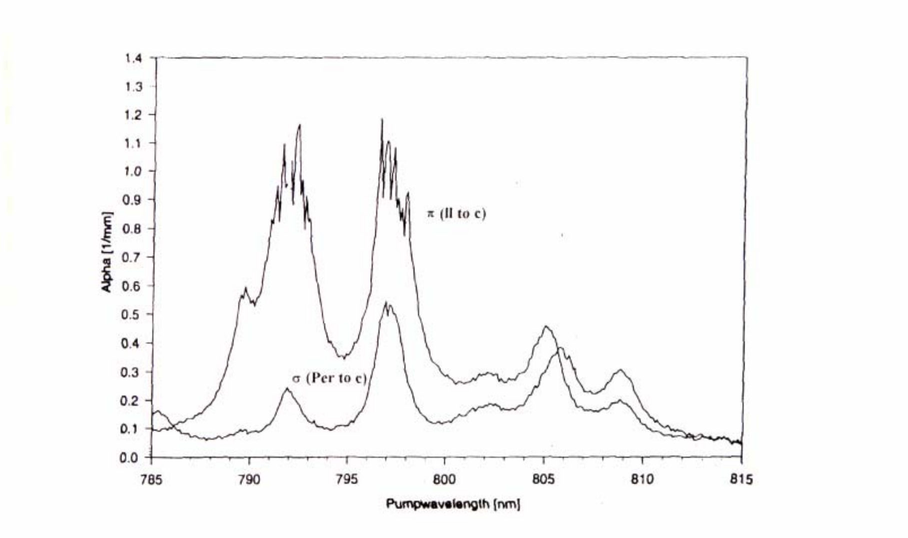

Figure 3.3 The measured absorption of Nd: YLF NB. The noise on the two largest absorption peaks is caused by the lack of sensitivity of the detector at the probe light wavelengths.

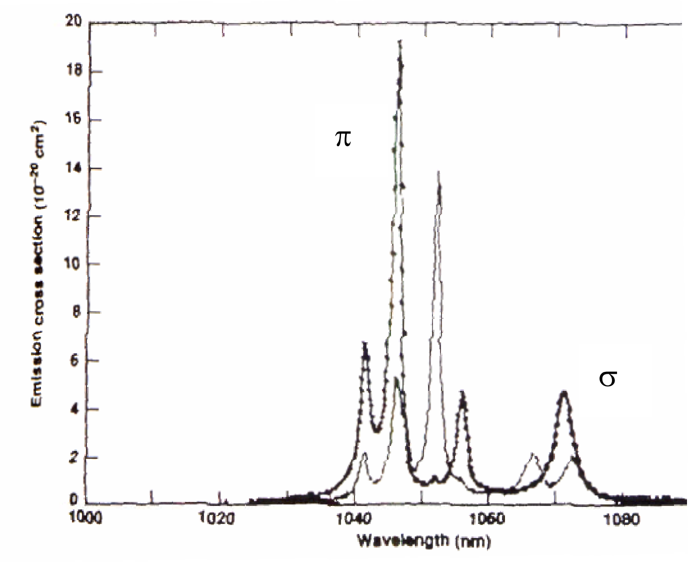

Figure 3.4 The calculated emission cross-section [17] for light polarised parallel to the crystal c-axis (π polarisation) and light perpendicular to the crystal c-axis (σ polarisation).

Figure 3.4 shows the calculated emission cross-sections for the Nd $^4F_{3/2}\rightarrow{}^4I_{11/2}$ transition in Nd:YLF [17]. The two lines with the largest cross-section occur at 1053nm (σ polarisation) and 1047nm (π polarisation). The upper-laser lifetime has been measured to be ~485μs [17] which is approximately twice that of Nd: YAG [4]. This feature of Nd: YLF was of particular interest for high power Q-switched operation and amplifier stages because of the longer energy storage time. It has been suggested and recently researched that degradation in the use of Nd: YLF for Q-switched operation [2] is due to energy transfer up-conversion.

3.1.2 Energy transfer up-conversion in Nd:YLF

Figure 3.5 shows the ETU mechanisms in Nd:YLF and their related energy levels. ETU is a dominant spectroscopic loss mechanism in Nd:YLF at high pump powers and has two degrading effects: Firstly, it reduces the upper laser level lifetime or storage lifetime hence degrading the performance of a Q-switched laser or amplifier.

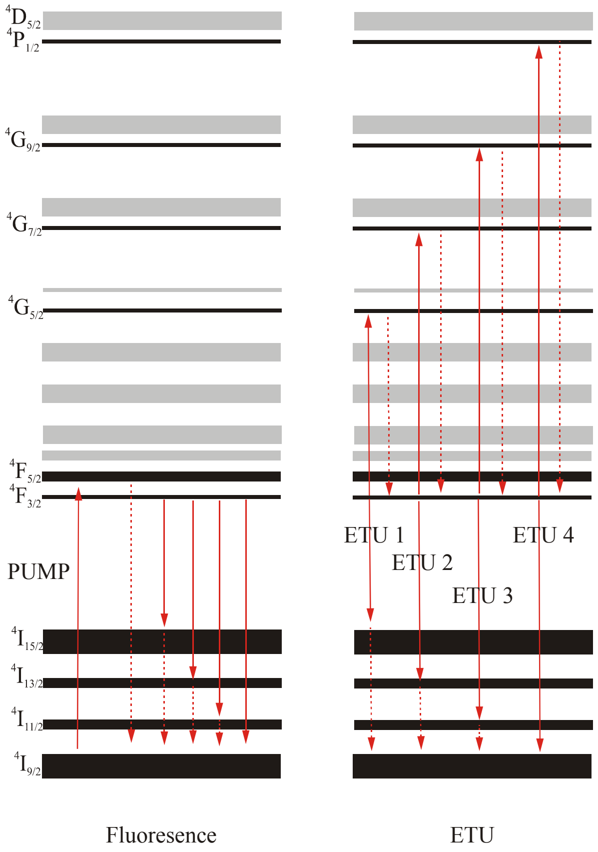

Figure 3.5 Diagram displaying expanded view of ETU mechanism in Nd: YLF

Secondly, ETU increases the heat generated inside the laser material via non-radiative decay, increasing thermal loading and hence, effects such as thermal lensing, stress induced birefringence (a negligible effect due to the natural birefringence exhibited by YLF) and the likelihood of thermal fracture.

3.1.3 The effect of ETU on Nd:YLF fluorescence lifetime

All the spectroscopic processes described in section 3.1.1 will increase heat loading via non-radiative decay indicated by the dotted lines on the diagrams (Figs 3.2 and 3.5), ETU, the dominant spectroscopic loss in Nd:YLF at high excitation densities, can be derived using a simple rate-equation approach describing an approximate analytical model for the effect on the upper laser level storage lifetime within Nd: YLF due to ETU:

Levels $^4I_{11/2}$, $^4I_{13/2}$, and $^4I_{15/2}$ exhibit a fast decay to the ground state and levels $^4F_{5/2}$, $^4G_{5/2}$, $^4G_{7/2}$ and $^4G_{9/2}$ exhibit fast decay to the upper laser level, and we can describe the combined effect of different ETU processes expressed by a single up-conversion parameter *W*. Also, we make the assumption that the net effect is the removal of only one excited ion from the $^4F_{3/2}$ level by each up-conversion process since an up-converted ion will decay back to the upper-laser-level.

Under steady-state non-lasing conditions:

$$\frac{dn(x,y,z)}{dt} = r(x,y,z) - \frac{n(x,y,z)}{\tau} - Wn(x,y,z)^2 = 0$$

[3.1]

where *R(x,y,z)* is the pump rate per unit volume, τ is the fluorescence lifetime of the laser material and *n(x,y,z)* is the upper laser level population density.
From equation 3.1 we obtain

$$n(x,y,z) = \frac{-\tau^{-1} + \left[\tau^{-2} + 4Wr(x,y,z)\right]^{\frac{1}{2}}}{2W}$$

[3.2]

We can also include a term for ground state bleaching (GSB) where in cases of sufficiently intensely pumped lasers, there are sufficient ions excited to the upper-laser level to significantly deplete the ground-state. This process reduces the pump absorption efficiency so we can modify the pump rate *R(x,y,z)*:

$$r(x,y,z) \approx \sigma_P N_0 \frac{I_P}{h\nu_P}$$

[3.3]

Where $N_0 = N_d - n(x,y,z)$ and N_d is the Nd^{3+} dopant concentration and *n(x,y,z)* is the excited population density. So the steady state excitation density including the effects of ground-state bleaching becomes [2, 10-12]:

$$n(x,y,z) = \frac{-\left(\tau^{-1} + C\right) + \left[\left(\tau^{-1} + C\right)^2 + 4WCN_d\right]^{\frac{1}{2}}}{2W}$$

[3.4]

where $C = \sigma_P I_P / h \nu_P$

Hence, the effective storage lifetime, taking into account up-conversion and ground-state bleaching is:

$$\tau_{eff}^{-1} = \tau^{-1} + Wn(x,y,z)$$

[3.5]

From this equation we can compare the effect of up-conversion on the fluorescence lifetime of Nd:YLF for different dopant concentrations under different pumping conditions. For example a Nd:YLF rod absorbing 20W of incident pump power in a spot size of 250μm (under non-lasing conditions) would show a dramatic reduction in fluorescence lifetime τ =485μs down to 355μs for a rod with 1% atomic dopant concentration. Under the same pumping conditions, the lifetime would be reduced to only 402μs for a 0.5% dopant concentration. Under lasing conditions, when the upper population is clamped at threshold (say 1.5W), a 1% dopant concentration rod would have its lifetime reduced to 467μs and a 0.5% rod would be reduced to 476μs. From these simple calculations the importance of reducing the dopant concentration within the laser rod and increasing its length to reduce the thermal loading per unit volume via optical pumping using pump sources of reasonable beam quality seems paramount when reducing the effects of up-conversion.

3.1.4 The effect of ETU on Nd:YLF laser threshold

The derivation in Appendix 2 modifies the analysis of Kubodera and Otsuka [18] and Clarkson *et al* [19] to include terms for ETU in the calculation of diode-end-pumped solid-state laser.

The rate equation of the excited state population can be given by:

$$\frac{dn(x,y,z,t)}{dt} = r(x,y,z,t) - c_n \sigma s(x,y,z,t) n(x,y,z,t) - \frac{n(x,y,z,t)}{\tau_f} - Wn^2(x,y,z,t)$$

[3.6]

where σ is the stimulated emission cross-section. The rate equation of the total number of photons in the laser cavity mode can therefore be expressed as:

$$\frac{dS}{dt} = \int_{Cavity} c_n \sigma n(x,y,z,t) s(x,y,z,t) dV - \gamma S(t)$$

where [3.7]

$$S(t) = \int_{Cavity} s(x,y,z,t) dV$$

n(x,y,z,t) is the population inversion density, *r(x,y,z,t)* is the pump-rate per unit volume, *s(x,y,z,t)* is the photon density, c_n is the velocity of light in the laser medium, $\gamma = 1/\tau_c$ where τ_c is the cavity photon lifetime and W is the up-conversion parameter of the laser material.

Under steady state conditions

$$\frac{dn}{dt} = \frac{dS}{dt} = 0 \qquad [3.8]$$

When the up-conversion parameter $W \to 0$ we get the expression for threshold without ETU:

$$P_{th\alpha 0} = \frac{\gamma I_0 c_n l_c \pi h \nu_P w_P^2}{2 c \eta_q} \left[1 - \exp\left[\frac{-2 w_P^2}{w_L^2} \right] \right]^{-1} \qquad [3.9]$$

substituting for $\gamma = c(L+T)/2l_c$ and I_0 we get:

$$P_{th\alpha 0} = \frac{\pi h \nu_P (L+T) w_P^2}{4 \sigma_{SE} \tau_f \eta_q} \left[1 - \exp\left[\frac{-2 w_P^2}{w_L^2} \right] \right]^{-1} \qquad [3.10]$$

where L is the intracavity loss of the laser not including the output coupler transmission T, σ_{SE} is the stimulated emission cross-section, w_p and w_L are the pump and laser spot sizes respectively, ν_p is the pump frequency, α_p is the laser material absorption coefficient, η_q is the quantum defect and τ_f is the fluorescence lifetime. So finally we can express the equation for laser threshold including the effects of ETU in terms of the expression for laser threshold without the effects of ETU:

$$P_{th} = P_{th\alpha 0}\left[1+\frac{\tau_f W\alpha_P(L+T)}{4\sigma_{SE}}\left[1-\exp\left[\frac{-2w_P^2}{w_L^2}\right]\right]^{-1}\right] \quad [3.11]$$

A numerical analysis and comparison with experimental result of the effect of ETU of laser threshold can be found later in this chapter.

3.1.5 Thermal lensing effects in Nd:YLF due to ETU

With ETU still being expressed as a single parameter *W* [10] it can be shown that the ratio of the heat loading and hence thermal lens power with and without upconversion under non-lasing conditions can be shown to be [2]:

$$\Gamma = \frac{1}{\rho_{nl}}\left\{1-\frac{2(1-\rho_{nl})}{\beta}\left[2\left(\sqrt{1+\beta}-1\right)+\ln\left(\frac{4}{\beta}\left(\frac{\sqrt{1+\beta}-1}{\sqrt{1+\beta}+1}\right)\right)\right]\right\}$$

[3.12]

where ρ_{nl} is the fraction of absorbed pump power converted to heat without ETU, and β is a dimensionless parameter described as being the measure of the magnitude of the effect of up-conversion on the overall decay rate from the upper laser level:

$$\beta = \frac{8WP_P\alpha_P\tau^2}{\pi w_P^2 h\nu_p}$$

[3.13]

where W is the up-conversion parameter, P_P in the incident pump-power, α_P is the absorption coefficient for the pump radiation, τ is the fluorescence lifetime of the upper laser level, w_P is the pump spot size and ν_p is the pump frequency.

Figure 3.7 shows Γ as a function of β for the situation where $\rho_{nl} \approx 0.25$.

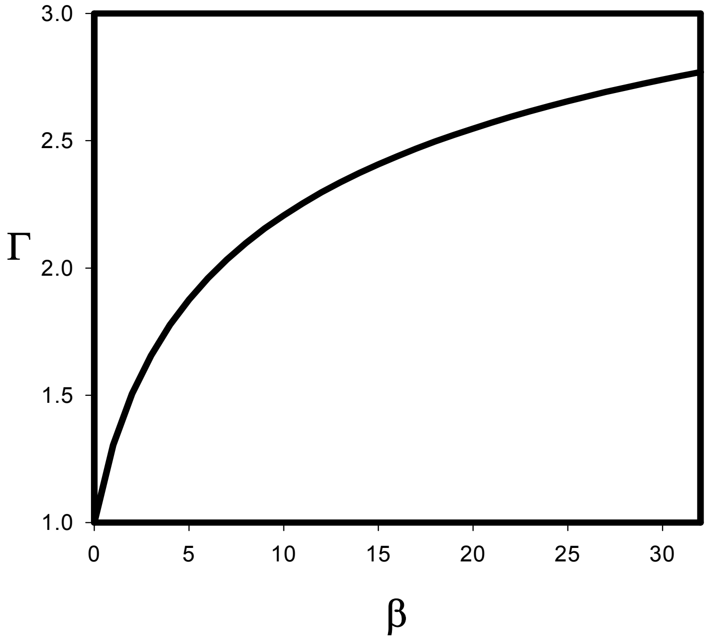

Figure 3.6 The dimensionless parameter Γ against β for ρ_{nl}=0.25.

The significance of the graph in figure 3.6 is that it shows the net effect of the combination of pump power, absorption, up-conversion and spot-sizes on the ratio of thermal lens powers with and without ETU under non-lasing conditions (i.e. where the population inversion is not clamped at threshold as it would be under lasing conditions). If β was 0 then it would follow that the ratio of the thermal lens with and without up-conversion would be equal.

If β ≈1.3 then the power of the thermal lens will have increased by ~ 30% due to up-conversion; to ensure that the increase in power of the thermal lens due to up-conversion is less than 30%, the upper-limit on β must be 1.3. It must also be noted that since equation 2.12 in Chapter 2, shows the dioptric power of the centre of the pump region, and since ETU is much smaller in the wings of this region due to the transverse distribution of the pump, the upper limit on β can be somewhat more relaxed.

3.1.6 Design strategy for Nd:YLF lasers

The presence of ETU in Nd:YLF lasers operating at high incident pump intensities combined with its low thermal fracture limit, has limited Nd:YLF lasers to relatively low output powers. However, with new higher brightness pump beam delivery systems enabled by developments such as the two mirror beam-shaper [20], a solution to thermally related problems can be presented.

This solution involves the use of longer laser rods combined with distributing the pump deposition over a longer length of rod by detuning the pump sources away from the absorption peak or, alternatively, by using laser rods with a lower Nd^{3+} dopant concentration. The pump beam, with its improved beam quality, can be focused to a relatively small size, but with a longer Rayleigh range, chosen to be comparable or longer than the absorption length for the pump wavelength. Because of this, the pump waist size can be kept reasonably constant over the length of the Nd:YLF crystal. As mentioned before, previously adopting this strategy, for a 1% dopant concentration Nd:YLF rod, experimental results showed that thermal fracture of the rod occurred between 10-14W of absorbed pump power, when using a pump beam radius of ~300µm. Using a 0.5% dopant concentration however, in a crystal length of 15mm, and using a wavelength, slightly detuned away from peak absorption at ~792nm giving an absorption length of ~6mm, allowed diode-end-pumping through the opposite end faces of a Nd:YLF laser rod by two 20W diode-bars [2], both of whose outputs were focused to ~300µm, without the risk of fracture. Using this approach, up to 11W cw output has been demonstrated at 1053nm TEM_{00} beam with $M^2<1.1$. The major attraction to this approach was the relatively weak thermal lens as the laser mode size typically varied by less than 10% over the full range of pump power. Adopting this design strategy allows for more flexibility in cavity design since the phase aberration is relatively small. Further reduction in dopant concentration, improvements to diode output beam quality and the possible use of multiple rod geometries could allow significant further power-scaling of TEM_{00} output, without risk of thermally induced stress-fracture. Because of these properties, Nd:YLF is an attractive alternative to more commonly used laser materials such as Nd:YAG and $Nd:YVO_4$ for high-power end-pumped solid-state laser systems.

3.2 Single-frequency selection, Mode Hopping and Mode Hop Suppression

3.2.1 Introduction

In all lasers, small changes in the optical path length, of one wavelength or more, can give rise to a mode-hop of the operating frequency (or frequencies) of the laser. This effect is particularly noticeable in single-frequency lasers since at the point of mode-hopping the laser oscillates on two frequencies. Mode-hopping can be caused by temperature fluctuations, pressure changes and mechanical vibrations.

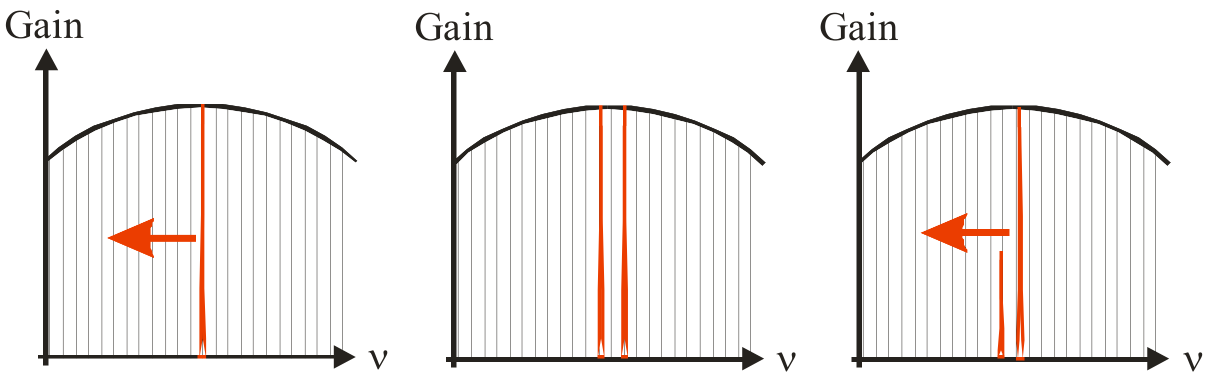

Oscillating frequency ν_0 moves from gain line centre by $\nu_c/2$

Non-oscillating mode extracts gain and starts oscillating -mulitifrequency operation

New mode saturates gain as it moves to gain line centre suppressing original mode -mode hop

Fig 3.7 Diagram showing the mode-hopping mechanism within a single-frequency laser.

The mode-hopping action due to these changes in optical path length [21] occurs, as the gain of an adjacent non-lasing mode equals that of the lasing mode. When the gain of these two modes is equal they will both lase, as the cavity is extended further, the original laser mode will be suppressed as its adjacent mode moves closer to gain line centre (Fig 3.7). The net effect observed over longer periods of time, is that the lasing mode will travel away from gain line centre with a variation in cavity length and will appear then hop back as it is suppressed and an adjacent mode starts to lase and then dominates the gain.

One solution to this problem that is normally adopted is to actively stabilise the cavity length by locking it to an external reference cavity. By locking the cavity in this way and also by actively stabilising the temperature of the laser crystal to prevent the frequency peak of the gain curve changing, it is possible to obtain reliable single-frequency operation of the laser output. One drawback of this technique is that it is very costly and complicated to implement.

3.2.2 Passive Technique for Mode Hop Suppression

In this work we employ a simple passive technique to suppress axial mode-hopping. Our approach exploits the different nonlinear losses experienced by lasing and non-lasing axial modes when a frequency doubling crystal is inserted into the laser cavity [21].

The mechanism behind mode-hop-suppression can be explained as follows: the lasing mode sees a loss due to the second harmonic generation (SHG) in the non-linear crystal equal to the second-harmonic conversion efficiency. However, non-lasing modes, within the phase-matching bandwidth, experience a loss that is approximately twice that of the lasing mode due to sum-frequency generation with the lasing mode (Figure 3.8).

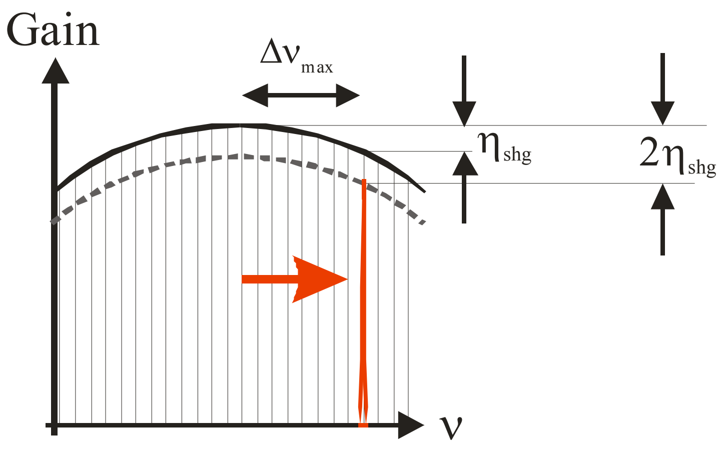

Oscillating frequency ν_0 moves from gain line centre by $\Delta\nu_{max}$

Fig 3.8 Diagram showing the action of mode-hop-suppression.

The net result is that the lasing mode can now be tuned over many axial mode spacings without it mode hopping by simple adjustment of the cavity length of the laser since the non-lasing modes are suppressed. The mode-hop-free tuning range $\Delta\nu_{\max}$ is given by the following approximate expression [22]:

$$\Delta\nu_{\max} = \frac{\Delta\nu_L}{2}\sqrt{\frac{\eta_{SHG}}{2(\eta_{SHG}+L)}}$$

[3.14]

where $\Delta\nu_L$ is the gain line-width of the laser, η_{SHG} is the second-harmonic conversion efficiency and L is the round trip cavity loss of the laser (not including the non-linear loss). Where the second harmonic conversion efficiency can be calculated from the following expression [4]:

$$P_{2\omega} = l_c^{\,2} K \frac{P_\omega}{A} \frac{\sin^2\left(\frac{\Delta k l_c}{2}\right)}{\left(\frac{\Delta k l_c}{2}\right)^2}$$

[3.15]

Where $K = 2\eta^3 \nu_1^2 d_{eff}^2$

$\eta = \sqrt{\mu_0 / \varepsilon_0 \varepsilon} = 377 / n_0$ [V/A] is the plane-wave impedance, l_c is the length of the nonlinear crystal, A is the area of the fundamental beam, ν_1 is the frequency of the fundamental beam and d_{eff} is the effective nonlinear coefficient of the nonlinear polarizability tensor $\boldsymbol{X}^{(2)}$.

A graph of equation 3.34 (Figure 3.9) illustrates the normalised conversion efficiency of an intracavity frequency doubled Nd:YLF laser operating at 1053nm as a function of LBO phase matching temperature.

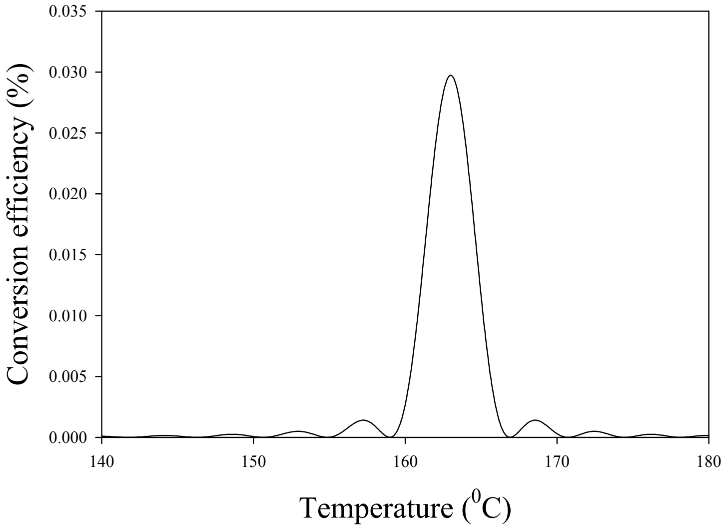

Figure 3.9 Graph showing normalised second harmonic conversion efficiency as a function of phase-matching temperature for an intra-cavity frequency doubled Nd:YLF laser operating at 1053nm.Using15mm long LBO crystal with a fundamental laser spot size of ~50μm.

From equation 3.33 it can be seen that $\Delta\nu_{\max}$ is largest when the laser cavity is optimised for second harmonic generation (i.e. the cavity loss is made to be as small as possible). However, even when the laser design is optimised for operation at the fundamental wavelength, it can also be seen from equation 3.33 that a useful mode-hop-free tuning range can still be achieved.

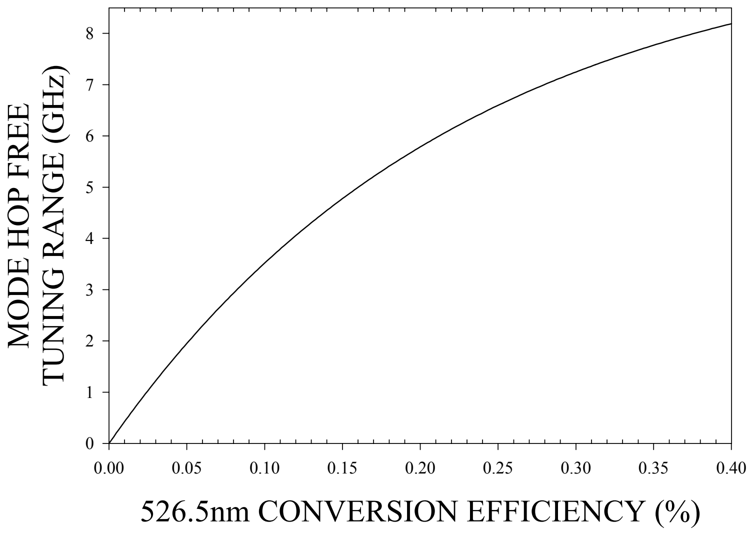

Figure 3.10 Graph showing mode hop free tuning range of a typical diode end pumped Nd:YLF ring laser featuring an intra cavity nonlinear crystal configured for mode hop suppression. The laser has a 10% output coupling and a 4% intra cavity loss.

Figure 3.10 shows the mode hop free tuning range of a typical diode end pumped ring laser featuring an intra cavity nonlinear crystal configured for mode hop suppression. The laser has a 10% output coupling and a 4% intra cavity loss. The graph shows that even for a maximum second harmonic conversion efficiency of only ~0.4% the laser has a mode hop free tuning range of ~8GHz.

If the cavity length remains constant therefore, barring mechanical vibrations, thermal effects and pressure changes, the fundamental wavelength will not mode-hop for very long periods of time providing robust and reliable single-frequency operation.

3.3 Pump source design and performance

The pump source for the master oscillator was a 40W Coherent diode device, operating at 792nm at 40A. This source was then fibre lens collimated and beam shaped in order to equalise the beam quality of the output in both planes. The output from the beam shaped diode-bar was then fibre coupled allowing us to directly send the output from the diode to the laser oscillator without the need for expensive and spatially wasteful beam steering mirrors. After beam shaping the diode-bar output power will have a *top-hat* power distribution in the array-plane and a Gaussian power distribution in the orthoganol-plane, however one of the major effects of fibre coupling is the output from the fibre will have a symmetrical power distribution in both planes. The fibre itself was 3m long with a 250μm core radius and numerical aperture of 0.22 allowing us up to 85% coupling efficiency in terms of the output power from the beam-shaped diode-bar to incident fibre-coupled output diode power on the laser rod. Figure 3.11 displays a graph showing the output powers from the diode that was initially used to pump the master oscillator. An added advantage of fibre-coupling diode-bars is that the output from the fibre in effectively homogenised as the symmetrical output from the fibre has a smoothed power distribution throughout its mode profile meaning that there is a reduced chance of *hot-spots* within the pumped laser medium.

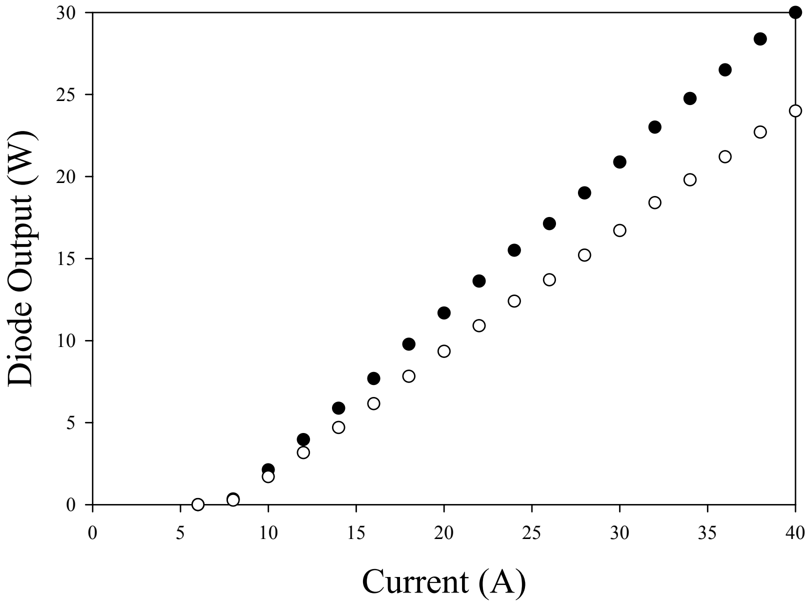

Figure 3.11 Graph displaying output power from the beam-shaped diode-bar operating at 792nm (solid dots) and the fibre coupled output incident on the laser rod (hollow dots).

By utilising the beam shaping approach and by fibre coupling the output, we have produce a flexible pump source capable of delivering ~25W of incident pump power to a diode-end –pumped Nd:YLF laser. The pump spot size within the laser rod could then be modified via relay imaging the end of the coupling fibre using conventional optics.

3.4 Nd: YLF bow-tie ring cavity

3.4.1 Cavity Design

In order to achieve single-frequency operation and eliminate spatial-hole-burning, the master-oscillator was designed to be a bow-tie ring-cavity. The pump source was a fibre-coupled 40W beam-shaped diode bar [20] (delivering a maximum of ~21W of incident pump power). The pump light was collimated and then focused to a spot size of $W_{x,y}$=250µm, end pumping a 15mm long YLF rod with a 0.5% dopant concentration. The non-linear crystal in the cavity was a Brewster cut LBO crystal that was housed in an oven maintaining it at ~165 ^{0}C in order to achieve type

1 non-critical phase matching. The pump input mirror was HT@792-797nm and HR@1053nm, the output coupler was 90%R@1053nm and optimised the fundamental 1053nm output resulting in only a small amount of intracavity green light was generated. The two curved mirrors had ROC=100mm and were HR@1053nm and HT@526.5nm (see Figure 3.12).

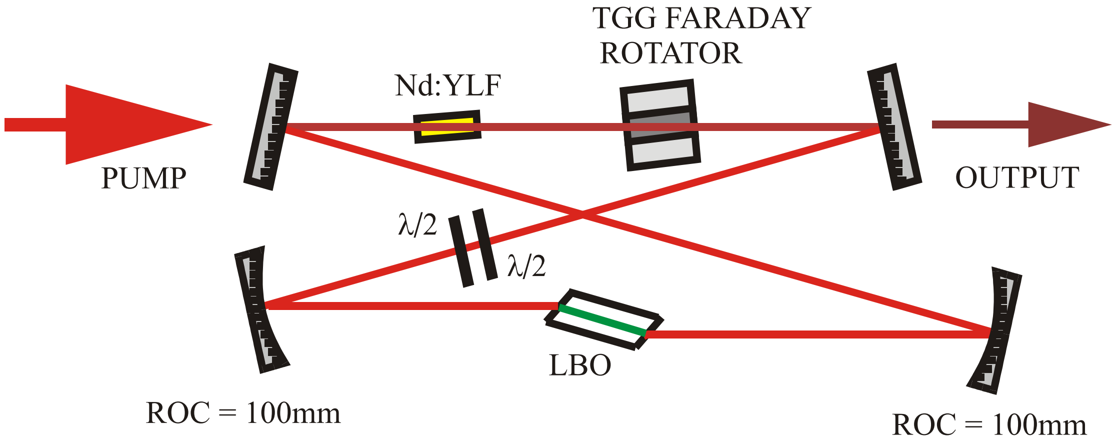

Fig 3.12 Diagram showing master oscillator cavity design.

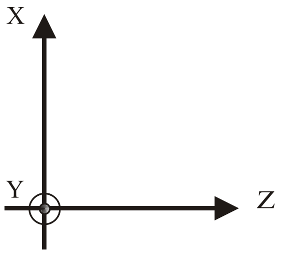

The angles between the mirrors were chosen to compensate for astigmatism generated by the Brewster cut LBO. The coordinate system used when describing the path of the laser beam throughout the cavity is displayed by the small diagram, where the z-axis is the direction of propagation of the laser light, the *zx* plane is the plane of the laser ring and the y axis is perpendicular to the plane of the ring: The astigmatism in the LBO occurs due to the light seeing two effective distances in the tangential (*yz*-orthoganol to plane of the ring) and sagittal (*xz*-plane of the ring) planes [23].

$$d_x = \frac{t\sqrt{n^2+1}}{n^2}$$

[3.16]

$$d_y = \frac{t\sqrt{n^2+1}}{n^4}$$

[3.17]

where n is the refractive index of the LBO and t is the thickness of the crystal. From the papers by Kogelnik *et al* and Hanna [23, 24] , it was shown that using a curved mirror at an oblique angle θ, the incident ray bundle was also focused at different locations in the tangential (yz) and sagittal planes (xz).

$$f_x = \frac{f}{\cos\theta}$$

[3.18]

$$f_y = f\cos\theta$$

[3.19]

Where f is the focal length of the mirror. The purpose of astigmatic compensation is to a maximise the overlap in the x and y planes, in this case within the Brewster cut LBO, whereby we compensate for the astigmatism due to the curved mirror with the astigmatism of the LBO. According to Kogelnik *et al* [23], this is assured when:

$$2Nt = 2f\sin\theta\tan\theta = R\sin\theta\tan\theta$$

[3.20]

where

$$N = \frac{(n^2-1)\sqrt{n^2+1}}{n^4}$$

[3.21]

Where R is the radius of curvature of the mirror. The angle of incidence for astigmatism compensation was calculated to be ~12^0 and this result was used in the final master design. The astigmatism compensation was confirmed by modelling the cavity using ABCD matrices where it could be seen that the size of the laser mode with the laser rod was the same in both the x and y planes (see figure 3.13).

The curved mirrors were also housed on piezoelectric actuators that had a maximum travel of 12µm which, when operated together, allowed us to tune the laser cavity length over a distance of 24µm without cavity misalignment. The distance between the pump input mirror M1 and the output coupler M2 was 106mm, the output coupler and the first curved mirror M3 was 105mm. The distance from M3 to the input face of the LBO was 53mm, and then output face to the LBO to the second curved mirror

M4 was again 53mm, M4 back to M1 was measured to be 131mm. The overall cavity length was measured to be ~0.5m and the cavity was optimised so that the laser mode was $W_{x/y}$ = 250μm ensuring excellent mode overlap with the pump mode. The cavity was modelling using ABCD matrices (figure 3.13), to calculate the spot sizes of the laser beam in the saggital and tangential planes, throughout one cavity length of the master oscillator to waist radii in the Nd: YLF and the LBO:

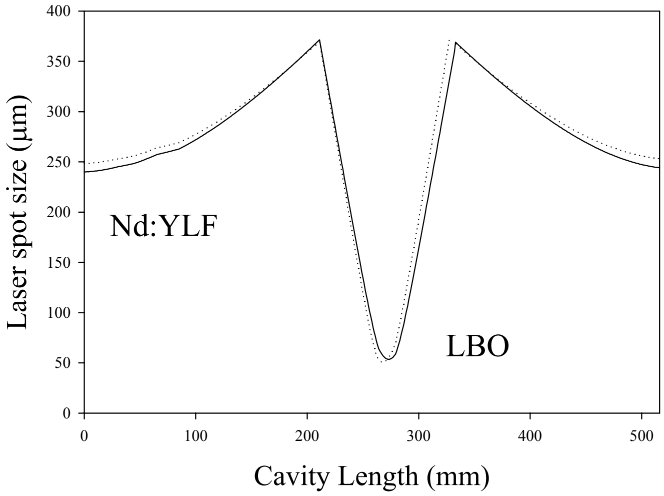

Figure 3.13 Spot sizes within the master oscillator as a function of cavity length in the tangential and saggital planes.

The start of the round trip occurs at the input face of the Nd: YLF confirming that the waist size is ~250μm. The waist size of the light within the LBO was found to be ~50μm.

3.4.2 Master Oscillator Cavity Loss-Difference

In laser cavities containing birefringent crystals such as Nd: YLF and LBO, the loss-difference can be significantly reduced. These components do not affect the forward direction within the cavity, as the polarisation of the laser will be aligned with the axis of the crystal. However, in the reverse direction, the lowest loss eigen polarisation will typically not be an eigen polarisation of the crystal alone, and so these birefringent crystals can have a significant effect on the loss difference [22]. Jones matrix analysis of the cavity also allowed us to calculate the loss-difference produced by the Faraday rotator and half-wave plates, in the cavity, in both directions. The loss-difference, assuming that the axes of the birefringent element are aligned with the polarisation of the forward propagating beam, is given by:

$$\text{Loss-Difference} = 1 - \left| \frac{\left(1+\sqrt{T}e^{i\delta}\right)\cos 2\theta + \sqrt{\left(1+\sqrt{T}e^{i\delta}\right)^2 \cos^2 2\theta - 4\sqrt{T}e^{i\delta}}}{2} \right|^2$$

[3.22]

Where δ is the retardation of the birefringent crystal (either YLF or LBO), in radians, θ is the rotation of the Faraday rotator and T is the minimum transmission of the cavity polarising element (Brewster cut LBO).

Since the loss-difference is dependent on the retardation of the crystal (i.e. the crystal could act say, like a half-wave plate or a full wave plate), as a result, the loss-difference will become dependent on the angle of incidence of the crystal, this, in turn could make alignment of the cavity quite difficult. However, in the case of a cavity containing a strong polarising element, like the Brewster angled LBO crystal in the master oscillator, T≈1 in the E_x plane due to the Brewster face and T≈0 in the E_y plane due to the reflection from the Brewster face. Therefore, by ensuring that we have the correct polarisation alignment using the half-wave plates before entry to the Brewster cut LBO crystal, and by ensuring that the lasing polarisation of the rod is also orientated in this plane, the loss-difference becomes dependent only on the angle of rotation of the Faraday rotator, a graph of equation 3.41 can therefore be plotted as in figure 3.14:

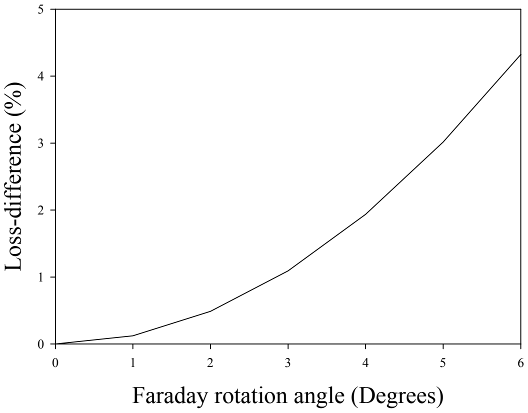

Figure 3.14 Graph showing uni-directional ring laser loss-difference as a function of Faraday rotation angle for T≈0 and retardation due to birefringent crystal δ≈0.

Although this will reduce the overall loss-difference within the cavity compared to what would be possible with a weaker polariser, it can be seen that the loss-difference is independent of any intra-cavity birefringence [21].

The TGG Faraday rotator enforced unidirectional and hence single-frequency operation. Within the cavity we also used two half-wave plates at an angle α to each other. The effect of these two wave plates could be specified via Jones matrix analysis:

$$\left(\frac{E_x}{E_y}\right)=\begin{pmatrix}1 & 0\\ 0 & -1\end{pmatrix}\left[\begin{pmatrix}\cos\alpha & \sin\alpha\\ -\sin\alpha & \cos\alpha\end{pmatrix}\begin{pmatrix}1 & 0\\ 0 & -1\end{pmatrix}\begin{pmatrix}\cos(-\alpha) & \sin(-\alpha)\\ -\sin(-\alpha) & \cos(-\alpha)\end{pmatrix}\right]=\begin{pmatrix}\cos 2\alpha & -\sin 2\alpha\\ \sin 2\alpha & \cos 2\alpha\end{pmatrix}$$

[3.23]

In equation 3.42 it can be seen, that the net effect of the two half-wave plates is to produce a rotation of twice the angle between the axes of the plates independent of the orientation of the polarisation of the input light [21]. This allows us to achieve near perfect match in polarisation with any Faraday rotator. The two λ/2 plates within the cavity corrected for the 6^0 offset in polarisation from the Faraday rotator so that the polarisation was horizontal at the LBO and remained horizontal to re-enter the Nd:YLF and see the maximum gain on the 1053nm transition. In the other direction however, the wave plates and the Faraday rotator act together to produce a rotational off-set away from the 1053nm axis of the crystal, thus reducing the gain seen in that direction and suppressing it from lasing. This meant that the loss-difference for our cavity, in theory, was ~ 4% in the reverse direction due to the Faraday rotator and this result was confirmed by using a computer model based on the laser cavity.

The loss-difference within the cavity was also measured by inserting a chopper, which when rotating, acted as a crude Q-switch. Since the gain of the laser rod in both directions was the same, by inducing the laser to operate firstly in the forward, and then in the reverse directions and by measuring the normalised pulse size in both directions as a function of Δ*t,* the difference in pulse duration. The experimental set-up can be seen in figure 3.15:

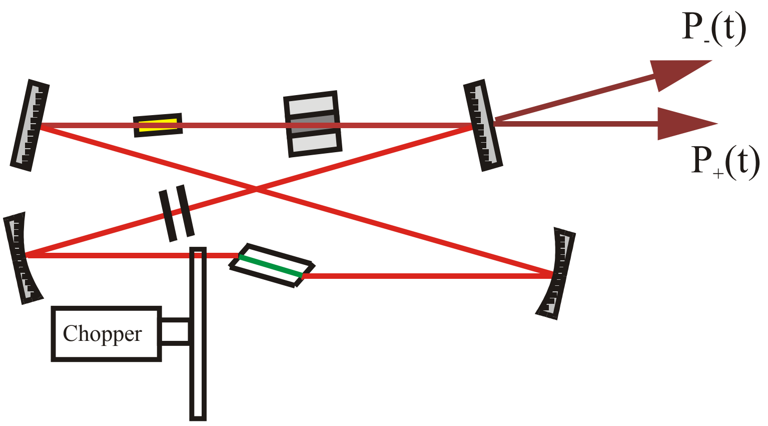

Figure 3.15 Diagram showing experimental set-up for measuring master-oscillator cavity loss-difference with the inclusion of a chopper.

Starting with expressions for the peak pulse powers in the forward and reverse propagating directions:

$$P_+(t_1) = P_0(G_+)^{\frac{t_1}{t_c}} \qquad [3.24]$$

and

$$P_-(t_1) = P_0(G_-)^{\frac{t_1}{t_c}} \qquad [3.25]$$

where + and – represent the forward and backwards directions respectively, *G* represents the gain in these directions, t_1 is the pulse duration and t_c is the cavity lifetime. The small loss seen with respect to the direction of propagation γ can be expressed as follows:

$$\gamma(t_1) = \frac{P_+}{P_-} = \left(\frac{G_+}{G_-}\right)^{\frac{t_1}{t_c}} \qquad [3.26]$$

The gain in the forwards direction G_+ is now expressed in terms of the gain in the backward direction G_- and the loss-difference Δl:

$$G_+ = G_- + \Delta l$$

[3.27]

$$\therefore \gamma(t_1) = \left(\frac{G_- + \Delta l}{G_-}\right)^{\frac{t_1}{t_c}}$$

Increasing the pulse length now by Δt whereby $t_2=t_1+\Delta t$ will give the following:

$$\gamma(t_1)=\left(1+\frac{\Delta l}{G_-}\right)^{\frac{t_1}{t_c}}=1+\left(\frac{\Delta l}{G_-}\right)\left(\frac{t_1}{t_c}\right)$$

$$\gamma(t_2)=1+\left(\frac{\Delta l}{G_-}\right)\left(\frac{t_2}{t_c}\right)$$

$$\therefore \gamma(t+\Delta t)=1+\left(\frac{\Delta l}{G_-}\right)\left(\frac{t+\Delta t}{t_c}\right)$$

From this equation we arrive at the following expression for (a straight line):

$$\gamma(t+\Delta t)=1+\left(\frac{\Delta l}{G_-}\right)\left(\frac{t}{t_c}\right)+\left(\frac{\Delta l}{G_-}\right)\left(\frac{\Delta t}{t_c}\right)$$

[3.28]

The ratio of the pulse average powers are plotted against Δt, after calculating a value for the gain G of the laser and knowing τ_c, the cavity lifetime, we could directly measure the cavity loss-difference ΔL. The graph of equation 3.47 can be seen in figure 3.16:

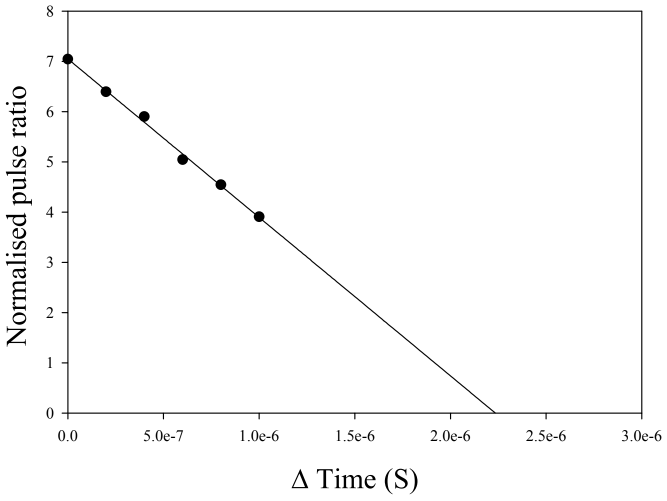

Figure 3.16 Graph showing the ratio of pulse powers in the forwards and backwards directions within the laser cavity and a function of difference in pulse duration.

From figure 3.16, we were able to calculate that that the loss-difference experienced by the cavity between the forward and backward directions was ~4%, in excellent agreement with the predictions from theory.

An associated problem with the master oscillator loss-difference however, was due to the passive technique employed for mode-hop-suppression. Since the process contributed to the total intracavity loss of the laser, we could conclude that the loss-difference of the cavity had to be larger than the second harmonic conversion efficiency in order for the laser to operate uni-directional and hence single-frequency. If the non-linear loss within the cavity exceeded the loss-difference in the reverse direction, the laser in the backward direction would see enough gain to start oscillating.

3.4.3 The Effects of Up-conversion on the Master Oscillator

Various measures were employed to reduce the effects of up-conversion and thermal loading within the Nd: YLF master oscillator laser rod. Using equation 3.5 it was possible to calculate the net effect of up-conversion on the upper laser level storage lifetime within the Nd: YLF master oscillator laser rod at maximum incident pump power from the fibre-coupled beam-shaped diode-bar described in section 3.3. The storage lifetime was taken to be τ=485μs for all calculations. By introducing the effect of up-conversion within a laser rod with a 1% dopant concentration, the storage lifetime would be reduced to 430μs. For a dopant concentration of 0.5%

however the storage lifetime would be reduced to 454μs (meaning the net effect of ETU on pulsed laser operation or storage lifetime in an Nd: YLF amplifier would be minimised) and by utilising the beam-shaped diode pump source as described in section 3.3 in conjunction with a longer laser rod (15mm), we could ensure that the effects of up-conversion and thermal loading per unit volume within the laser rod were reduced. Using a reasonably small pump and laser spot size of 250μm it was possible to calculate the β parameter, using equation 3.32, for the master oscillator. For the laser it was important to note that the pump power was clamped at the laser threshold value (calculated using equation 3.30 assuming ~ 4% loss within the cavity due to the various intracavity components) where $P_{TH} \approx 1.5W$ and so $\beta \approx 0.3$ giving $\Gamma = 1.08$, that is to say that the power of the thermal lens due to up-conversion would increase by approximately 8%.

The effect of ETU on the laser threshold was calculated using equations 3.29 and 3.30. Using the same design specifications already mentioned in the chapter, the incident threshold pump power of the laser with the effects of ETU was calculated to be 1.10W and 1.113W with the effects of ETU. This negligible change in threshold was due to the nature of the effect of ETU on the upper level population. Only when a high pump rate is applied to a gain material under non-lasing conditions (such as a Q-switched laser during build-up or an amplifier) are the effects of ETU going to be much more noticeable.

3.4.4 Summary

Figure 3.18 shows a photograph of the final working master oscillator, the red/pink light visible is excess pump light picked up by the silicon detector array within the digital camera. The green light is generated via the LBO and is non-resonant in order to produce the small nonlinear loss required to prevent mode hopping. The laser rod is housed in the brass mount at the top of the picture; the LBO is mounted in the aluminium oven at the bottom. The path of the 1μm light as it travels throughout the cavity has been highlighted in red.

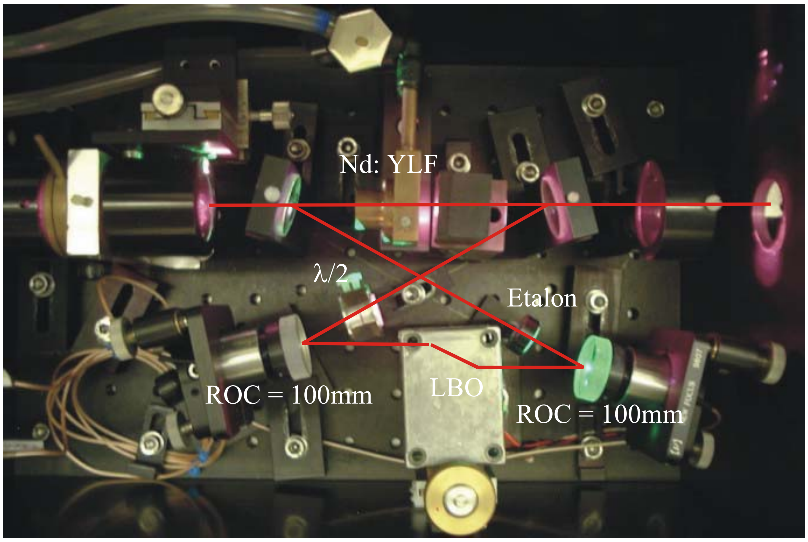

Figure 3.18 Picture of final master oscillator cavity.

The overall path length of the master oscillator was measure to be 463mm. In top left of the photograph, the two pump lens mounts can be seen separated by a half-wave plate for the pump. The small black box after the laser rod mount travelling left to right is the TGG Faraday rotator, followed by a 10% output coupler at 1053nm.

3.5 Experimental Results

Figure 3.19 shows the 1053nm output from the master oscillator as a function of incident pump power on the laser rod. Theory predicted that including an expression for up-conversion in the simplified rate equations for a 4-level laser system in equation 3.9, the threshold could be calculated to be 1.48W, and the slope efficiency could be calculated as being ~25% (equation 2.2).The actual laser threshold was measured to 1.5W (via observational confirmation of the laser output) and the laser had ~24% slope efficiency allowing a maximum output power of ~5W, which were in good agreement with theory.

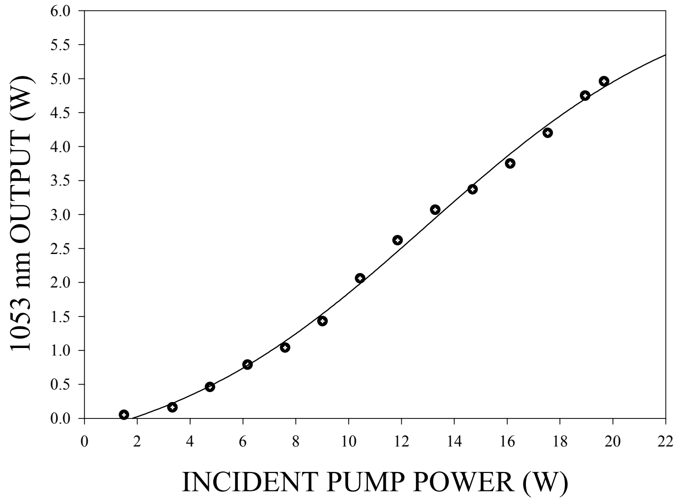

Fig 3.19 Graph to show master oscillator output power as a function of incident pump power.

In order to establish whether or not the thermal lens generated within the laser had any degrading effects on the output with increasing incident pump power, a Coherent Modemaster was used to monitor the beam quality of the output light in both orthogonal planes. With increasing pump power, the beam quality M^2 was measured to be <1.1 at all power levels. A plot of beam quality M^2 as a function incident pump power can be seen in figure 3.20.

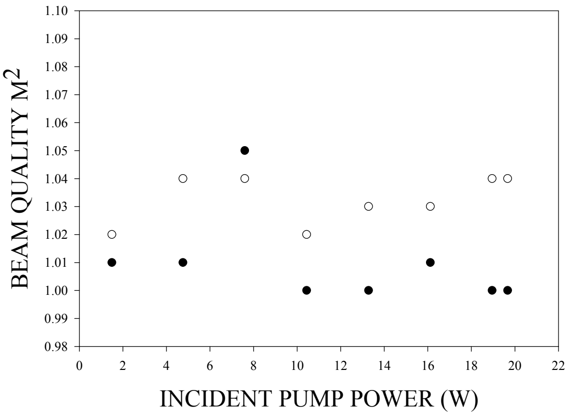

Figure 3.20 Graph showing beam quality of 1053nm output for entire incident pump range. Solid points M^2_x and hollow point M^2_y.

The fact that the beam quality remained $M^2<1.1$, in both orthogonal planes of the laser output throughout the entire available pump power range suggested that the small thermal lens power had a negligible effect. Figure 3.21 shows the generated 526.5nm output from the LBO with increasing incident pump power, which on the following page will correspond to mode hop free tuning range. 5W of 1053nm output from the master oscillator corresponded to ~150mW of generated second harmonic light at 526.5nm. This conversion efficiency was in good agreement with the theory predicted by equation 3.34 of ~0.5%.

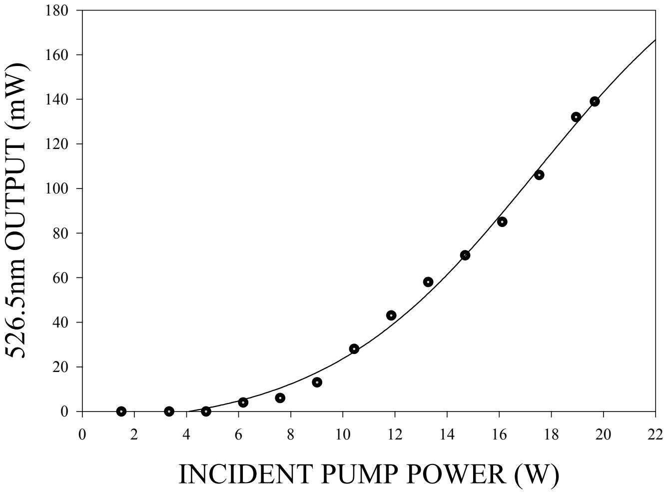

Figure 3.21 Generated 526.5nm “green” light from LBO for increasing incident pump power.

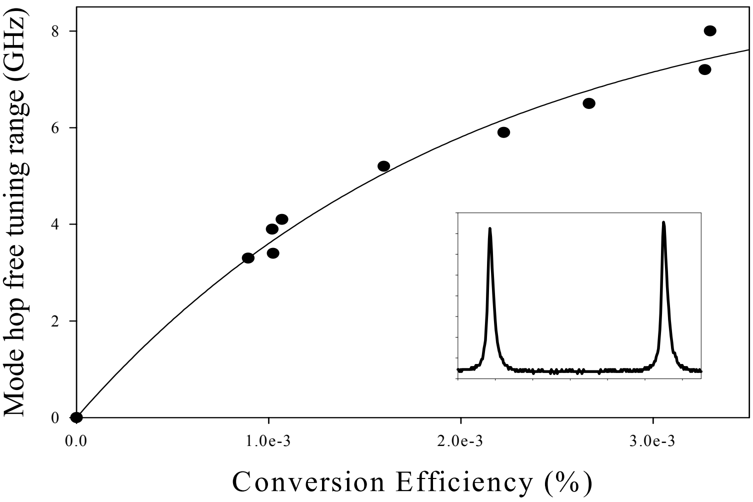

Fig 3.22 Graph to show the maximum mode hop free tuning range as a function of second harmonic conversion efficiency intra cavity within the maser oscillator. Inset shows the single-frequency nature of the master oscillator output.

Figure 3.22 shows the mode-hop-free tuning range as a function of 526.5nm conversion efficiency (%). The inset on the graph shows the output from a confocal Fabry-Perot (8GHz FSR), demonstrating robust and reliable single-frequency operation. The mode-hop-free tuning range was measured for various incident pump power levels, relating to the increasing non-linear loss within the cavity with increasing intra-cavity power. At maximum power, the tuning range was measured to be up to 14 axial mode spacing or tuneable over 8GHz. With the exception of a slight drift in the single-frequency output from the laser across the gain line centre, it was again noted that that even at maximum pump power the laser displayed no degradation in the reliability of its single-frequency nature, again confirming the suppression of thermal effects due to energy transfer up-conversion.

Due to previous research undertaken, our understanding of the thermal behaviour of Nd:YLF has enabled us to design and construct a small, robust and reliable single-frequency laser capable of producing up to 5W out 1053nm output in a near diffraction limited beam. The option of further power scaling could be considered with the development of higher power diode-bars that, when beam shaped and fibre-coupled, could provide an even greater amount of incident pump power on the laser rod. This fact, coupled with the potential of using a longer laser rod or even a multiple rod geometry, could lead to output powers of >10W. However, even though precautions are taken to reduce the effects of energy transfer up-conversion within the laser, as an oscillator is scaled in power, re-design of cavity and components will become essential in maintaining optimum output characteristics, which can prove both costly in the sense of both money and time. The end result however, will always be that no matter how many precautions are taken in the power scaling process, the thermal fracture limit of the material in question (which in the case of Nd:YLF, is quite low in comparison with other materials) has to be the upper limit on power scaling capability.

An alternative technique to power scaling however is to adopt a master oscillator power amplifier approach, whereby the output from a low power laser is amplified via one or more stages. This approach has the benefit of de-coupling problems normally attributed to power-scaling in terms of single-frequency maintenance, whereby as long as the output from the master is robust and reliable, then the increase in output power and maintenance of beam quality a matter of careful amplifier design.

3.6 Summary

In summary, we have discussed the problems associated with designing and constructing a robust and reliable single-frequency laser oscillator. By using Nd: YLF and taking advantage of its naturally weak thermal lens and natural birefringence we have developed a laser capable of producing up to ~4.5W output, with a diffraction limited beam quality factor $M^2<1.1$. The laser is single-frequency and displays no signs of mode-hopping over long periods of time (~15mins), or alternatively can be tuned over 14 axial mode spacings by simply tuning the cavity length. This source should therefore be an ideal candidate for power scaling by means of one or more amplifier stages built on the same principles.

3.7 References

1. Baer, T., *Large-Amplitude Fluctuations Due to Longitudinal Mode-Coupling in Diode-Pumped Intracavity-Doubled Nd-Yag Lasers.* Journal of the Optical Society of America B-Optical Physics, 1986. **3**(9): p. 1175-1180.
2. Hardman, P.J., PhD *Power-scaling of diode-end-pumped solid-state lasers*, in *Optoelectronics Research Centre*. 1999, University of Southampton.
3. Harmer A.L., *Fluorescence of Nd3+ in Lithium Yttrium Fluoride.* Journal of Physical Chemical Solids, 1969. **30**: p. 1483.
4. Koechner, W., *Solid-State Laser Engineering*. 4th ed. 1996, New York: Springer-Verlag.
5. Anderson, F.G., Weidner H., Summers P.L., and Peale R.E., *Spectroscopy and crstal-field analysis for Nd+3 in GdLiF4.* J.Lumin, 1994. **62**: p. 77-84.
6. Harmer, A.L., Linz A. and Gabbe D.R., *Fluorescence of* Nd^{3+} *in Lithium Yttroium Fluoride.* Journal of Physical Chemical Solids, 1969. **30**: p. 1483.
7. Guyot, *Excited-state absorption in the infra-red emmision domain of Nd+3 doped* $Y_3Al_5O_{12}$, $YLiF_4$ *and* $LaMgAl_{11}O_{19}$. Journal of Applied Physics, 1993. **73**: p. 8526-8530.

8. da Gamma, Poorcher P.and Caro P., *Energy Levels of Nd+3 in LiYF4.* Journal of Chemical Physics, 1981. **6**(75): p. 2583-2587.

9. Malinowski, M., Jacquier B., Bouazaoui M., Joubert M.F. and Linares C., *Laser-induced fluorescence and up-conversion processes in* $LiYF_4:Nd^{3+}$. Physcial Review B, 1990. **41**: p. 31.

10. Pollnau, M., *Upconversion, lifetime quenching, and ground-state bleaching in Nd3+: LiYF4.* Optics Communications, 1998. **147**(1-3): p. 203-211.

11. Pollnau, M., *Upconversion-induced heat generation and thermal lensing in Nd : YLF and Nd : YAG.* Physical Review B-Condensed Matter, 1998. **58**(24): p. 16076-16092.

12. Hardman, P.J., et al., *Energy-transfer upconversion and thermal lensing in high-power end-pumped Nd : YLF laser crystals.* IEEE Journal of Quantum Electronics, 1999. **35**(4): p. 647-655.

13. Chen, Y.F., Y.P. Lan, and S.C. Wang, *Influence of energy-transfer upconversion on the performance of high-power diode-end-pumped CW lasers.* IEEE Journal of Quantum Electronics, 2000. **36**(5): p. 615-619.

14. Guy, S., *High-inversion densities in Nd : YAG: Upconversion and bleaching.* Ieee Journal of Quantum Electronics, 1998. **34**(5): p. 900-909.

15. Payne, S.A., *Auger up-Conversion Losses in Nd-Doped Laser Glasses.* Optics Communications, 1994. **111**(3-4): p. 263-268.

16. Zuegel, J.D. and W. Seka, *Upconversion and reduced F-4(3/2) upper-state lifetime in intensely pumped Nd : YLF.* Applied Optics, 1999. **38**(12): p. 2714-2723.

17. J.R.Ryan and R.Beach, *Optical absorption and stimulated emission of neodymium in yttrium lithium fluoride.* Journal of the Optical Society of America B-Optical Physics, 1992. **9**(10): p. 1883-1887.

18. K.Kubodera K.Otsuka, *Single-transverse-mode* $LiNdP_4O_{12}$ *slab waveguide laser.* Journal of Applied Physics, 1979. **50**: p. 653-659.

19. W.A.Clarkson, D.C.Hanna, *Effects of Transverse-Mode Profile on Slope Efficiency and Relaxation Oscillations in a Longitudinally-Pumped Laser.* Journal of Modern Optics, 1989. **36**(4): p. 483-498.

20. Clarkson, W.A. and D.C. Hanna, *Two-mirror beam-shaping technique for high-power diode bars.* Optics Letters, 1996. **21**(6): p. 375-377.

21. Martin, K.I., W.A. Clarkson, and D.C. Hanna, *Self-suppression of axial mode hopping by intracavity second- harmonic generation.* Optics Letters, 1997. **22**(6): p. 375-377.

22. Martin, PhD *High power diode pumped single frequency lasers*, in *Optoelectronics Research Centre*. 1996, University of Southampton.

23. Kogelnik, H.W., Ippen E.P., Dienes A. and Shank C.V., *Astimatically compensated cavities for cw dye lasers.* IEEE Journal of Quantum Electronics, 1972. **QE-8**(3): p. 373.

24. Hanna, D.C., *Astigmatic gaussian beams produced by axially asymmetric laser cavities.* IEEE Journal of Quantum Electronics, 1969. **QE-5**(10): p. 483-488.

Chapter 4: High-Power Single-Frequency Master-Oscillator-Power-Amplifier

4.1 Introduction

At low powers, diode-end-pumped solid-state lasers offer, cheap, robust and reliable readily achievable operation, with diffraction-limited, single-frequency output powers of multiple Watts. Applications requiring such devices are becoming increasingly more demanding in terms of frequency stability and power, emphasising the need for appropriate schemes for scaling laser power without any degradation in beam quality and efficiency, and without reducing flexibility in operation. The problems associated with power scaling lasers have been outlined in Chapters 2 and 3 with particular emphasis on the advantages and disadvantages of Nd:YLF as the gain material. With careful cavity design it is possible to scale the output from a laser to >10W maintaining diffraction-limited output and single-frequency operation [1, 2], but the difficulties in maintaining reliable and robust operation are considerable. The simplest and most attractive method of de-coupling the problems of power scaling from the maintenance of robust and reliable single-frequency operation is to adopt a master oscillator power amplifier (MOPA) approach. This was found to be a reasonably popular method for power scaling [3-16], where the output from a small, robust and reliable laser is amplified using either a solid-state or fibre amplifier. Nevertheless, this approach is quite challenging in terms of amplifier design and requires careful consideration of a number of issues. This chapter will describe the design strategy and results for the performance of a novel multi-pass diode-end-pumped Nd:YLF amplifier operating on the low gain 1053nm line. This chapter will overview thermal problems associated with amplifier stages, deriving expressions for unsaturated small signal gain taking into account ETU. Finally, the prospects for further power scaling via this approach are considered.

4.2 Amplifier theory

4.2.1 Small signal gain

In an end-pumped four-level amplifier, the gain per unit length $g_0(r,z)$ for a single ray at position (r,z) under steady state conditions is given by the following expression:

$$g_0(r,z) = \sigma_{SE} n(r,z) \qquad [4.1]$$

where σ_{SE} is the stimulated emission cross-section and $n(r,z)$ is the upper laser level population inversion density. The population inversion density under steady-state conditions, neglecting the effects of ETU is given by:

$$n(r,z) = R(r,z)\tau \qquad [4.2]$$

where τ is the fluorescence lifetime of the upper laser level and $R(r,z)$ is the pumping rate density at (r,z) given by:

$$R(r) = \frac{\alpha_P I_p(r)}{h\nu_P} \exp\left(-\alpha_P z\right) \qquad [4.3]$$

where $I_P(r)$ is the incident pump intensity and α_P is the pump absorption coefficient. For a pump beam with a top-hat transverse intensity distribution:

$$I_P(r) = \frac{P_P}{\pi w_P^2} \qquad \text{for } r \leq w_P$$

$$\text{and } I_P(r) = 0 \qquad \text{for } r \geq w_P \tag{4.4}$$

where w_P is the pump beam radius which is assumed to remain constant over the length of the laser medium. For a pump beam with a Gaussian intensity distribution:

$$I_P(r) = \frac{2P_p}{\pi w_P^2} \exp\left(\frac{-2r^2}{w_p^2} \right) \tag{4.5}$$

For a fibre-coupled multi-mode diode pump source, the actual transverse intensity distribution lies somewhere between the top-hat and Gaussian distributions.

For a signal beam with a Gaussian transverse intensity distribution:

$$I_s(r,z) = \frac{2P_S(z)}{\pi w_S^2} \exp\left(\frac{-2r^2}{w_S^2} \right) \tag{4.6}$$

where $P_S(z)$ is the signal power at position z and w_S is the signal beam radius, also assumed to remain constant over the length of the gain medium. We can now write an expression for the effective gain per unit length at position z as :

$$g_{eff}(z)=\frac{\int_0^\infty g_0(r)I_S(r)2\pi r dr}{\int_0^\infty I_S(r)2\pi r dr}$$

$$=\frac{\sigma_{SE}\tau\alpha_P\exp\left(-\alpha_P z\right)}{h\nu_P}\frac{\int_0^\infty rI_P(r)I_S(r)dr}{\int_0^\infty rI_S(r)dr} \qquad [4.7]$$

Solving for $g_{eff}(z)$ assuming a top-hat pump distribution and a Gaussian signal gives:

$$g_{eff}(z)=\frac{\sigma_{SE}\tau\alpha_P\exp(-\alpha_P z)P_p(z)}{\pi h\nu_P w_P^2}\exp\left[1-\frac{2w_P^2}{w_s^2}\right] \qquad [4.8]$$

Solving for $g_{eff}(z)$ assuming a Gaussian pump distribution and a Gaussian signal gives:

$$g_{eff}(z)=\frac{2\sigma_{SE}\tau\alpha_P\exp(-\alpha_P z)P_p}{\pi h\nu_P\left(w_P^2+w_S^2\right)} \qquad [4.9]$$

where σ_{SE} is the stimulated emission cross-section, τ is the upper laser level fluorescence lifetime, α_P is the absorption coefficient, P_P is the incident pump power w_P is the pump spot radius, v_P is the pump frequency and w_S is the signal spot radius. We can illustrate the effect of assuming a top-hat or Gaussian pump profile by plotting equations 4.8 and 4.9. We substitute $z=l_c$ where l_c is the length of the gain medium and assuming a single pass, in this case a 1.2% dopant concentration, 18mm long Nd:YLF crystal, pumped by 20W at 792nm (meaning α_P=250m^{-1}) and using w_S=w_P=250µm. The intensity distributions of the top-hat and Gaussian pump intensity distributions can be seen in figure 4.1:

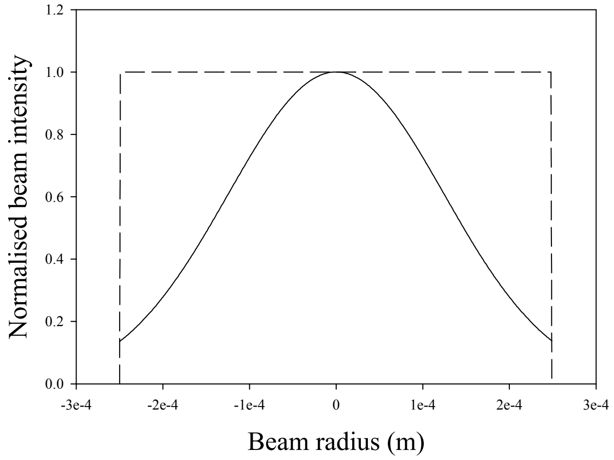

Figure 4.1 Graph showing pump intensity profiles for Gaussian (solid line) distribution and top-hat (dashed line) distribution.

The resultant graph of unsaturated small signal gain as a function of incident pump power for pump beams with a top-hat transverse profile and Gaussian transverse profile can be seen in figure 4.2:

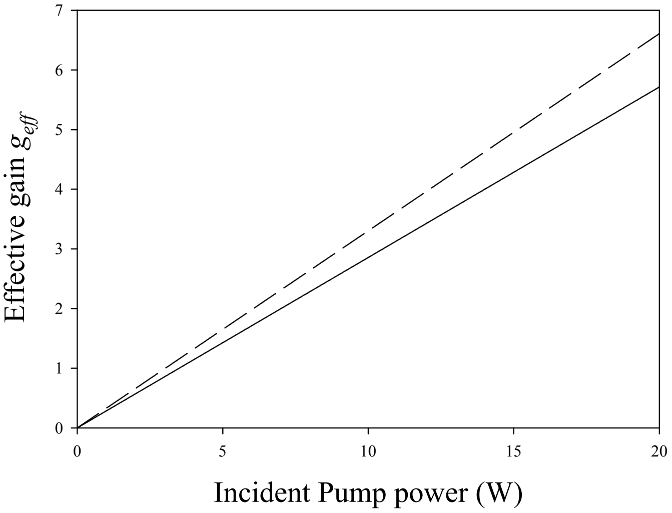

Figure 4.2 Graph showing effective gain as a function of incident pump power assuming top-hat transverse pump distribution (solid line) and Gaussian transverse pump distribution (dashed line).

Figure 4.2 shows the effective gain for top-hat and Gaussian transverse pump power distribution respectively in a common set-up. The top-hat distribution implies that the gain the signal sees will be constant across the mode profile and will drop off quickly at the edges. The effective gain seen when the amplifier is pumped by a

Gaussian profile is higher due to the mode overlap with the signal mode, the signal will see a higher amount of gain within the central part of the pump mode and less due to the lower power levels in the wings of the mode profile.

The increase in signal intensity as it passes through the amplifier medium can then be calculated from the following equation:

$$\frac{dI(z)}{dz} = \frac{g_{eff}(z)I(z)}{1 + \frac{I(z)}{I_{SAT}}} \qquad [4.10]$$

where I_{SAT} is the saturation intensity of the laser medium given by:

$$I_{SAT} = \frac{hc}{\lambda_S \sigma_{SE} \tau} \qquad [4.11]$$

where λ_S is the wavelength of the amplified signal. The saturation intensity is the signal intensity at which the gain of the amplifier has dropped by half causing significant depletion of the upper laser level population inversion. Assuming that the transverse pump intensity has a Gaussian distribution (equation 4.6), we can substitute equation 4.9 into 4.10 to give:

$$\int_{I_{in}}^{I_{out}} \left(\frac{1}{I(z)} + \frac{1}{I_{SAT}} \right) dI(z) = \int_0^l g_{eff}(z) dz \qquad [4.12]$$

where G_0, the unsaturated small signal gain is given by:

$$G_0 = \exp\left(\int_0^l g_{eff}(z) dz \right) \qquad [4.13]$$

We can now solve this expression for a single pass of an amplifier by assuming incident intensity I_{in} at the point $z=0$ and I_{out} at the point $z=l$:

Taking a logarithum and integrating both sides of this equation, assuming a top-hat transverse intensity distribution (equation 4.8) gives us an expression for the unsaturated or small signal gain within the amplifier as being:

$$\ln(G_0) = \frac{\sigma_{SE}\tau\alpha_P[1-\exp(-\alpha_P l)]P_P}{h\nu_P \pi w_P^2}\exp\left[1-\frac{2w_P^2}{w_S^2}\right] \qquad [4.14]$$

Plotting equation 4.14, we can illustrate the increase in small signal gain with incident absorbed pump power in the gain medium, in this case the same laser rod used in example figure 4.1:

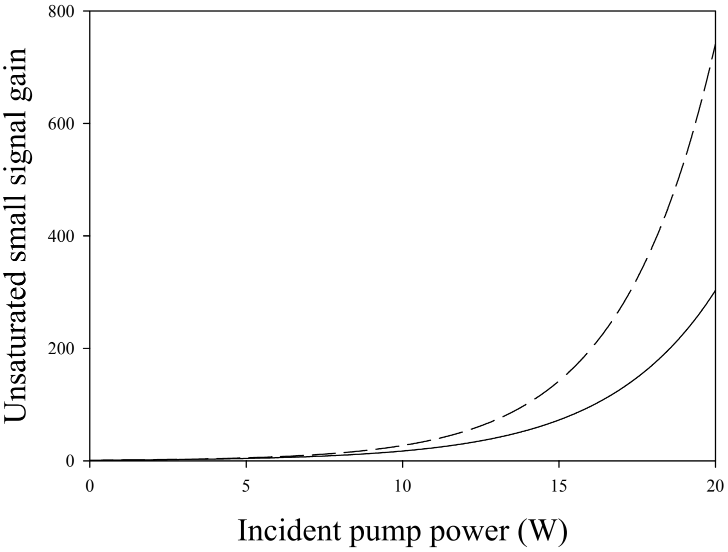

Figure 4.3 Graph showing the unsaturated small signal gain of a single 18mm 1.2% dopant concentration Nd:YLF amplifier rod as a function of incident pump power (the dashed line indicates a Gaussian pump profile, the solid line indicates a top-hat pump profile).

4.2.2 Saturated gain operation

The gain within the amplifier will start to saturate as the input signal intensity is increased i.e. where $I_S \rightarrow I_{SAT}$. Integrating the left-hand side of equation 4.12 with respect to I_{in} and I_{out} gives:

$$\int_{I_{in}}^{I_{out}}\left(\frac{1}{I(z)}+\frac{1}{I_{SAT}}\right)dI(z) = \ln\left(\frac{I_{out}}{I_{in}}\right)+\frac{1}{I_{SAT}}\left(I_{out}-I_{in}\right) = \int_0^l g_{eff}(z)dz \qquad [4.15]$$

Re-arranging this expression and including our expression for unsaturated small signal gain from equation 4.14 gives the actual gain of the amplifier G as:

$$\ln(G) = \ln(G_0) - \frac{1}{I_{SAT}}\left(I_{out} - I_{in}\right)$$

$$\therefore \quad G = G_0 \exp\left(-\frac{I_{extracted}}{I_{SAT}}\right) \qquad [4.16]$$

Equation 4.16 gives a expression for the actual gain of the amplifier as a function of unsaturated small signal gain and the extracted output intensity of the amplifier. If we plot this equation (figure 4.4) as a function of the ratio of the extracted power to the saturation power of the amplifier (assuming a top-hat pump distribution) using the example in figures 4.2 and 4.3 we get:

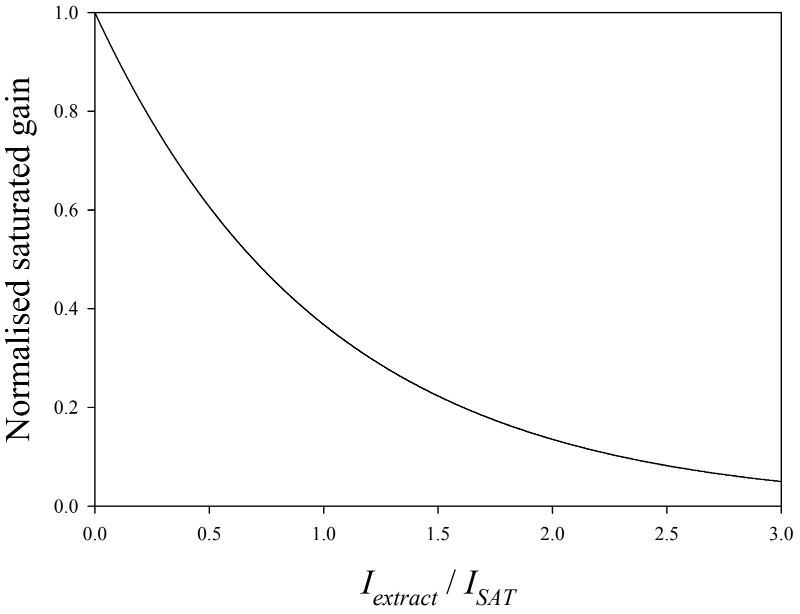

Figure 4.4 Graph showing the normalised saturated gain as a function of the ratio of extracted amplifier intensity and the saturation intensity.

Figure 4.4 shows that as the input signal intensity is increased so that $I_{extract} \rightarrow I_{SAT}$, the gain of the amplifier will drop to less that 40% of the unsaturated small signal gain.

4.2.3 Amplified spontaneous emission

Although, as we have already established, the dominant spectroscopic loss processes in Nd:YLF is energy-transfer-upconversion, the level of population inversion, which can be achieved within an amplifier, can also be limited by other processes such as amplified spontaneous emission (ASE). The favourable condition for strong ASE is high gain, combined with a long path length in the active material [17]. Under these conditions, spontaneous decay occurring near one end of the laser rod can be amplified to a significant level before leaving the active material at the other end. A threshold for ASE does not exist, however, the power emitted as ASE increases rapidly with gain, and hence, as the pump power increases, ASE can become a large loss mechanism within the laser amplifier. At this point, an intense emission is observed within a solid-angle Ω around the axis of the active material (figure 4.5), from each end.

$$\Omega = \frac{A}{L^2} \tag{4.17}$$

where L and A are the laser rod length and cross-sectional area respectively. As a result of refraction at the end faces, the aperture solid-angle at the end of the rod is increased by n^2. Figure 4.3 shows the directionality and maximum path length for ASE in a laser rod.

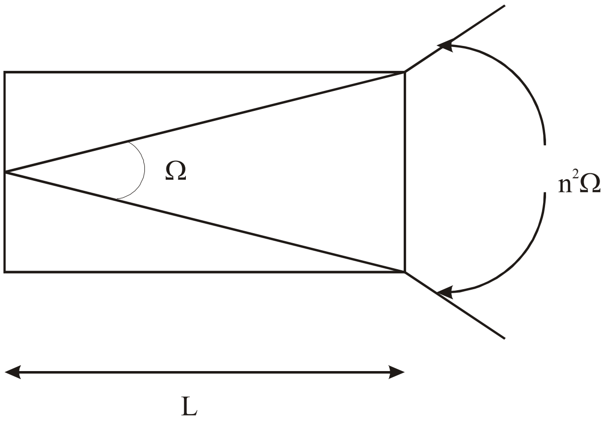

Figure 4.5 Directionality and maximum path length for ASE in a laser rod.

No mirror reflections are required for ASE to occur, however, reflections from a mirror or internal reflections from the curved surfaces of the inside of the rod will increase the ASE path length, leading to an increase in intensity.

In high gain multi stage amplifier systems therefore, ASE can be a serious problem in limiting the upper-state inversion and hence gain. An analytical expression for the fluorescence flux I_{ASE} from a laser rod as a function of small signal gain is very useful in estimating the severity of ASE: It can be shown [17] that I_{ASE} is given by:

$$\frac{I_{ASE}}{I_{SAT}} \approx \frac{\Omega}{4} \frac{G_0}{[\ln(G_0)]^{\frac{1}{2}}}$$

[4.18]

For a Nd:YLF amplifier rod length l_c=18mm and with 3mm diameter, with 20W incident pump power at 797nm, where $I_{SAT}=3.2\times10^{7}\mathrm{Wm}^{-2}$, the intensity of the ASE produced can be calculated to be $I_{ASE}=5.6\times10^{7}\mathrm{Wm}^{-2}$. Given the surface area of the laser rod, the ASE power from the end of a typical Nd:YLF amplifier rod can be calculated as being ~ 4W.

4.2.4 Parasitic oscillations

Laser action, occurring as the amplifier is being optically pumped, results from residual feedback from the various interfaces within the amplifier itself. The conditions for stable operation can be found by considering the gain in an amplifier rod of length L, pumped to an inversion level characterised by a gain coefficient g per unit length. If the end faces of the laser rod have reflectivities r_1 and r_2, then the spontaneous emission coming from any point within the rod will experience a loop gain after one round trip of about $r_1r_2\exp(2gL)$. If this loop gain satisfies the condition:

$$r_2 r_2 \exp(2gL) > 1$$

[4.19]

then oscillations will build-up reducing the energy storage of the amplifier. Therefore, in order to eliminate the possibility of laser action with the amplifier rods they must follow the requirement:

$$r_2 r_2 \exp\left(2gL\right) < 1$$

[4.20]

This sets an upper limit on the length of the laser rods used in the amplifiers.

Internal reflections at the boundaries of the active amplifier medium can dramatically increase the effect of ASE, particularly in the cases where those reflections follow a closed path. In this case, there exists a strong feedback mechanism and as soon as the gain in the laser medium exceeds the reflection losses, parasitic oscillations will occur. For example, rods with polished walls can support internal modes that are completely contained by total internal reflection. Longitudinal modes can be suppressed by wedging or anti-reflection coatings on the end faces of the rod.

In order to minimise pre-lasing in amplifiers, the rods can often be anti-reflection coated or Brewster cut. Reflections causing off axis spontaneous emission are minimised by either coating the rod in index matching fluid or by rough grinding the cylindrical walls. For the case of multiple stage amplifiers, the separate stages are decoupled by one or more of the following methods: the distance between the stages may be made to be as large as possible, since the ASE has a relatively large beam angle, the distance will effectively reduce feedback between them. More effectively, the use of spatial filters can achieve the same effect. If the small signal gain of the amplifiers is very high, then it may be necessary to separate the amplifiers with Faraday isolators.

4.3 Energy transfer up-conversion and small signal gain

4.3.1Impact of ETU on small signal gain

In chapter 3, in order to include the effects of ETU in the expression for laser threshold, we modified the population inversion density, hence reducing the potential gain. The effects of up-conversion with the population inversion clamped at threshold were found to be negligible, however in the case of an amplifier, under non-lasing conditions, the expression for population inversion with ETU becomes:

$$n(r,z) = \frac{-1+\sqrt{1+4R(r,z)W\tau^2}}{2W\tau} \qquad [4.21]$$

where *W* is the up-conversion parameter and *R(r,z)* is the pump rate, with a top-hat intensity profile given by:

$$R(r,z) = \frac{\alpha_P P_P}{h\nu_P \pi w_P^2}\exp(-\alpha_P z) \text{ for } r < w_p$$

$$R(r,z) = 0 \qquad \text{for } r > w_p \qquad [4.22]$$

Substituting equations 4.21 and 4.22 into equation 4.1 leads to the following expression:

$$g(r,z) = \frac{\sigma_{SE}}{2W\tau_f}\left(-1+\sqrt{1+\frac{4\alpha_P P_P W\tau^2}{h\nu_P \pi w_P^2}\exp(-\alpha_P z)}\right) \qquad [4.23]$$

Now, substituting in expressions for the Gaussian signal and 4.21 into the expression 4.9 for g_{eff} gives:

$$g_{eff}(z)=\frac{\sigma_{SE}}{2W\tau_f}\left(-1+\sqrt{1+\frac{4\alpha_P P_P W\tau^2}{h\nu_P\pi w_P^2}\exp(-\alpha_P z)}\right)\left(1-\exp\left(\frac{-2w_P^2}{w_S^2}\right)\right) \quad [4.24]$$

Integrating this equation over the crystal length gives the unsaturated small signal gain [18]:

$$\ln(G_0)=\frac{\sigma_{SE}}{W\tau_f}\left(1-\exp\left(\frac{-2w_P^2}{w_S^2}\right)\right)$$
$$\left(\sqrt{1+\frac{4\alpha_P P_P W\tau^2}{h\nu_P\pi w_P^2}}-\sqrt{1+\frac{4\alpha_P P_P W\tau^2}{h\nu_P\pi w_P^2}\exp(-\alpha_P z)}+\ln\left[\frac{\sqrt{1+\frac{4\alpha_P P_P W\tau^2}{h\nu_P\pi w_P^2}\exp(-\alpha_P z)}}{1+\sqrt{1+\frac{4\alpha_P P_P W\tau^2}{h\nu_P\pi w_P^2}}}\right]\right)$$

[4.25]

Assuming all the pump power is absorbed in the amplifier gain medium, this expression can be simplified to:

$$\ln(G_0)=\frac{\sigma_{SE}}{W\tau_f}\left(1-\exp\left(\frac{-2w_P^2}{w_S^2}\right)\right)\left(\sqrt{1+\frac{4\alpha_P P_P W\tau^2}{h\nu_P\pi w_P^2}}-1+\ln\left[\frac{2}{1+\sqrt{1+\frac{4\alpha_P P_P W\tau^2}{h\nu_P\pi w_P^2}}}\right]\right)$$

[4.26]

If we now make a comparison between these expressions for an 18mm long Nd:YLF rod with 1.2% dopant concentration operating as an amplifier where $w_S = w_P = 250\mu m$, α_P=250m^{-1} for 1.2% dopant concentration, for 20W of incident pump power the effect of ETU on small signal gain can be quite noticeable (figure 4.6) in comparison with figure 4.3:

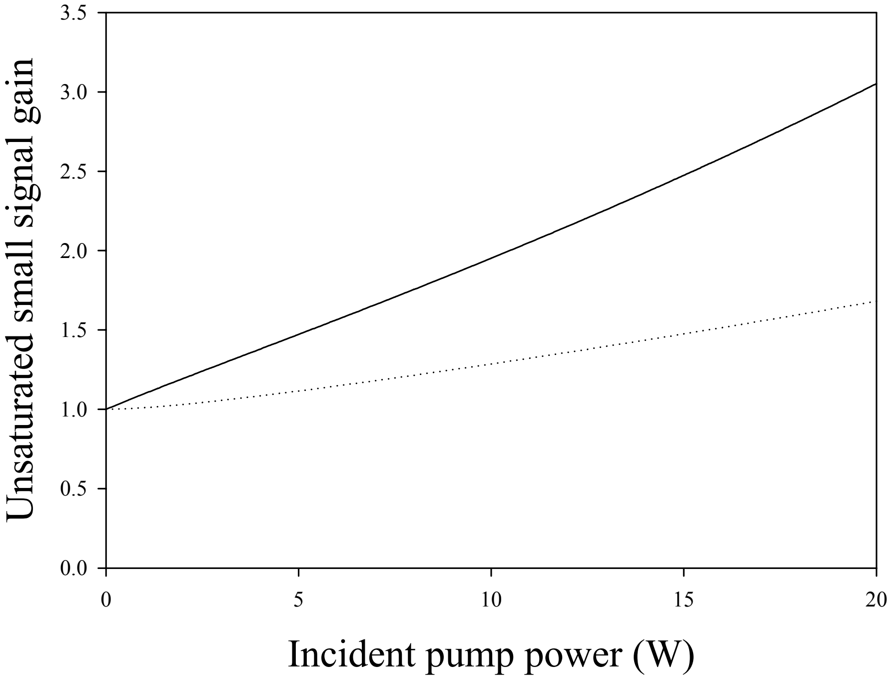

Figure 4.6 Graph showing unsaturated small signal gain as a function of incident absorbed pump power with the effects of ETU and finite absorption (dashed line) and with total pump absorption (solid line).

It can be seen from the single pass regime, including the effects of up-conversion for a top-hat transverse pump beam profile that the effects of ETU itself will considerably reduce the small signal gain from that calculated from the simplified rate equations without the effects of ETU.

4.4 Thermal lensing in amplifier

4.4.1 Reducing thermal loading in the amplifier

In chapter 3 we discussed in depth the motivations for the reduction of energy transfer up-conversion in the Nd:YLF master-oscillator based on numerous figures of merit related to material properties and pumping conditions (equation 3.32). The same strategy must apply to the Nd:YLF amplifiers since in order to provide enough gain to successfully power scale the output from the master oscillator to very high powers, the incident absorbed pump powers that need to be involved will cause ETU to be a dominant problem within the system. Heat generation within the amplifiers caused by quantum defect heating and ETU will generate a highly aberrated thermal lens, a small amount of stress induced birefringence (which should be negligible due to the natural birefringence of YLF) and could ultimately lead to thermal fracture. The upper limit on the amplifiers successfully power scaling the master oscillator, due to the need for good beam quality during applications of the MOPA system, must be the maintainence of the output having $M^2<1.1$.

We can reduce thermal loading per unit volume within the amplifier rods in two ways, firstly, we can lower the dopant concentration in the amplifier laser rods to reduce the effects of ETU. This strategy will require longer laser rods however, in order to absorb the majority of the incident pump light,which in turn will put pressure on the output beam quality of the pump sources themselves to reduce diffraction spreading along the length of the laser rod. Secondly, we can de-tune the pump light wavelength away from the absorption peak of the gain material, this again will reduce the pump absorption per unit volume and will hence require longer laser rods.

4.4.2 Thermal lensing on the 1053nm line in an Nd:YLF amplifier

As has already been mentioned in Chapter 3, Nd:YLF has a natural advantage over other common laser materials in terms of the nature of its thermal lensing due to the negative change in refractive index with temperature. Although this effect on the higher gain 1047nm line will result in a negative focal length thermal lens being generated, the weaker change in refractive index on the lower gain 1053nm line, off-set by the positive lens generated by the bulging end-faces of the laser rod, has the net effect of producing a very weak positive focal length thermal lens. We can model the thermal lens power *D* [1] in the amplifier generated by the change in refractive index dn/dT as a function of absorbed pump power using the following expression:

$$D=\left[D_{\max}\left\{1-\frac{2\left(1-\rho_{nl}\right)}{\beta}\left[2\left(\sqrt{1+\beta}-1\right)+\ln\left(\frac{4}{\beta}\left(\frac{\sqrt{1+\beta}-1}{\sqrt{1+\beta}+1}\right)\right)\right]\right\}\right]+\Delta \qquad [4.27]$$

ρ_{nl} is the fraction of absorbed pump coverted to heat in the absence of ETU under non-lasing conditions. D_{max} is the maximum thermal lens power from the dn/dT contribution under operating conditions where up-conversion is very strong and all the absorbed power is converted to heat (i.e. $\beta\rightarrow\infty$). D_{max} is given by the expression:

$$D_{\max}=\frac{P_p\frac{dn}{dT}}{\pi W_P^2 K_C} \qquad [4.28]$$

Δ is the positive contribution to the overall thermal lens power by the bulging end-faces of the laser rod (numerical figure of merit based on the thermal lens measurements given by [1]).The same figure of merit β that we used in chapter 3 for the master can be applied to the amplifier rods where:

$$\beta=\frac{8WP_P\alpha_P\tau^2}{\pi w_P^2 h\nu_p} \qquad [4.29]$$

where W is the up-conversion parameter, P_P in the incident pump-power, α_P is the absorption coefficient for the pump radiation, τ is the fluorescence lifetime of the upper laser level, w_P is the pump spot size and ν_p is the pump frequency. If we take the example of an 18mm long laser rod with a 0.5% dopant concentration (reducing

α_P to 12.39m^{-1}) and assuming a pump spot size of 250μm we can plot β as a function of incident pump power (figure 4.7):

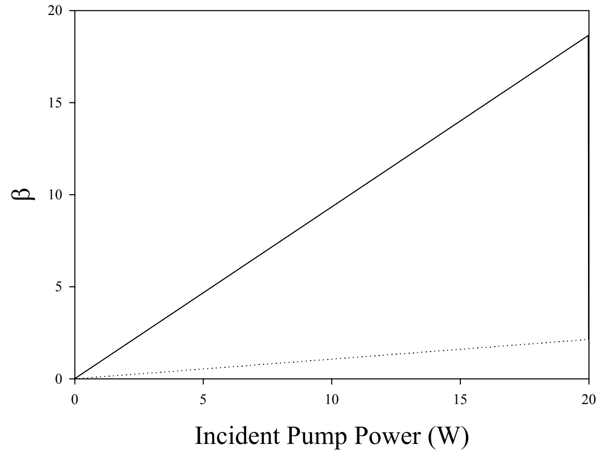

Figure 4.7 Graph showing β as a function of incident pump power for a 0.5% dopant concentration (dashed line) and a 1.2% dopant concentration (solid line) 18mm long Nd:YLF amplifier rod.

β is a measure of the magnitude of the effect of up-conversion on the overall decay rate from the upper-laser level and is proportional to the absorbed pump power per unit volume in the laser rod and the up-conversion parameter *W*.

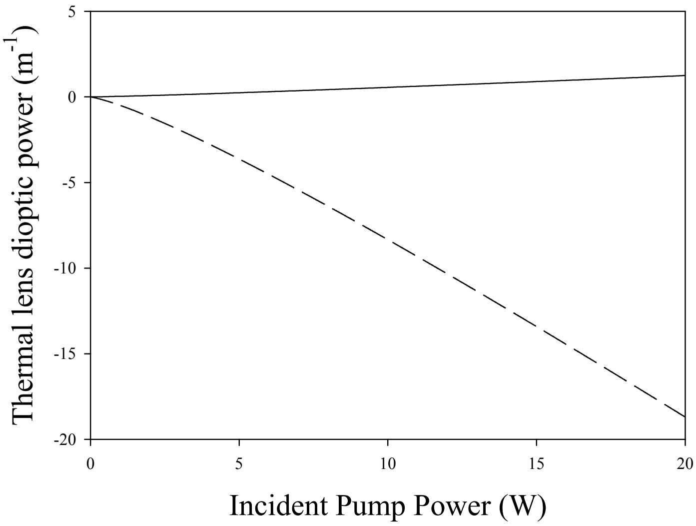

Figure 4.8 Graph showing the thermal lens power of an amplifier laser rod as a function of incident pump power for 1.2% dopant concentration on the 1047nm line (dashed line) and the 1053nm line (solid line).

Figure 4.8 shows the thermal lens power of the amplifier rod increasing as the pump power increases. In chapter 3 the ratio of the thermal lens power with and without the effects of up-conversion was plotted using the following equation:

$$\Gamma = \frac{1}{\rho_{nl}}\left\{1-\frac{2(1-\rho_{nl})}{\beta}\left[2\left(\sqrt{1+\beta}-1\right)+\ln\left(\frac{4}{\beta}\left(\frac{\sqrt{1+\beta}-1}{\sqrt{1+\beta}+1}\right)\right)\right]\right\} \qquad [4.30]$$

From this expression, we can plot a graph showing the magnitude of the effect of up-conversion on an amplifier laser rod as a function of incident pump power:

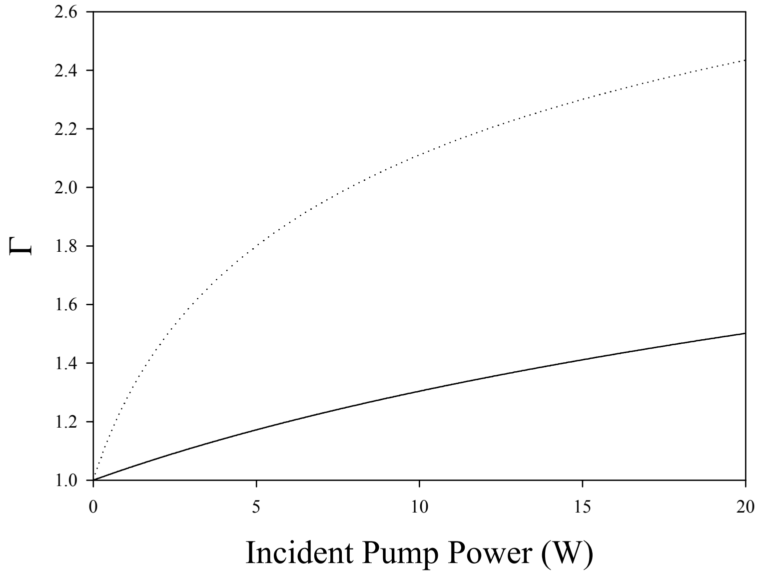

Figure 4.9 Graph showing Γ, the ratio of the thermal lens power with and without the effects of ETU on an amplifier laser rod as a function of incident pump power. Dashed line shows 1.2% dopant concentration, solid line shows 0.5% dopant concentration.

Figure 4.9 shows a comparison between 1.2% and 0.5% dopant concentrations in the laser rod regarding the effect of ETU on the thermal lens. It can be seen from the graph that a 1.2% dopant concentration will show a 140% increase in thermal lens strength due to ETU for 20W of absorbed incident pump power where, as a 0.5% dopant concentration will show an increase in thermal lens power of only 50% in comparison. We can compare the effects of lowering the dopant concentration in the laser amplifier rod in Nd:YLF by again plotting the thermal lens power as a function of incident pump power for the 1053nm line (figure 4.10):

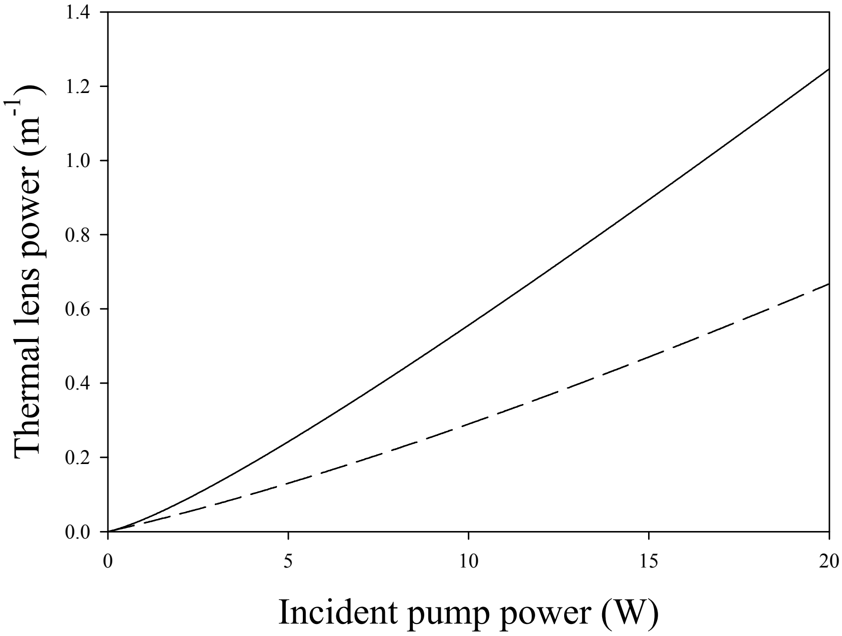

Figure 4.10 Thermal lens power as a function of incident pump power for lower gain 1053nm line in Nd:YLF for 1.2%(solid line) and 0.5%(dashed line) dopant concentrations.

The model in figure 4.10 demonstrates that for a single laser rod, acting as an amplifier, we can dramatically reduce the thermal lens power generated by reducing the dopant concentration. This in turn will reduce the effects of ETU within the Nd:YLF but will mean that we will have to use longer amplifier rods in order to absorb the same amount of pump light putting greater pressure on pump sources with good beam quality.

4.4.3 Degradation in signal beam quality

In chapter 1 we gave an expression for the brightness B of a laser as being:

$$B = \frac{P}{\lambda^2 M_x^2 M_y^2} \qquad [4.31]$$

where P is the laser power, λ is the laser wavelength and $M^2_{x/y}$ is a measure of the beam quality in the x and y planes respectively. In order for an amplifier to operate well, it must not only increase the output power of the signal laser efficiently, but must also preserve the brightness of the output by preserving the beam quality of the output. A limit on power scaling the output from the master oscillator is therefore, degradation in beam quality due to the aberrations in the thermal lens. Since our applications of the MOPA were generally reliant on the brightnesss of the output from the laser, an upper limit was set on the amplifier in terms of output beam quality. In chapter 2 we discussed the effects of thermal lens aberrations whereby, a laser beam with a Gaussian intensity profile and initial beam quality M_i^2 after propagating through a lens of focal length f will producing a phase distortion $\Delta\o(r)$:

$$\Delta\phi(r) = \frac{2\pi}{\lambda}\left[\frac{r^2}{2f} - C_4 r^4\right] \qquad [4.32]$$

leading to a degradation in beam quality such that the resultant beam quality factor M_f^2 is given by:

$$M_f^2 = \sqrt{\left(M_i^2\right)^2 + \left(M_q^2\right)^2} \qquad [4.33]$$

where M_q^2 is due to the quartic phase aberrations of the lens and is given by:

$$M_q^2 = \frac{8\pi C_4 w_S^4}{\lambda\sqrt{2}} \qquad [4.34]$$

where w_L is the beam radius and C_4 is the quartic phase aberration coefficient. In general, a thermal lens will produce a more complicated phase distortion than a standard optical lens but restricting the consideration to situations where $w_L < w_P$, so that higher order terms than the quartic can be neglected, the resulting expression for the beam quality degradation of the thermal lens M_q^2 is given by [19]:

$$M_q^2 = \frac{\rho\eta_{abs}\left(\frac{dn}{dT}+\Delta\right)}{K_C\lambda}\left[\frac{\pi w_S^2 B}{2\sqrt{2}}\right]$$

where

$$B = 0.5 d^2 I_P(r)/dr^2 \text{ at } r = 0$$

[4.35]

and where Δ is the contribution of the positive lens generated by the bulging of the end faces of the laser rod. Thus from equation 4.33 and 4.35 we can estimate the degradation in beam quality which results after a passage of the laser beam through an aberrated thermal lens, generated by a pump beam with an arbitrary intensity profile.

For a top-hat pump beam $B = 0$ so there is no degradation in pump beam quality, however, for a Gaussian beam profile, $B = 4P_p/\pi w_P^4$ and hence

$$M_q^2 = \left(\frac{P_p\gamma\eta_{abs}\left(\frac{dn}{dt}+\Delta\right)}{\lambda K_c\sqrt{2}}\right)\cdot\left(\frac{w_L^4}{w_p^4}\right)$$

[4.36]

where $\eta_{abs} = 1-\exp(-\alpha_P l)$

This expression shows that in addition to the dependence on power dissipated as heat, thermo-mechanical and thermo-optical properties of the laser material, the degradation in beam quality also depends strongly on the ratio of laser beam radius to pump beam radius. Hence, if $w_L << w_P$, then the beam quality is less influenced by thermally induced aberrations and the limit where $w_L/w_P \to 0$, then $M_f^2 \to 1$. Also, if $w_L \geq w_P$, even a weakly aberrated thermal lens can result in a large degradation in beam quality. If we plot equation 4.33 as a function of the ratio of signal spot size to pump spot size in equation 4.36, we get the result:

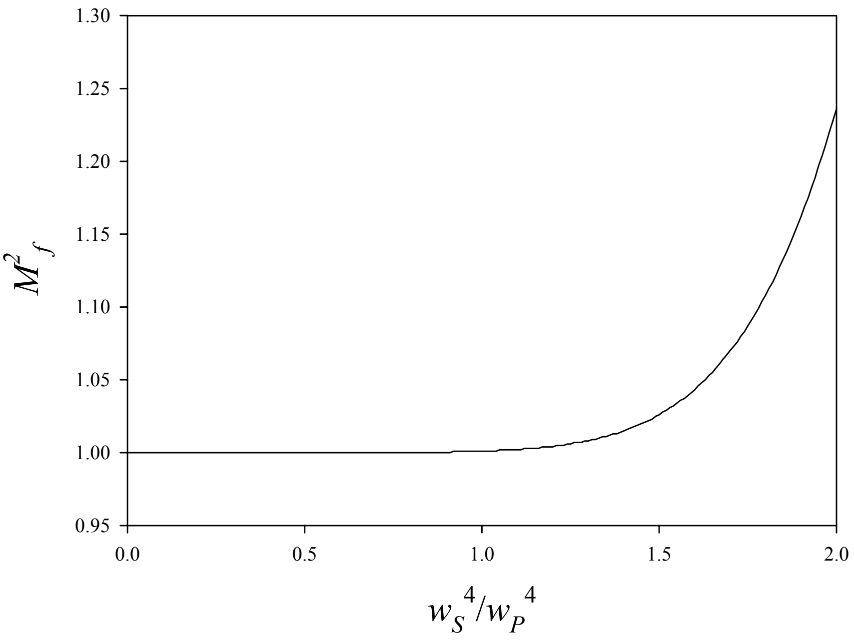

Figure 4.11 Graph showing M_f^2 as a function of the ratio of signal to pump spot size within the amplifier for an incident pump power of 20W.

Figure 4.11 shows that for the output from the amplifier to remain near diffraction limited, the signal spot size must not exceed the pump spot size. This example is for an 18mm 0.5% doped Nd:YLF rod pumped by 20W at 792nm. In order for $M^2 \leq 1.1$, the signal spot size to pump spot size ratio must not exceed ~1.7. In section 4.2.1 we established that as the signal beam decreases in sizes, it will see a flatter portion of the gain profile towards the centre of the Gaussian pump region and hence the gain will become uniform. Provided that the signal beam in this area has relatively small beam radius, hence short Rayleigh range and high radius of curvature, any relative deviation in phase due to an aberrated thermal lens will be much smaller than in the case of a large laser beam. This means that, provided the transverse laser mode size is a little smaller than the pump mode size in the amplifier, we should see less distortion in beam quality at the slight expense of a reduced amount of power extraction and the possibility of increased spontaneous emission.

4.4.4 Minimum pump beam spot size

The ultimate power-scaling limit of any laser must essentially be determined by the stress fracture limit of the material used, in the case of Nd:YLF, this is comparatively low in comparison with other more commonly used laser materials such as Nd:YAG. However, in the case of our amplifier and the limit on degradation to output beam quality it is degradation due to the highly aberrated nature of the thermal lens that limits the maximum power that can be achieved. We can establish a very rough guide to power scaling limitation by saying that $M_q^2 \leq 0.46$ (corresponding to $M^2 \leq 1.1$) from equation 2.26. The net result from equation 2.26 is that the maximum pump power used P_{pmax} must satisfy the following condition for good beam quality:

$$P_{\max} \leq \frac{0.65 K_C \lambda}{\rho^4 \gamma \eta_{abs} \left(\frac{dn}{dT} + \Delta \right)}$$

[4.37]

where $\rho = w_S / w_P$, and Δ is the positive contribution of the bulging end faces of the laser rod. It should be noted that this condition is a very rough guide since it considers only a single pass of the laser rod and is only valid for $w_L \leq w_P$. Plotting P_{max} as a function of the ratio of signal to pump beam spot sizes gives:

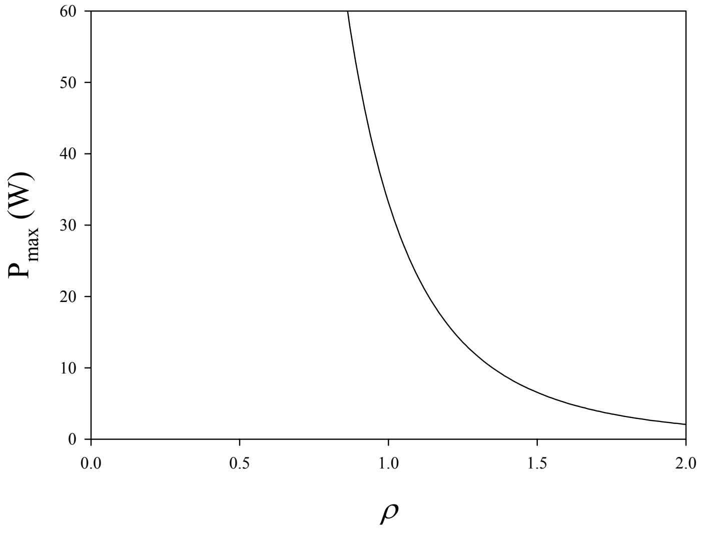

Figure 4.12 Graph showing maximum incident pump power whilst maintaining output signal beam quality as a function of ratio of signal to pump spot sizes.

Figure 4.12 gives us a rough guide for incident pump power in the amplifier as a function of the ratio of pump and signal spot sizes in order to maintain signal beam quality. We can see from the graph that for a single 0.5% doped Nd:YLF rod pumped by 20W the signal spot size can increase in size to around 10% larger than the pump spot size and still maintain diffraction limited. By going to a signal mode size slightly smaller than the pump, we can see from the graph that the amplifier should be capable of being pumped by considerably more light without degradation to signal beam quality. Using a larger pump beam size in order to reduce the pump intensity and hence the phase aberration would mean that we have to increase the size of the signal mode in the amplifier in order to extract more gain, which in turn would require a longer Rayleigh range. Since beams with long Rayleigh ranges are more susceptible to beam distortions, via phase aberrations, the net result of increasing the pump beam size would leave the M^2 value of the signal approximately the same. It could therefore be argued that in order to optimise the extraction efficiency from an amplifier, it may well be better to use as small a pump spot size as possible and hence signal spot size in order to allow efficient use of the population inversion in the wings of the pump. This again will put demands on the pump beam quality as for a lower dopant concentration we have to absorb the pump over a longer length of laser rod.

4.3.5 Amplifier double rod geometry

The weak thermal lens of Nd:YLF at 1053nm (σ polarisation) due to the contributions of the small negative change in refractive index combined with the weak positive lens contribution of the bulging end-faces makes it an interesting alternative regarding amplifier design to other commonly used laser materials. Although the 1053nm line in Nd:YLF has a lower stimulated emission cross-section, meaning that amplifiers in this configuration will produce less gain, the weak thermal lens will minimise degradation in beam quality hence allowing the amplifier to considerably increase the brightness of the input signal (equation 4.31). We have established that the use of a lower dopant concentration of 0.5% in longer rods, to reduce the overall thermal loading per unit volume whilst maintaining good pump absorption (using pump sources with good beam quality), will provide us with an amplifier strategy for maintaining good beam quality of the signal beam whilst power scaling to useful levels for cw nonlinear frequency conversion (typically >10W), whilst maintaining TEM_{00} beam quality.

In order to increase the extraction efficiency of the single-pass amplifier model (equation 4.16), we can extend the model via Rigrod analysis to a double pass of the amplifier whereby:

$$\eta_{extract} = \left(\frac{I_{extract}}{I_{\max}} \right) = \frac{\ln(G_0) - \ln(G)}{\ln(G_0)} \qquad [4.38]$$

becomes:

$$\eta_{extract} = 1 - \frac{\ln(G)}{\ln(G_0)} \qquad [4.39]$$

The final amplifier design consisted of a dual rod scheme. Two 0.5% Nd:YLF rods both 18mm long were pumped from either end by two 792nm fibre-coupled diode bars (figure 4.13) providing a combined incident pump power of ~ 40W.

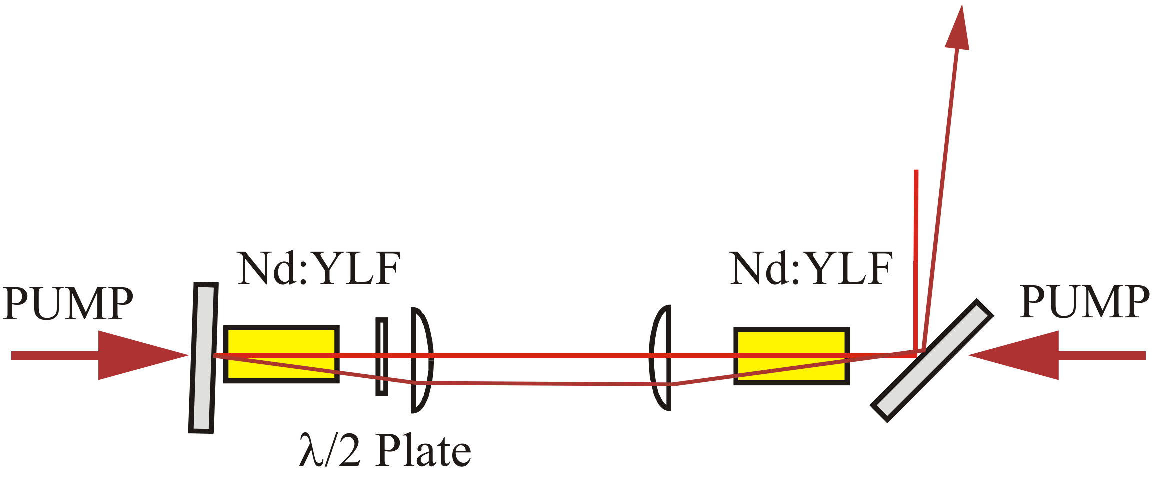

Figure 4.13 Diagram showing the double-pass amplifier configuration. The angles have been exaggerated for the purposes of displaying the ray path throughout the amplifier.

The signal beam was relay imaged from the master oscillator to the first amplifier rod in order to preserve the beam waist size. Two 50mm focal length lenses then relay imaged the signal waist in the first rod to the second. These two lenses also relay imaged the pump waist in one rod to the other and vice versa, again maintaining the waist size within both amplifier rods and ensuring that any unabsorbed pump light in the first rod was absorbed by the second. The axes of the laser rods were crossed to compensate the astigmatism in the generated thermal lens. The signal is double passed through both amplifier rods to increase the gain and the extraction efficiency on the 1053nm. A half-wave plate was placed between the laser rods to rotate the polarisation of the signal through 90^0 in order to ensure that it sees the maximum gain on the 1053nm line within the Nd:YLF rods. This also acted as a whole wave-plate for the pump light.

The small signal gain was calculated for a single pass of the amplifier using equation 4.26. Modelling the expected small signal gain from the amplifier, including the effects of up-conversion for a single-pass and a double-pass gave the following result:

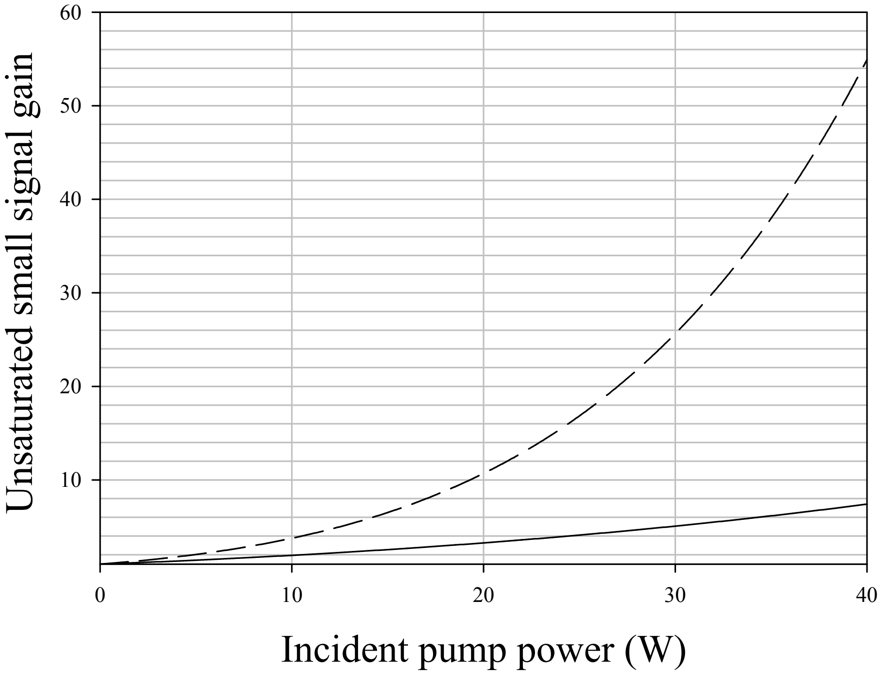

Figure 4.14 Unsaturated small signal gain of a single pass (solid-line) and double pass (dashed-line) of dual rod amplifier.

Figure 4.14 show the resultant unsaturated small signal gain for a single and double pass through the dual rod amplifier pumped by 40W at 792nm, with pump and signal spot sizes 250µm and 240µm respectively. An initial experiment was conducted with an amplifier prototype. The pump light was relay imaged into the laser rods to a focused spot size of $w_{x,y}$=250µm and two f=50mm lens between the rods. These two lenses also relay imaged the signal through the amplifier rods which was carefully focused to 240µm in both planes to ensure excellent mode matching within the gain regions.

Finally, in order for the signal to see the maximum gain on the 1053nm transition between the two crossed laser rods, we employed a λ/2 plate at 1053nm (λ plate at the pump wavelength) to rotate the polarisation from horizontal to vertical and vice versa. The back mirror of the amplifier was slightly misaligned by a very small angle so that the output from the amplifier could be picked off using an appropriate mirror.

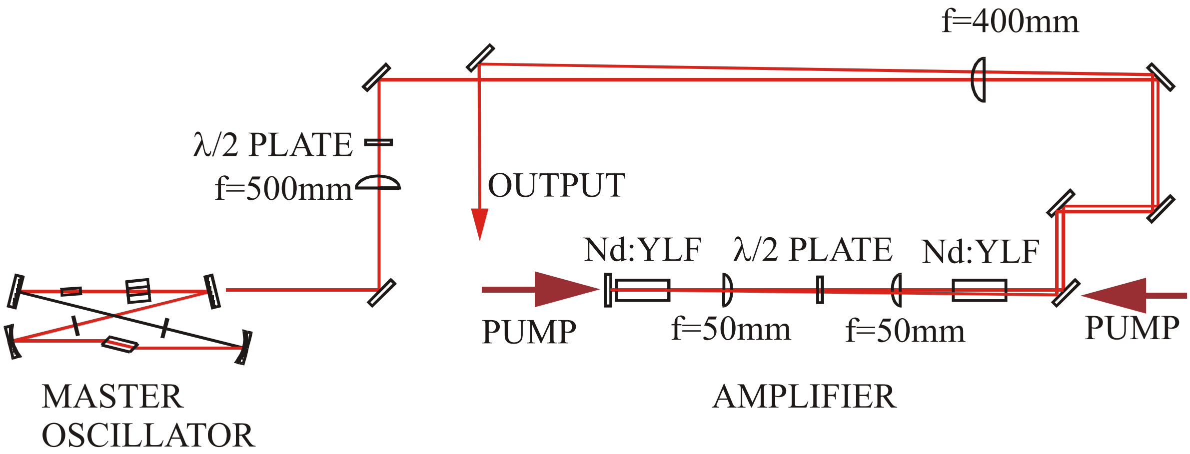

Fig 4.15 Diagram to show the MOPA set-up including optics for rely imaging spot-sizes from master oscillator to amplifier.

Figure 4.15 shows the initial cw MOPA set-up. The first λ/2 plate after the master ensures that the signal will see the maximum 1053nm gain line in the first laser rod within the amplifier and the 500mm and 400mm focal length lenses relay image the signal to ensure good beam overlap in the same position. Once the amplifier alignment was optimised, the output was fully characterised. It was found that the amplifier did not affect the beam quality of the master oscillator, maintaining $M^2<1.1$ throughout the entire incident pump power range, and since using a MOPA configuration de-coupled power scaling from the initial output characteristics of the master, the output also remained robustly and reliably single-frequency with its mode-hop-free characteristics.

The small signal gain of the amplifier was measured by attenuating the output from the master-oscillator to 5mW, the results of which can be seen in figure 4.16.

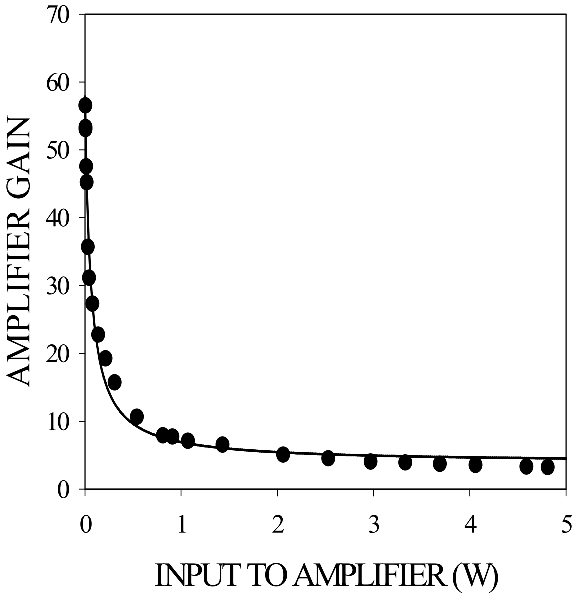

Figure 4.16 Graph showing amplifier small signal gain as a function of master signal input.

Figure 4.16 shows the measured small signal gain for a double pass of the amplifier. Including the effects of ETU our model gave an excellent representation of practical results, predicting an unsaturated small signal gain of ~60.

We measured the maximum small signal gain to be ~60 corresponding to a small signal input power of ~5mW. Beyond this point it was found very difficult to reduce the output of the master oscillator further without the need for more equipment in the system. cw gain for the double pass amplifier (figure 4.16) was measured at maximum master output power (~4.5W) giving us a value for the power gain of the amplifier to be ~ 3.3.

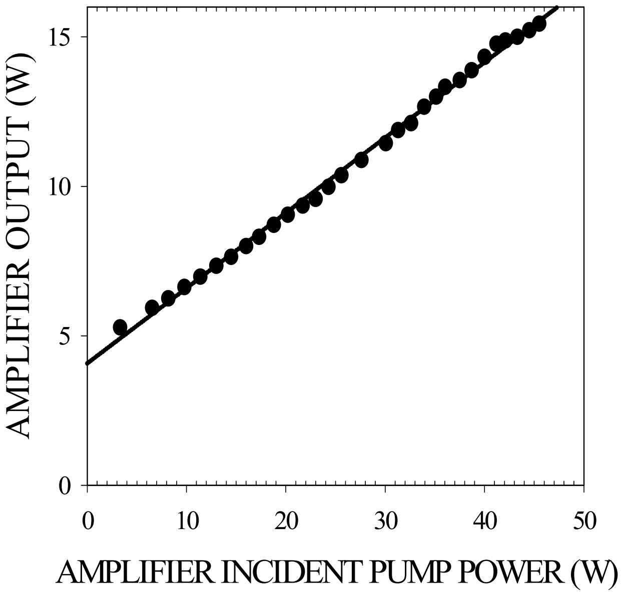

Fig 4.17 Graph showing maximum amplifier output as a function of incident amplifier pump power with constant master input of ~ 4.5W.

The amplifier still maintained the beam quality of the signal throughout this power range showing that the thermal lensing action was still very weak. From equation 4.27 we could calculate the dioptric power of the thermal lens (within Nd:YLF operating at 1053nm) with incident pump power for the dual-rod amplifier regime as being (figure 4.18):

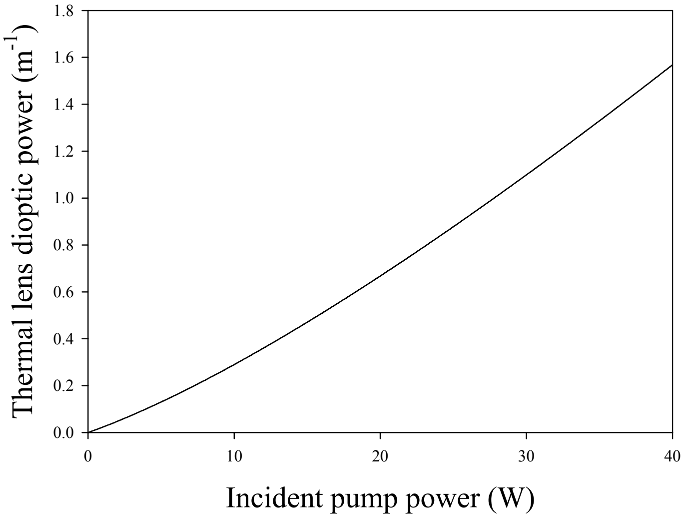

Figure 4.18 Thermal lens dioptric power as a function of incident pump power for dual-rod amplifier geometry.

The effect of the weak thermal lens was noted as the spot-size, which was observed in the far-field, increased by 3% throughout the pump power range and remained circular to within a 5% tolerance in the x and y planes. No degradation in beam quality was noticed via the diagnostics, this result was confirmed when the theory of section 4.4.3 was applied to the dual-rod geometry, assuming an initial beam quality of the signal to be M2=1.05 (a measured value), the degradation in beam quality as a function of incident pump power was found to be as in figure 4.19:

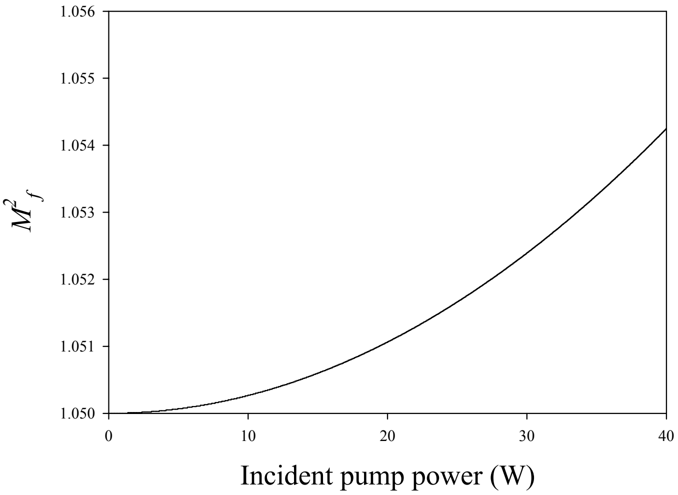

Figure 4.19 Graph showing degradation in signal beam quality as a function of incident amplifier pump power for the dual rod amplifier geometry.

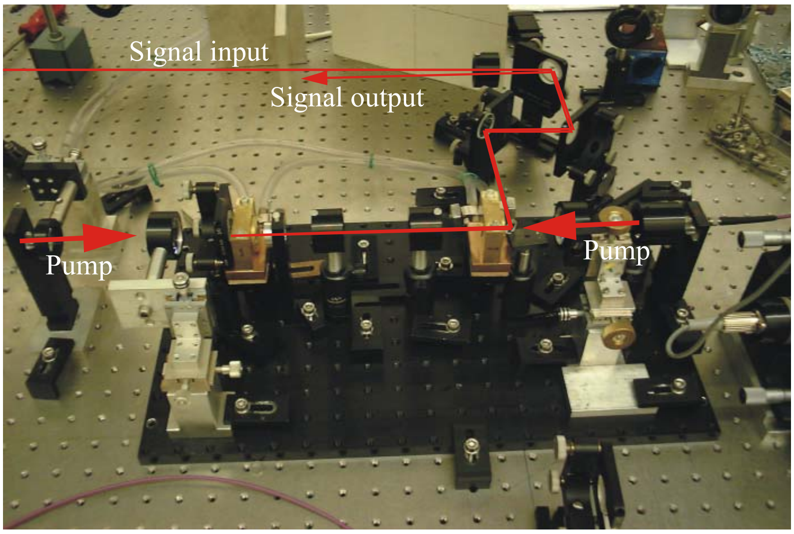

Figure 4.20 Photograph of beam path through the initial cw set-up of amplifier.

The initial results from the amplifier were promising (figure 4.20). The maintenance of diffraction limited beam quality suggested that Nd:YLF was, under the appropriate design schemes, a very viable choice for power scaling diode-end-pumped solid state lasers. The small signal gains that we calculated, taking up-conversion into account appeared to fit very closely to the experimental results, ignoring losses incurred through the amplifier and gain saturation.

4.3.5 Qcw Operation master oscillator configuration

In order to take advantage of the potentially very high small signal gain offered by the first amplifier configuration, to achieve high peak powers, an acousto-optic modulator (AOM) was placed after the output of the master oscillator to effectively “slice” the signal beam into pulses. The AOM was a Gooch and Housego 175MHz Tellurium Dioxide modulator that was AR coated at 1053nm, the rise-time of the device was quoted to be 25ns with a maximum modulation bandwidth of 20MHz and a maximum RF drive power of 2W giving in turn a maximum diffraction efficiency of ~80% (figure 4.22) in the first order diffracted beam. This meant adding a considerably larger amount of optics to the system in order to relay image the output from the master oscillator to the amplifier and to reduce any back reflections to the master-oscillator (which it was noted was still quite sensitive to any feedback).

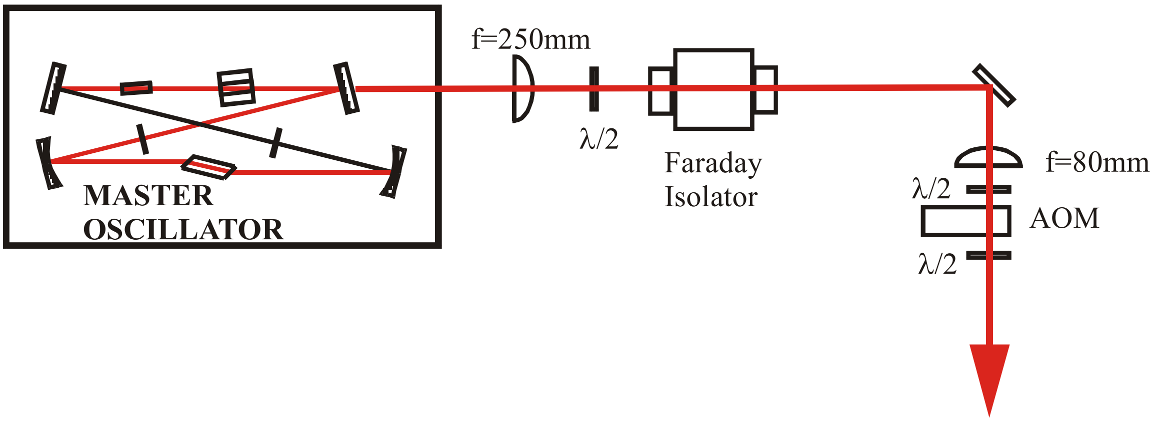

Figure 4.21 Optics to suppress feedback to the master oscillator and to allow pulsed operation.

Figure 4.21 shows the added equipment after the master-oscillator. The f=250mm lens collimated the output before the Faraday isolator (transmission 90% at 1053nm) that was employed to eliminate feedback. The output beam was then relay-imaged to form an 80μm spot within the AOM to optimise diffraction efficiency in the first order diffracted beam. The RF power to the AOM could then be modulated or operated continuously to produce a pulsed or cw output to the amplifier. Figure 4.22 shows a graph of the AOM diffraction efficiency as a function of cw RF power.

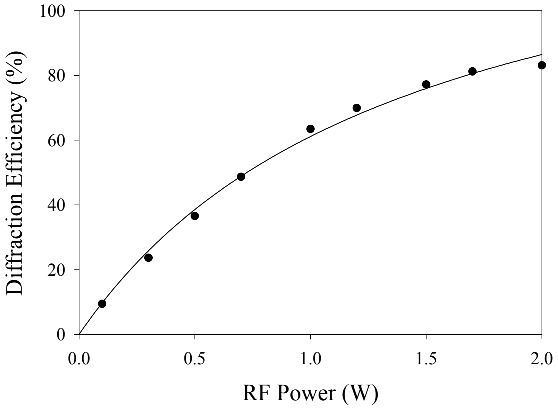

Figure 4.22 Graph showing AOM diffraction efficiency as a function of RF power.

Due to the poor transmission of the Faraday isolator (<90%), the 80% diffraction efficiency of the AOM first order beam, degradation in output power from the diode pump source for the master oscillator and from cost restrictions, the output from the master-oscillator was considerably reduced. Figure 4.21 giving a maximum cw output power of ~2.4W.

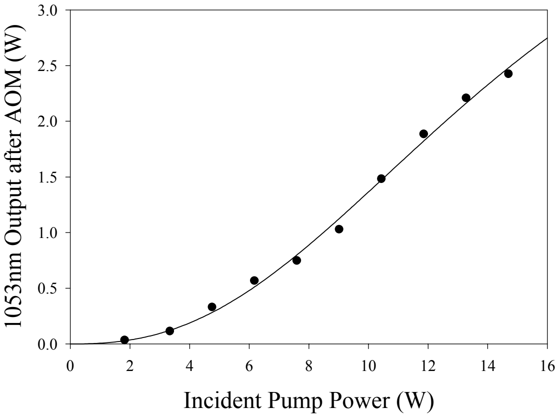

Figure 4.23 Graph showing reduced output from master oscillator.

Due to the losses in the amplifier, the poor transmission of the Faraday rotator and the limited diffraction efficiency of the AOM, a second amplifier was constructed to exactly the same specifications as the first. It was hoped that the end result therefore would be a very much improved increase in the unsaturated small signal gain of the system and a cw power gain that would allow us to demonstrate various high power nonlinear frequency conversion experiments.

4.5 Experimental results

The output from the master oscillator was double-passed through two amplifier stages. Figure 4.24 shows the system design. From the diagram it can be seen that the beam is relay imaged into the first amplifier via the f=150mm and f=300mmm lenses. The amplifiers are separated with a Faraday isolator and the beam is picked off after a double pass of the second amplifier.

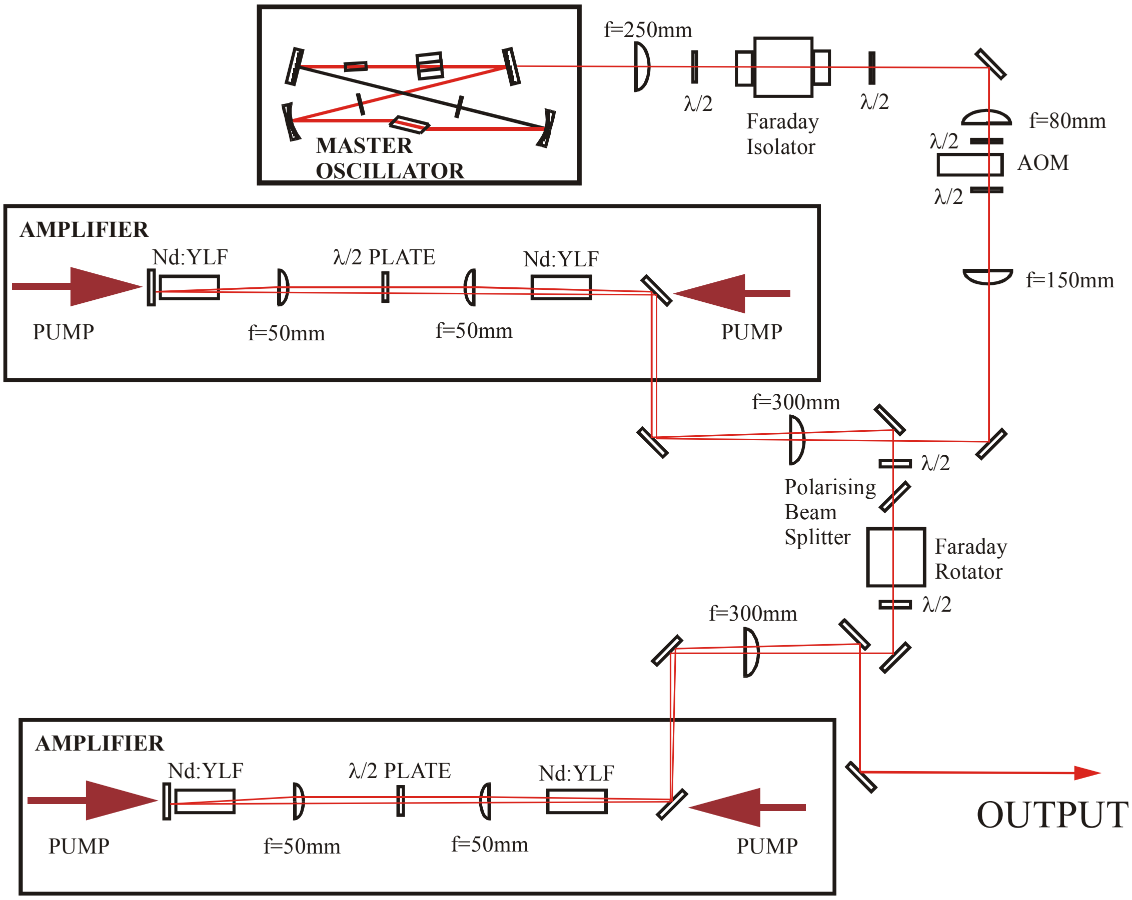

Figure 4.24 MOPA configuration capable of cw and Qcw output using two amplifier stages.

The unsaturated small signal gain was modelled using equation 4.25. The following graph (figure 4.25) shows the unsaturated small signal gain for a double pass of two amplifiers, the data points on the graph were collected for small amounts of cw power (~μW) (via adjustment of the diffraction efficiency of the AOM):

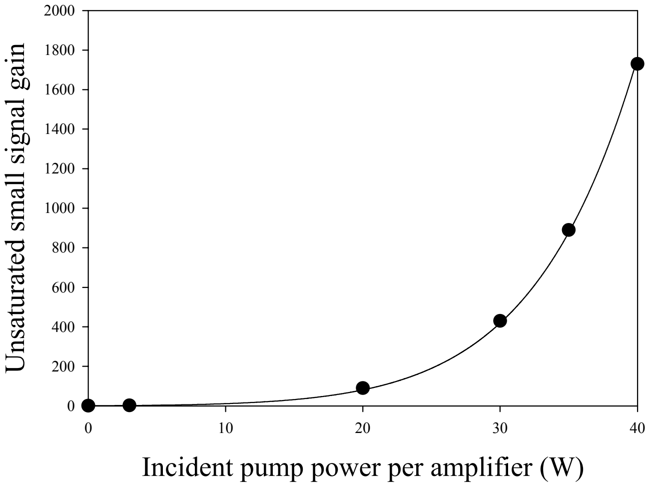

Figure 4.25 Graph showing unsaturated small signal gain as a function of incident pump power per amplifier for a double pass of both amplifiers, the line on the graph shows theory.

The double-pass loss was measured for amplifiers 1 and 2 and found to be ~10% for each. This meant that the output signal from the master-oscillator after a double pass of each amplifier was measured to be ~1.9W. Cw power gain was measured for this new set-up, the results of which can be seen in figure 4.26.

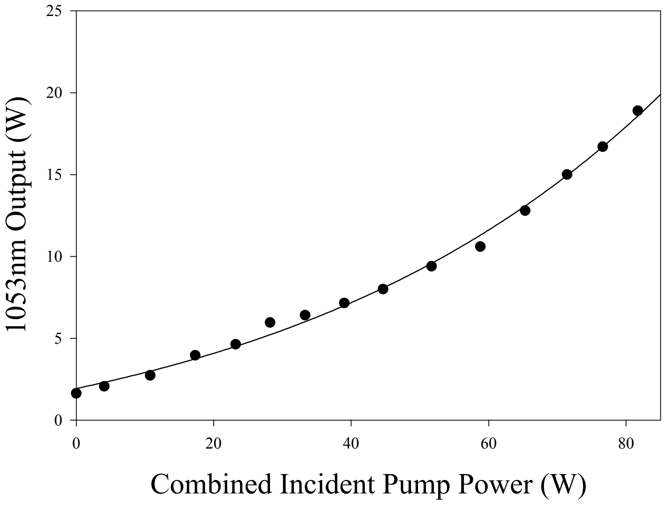

Figure 4.26 Graph showing 1053nm output as a function of incident amplifier pump power for the two amplifier double pass configuration.

The incident combined pump power for the amplifiers was measured to be ~85W. Figure 4.24 shows the power gain of the amplifiers in this configuration. The MOPA produced a maximum of 18.9W of cw output. Again it was discovered that the effect of the thermal lens was negligible, plotting the theory from section 4.4.3 for a two dual-rod amplifiers with a maximum incident pump power of ~80W gave (figure 4.27):

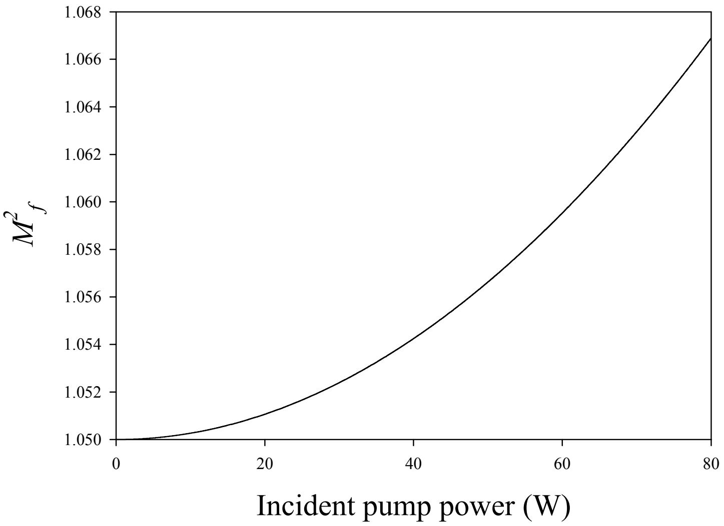

Figure 4.27 Signal beam quality after a double pass of two dual-rod amplifiers pumped with a combined pump power of 80W.

with the result that there was only a small increase in output spot size with increasing incident pump power and the beam quality of the output remained $M^2 < 1.1$.

4.5.1 Final MOPA implementation and characterisation

In order to try to optimise the small signal gain further, another modification was made to the MOPA by means of retro-reflecting the beam down its original path in amplifier 2 and picking the beam off after the Faraday isolator by means of the polarising beam splitter in figure 4.28. Although the set-up was carefully aligned, the reflectivity of the beamsplitter was found to be ~89% so that at higher power there was enough feed back to the master oscillator to lase bidirectionally causing multi-frequency operation, plus, due to the losses of the beamsplitter and the passive loss of amplifier 2, the single pass throughput of the master oscillator was now reduced to be ~1.5W.

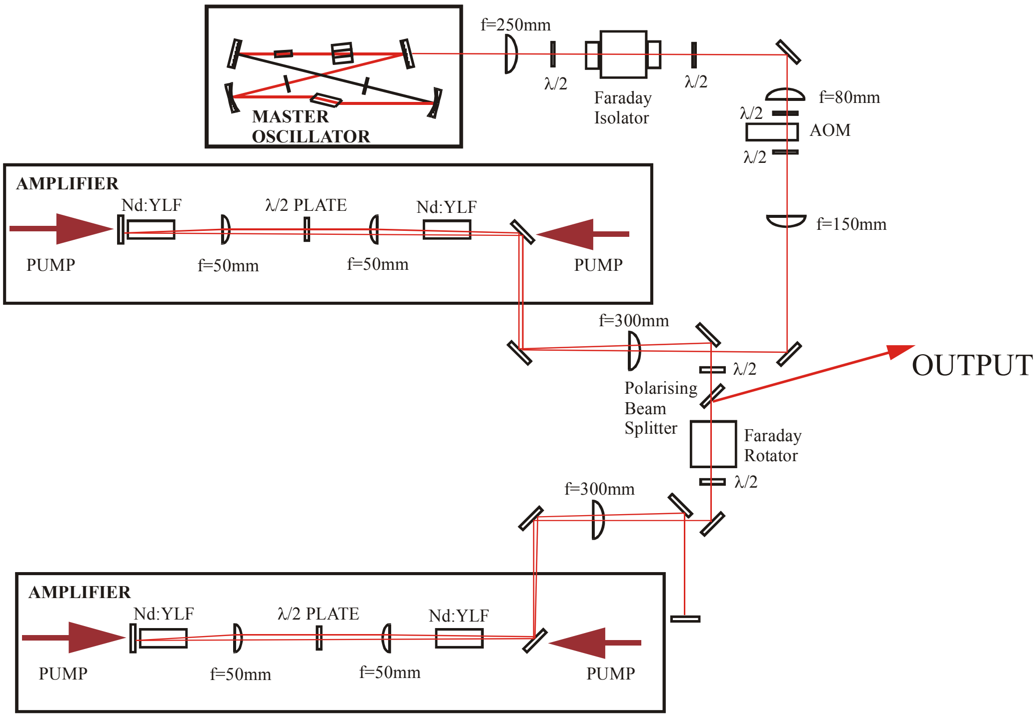

Figure 4.28 Final MOPA design including retro-reflected pass of amplifier 2 and pick off at the polarising beamsplitter.

The losses due to the system were measured directly and calculated. It could be seen that there was a 10% loss in signal power for each double pass of the amplifiers (that is, 10% due to the double pass of amplifier 1 and 20% due to two double passes of amplifer 2: see figure 4.29).

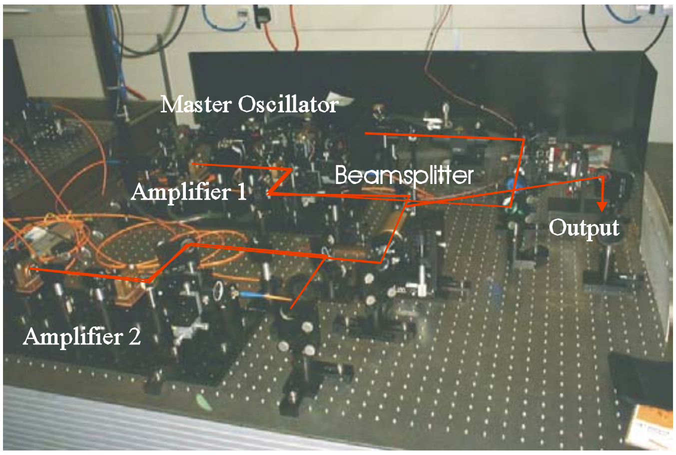

Figure 4.29 Photograph of final MOPA set-up.

ASE generated in a single laser rod was calculated and expressed in terms of un-useable absorbed pump power, that is to say, that due to ASE, a fraction of the absorbed pump power per laser rod could not be converted to gain. Taking this into consideration, the small signal gain for the system (one double pass of amplifier 1 and two double passes amplifier 2 assuming not significant upper laser level depletion) was calculated to be ~5000. This was modelled to give the following result (figure 4.30):

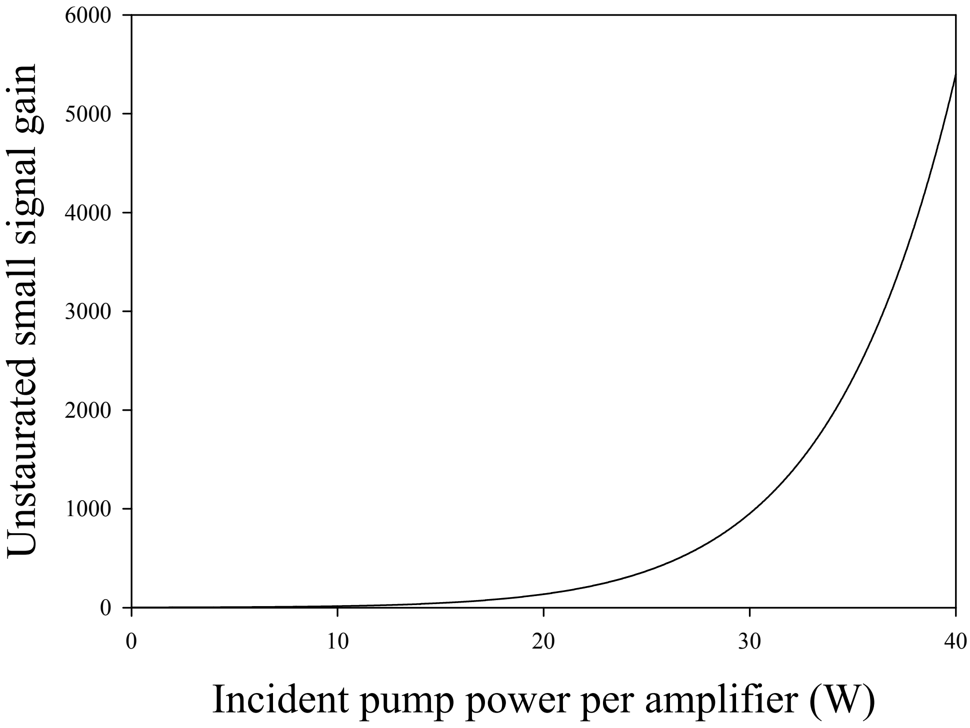

Figure 4.30 Graph showing the unsaturated small signal gain including expressions for up-conversion and ASE per amplifier laser rod for a double pass of amplifier 1 and a quadruple pass of amplifier 2.

The diagnostics used to characterise the MOPA consisted of the following: a Coherent Fieldmaster power meter, a fast Si photodiode and a confocal Fabry-Perot for monitoring the single-frequency nature of the output. The beam quality of the output was measure for various amplifier pump powers using a Coherent Modemaster beam analyser (figure 4.31).

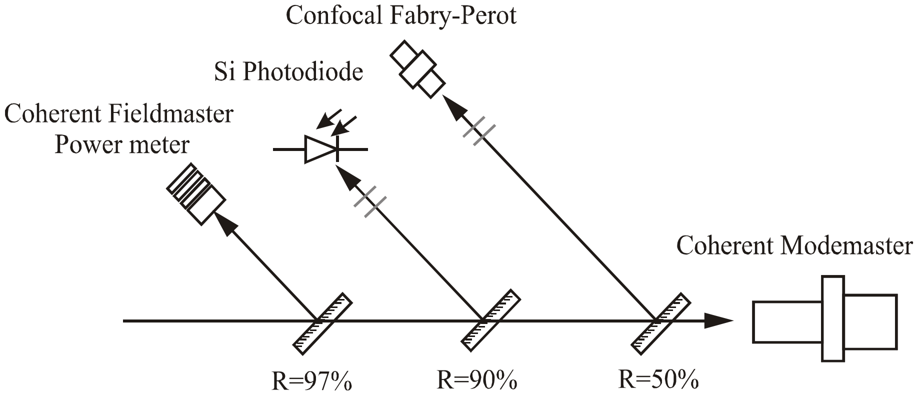

Figure 4.31 Diagnostic set-up for MOPA characterisation.

The maximum cw power available was measured in the final MOPA configuration to give up to 17.5W 1053nm output with $M^2 < 1.1$. Checking that the output was single frequency was a reliable method to make sure that there were no amplified back reflections to the master oscillator, allowing it to operate bi-directionally at any point through the incident amplifier pump range.

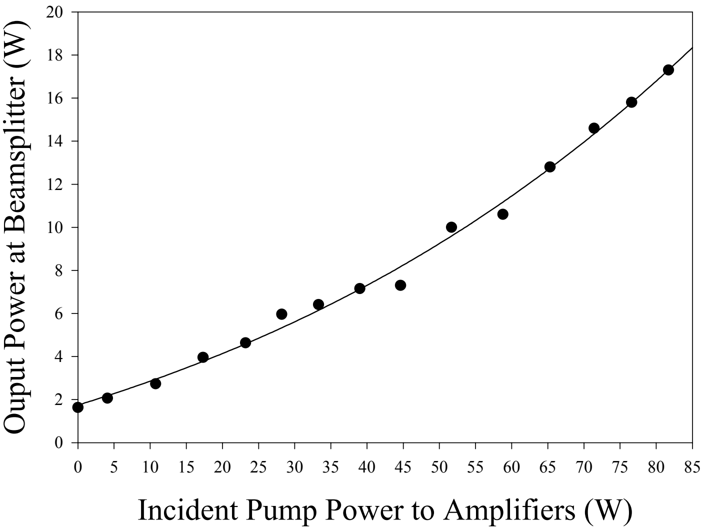

Figure 4.32 CW power output for the final MOPA set-up.

The slightly lower cw output from the system was due to the high transmission losses of the two amplifiers and the high loss from the beam splitter. Taking these into account, by assuming that that the transmission losses of both amplifiers were much lower and by assuming that the beamsplitter had a reflectivity >95%, we would have expected as much as 25W from the system. The small signal gain at the beamsplitter was then measured as a function of master-oscillator input power. The first of these results was simply measure in terms of cw output power from the amplifiers as can be seen in figure 4.32. During the measurement of the small signal gain of the amplifiers they were pumped by the maximum available pump power of ~85W combined.

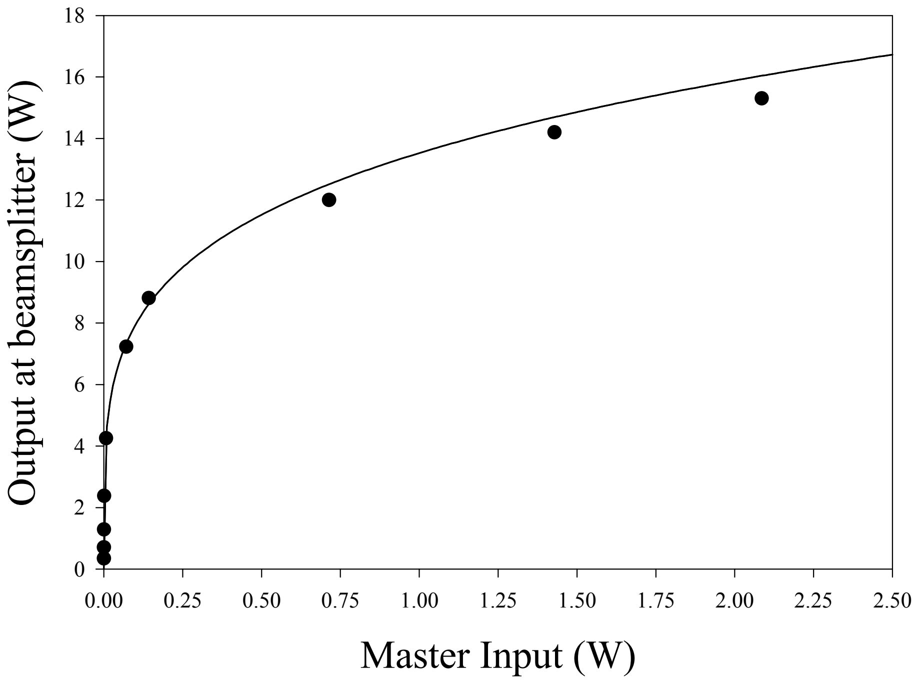

Figure 4.33 Graph showing MOPA output as a function of master input with amplifiers at maximum incident pump power.

The gain tails off in figure 4.33 as the amplifiers enter a saturated regime depleting the upper laser level population inversion. The gain for the MOPA was measured, that is, the cw input signal power and the cw output signal power, were measured at the maximum available incident amplifier pump power. These results can be seen in figure 4.34.

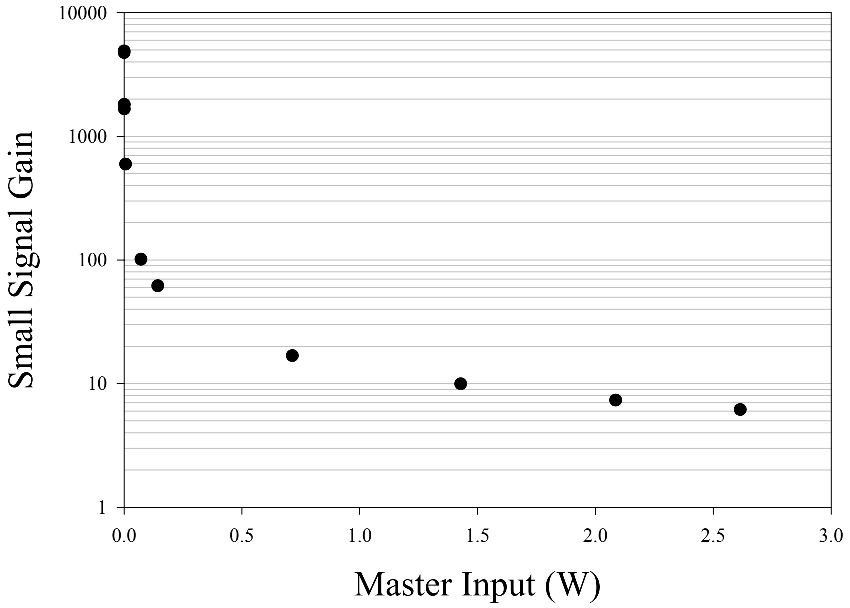

Figure 4.34 Graph showing the small signal gain of the MOPA as a function of cw master oscillator input.

Figure 4.34 shows again the amplifier tailing off in saturated operation as the signal cw power is increased. Regarding the theoretical model for the amplifier system however, we confirmed a maximum small signal gain of ~5000 experimentally.

The next series of results were taken using the acousto-optic modulator to pulse the output from the master oscillator in order to characterise the MOPA in pulsed operation. The frequency of the pulses was set at 100Hz and results were taken in terms of amplified pulse energy, small signal gain and amplified peak power. The acousto-optic modulator was capable of generating pulses from the master oscillator as small as 50ns, although, at these speeds it was also noted that its turn-off time slowed considerably producing a lower power tail of around 80ns in duration. It was also noted that the extinction ratio of the device was 50dB, so that there would be a significant amount of cw power between the amplified pulses due to the large small signal gain of the amplifiers. This was accounted for by measuring the average power of the pulses from the amplifer and subtracting the cw power off-set brought about by the leakage from the AOM.

Amplified pulse energies were measured as a function of pulse duration as can be seen in figure 4.35.

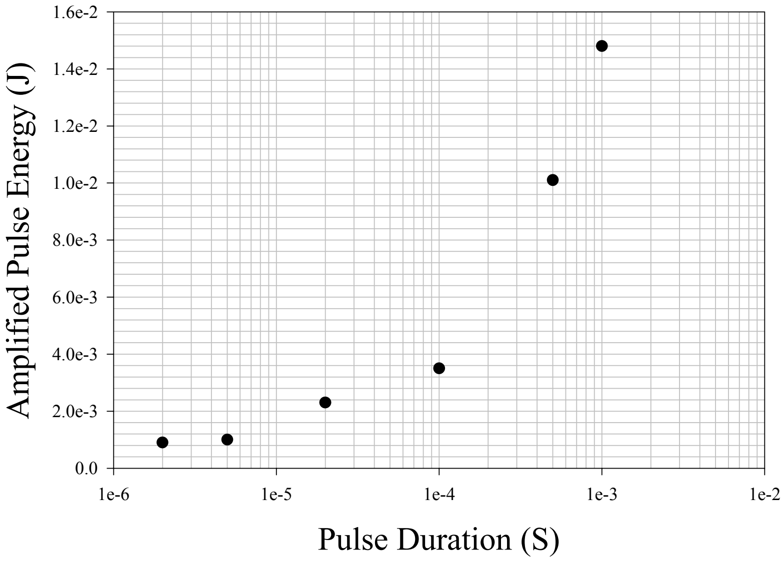

Figure 4.35 Graph showing amplified pulse energy as a function of pulse duration for the MOPA.

The small signal gain was then measured as a function of pulse duration and we were hoping for a repeat of the previous cw small signal gain, however it can be seen in figure 4.36 that the small signal gain was found to be considerably lower than was expected for the system.

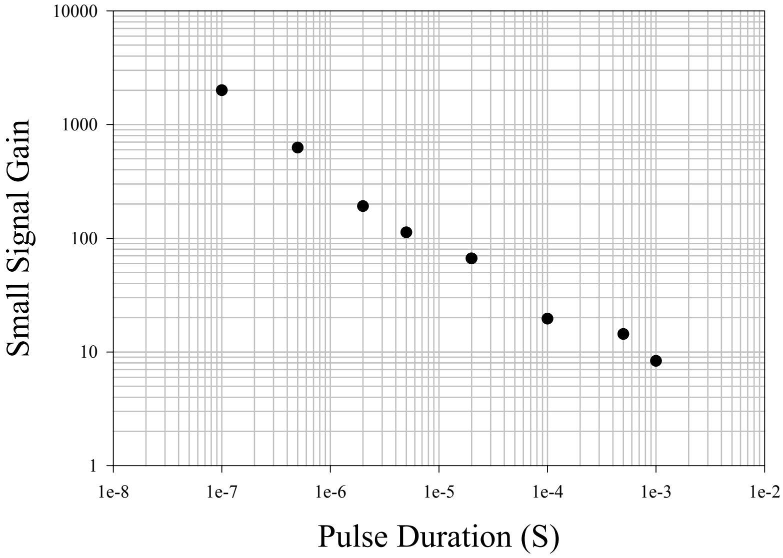

Figure 4.36 Graph showing pulsed small signal gain as a function of pulse duration for the MOPA.

In figure 4.36 it can be seen that the maximum small signal gain for pulses within the system was measured to be ~2000 (100ns pulse width). This reduction was attributed to two things. The extinction ratio of the AOM, allowing a small cw signal through the system depleting the upper laser level of the amplifiers and hence reducing the small signal gain. The long turn off time for the AOM, leading to long tails on the shorter pulses again effectively increasing the pulse width and depleting the small signal gain along the length of the amplifiers. This result was confirmed by measuring the amplified peak powers and comparing them with what would be expected assuming a small signal gain of ~5000. The results of this can be seen in figure 4.37.

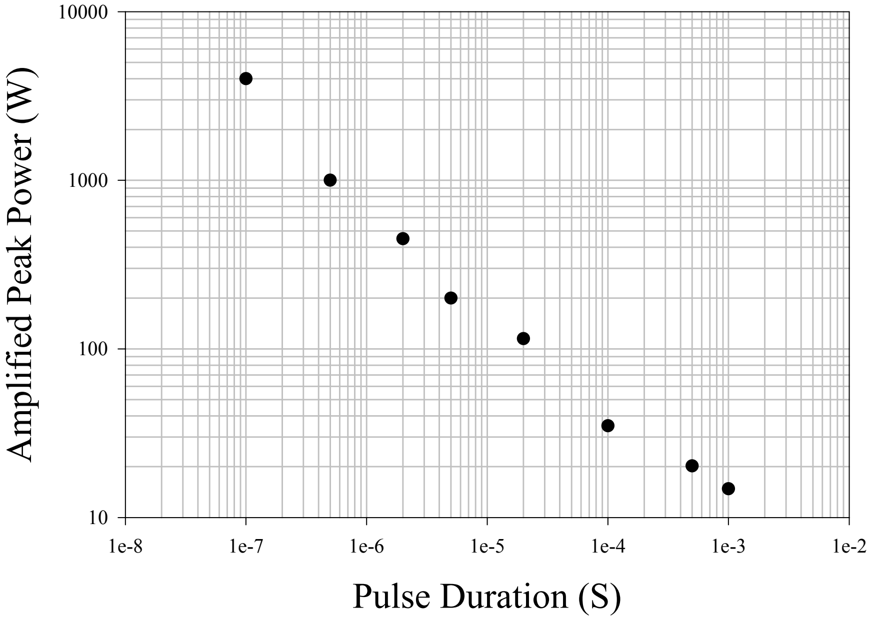

Figure 4.37 Graph showing the amplified peak powers as a function of pulse duration for the MOPA.

Figure 4.37 clearly showed that the small signal gain for the system was lower than had been expected. In order to more closely examine the amplified pulses, a series were captured and scaled accordingly using the Si photodiode and oscilloscope.

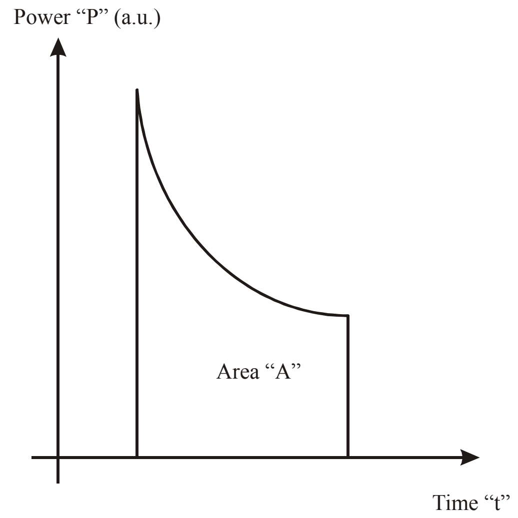

Figure 4.38 Diagram of simplified amplified output pulse from MOPA.

Since the amplified pulses were not going to remain square, due to the front edge of the pulses picking up the small signal gain from the amplifier and the tail ends travelling towards the saturated gain regime, once a pulse was captured on the digital scope used in conjunction with the diagnostics, the image needed scaling to allow us to analyse the result. Figure 4.38 shows an example pulse as a function of power and time. Since the area under the pulse was equal to the pulses energy, which could be measured from the average power, the images could be scaled as follows:
The energy *E* of the pulse recorded is equal to the area *A* under that pulse.

$$E = \int_0^t P(t)dt = A$$

[4.40]

The real power of the pulse must be the arbitrary power measured by the photodiode, multiplied by some factor γ.

$$P(t) = P_{real}(t)\gamma$$

[4.41]

Therefore,

$$A = \gamma \int_{0}^{t} P_{real}(t)dt$$

[4.42]

So γ must be equal to the energy of the pulse divided by the area under the pulse.

$$\gamma = \frac{E}{A}$$

[4.43]

By scaling any pulses captured in this way, we were able to show the actual peak powers as a function of time. In figure 4.39 numerous example pulse durations are presented before and after amplification.

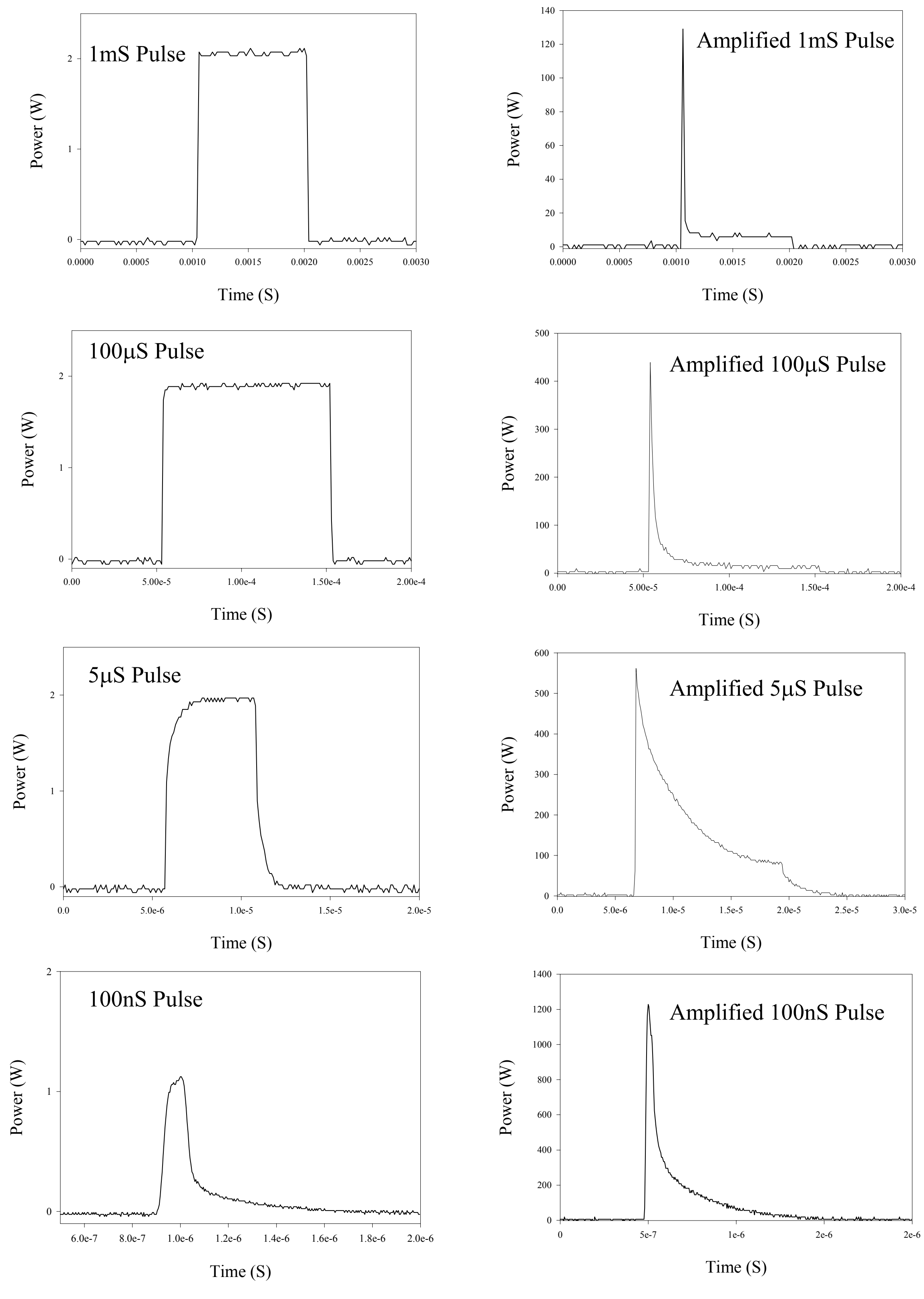

Figure 4.39 Pulses generated by the AOM and their amplified forms.

From the example pulses displayed in figure 4.37, it can be seen that as the pulses are shortened to the order of a few μs, a tail is present at the back of the pulse, which is amplified considerably. Although this effect limited us from realising the total potential small signal gain of the amplifier chain in terms of small signal gain, the output from the MOPA was deemed to be suitable for non-linear frequency conversion.

4.6 Discussion

The design strategy that we have established, derived from the theory for diode-end-pumped solid-state laser amplifiers has shown us that a successful amplifier cannot merely scale the output power from a laser efficiently. A successful amplifier must also preserve the output beam quality from the master oscillator in order to increase the brightness to levels suitable for applications such as nonlinear frequency conversion. Common laser materials such as Nd:YAG and Nd:YVO$_4$ exhibit very high gains (due to their high stimulated emission cross-sections) in amplifier configurations but suffer degradation to beam quality due to aberrations in thermal lens due to excessive heat generation within laser rod, hence high output powers are readily achievable, but maintaining diffraction limited operation is a continuing challenge.

Our solution was to use Nd:YLF on its lower gain transition. Thermal lens generated by weak negative change in refractive index, coupled with the positive lens produced a net effect of a weak positive thermal lens. Since energy-transfer-up conversion was found to be the dominant spectroscopic loss mechanism, leading to high thermal loading per unit length in the laser rods under non-lasing conditions within Nd:YLF, a lower dopant concentration was used in a longer laser rod to reduce its effects. This in turn put higher demands on the diode pump source beam-quality, which was met by beam shaping and fibre coupling the diode outputs. A dual-rod amplifier geometry in double-pass configuration allowed us to demonstrate high gains within an amplifier, coupled with relay imaging that ensured constant spot sizes within gain regions of amplifiers for pump and signal. Rods in the amplifiers were crossed to equalise aberrations in thermal lens generated within the amplifier rods.

Power scaling limitations are based on thermal stress fracture limit of laser rods in amplifiers. From [17] we could calculate that each laser rod could absorb a maximum of 29.2W, meaning each amplifier could absorb up to 58.4W of incident pump power before thermal fracture. At these power levels the small signal gain of double-pass one amplifier, double-pass two amplifier and the final triple pass configuration of the MOPA at this incident absorbed pump power would give small signal gains (including effects of ETU) as follows (figure 4.40):

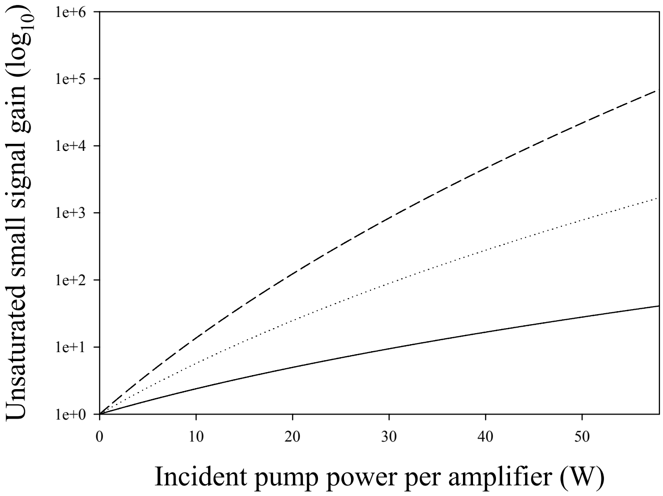

Figure 4.40 Speculated possible small signal gains given the maximum absorbed pump power before thermal fracture of the amplifier laser rods for single-pass (solid-line), double-pass (dotted-line) and the final triple-pass (dashed-line) of an amplifier stage.

At the same incident pump power level (maximum pump of 58.4W per amp), thermal lens power generated per amplifier would be as follows:

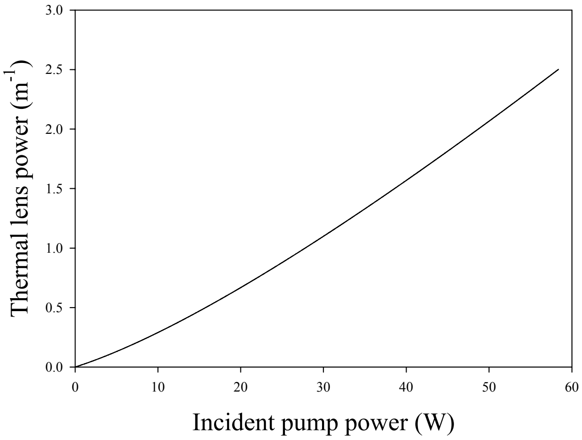

Figure 4.41 Graph showing thermal lens power as a function of incident pump power up to the limit of thermal stress fracture.

Finally with the upper limit on power-scaling being the thermal stress fracture limit, the degradation in beam quality due to aberrations in the thermal lens could be modelled as being:

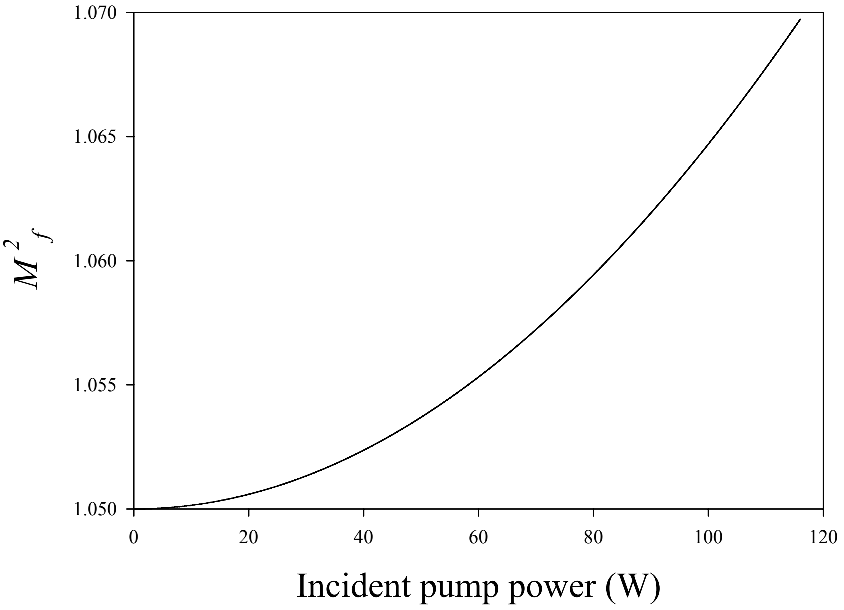

Figure 4.42 Graph showing degradation in signal beam quality as a function of incident pump power for the Nd:YLF MOPA up to the point of thermal stress fracture in the amplifier laser rods.

This modelling shows us that even at the point of thermal stress fracture within the MOPA (assuming that the pump sources were scaled accordingly), the output signal would remain diffraction limited, the thermal lens power would remain comparatively weak and the small signal gains would continue to rise until the amplifier rods broke.

We can speculate therefore, that longer laser rods with a lower dopant concentration, absorbing less incident pump power per unit volume, hence generating less heat per unit volume will allow us to scale the output from the master oscillator to even higher powers. Taking the upper limit of power scaling to be that the beam quality will have degraded due to the aberrrated thermal lens in the amplifier so that $M^2{}_f$=1.1 (an arbitary value taken to mean that the aberrations of the thermal lens are too high to allow the laser to be used for brightness related experiments), we will have to have absorbed up to 187W. If we then work backwards (calculating that this amount of absorbed pump will generate a thermal lens power of D=10m^{-1}) and giving the laser rods in the amplifier a reasonable length, so as to not place too much pressure on the pump beam quality, we can calculate that for a 25mm amplifier rod, the absorption coefficient needs to be α_P~5m^{-1} meaning that the dopant concentration will be ~0.2%. An alternative method for power scaling may be to employ a fibre amplifier stage, possibly pumped by a diode stack (a comparatively new device based on a stack of diode-bars, capable of producing >1000W cw output power). However, the nonlinear effects associated with high power guiding in fibres is not a subject area being covered within this work and hence will only be mentioned.

4.7 Summary

In summary for this chapter of work, we discussed the relative theory of amplifier stages with regards to Nd:YLF, deriving expressions for small signal gain with the inclusion of the effects of ETU, and we have modelled the thermal problems associated with heat loading per unit volume within a non-lasing amplifier laser rod. In doing so, a design strategy was formulated to reduce the effects of ETU within an amplifier in order to achieve gains that maintained diffraction limited, single-frequency operation. Experimentally, we have developed an amplifier chain capable of power scaling the output from a robust and reliable, relatively low power oscillator to powers suitable for non-linear frequency conversion in both cw and qcw arrangements. The amplifiers maintain beam quality of the master oscillators, without incurring any excessive losses through parasitic mechanisms, which might have ordinarily critically affected performance. Although the achieved extraction of small signal gain from the amplifiers was much lower in a pulsed regime from the results expected during cw experimentation, the final pulsed results were still considered a success.

4.8 References

1. Hardman, P.J., PhD *Power-scaling of diode-end-pumped solid-state lasers*, in *Optoelectronics Research Centre*. 1999, University of Southampton.
2. Martin, PhD *High power diode pumped single frequency lasers*, in *Optoelectronics Research Centre*. 1996, University of Southampton.
3. Bourderionnet, J., *Intracavity beam steering of compact diode-pumped Nd : YVO4 master-oscillator power amplifier.* Electronics Letters, 2000. **36**(4): p. 350-351.
4. Brignon, A., *Compact Nd : YAG and Nd : YVO4 amplifiers end-pumped by a high- brightness stacked array.* IEEE Journal of Quantum Electronics, 1998. **34**(3): p. 577-585.
5. Brown, D.C., *Nonlinear thermal and stress effects and scaling behavior of YAG slab amplifiers.* IEEE Journal of Quantum Electronics, 1998. **34**(12): p. 2393-2402.
6. Butterworth, S.D., *High-power quasi-cw laser pulses via high-gain diode-pumped bulk amplifiers.* Optics Communications, 1996. **131**(1-3): p. 84-88.
7. Chazan, P., *High-power near-diffraction-limited tapered amplifiers at 1064 nm for optical intersatellite communications.* Ieee Photonics Technology Letters, 1998. **10**(11): p. 1542-1544.
8. Hirano, Y., *100-W, 100-h external green generation with Nd : YAG rod master-oscillator power-amplifier system.* Optics Communications, 2000. **184**(1-4): p. 231-236.
9. Honninger, C., *Diode-pumped thin-disk Yb:YAG regenerative amplifier.* Applied Physics B-Lasers and Optics, 1997. **65**(3): p. 423-426.
10. Honninger, C., *Ultrafast ytterbium-doped bulk lasers and laser amplifiers.* Applied Physics B-Lasers and Optics, 1999. **69**(1): p. 3-17.
11. Knights, M.G., *Very High-Gain Nd-YLF Amplifiers.* IEEE Journal of Quantum Electronics, 1988. **24**(5): p. 712-715.
12. Olson, T.E., *Multipass Diode-Pumped Nd:YAG Optical Amplifiers at 1.06 Mu-M and 1.32 Mu-M.* IEEE Photonics Technology Letters, 1994. **6**(5): p. 605-608.

13. Plaessmann, H., *Multipass Diode-Pumped Solid-State Optical Amplifier.* Optics Letters, 1993. **18**(17): p. 1420-1422.

14. Pliska, T., D. Fluck, and P. Gunter, *Blue-green laser by frequency doubling a master oscillator power amplifier diode laser in a $KNbO_3$ crystal.* Helvetica Physica Acta, 1995. **68**(5): p. 502-503.

15. Roisse, E. and A. Barthelemy, *Diode pumped multipass laser amplifier.* Annales de Physique, 1995. **20**(5-6): p. 627-628.

16. Yu, A.W., M.A. Krainak, and G.L. Unger, *1047-nm Laser-Diode Master Oscillator Nd-YLF Power-Amplifier Laser System.* Electronics Letters, 1993. **29**(8): p. 678-679.

17. Koechner, W., *Solid-State Laser Engineering*. 4th ed. 1996, New York: Springer-Verlag.

18. I.O.Musgrave, *Private communication.* 2003.

19. Clarkson, W.A. *Resonator design considerations for efficient operation of solid-state lasers end-pumped by high-power diode-bars.* Optical Resonators - Science and engineering., R. Kossowsky 1998, Kluwer Academic Publishers. 327-361.

Chapter 5: Singly resonant cw Optical parametric oscillators

5.1 Introduction

5.1.1 Optical parametric oscillators

It was mentioned in Chapter 1 that non-linear devices such as optical parametric oscillators could be used to extend the operating frequency range of a laser source. Frequency conversion utilizes the non-linear optical response of a medium under intense radiation fields to generate new frequencies via elastic processes (optical energy conserving) such as harmonic generation or inelastic processes (depositing some energy into the medium) such as stimulated Raman or Brillouin scattering. Nonlinear optical effects can be analysed by considering the response of a dielectric material at the atomic level to the electric fields of an intense beam of light. In previous chapters we have described, in principle, the conditions under which the efficient operation of a high-power single-frequency solid-state laser can be achieved. Numerous analogies can be seen between the operation of single frequency lasers and optical parametric oscillators.

In simplified terms, much like a laser, an OPO amplifies light of a specific wavelength and polarisation. The action of parametric oscillation will only occur (dependant on the nonlinear crystal used) at a certain threshold dictated by the losses within the cavity and the output coupling. However, the nature of a laser can lead to multi-frequency operation due to spatial-hole burning (section 2.2.2), parametric gain however involves no energy storage with the nonlinear crystal, instead the energy in the pump light is directly transferred to the signal and idler fields, this eliminates the effects of spatial-hole burning in the nonlinear crystal.

The fundamental principles behind the operation of Optical Parametric Oscillators has been well understood for some time, however it has only been in the last decade that OPOs have been developed as significant practical sources of coherent radiation. The main reason for this progress has been due to the improvements that have been made in the quality of non-linear materials. Due to the high continuous wave powers that have been required in the past to operate a cw OPO however, the current development of cw OPOs have been relatively recent due to the high demands on the pump sources in terms of output power, beam quality and frequency stability. Numerous groups throughout the world have successfully demonstrated cw OPOs by reducing thresholds to acceptable levels via quasi-phase matching and careful resonator design, the effects of which will be covered within this chapter.

In this chapter we are concerned with a commonly used elastic process: we will describe the process of optical parametric generation and oscillation, quoting threshold equations and discussing design issues related to quasi phase matching, spectral stability and output beam characteristics. Due to the availability and engineering techniques used to grow such nonlinear crystals, it has been only until recently that the direction of some research has looked into nonlinear frequency conversion as useful and efficient replacement for more conventional sources of tuneable laser radiation such as dye lasers. Still, the nonlinear gains required to allow cw frequency conversion have been limited until very recently by the available lengths and hence available parametric gain coefficients of these crystals, meaning that nonlinear frequency conversion by means of optical parametric oscillators has been limited to the high intensity outputs of pulsed laser systems. However, with the advent of quasi-phase matching, and new engineering processes, allowing the manufacture of much longer crystal samples, the ability to use nonlinear frequency conversion in the cw regime has become a reality [1-9].

cw singly resonant OPOs are inherently single-frequency by nature due the lack of spatial-hole burning. Pumping an SROPO with a multi-frequency pump source will still lead to a single frequency output in the resonant field as the non-resonant field will naturally fulfil the requirements of phase-matching. In the case of an SROPO pumped by a single-frequency source, both the resonant and non-resonant fields will oscillate single-frequency. By tuning single-frequency pumped SROPOs therefore we have the potential for creating a tool that is ideally suited for uses such as LIDAR and spectroscopy.

OPOs suffer from numerous disadvantages however, short crystal lengths (even with the advantages of QPM) and intracavity losses increase the threshold of such devices beyond the usefulness of cw nonlinear frequency conversion. Provided that the length and quality of the crystal will allow cw operation, as with diode-pumped solid-state lasers, the threshold of such devices is also dictated by pump beam quality. Another disadvantage is the sensitivity of an OPO to temperature and cavity length fluctuations means that mode hopping (section 3.2) becomes a dominant effect in the spectral instabilities of the OPO output.

Therefore numerous issues have to be addressed when considering the development of a cw SROPO with the intention of using it for spectroscopy or other use requiring a spectrally stable output. If we take a nonlinear crystal sample pumped by the single-frequency, diffraction limited Nd:YLF MOPA we have in turn to address issues such as intracavity OPO loss, temperature tuning, angular acceptance and phase-matching bandwidth. In order to decrease the threshold of any OPO device to be pumped by the MOPA, the pump spot size must be suitably small with the signal and idler waist sizes to provide a good overlap with the pump. Intracavity losses must be kept as small as possible in order to further reduce OPO threshold and the cavity needs to be stable in order to reduce the effect of mode hopping of the resonant output field.

Chapter 5 considers the influence of various parameters on OPO performance with a view to establishing a design strategy for cw, single-frequency SROPOs based on periodically-poled nonlinear crystals. This chapter briefly reviews earlier results and focuses in particular on the problem of axial-mode-hopping in SROPOs. The origin of mode-hopping in OPOs is discussed and standard techniques for preventing mode-hopping are considered. Finally, a new passive approach for suppressing mode-hopping is proposed. The rationale for this approach and its limitations are considered.

5.1.2 Phase matching

In 1965 the first experimental demonstration of an OPO was reported by Giordmane and Miller using Lithium Niobate [10] as the nonlinear crystal. Two beams with different frequencies travelling through a nonlinear crystal will generate a travelling polarisation wave at this different frequency. Provided that the polarisation wave travels with the same velocity as the freely propagation electromagnetic waves, cumulative growth will result. The two incident waves are termed *pump* and *signal*, having the frequency ν_p and ν_s, and the resulting third wave is termed as the *idler* with frequency ν_i. Under proper conditions, the idler wave can mix with the pump beam to produce a travelling polarisation wave at the signal frequency, phased such that the growth of the signal wave results. The process continues with the signal and the idler waves both growing and the pump wave decaying as a function of distance within the crystal. We mentioned before that, provided the polarisation wave travels at the same velocity as the freely propagating em wave, cumulative growth would result. The fundamental beam is labelled the pump beam, and the generated beams are labelled the signal and idler beams respectively, with the signal beam possessing the greater energy (shorter wavelength).

$$\frac{1}{\lambda_p} = \frac{1}{\lambda_s} + \frac{1}{\lambda_i} \qquad [5.1]$$

where the subscripts *p*, *s* and *i* refer to the pump, signal and idler waves respectively. Within an OPO, the signal and idler outputs are generated by the interaction between the intense pump light and the weak quantum noise at the signal and idler frequencies. This interaction occurs via the second-order non-linearity of the crystal medium, and results in the amplification of the signal and the idler frequencies at the expense of the pump. Energy conservation ensures that:

$$E_p = E_s + E_i$$

[5.2]

where E_p, E_s and E_i are the energies of the pump, signal and idler photons respectively. For the interaction to occur, the three waves must be phase-matched within the crystal. As with frequency doubling (the exact opposite of optical parametric amplification at degeneracy – where the signal and idler photons have the same energy), phase matching can be achieved by temperature tuning or angle tuning the crystal however, in the case of an OPO, the signal and idler wavelengths change to follow the phase-matching conditions defined by the angle or temperature.

To understand the conversion process, it is necessary to re-write the equation in terms of the conservation of momentum:

$$k_P = k_S + k_I$$

[5.3]

where k is known as the wave-vector:

$$\left|\vec{k}\right| = \frac{n(\lambda)\omega}{c}$$

[5.4]

where $n(\lambda)$ is the wavelength dependent refractive index (dispersion).

The three refractive indices associated with the pump, signal and idler can be changed either in the propagation direction through the crystal (angle tuning) or by temperature variation (temperature tuning). When the three frequencies see refractive indices that satisfy equation 5.3 they are considered to be phase-matched.

Since the refractive index of a crystal is angularly (or temperature) dependent (depending on the polarisation direction within the crystal), the constraints of phase matching can typically require the non-linear crystal to be cut at a specific angle determined by dispersion, therefore, efficient frequency conversion can only be achieved within a narrow band of angles around the so-called “phase-matched angle”. Furthermore, once the angle is determined, phase matching can only be achieved for a narrow band of pump-frequencies [11]. Since the signal and idler intensities build up from quantum noise and hence are initially very low, typically of the order of 10^{-13} times lower than the pump intensity I_P, they must be greatly amplified before any significant depletion of the pump occurs. The threshold condition for an optical parametric oscillators is exactly the same for that of a laser whereby oscillation will commence as soon as the parametric gain (in the case of the OPO) equals the intracavity loss (including loss due to the output coupler) of the OPO.

Provided therefore, that the phase-matching condition described by equation 5.3 is maintained, the signal and idler wavelengths will tune to satisfy equation 5.3 over a wide range of temperatures or angles. There are three different types of phase matching conditions within birefringent crystals (types 1, 2 and 3) whereby:

TYPE	PUMP	SIGNAL	IDLER
1	*e*	*o*	*o*
2	*e*	*o*	*e*
3	*e*	*e*	*o*

Table 5.1 Showing the three phase-matching types within birefringent crystals.

In the table 5.1 *o* and *e* correspond to the ordinary and extraordinary refractive indices of the birefringent material in question (refractive indices in orthogonal directions to the direction of pump propagation). When comparing the more common type 1 and type 2 phase matching, we find that type 1 is more favourable when θ_m is near 90^0, whereas, type 2 leads to higher d_{eff} when θ_m lies near 45^0. For the purposes of this work we adopted type 1 phase-matching conditions in order to reduce the effect of Poynting vector walk-off. Poynting vector walk-off can occur in birefringent phase matching when the Poynting vector of an e-wave moves away from the k-vector when a wave propagates at an angle to the optic axis, whereas those of the o-wave remain collinear. This means that the interaction length is greatly reduced.

So within an OPO, under the proper conditions, the idler wave can mix with the pump beam to produce a travelling polarisation wave at the signal frequency, phased such that the growth of the signal wave results and vice versa for the idler wave.

5.1.3 Quasi phase matching

The reasoning for the choice of non-linear crystal to be used as a parametric amplifier or in an OPO is very important. It is obvious that the material used should be both cheap and robust but it must also have a good transparency range (i.e. to minimise the loss at all the frequencies involved). A large number of mature nonlinear optical materials exist but nonlinear coefficients are limited by the need for birefringent phase matching.

Quasi-phase matching (QPM) [12, 13], an idea first proposed by Armstrong *et al* in 1962, is an alternative method for compensating the phase-velocity dispersion (wavelength dependent refractive index) in frequency-conversion applications. In a first-order QPM device, the non-linear coefficient is modulated with a period that has twice the coherence length (the maximum crystal length that is useful for producing parametric gain in terms of an OPO or second harmonic power in a doubling crystal) of the interaction to offset the accumulated phase mismatch. The main attraction of quasi-phase matching therefore is that any interaction within the transparency range of the material can be non-critically phase matched at a specific temperature, allowing access to the highest nonlinear coefficients, even interactions for which birefringent phase-matching alone is impossible.

Also, within QPM materials the coupling of the electric fields can be engineered to occur through the largest element of the $\chi^{(2)}$ tensor giving access to much higher non-linearities within a crystal. QPM permits the engineering of the phase-matching behaviour, rather than relying on inherent non-linear properties of a certain material, and to an extent has replaced the search for new non-linear crystals with the search for patterning techniques for materials that already exist [13, 14]. The simplest implementation of QPM is that the nonlinear crystal is divided up into segments, each segment being one coherence length long and being rotated relative to its neighbour by 180^0 about the axis of propagation through the crystal. This has the effect of changing the sign of the components of the nonlinear susceptibility tensor ($\chi^{(2)}$), hence the nonlinear polarisation wave is shifted by π radians every coherence length. The coherence length for a frequency conversion process is sometimes only a few microns. The effect of producing these segments within the crystal is a single periodic grating within a suitable non-linear crystal that shifts the phase-matching bandwidth peak of the crystal to the desired operating wavelength.

$$\frac{2\pi n_p}{\lambda_p} = \frac{2\pi n_s}{\lambda_s} + \frac{2\pi n_i}{\lambda_i} + \frac{2\pi}{\Lambda}$$

[5.5]

Where n is the refractive index as seen by the three different wavelengths (λ_p-pump, λ_s -signal, λ_i - idler) and Λ is the grating period in the phase-matching equation and we can get any combination of signal and idler at a specific temperature within the transparency range of the crystal by changing Λ. Although it must be noted that QPM cannot be implemented with any material, as the poling process requires the material to be ferroelectric.

A material for an OPO experiment that can be conducted with the Nd:YLF MOPA is Lithium Niobate ($LiNbO_3$) [12]. This material has a very broadband transparency range of 0.35 to 4.5μm and when used in the correct orientation, also has a high nonlinear coefficient of $d_{eff} = 15pmV^{-1}$.

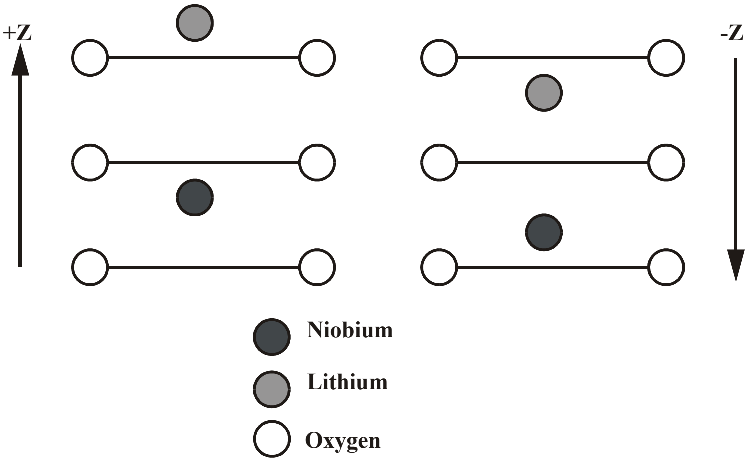

Fig 5.1 Diagram showing the basic effect of poling on Lithium Niobate.

In fig 5.1 it can be seen that the polarity of the ferroelectric domain is determined by the offset of the metal ions either above or below the oxygen layers. Domain reversal involves re-orientating the crystal from one stable configuration to another, which can be achieved by the application of the large external electric field.

The simplest implementation of a QPM device is that of a single period grating, but engineering more complex behaviour, such as broadband phase matching or multiple narrow-band wavelength geometries in principle only involves the design of a more sophisticated lithographic mask. Figure 5.2 shows the effect of quasi phase matching on nonlinear conversion in comparison with the cases of phase matching and phase mismatch over the crystal length. It can be seen that the effect of periodically changing the polarity of the ferroelectric domain compensates for dispersion along the crystal length allowing the signal and idler to build up.

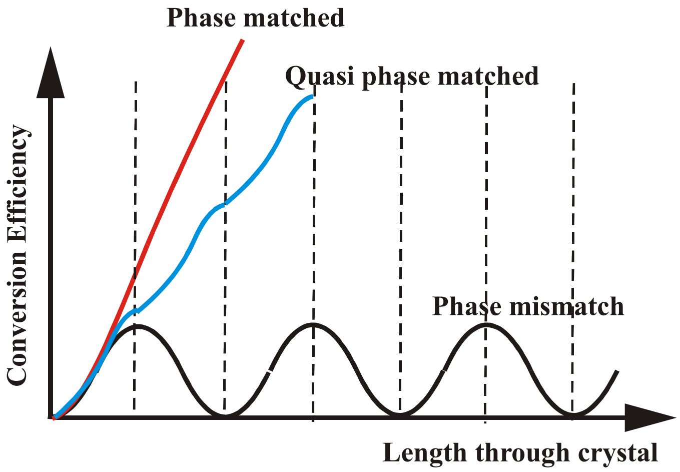

Figure 5.2 Diagram showing the effect of quasi-phase matching in comparison with phase-matched and phase-mismatched conditions within the same crystal.

Standard OPO theory still applies to quasi phase matched devices with simple substitutions for effective nonlinear coefficient and wave-vector mismatch [12]. A quasi phase matched OPO can be non-critically phase matched and hence does not suffer from the problem of Poynting vector walk-off. One existing problem with lithium niobate however is the effect of photorefractive damage which can severely degrade the output performance of an OPO. Higher energy visible wavelength photons can excite charge carriers from impurities in the medium which then migrate, this gives rise to space-charge fields and electro-optic refractive index changes arise. The effects of photorefractive damage are well known, [3, 11-19], and research has led to a number of techniques to suppress the effects: heating the crystals to a temperature in excess of ~110^{0}C, doping the lithium niobate wafer with MgO, ZnO, In_2O_2 or changing the Li/Nb ratio can reduce the likelihood of photorefractive damage.

From the paper by Jundt [20], the Sellmeier equation has been obtained for the extraordinary refractive index of lithium niobate dependent on wavelength and temperature, and can be written as follows:

$$n_e^2 = a_1 + b_1 f + \frac{a_2 + b_2 f}{\lambda^2 - \left[a_3 + b_3 f\right]^2} + \frac{a_4 + b_4 f}{\lambda^2 - a_5^2} - a_6 \lambda^2$$

[5.6]

where

$$f = (T - T_0).(T + T_0 + 2 \times 273.16)$$
$$\therefore f = (T - 24.5^0 C).(T + 570.82)$$

[5.7]

This expression allows us to calculate the value of n_e as a function of wavelength and temperature. The values for the various *a* and *b* parameters are given in table 5.2 [20] and wavelength λ is in microns (μm):

Parameter	**Value**
a_1	5.35583
a_2	0.100473
a_3	0.20692
a_4	100(μm^2)
a_5	11.34927
a_6	1.5334×10^{-2}
b_1	4.629×10^{-7}
b_2	3.862×10^{-8}
b_3	-0.89×10^{-8}
b_4	2.657×10^{-5}

Table 5.2 Table displaying a and b parameters for Sellmeier equation for the n_e of lithium niobate [20].

From this expression, we can display the effects the refractive index of lithium niobate as a function of wavelength for a set operating temperature of 195^{0}C:

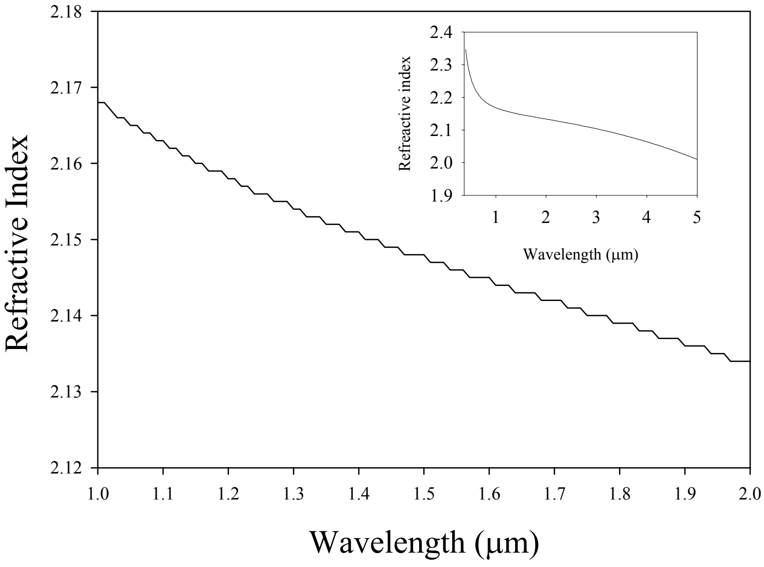

Figure 5.3 Graph showing extraordinary refractive index of Lithium Niobate as a function of wavelength at an operating temperature of 195^0C (the inset shows the change in refractive index at 195^0C for the transparency range of lithium niobate).

Figure 5.3 shows an example of the application of equation 5.6, the lithium niobate is held at a constant temperature of 195^0C, assuming that we are pumping a grating period Λ=28.414µm, at a wavelength of 1053nm and are generating a signal around 1468nm with a corresponding idler wavelength of 3725nm, the associated refractive indices are n_p=2.164, n_s=2.147 and n_i=2.075.

Using the equation:

$$\Lambda = \left(\frac{n_p}{\lambda_p} - \frac{n_s}{\lambda_s} - \frac{n_i}{\lambda_i} \right)^{-1}$$

[5.8]

and, taking into account fractional thermal expansion α_T of the PPLN at this temperature, using the equation [21]:

$$\alpha_T = 1 + \alpha(T - T_0) + \beta(T - T_0)^2$$

[5.9]

where α =1.54×10^{-5} K^{-1}, β =5.3×10^{-9} K^{-1} , T_0 is room temperature and T is the operating temperature of the PPLN.

The actual room temperature grating period Λ_{rt} :

$$\Lambda_{rt} = \frac{\Lambda}{\alpha_T}$$

[5.10]

We can calculate the actual room temperature grating period to be Λ_{rt}=28.428μm for this example.

We can plot the grating period as a function of signal and idler wavelength pairs using equation 5.8 for PPLN assuming a pump wavelength of 1.053μm and an operating temperature of 195^{0}C, the results of which can be seen in figure 5.4:

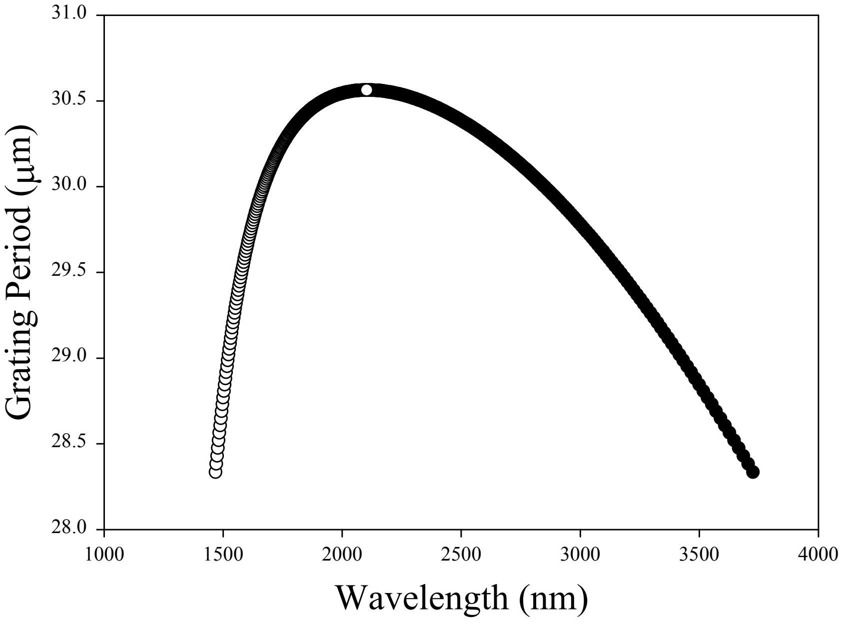

Fig 5.4 Graph showing grating period as a function of wavelength (signal and idler pairs).

Figure 5.4 shows the various signal and idler pair wavelengths as a function of gratings periods for a pump wavelength of 1.053μm.

5.1.4 Singly resonant oscillators (SROs)

The threshold of an OPO occurs when the parametric gain in the nonlinear crystal equals the cavity loss, in exactly the same way a laser reaches threshold. In order to reduce the threshold of an OPO therefore numerous cavity configurations have been developed as can be seen in figure 5.5. Table 5.2 shows the various cavity configurations affect on threshold.

Configuration	Typical Threshold value
DRO with pump enhancement	1's mW
DRO with single pass pump	10's mW
SRO with pump enhancement	100's mW
SRO with single pass pump	1's W

Table 5.2 Typical magnitudes of threshold pump powers need to drive various OPO cavity configurations.

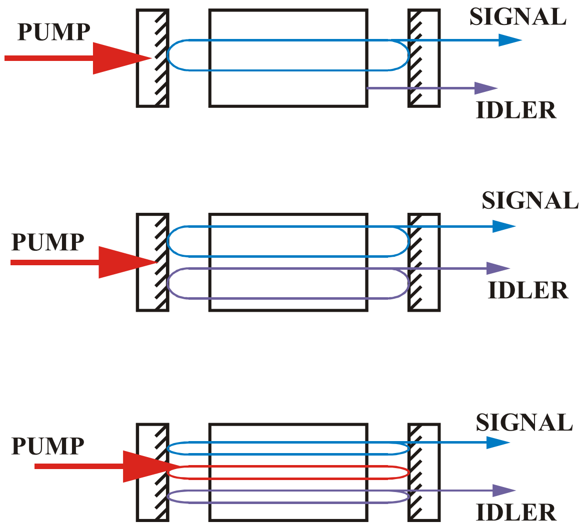

Fig 5.5 Diagram showing various resonant conditions for basic OPOs. Singly resonant oscillator where either the signal or idler is oscillated, doubly resonant oscillator whereby the signal and idler are both oscillated and finally pump enhancement in which the pump makes more than one pass through the crystal.

The doubly-resonant oscillator (DRO) shown in the middle of figure 5.5 has both the signal and idler fields resonating within the cavity. This leads to very low cw threshold of the order of 10mW's and with another technique called pump enhancement whereby the pump is reflected back through the crystal, increasing the parametric gain even further (bottom of figure 5.5), the threshold can be reduced even more to 1mW's. However, although this technique appears attractive for efficient cw OPO operation, the cavity length stability requirements (to within $\lambda_{s/i}/4$ for both the signal and idler wavelengths) mean that DROs suffer from large fluctuation in output power stability.

For the purposes of this research on OPO devices they will all be singly resonant. The reasoning behind the construction of singly-resonant oscillators (SROs) whereby only the signal or idler wavelengths are resonated within the optical cavity is due to issues both with cavity stability, ease of OPO design and construction and noise-free output power stability. In this case, where only one wave is resonated (SRO), the other is allowed to change phase (and frequency) to match that of the pump and therefore, a broadband pump can be just as effective as a single-frequency pump when driving the OPO. For these reasons SROs are normally used for more practical applications. The threshold of the OPO can also be reduced by pump enhancement (double passing the pump) or by resonating the pump but again both these configurations require a complex cavity design.

5.2 CW SRO threshold, slope efficiency and operation

5.2.1 CW SRO threshold

When the pump wave is incident on the nonlinear crystal, it will exhibit optical gain to the waves at the signal and idler frequencies. So, when the crystal is placed into an optical cavity, including mirrors with the appropriate coatings for the signal and idler wavelengths to provide the appropriate optical feedback, oscillation can occur when the parametric gain exceeds the cavity loss.

In general, the power gain G_P for the signal wave produced by a pump source with intensity I_P in a nonregenerative parametric amplifier is given by [13, 14, 22, 23]:

$$G_P = \Gamma^2 l_c^2 \operatorname{sinc}^2\left(\frac{\Delta k l_c}{2}\right)$$

[5.11]

where l_c is the effective length of the non-linear crystal, Δk is the phase-mismatch calculated from the material dispersion due to wavelength and temperature [20] and the parametric gain coefficient of the device Γ is given by [12, 24]:

$$\Gamma = \left[\frac{2\omega_S \omega_I d_{eff}^2 I_P g_s}{n_S n_I n_P \varepsilon_0 c^3} \right]^{\frac{1}{2}}$$

[5.12]

here d_{eff} is the effective non-linear coefficient of the material and is calculated from its second order non-linear tensor, I_p is the pump light intensity, ω_s and ω_i are the angular frequencies of the signal and idler fields respectively, n_s, n_i and n_p are the refractive indices seen by the signal, idler and pump wavelengths respectively and c is the speed of light in a vacuum. Also g_s [24] is:

$$g_s = \frac{w_p^2}{w_s^2 + w_p^2}$$

[5.13]

Where w_p and w_s are the pump and signal spot sizes respectively. This expression for the parametric gain assumes that the pump beam has a top-hat distribution, that the OPO in question is a singly resonant oscillator (whereby only the signal or the idler is resonated within the optical cavity with no pump feedback) and that there is no diffraction of the pump beam.

In the case of an OPO, at threshold the gain must equal the cavity losses and the loss induced by the cavity output coupler. In this case the loss of the output coupler L_{oc} and the intracavity losses L_{cav} add to produce a total loss L assuming that $L<<1$:

$$L = L_{oc} + L_{cav}$$

[5.14]

To fulfil the condition for cw singly resonant OPO threshold therefore [12, 13]:

$$G_P = L$$

[5.15]

where L is the intracavity loss and loss due to the output coupler. This expression is for a singly-resonant oscillator, in the case of a doubly-resonant oscillator there would have been loss terms for the signal and idler. Re-arranging equation 5.11 and 5.12 and substituting in expressions for pump power *P* and pump spot area *A*, we can derive an expression for the cw threshold of an SROPO as being:

$$P_{TH} = \frac{c^3 \varepsilon_0 n_i n_s n_p AL}{2\omega_s \omega_i d_{eff}^2 l_c^2 g_s \operatorname{sinc}^2\left(\frac{\Delta k l_c}{2}\right)}$$

[5.16]

In practice, the pump beam is tightly focused within the OPO cavity to ensure suitably high pump field intensities, so the plane wave approximation becomes no longer valid as diffraction effects become important [22]. In the far-field limit, the electric field shows an amplitude dependence in the *z* direction as well as a radial Gaussian amplitude dependence, this *z* dependence leads to complicated coupled nonlinear equations. In the near field focussing approximation, we can neglect the z dependent variation and only consider the radial Gaussian dependence.

In tight focussing analysis, a gain reduction factor can be introduced to allow for both amplitude dependence in the *z* direction and the radial Gaussian dependence. This is done by including an expression called h_s, the Guha focussing factor [25, 26]:

$$h_s = \frac{1}{4} \frac{(1+k)}{\xi_p + k\xi_s} I_1$$

[5.17]

The expression for h_s must be calculated numerically. The signal and pump beam sizes are given in terms of the ratio of the crystal length to confocal parameter i.e. $\xi = l_c/b$ and $k = k_p/k_s$ where:

$$b_{p,s} = w_{p,s}^2 k_{p,s}$$

[5.18]

In Guha's analysis, the signal spot size is determined by the OPO cavity, and the pump spot size is determined by the lens used to focus it into the crystal. In the papers by Guha and Boyd, a low gain approximation is taken so that there is no z dependence of the signal accounted for. Assumptions made during this analysis are therefore of the OPO having low gain, that the OPO is singly resonant and that there is negligible depletion of the pump.

For the complete derivation the appropriate papers referenced must be consulted but for the purposes of this work, h_s was substituted for g_s in the model to give the final expression for a cw SRO threshold as being:

$$P_{TH} = \frac{c^3 \varepsilon_0 n_i n_s n_p AL}{2\omega_s \omega_i d_{eff}^2 l_c^2 h_s \mathrm{sinc}^2\left(\frac{\Delta k l_c}{2}\right)}$$

[5.19]

The threshold of a simple confocal OPO cavity can therefore be calculated using this expression based on the following values. w_p=100μm and w_s=100μm giving a Guha focusing factor h_s=0.409. The PPLN grating period Λ=28.414μm giving signal and idler wavelengths of 1.468μm and 3.725μm respectively for an incident pump wavelength of 1.053μm. The refractive indices seen by the signal, idler and pump wavelengths in this case can be calculated from the temperature dependent Sellemier equations (assuming an operating temperature of 195^0C) to be 2.1652, 2.1485 and 2.0763 respectively. Assuming a 10% output coupling loss and a round trip cavity loss of 4% for a 10mm long PPLN sample, the threshold can be calculated as being 376W. Obviously this result means that the OPO cavity would only be capable of operating in a pulse regime with a suitable pump laser capable of producing peak powers well in excess of the threshold value. Maintaining the cavity conditions in this example constant, we can plot the OPO threshold as a function of PPLN crystal length (figure 5.6), thereby illustrating the importance of current PPLN fabrication techniques on the potential for cw SRO operation.

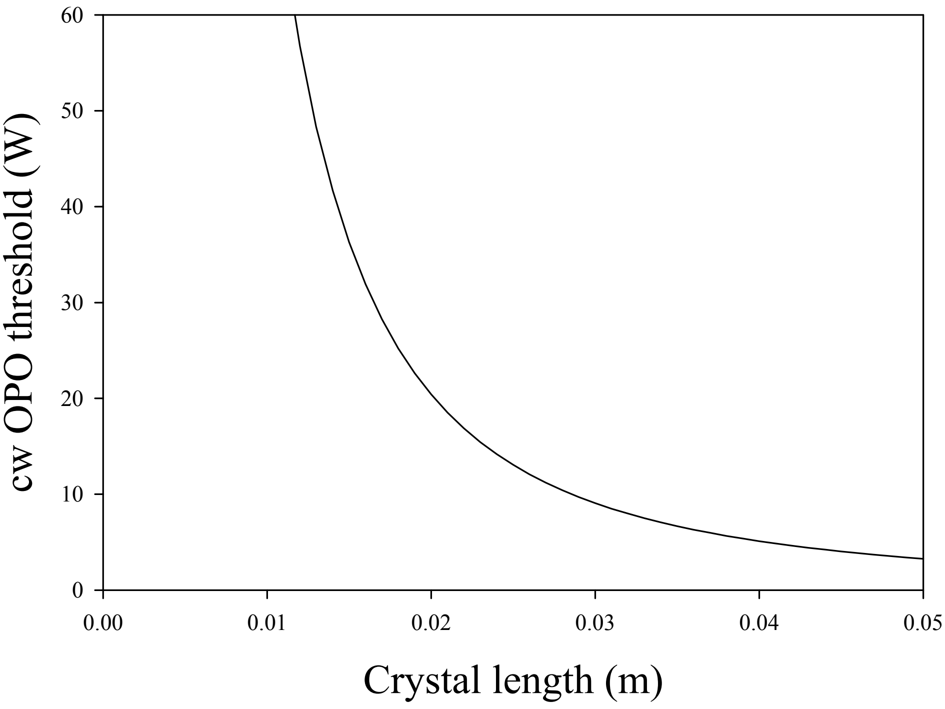

Figure 5.6 Graph showing approximate cw SROPO thresholds as a function of PPLN crystal length where w_p=100μm and w_s=100μm ,h_s=0.409, Λ=28.414μm, λ_s=1.468μm and λ_i=3.725μm, λ_p= 1.053μm, n_s= 2.1652, n_i=2.1485 and n_p=2.0763(assuming an operating temperature of 195^0C) respectively. Assumes a 10% output coupling loss and a round trip cavity loss of 4%.

Figure 5.6 shows the effect of crystal length on the threshold of the OPO. It can be seen from this graph that the crystal length (or effective grating length through the crystal) has a dramatic effect on threshold.

In order to reduce the threshold to an acceptable level, the crystal length must be well over 10mm in length. It is this fact alone that has limited the usefulness of nonlinear frequency conversion in the cw regime, since until only recently, short lengths of crystal could be fabricated and quasi phase matched, nonlinear frequency conversion has been limited to pulsed configurations. Only relatively new engineering and fabrication techniques have allowed the production of longer lengths of PPLN with the appropriate AR coatings to increase the nonlinear gain sufficiently enough to allow the nonlinear frequency conversion of cw laser sources.

5.2.2 CW SRO slope efficiency

The output signal or idler power from an SRO (dependent on whether the signal or idler fields are resonated) can be calculated in the same way as the output power from a laser. The following expression gives us the output power from an SRO as a function of incident pump power P_p, percentage pump depletion η_{dep}, output coupling T_{oc}, intra cavity loss L, Guha focussing factor h_s and pump and signal/idler frequencies ν_p and $\nu_{s/i}$:

$$P_{Signal} = (P_P - P_{TH})\eta_{dep}\left(\frac{T_{oc}}{T_{oc}+L}\right)\left(\frac{\nu_{s/i}}{\nu_p}\right)h_s$$

[5.20]

If we now illustrate another example (using the parameter from figure 5.6), however this time using a 50mm PPLN sample within a ring oscillator (halving the intracavity round trip loss to 2%) and reducing the output coupling to ~1%, the threshold for the OPO will be reduce to 3.23W, a result allowing commonly available cw laser sources to act as a pump. Plotting equation 5.20 (figure 5.7) should therefore allow us to illustrate the signal output power as a function of incident pump power:

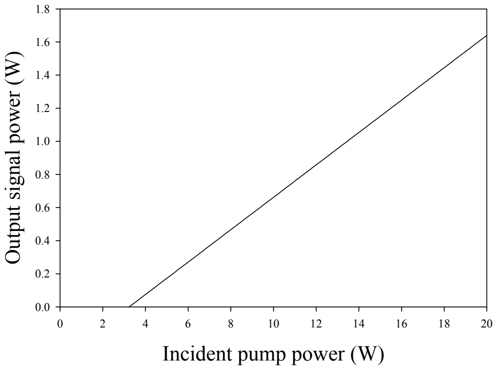

Figure 5.7 Graph showing theoretical signal output power as a function of incident pump power.

Figure 5.7 shows the signal output as function of incident pump power for the example OPO. The slope efficiency of the OPO is ~10%, however the output coupling value is not optimised for optimum slope efficiency.

5.3 CW SRO mode hopping

5.3.1 Mechanical vibration and pressure fluctuations

In a singly resonant optical parametric oscillator (SRO), the frequency of the resonant wave corresponds to the cavity mode closest to the parametric gain peak and it has been demonstrated that no extra frequency selective cavity components are needed to achieve single mode output [27]. The required stability for the cavity length of an SRO, to maintain single mode output and avoid mode hopping is identical to the condition for a conventional laser:

$$\Delta L_{stab} = \pm \frac{\lambda_{res}}{4} \tag{5.21}$$

where λ_{res} is the wavelength of the resonant wave. In the example from figure 5.6 case the resonant wavelength is λ_s=1.468μm meaning that in order to maintain single mode output, the cavity length must change over a distance of more than ±0.37μm. This factor alone would mean that robust and reliable single-frequency operation of an OPO would simply require careful cavity design and isolation from extreme temperature and pressure fluctuations, however, it has been noted by other researchers that mode-hopping is a dominant effect within cw OPOs and therefore requires more careful control.

In all lasers (and hence OPOs), small changes in the optical path length can give rise to a mode-hop of the operating frequency (or frequencies) of the laser. This effect is particularly noticeable in single-frequency lasers, since at the point of mode-hopping the laser oscillates on two frequencies as described in Chapter 3 (figure 5.8). Mode-hopping can be caused by temperature fluctuations, pressure changes and mechanical vibrations. Singly-resonant OPOs naturally operate single-frequency, the effect of mode-hopping is a particularly noticeable detrimental side-effect when using the OPO output as a source for applications such as spectroscopy when the output is required to be reliably single-frequency.

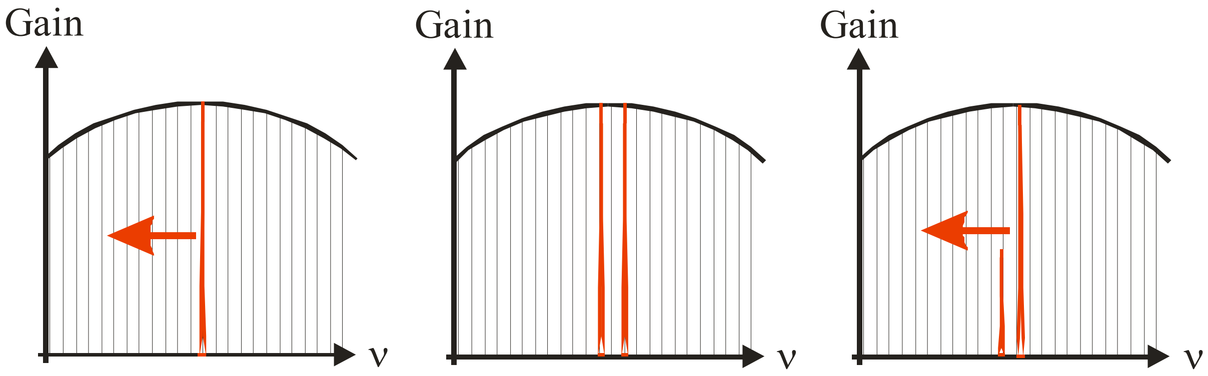

Oscillating frequency ν_0 moves from gain line centre by $\nu_c/2$

Non-oscillating mode extracts gain and starts oscillating -mulitifrequency operation

New mode saturates gain as it moves to gain line centre suppressing original mode -mode hop

Fig 5.8 Diagram showing the mode-hopping mechanism within a single-frequency laser.

Mode-hopping action due to these changes in optical path length occurs, as the gain of an adjacent non-oscillating mode equals and exceeds that of the lasing mode. When the gain of these two modes is equal they will both oscillate, as the cavity is extended further, the original oscillating mode will be suppressed as its adjacent mode moves closer to gain line centre (Fig 5.8). The net effect observed over longer periods of time, is that the oscillating mode will travel away from gain line centre with a variation in cavity length and will appear then to hop back as it is suppressed and an adjacent mode starts to oscillate and then dominates the parametric gain (the saturation of the gain can be compared to the homogeneous saturation seen by a solid-state laser).

In the case of SROs, there are two mechanisms that cause mode hopping. Fluctuations within the cavity length of the OPO brought about by mechanical vibrations, or pressure changes in the air will cause mode hopping. One solution to this problem that is normally adopted is to actively stabilise the cavity length by locking it of an external reference cavity. By locking the cavity in this way it is possible to obtain reliable single-frequency operation of the laser output. One drawback of this technique is that it is very costly and complicated to implement. However, in the SRO OPOs, isolating the cavity from pressure changes and vibration will not stop the action of mode hopping. Thermal fluctuations of the PPLN will cause the overall length of the PPLN to change in time and will also cause the parametric gain curve peak to tune in order to satisfy the phase-matching condition in equation 5.5.

5.3.2 Pump stability

The importance of the OPO pumping laser operating on a single frequency becomes apparent when considering the effect of pump wavelength tuning on the phase-matching condition of the OPO. The following calculations are based around a PPLN grating period of 28.414μm. The wavelength acceptance calculation requires a fixed value of signal wavelength, the desired pump wavelength is chosen λ_p and the quasi-phase matched period that satisfies the phase-matching equation 5.5. The value of λ_p is then slightly increased (increasing the idler wavelength to satisfy equation 5.5). The phase mismatch of the new wavelength, $\Delta k(\lambda_p)$ can now be calculated using the following equation[21]:

$$\Delta k(\lambda_p) = 2\pi\left(\frac{n_p}{\lambda_p} - \frac{n_s}{\lambda_s} - \frac{n_i}{\lambda_i} - \frac{1}{\Lambda}\right)$$

[5.22]

The FWHM pump wavelength acceptance for the interaction $\delta\lambda_{pFWHM}$ is therefore given by:

$$\delta\lambda_{pFWHM} = 2(\lambda_{pHM} - \lambda_{pPEAK})$$

[5.23]

The pump wavelength acceptance is inversely proportional to the crystal length. As the pump wavelength is tuned therefore the phase-mismatch will increase for one particular signal and idler pair and will approach 0 for another. The net effect is that as the pump wavelength is tuned, the signal and idler wavelengths will also tune in order to fulfil the phase-matching condition in equation 5.22 so that Δk=0.

Figure 5.9 demonstrates the tuning curve of this PPLN sample as a function of pump wavelength.

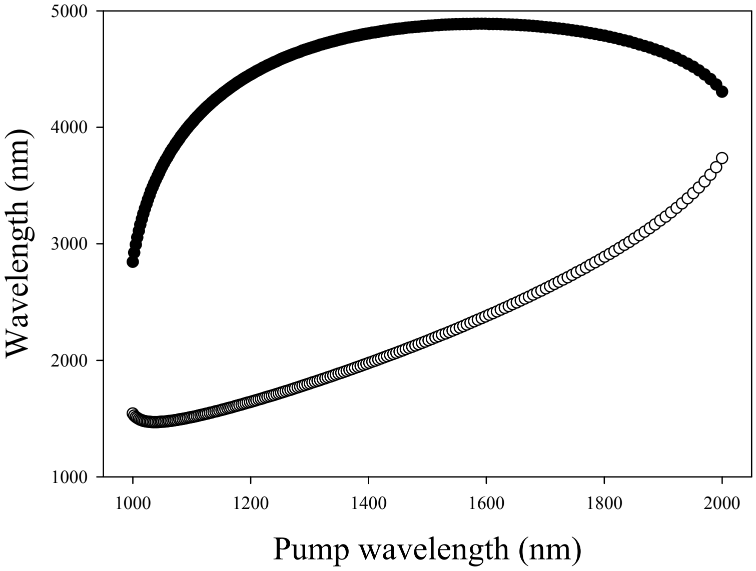

Figure 5.9 Graph showing the effects of pump wavelength tuning on the signal (hollow circles) and idler (solid circles) wavelengths for a PPLN grating period of Λ=28.414μm at 195^{0}C.

The relevance of the pump tuning in the case of the Nd:YLF MOPA it not as pronounced as figure 5.9 would show since under its own mode hop suppression regime, the fundamental pump frequency can only tune over 8GHz or 14 axial mode spacings before mode hopping occurs. The tuning of the signal over this range was considered to be negligible in effect.

5.3.3 Thermal expansion of PPLN

Equation 5.9 from Jundt [20] gives an expression for the fractional increase in PPLN length as a function of temperature. This in turn will alter the overall cavity length within an SRO leading to mode hopping. Plotting equation 5.9 as a function of temperature for a 50mm long PPLN sample (at room temperature) gave the following result (figure 5.10):

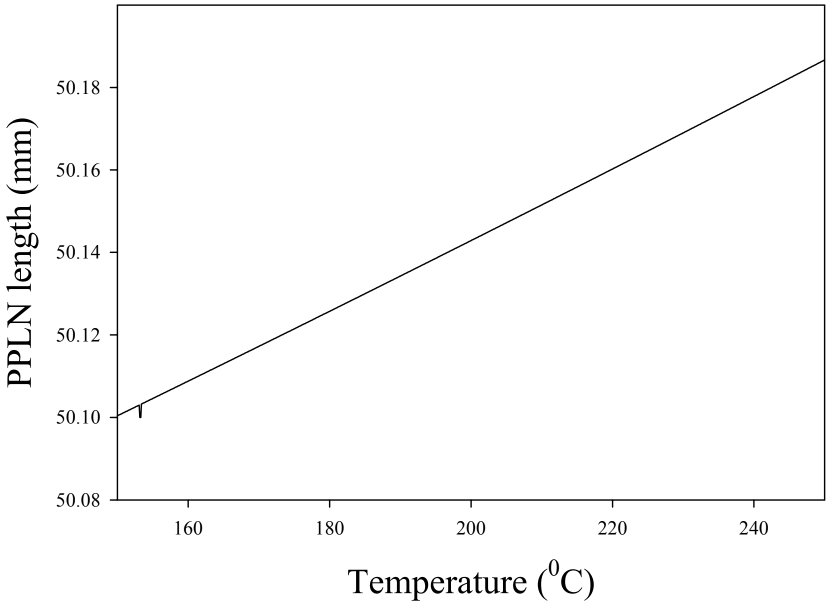

Figure 5.10 Graph showing the expansion in length of the PPLN sample as a function of increasing temperature.

Figure 5.10 shows the temperature dependence of the PPLN crystal length. The gradient of the graph shows us that the PPLN crystal will increase in length by 866nm/^{0}C. Given that the cavity length stability requirements for a mode hop to occur was ±370nm, it follows that to avoid mode hopping the PPLN operating temperature needed to be stabilised to within ±0.4^{0}C. Temperature stabilities of this order of magnitude are relatively easy to achieve with careful engineering, however the expansion of the PPLN length with temperature is not the only effect temperature fluctuations have on the SRO stability.

5.3.4 The temperature dependence of the parametric gain lineshape

Temperature tuning the PPLN crystal has a similar effect to that of pump tuning. The signal and idler wavelengths will tune with temperature to fulfil the phase matching condition of equation 5.22 so that phase-mismatch Δk=0. The temperature acceptance of a quasi-phase matched interaction defines the amount of temperature stabilisation required to maintain phase matching. The temperature acceptance is calculated in a similar fashion to wavelength acceptance. When in this instance, the temperature is allowed to deviate from its optimum value, the phase mismatch as a function of temperature can the expressed as follows [21]:

$$\Delta k(T) = 2\pi\left(\frac{n_p(T)}{\lambda_p} - \frac{n_s(T)}{\lambda_s} - \frac{n_i(T)}{\lambda_i} - \frac{1}{\Lambda(T)}\right)$$

[5.24]

Where the temperature dependence of the refractive index is calculated from the Sellmeier equations and the temperature dependence of the quasi-phase matched period is calculated from the thermal expansion equation 5.9. The temperature dependence to a good approximation is inversely proportional to the crystal length. In figure 5.11 we can see that the 28.414mm grating will have a phase mismatch Δk~0 at a temperature of 195^0C. As the temperature is tuned, the signal and idler wavelengths will again tune in order to fulifil the phase-matching condition:

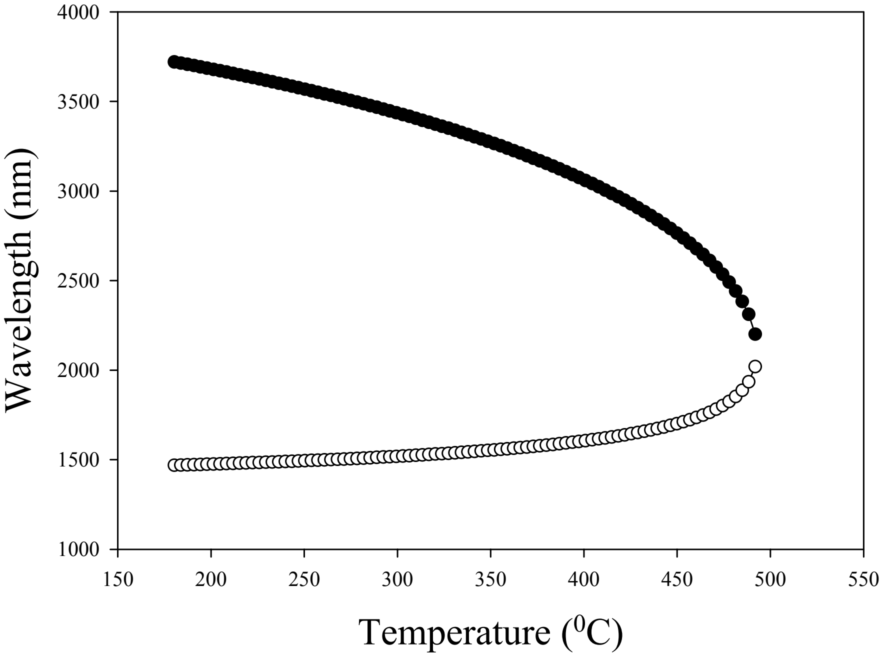

Figure 5.11 Graph showing temperature tuning curve of the signal (hollow circles) and idler (solid circles) wavelengths pumped by 1053nm.

Figure 5.11 shows the signal wavelength for a grating period of 28.414μm as a function of temperature. This change in wavelength corresponds to the movement of the gain curve as a function of temperature. An expanded view of figure 5.11 will therefore show us (over a range of 20^0C around the operating temperature of 195^0C by how much the gain curve will move with temperature (figure 5.12):

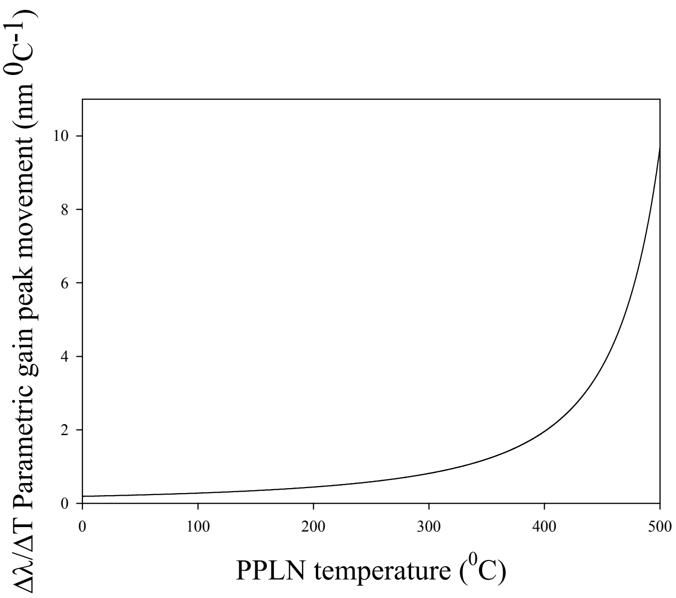

Figure 5.12 Graph showing the movement of the parametric gain curve peak in nm per ^{0}C as a function of the PPLN operating temperature.

Figure 5.12 shows the maximum movement of the parametric gain curve per ^{0}C change in temperature as a function of the PPLN temperature over the entire phase matched curve in figure 5.11. From the curve we can see that the parametric gain curve peak will move more as the OPO is temperature tuned towards degeneracy ($\lambda_s=\lambda_i=2\lambda_p$). At an operating temperature of 195^{0}C the gain peak will move ~0.4nm^{0}C^{-1} change in temperature, at degeneracy however, the gain peak can move up to ~10nm^{0}C^{-1}. It follows therefore that mode hopping will be most prevalent towards degenerate operation of the OPO at the point of which the OPO will be oscillating on two frequencies continually.

The phase-matching bandwidth of the OPO is defined as the full-width half-maximum of the OPO gain bandwidth as a function of signal wavelength. This can be calculated from equation 5.11 at a constant operating temperature of 195^{0}C, where by the change in signal wavelength will change the phase-matching condition as described by equation 5.5.

Figure 5.13 shows the phase-matching bandwidth of a PPLN OPO for various crystal lengths of 10,20,30,40 and 50mm, the wavelength dependent refractive indices are calculated from the temperature dependent expressions from Jundt [20], the other parameters used are from the example in figure 5.6.

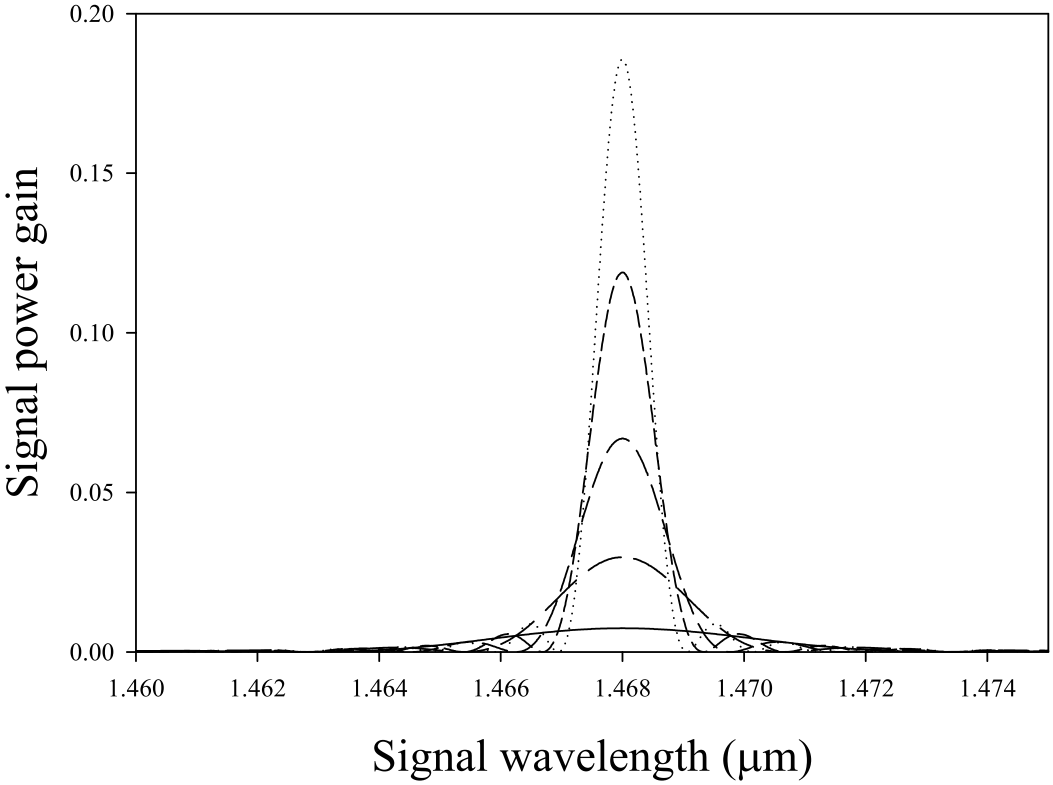

Figure 5.13 Graph showing phase matched gain curve for λs=1.468μm for various PPLN crystal lengths of 10 (lowest peak-solid line), 20,30,40 and 50mm (highest peak-dotted line).

Figure 5.13 show the parametric gain curves for a grating period of 28.414μm at an operating temperature of 1950C for various crystal lengths using the same example parameters set in figure 5.6. It can be seen from the graph that the phase-matching bandwidth is inversely proportional to the crystal length. From figure 5.13 it can be see that the phase-matching bandwidth of the 50mm long PPLN example is ~1nm corresponding to ~200GHz, with the oscillating fundamental mode at gain line centre. This parametric gain peak will move as a function of temperature therefore at a rate shown in figure 5.12.

The net effect of temperature instability of the PPLN on the parametric gain curve can therefore be plotted (figure 5.14). Here the travel of the gain curve can be plotted as a function of the offset in temperature for the operating temperature of 195^0C.

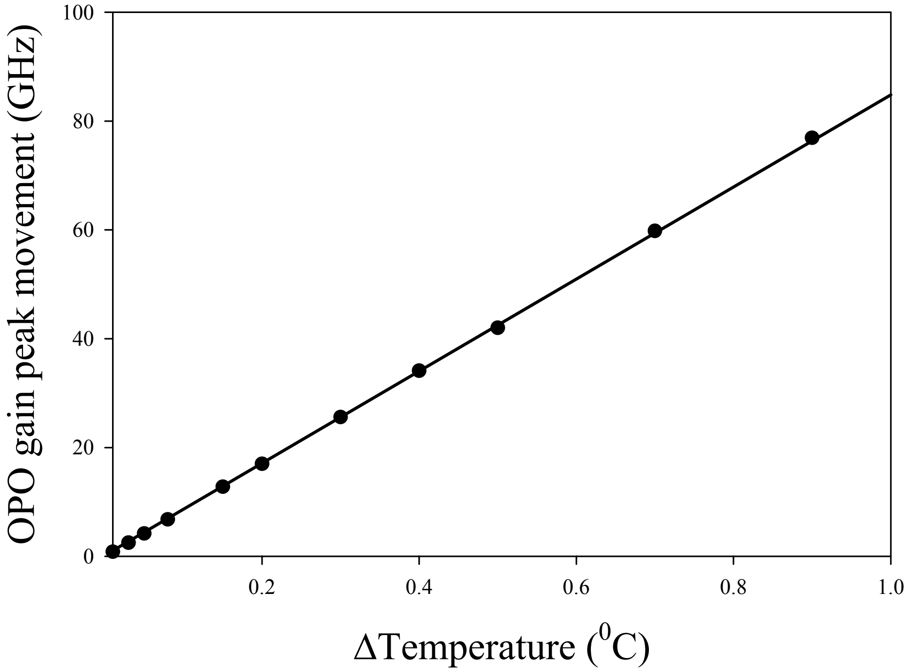

Figure 5.14 Graph showing OPO parametric gain peak movement as a function of temperature offset from the operating temperature of 195^0C.

It can be seen from figure 5.14 that for temperature instability of $\pm 0.5^0$C in the PPLN oven, the parametric gain peak will tune over 40GHz (approximately 20% of the width of the 50mm long crystal line shape). The net effect of this is that SROs suffer detrimentally from mode hopping due to temperature fluctuations within the PPLN crystal. Locking the OPO cavity length to a reference cavity will alleviate the problems of mode hopping due to cavity length instabilities, but extremely fine control of the PPLN temperature is needed to ensure mode hop free operation. In the extreme case, the OPOs degenerate wavelength (where $\lambda_s = \lambda_i$), the rate of change of the signal wavelength is much steeper, meaning that the OPO would be much more sensitive still to temperature fluctuations (~10nm / ^{0}C).

An alternative approach was to introduce the passive technique for mode hopping suppression already described in Chapter 3. By means of introducing a nonlinear loss at the signal wavelength, the loss seen due to sum frequency generation of the oscillating and non oscillating modes, by the non oscillating modes allow the fundamental frequency to be tuned over numerous mode spacings before a mode hop occurred.

5.4 CW SRO mode hopping suppression

5.4.1 The theory of mode hop suppression within an SRO

In this work we have already employed a simple passive technique to suppress axial mode-hopping within a 1μm single-frequency diode-end-pumped solid-state laser based on Nd:YLF. Our approach exploited the different nonlinear losses experienced by lasing and non-lasing axial modes when a frequency doubling crystal is inserted into the laser cavity (see Chapter 3).

Within an SRO, the phase-matching bandwidth of the parametric gain curve is dictated by the temperature dependent wavelength dispersion of the pump, signal and idler fields within the OPO material (in this case PPLN). In order to fulfil the phase-matching condition whereby the phase-mismatch $\Delta k=0$, the signal and idler wavelength pairs will tune with temperature fluctuations.

In this case therefore, the introduction of a nonlinear crystal into the SRO cavity, noncritically phase-matched for second harmonic conversion of the signal wavelength should allow for a certain amount of mode hopping suppression in the same way as it was introduced into the master oscillator cavity (figure 5.15).

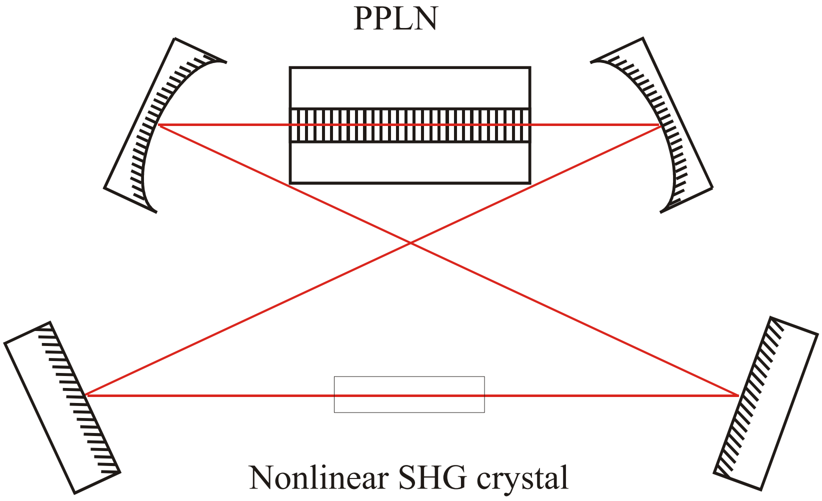

Figure 5.15 Diagram showing a simple four-mirror SRO with the inclusion of a nonlinear crystal noncritically phase-matched for the second harmonic conversion of the signal wavelength.

The mechanism behind mode-hop-suppression can be explained as follows: the oscillating signal mode sees a loss due to the second harmonic generation (SHG) in the non-linear crystal equal to the second-harmonic conversion efficiency. However, non-oscillating signal modes, within the SRO parametric phase-matching bandwidth, experience a loss that is approximately twice that of the signal mode due to sum-frequency generation with the oscillating signal mode (Figure 5.16):

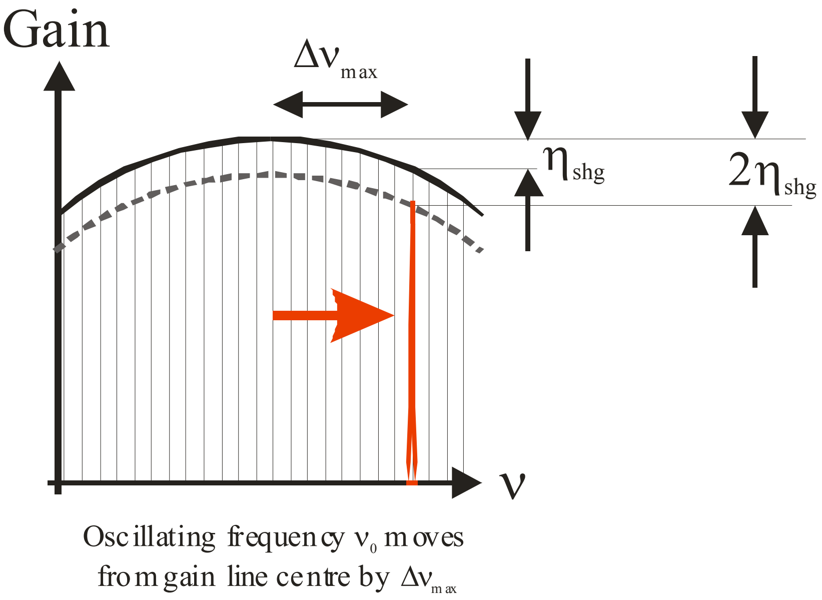

Fig 5.16 Diagram showing the action of mode-hop-suppression.

With the introduction of this nonlinear loss with the SRO cavity, it should now be possible for the fundamental signal frequency to tune over many axial mode spacings within the parametric gain curve before a mode hop occurs, provided that the loss seen by the non oscillating modes due to sum frequency generation is large enough.

The second harmonic conversion efficiency can be calculated from the following expression:

$$\eta_{SHG} = \frac{P_{2\omega}}{P_{\omega}}$$

[5.25]

where

$$P_{2\omega} = l_c^{\ 2} K \frac{P_\omega}{A} \frac{\sin^2\left(\frac{\Delta k l_c}{2}\right)}{\left(\frac{\Delta k l_c}{2}\right)^2}$$

[5.26]

and $K = 2\eta^3 v_1^2 d_{eff}^2$

$\eta = \sqrt{\mu_0 / \varepsilon_0 \varepsilon} = 377 / n_0$ [V/A] is the plane-wave impedance, P_ω is the power of the fundamental wavelength (in this case the signal wavelength), l_c is the length of the nonlinear crystal, A is the area of the fundamental beam, v_1 is the frequency of the signal light and d_{eff} is the effective nonlinear coefficient of the nonlinear polarizability tensor $X^{(2)}$. The parameter K is unique to the nonlinear crystal used for second harmonic generation, the second-harmonic conversion efficiency is therefore dependent on phase-mismatch within the nonlinear crystal, the crystal length and the incident fundamental frequency power, and the second-harmonic phase matching bandwidth (FWHM) is dependent on crystal length as in the case of the PPLN.

It is vitally important therefore that the phase-matching bandwidth of the nonlinear crystal generating the second harmonic for the signal wavelength is larger than the parametric gain bandwidth of the PPLN, or else the OPO will oscillate on an axial mode that sees no loss due to second-harmonic conversion. Figure 5.18 shows the normalised phase-matching bandwidths of a second-harmonic generating nonlinear crystal at the signal wavelength of 1.468μm for various lengths of crystal.

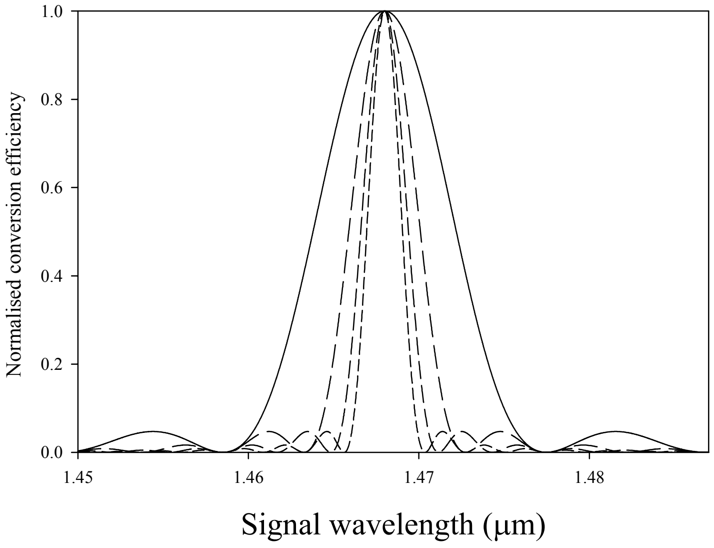

Figure 5.18 Graph showing the normalised second harmonic conversion efficiency of the signal wavelength as a function of wavelength for different lengths of nonlinear crystal (5,10,15 and 20mm).

Figure 5.18 shows that as with the PPLN the second harmonic phase-matching bandwidth increases with decreasing crystal length. Therefore in order to ensure that the bandwidth of the second harmonic generating crystal is in fact wider than the parametric gain bandwidth of the PPLN, a nonlinear crystal length of <50mm must be choosen.

The mode-hop-free tuning range $\Delta\nu_{\max}$ is given by the following approximate expression [28]:

$$\Delta\nu_{\max} = \frac{\Delta\nu_{OPO}}{2}\sqrt{\frac{\eta_{SHG}}{2\left(\eta_{SHG}+L\right)}}$$

[5.27]

where $\Delta\nu_{OPO}$ is the gain line-width of the OPO, η_{SHG} is the second-harmonic conversion efficiency and L is the round trip cavity loss of the OPO cavity (not including the non-linear loss). This expression is assuming that the parametric gain profile of the PPLN (a sinc function) has a Lorenzian profile like that of the diode-end-pumped solid-state laser, however at the FWHM point on each curve the difference was found to be negligible, and therefore the expression was assumed to be correct for low conversion efficiencies.

From equation 5.27 it can be seen that $\Delta\nu_{max}$ is largest when the laser cavity is optimised for second harmonic generation (i.e. the cavity loss is made to be as small as possible). However, even when the OPO cavity design is optimised for operation at the signal wavelength, it can also be seen from equation 5.27 that a useful mode-hop-free tuning range can still be achieved.

5.4.2 The implications of mode hopping suppression with an SRO

There are numerous ways in which an SRO can experience mode hopping. Simple cavity length fluctuations (due to pressure changes in the air, mechanical vibrations or even thermal expansion of the PPLN) can be overcome by locking the OPO cavity to a reference cavity via the application of relatively sophisticated electronics, however, in the case of the SRO, temperature instabilities of the PPLN will also cause the parametric gain profile to move considerable distances leading to mode hopping.

Given that in practice, the PPLN oven used in experiments maintained the crystal at a temperature of 195^0C ± 0.5^0C, we could expect the parametric gain curve to move over ~40GHz via temperature fluctuations around this point. This in practice meant that our passive technique for mode hoping suppression would require us to generate enough second harmonic of the signal wavelength as to equal or even exceed this range of travel.

For the purposes of this research, a Brewster angled; 15mm long LBO crystal was obtained to be included in the SRO cavity. The non-critical temperature phase matching curve for the LBO was plotted as a function of wavelength to give the following graph (figure 5.19):

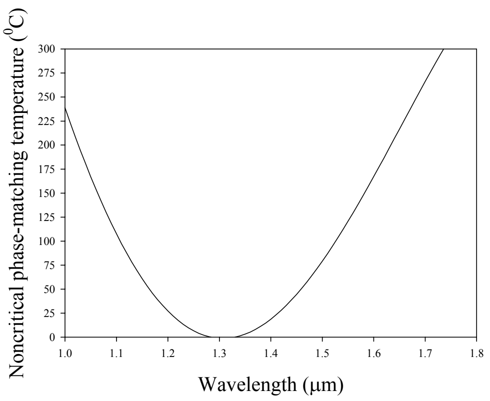

Figure 5.19 Graph showing noncritical phase matching temperatures as a function of wavelength.

Figure 5.19 allowed us to determine the non critical phase-matching temperature of the LBO in order to optimise the second harmonic generation of the signal wavelength. For a signal wavelength of 1.468nm therefore, non critical phase-matching will occur at a temperature of 57^0C. The phase-matching bandwidth of the LBO crystal is dependent on its length. In our case the LBO crystal was 15mm long giving the following normalised second harmonic gain curve (figure 5.20):

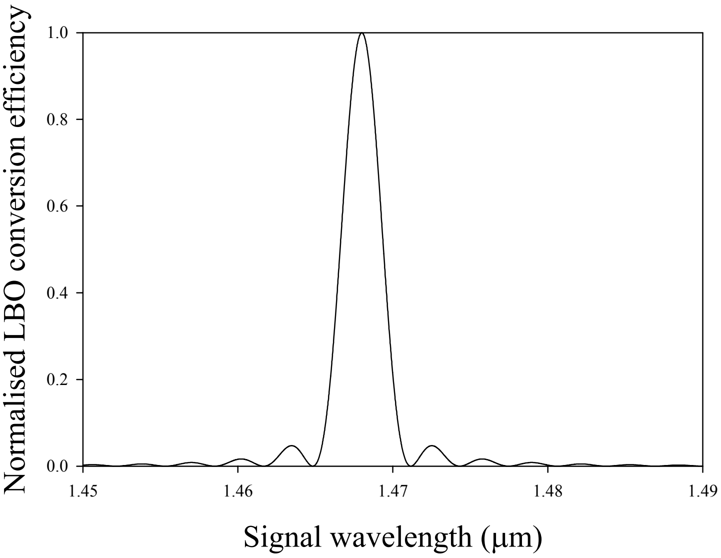

Figure 5.20 Graph showing the normalised second harmonic phase-matching bandwidth of LBO as a function of signal wavelength.

In this practical case in figure 5.20 it was measured that the second harmonic phase-matching bandwidth for the LBO was ~3nm. This meant that the OPO would not automatically tune itself to a signal and idler wavelength pair (within the constrictions of the phase-matching condition otherwise OPO threshold would fail to be reached) that saw a higher gain by avoiding loss due to second harmonic conversion. Therefore, in practice it was thought that the potential for the technique for demonstrating mode hop suppression within an SRO was high dependant on careful cavity design in order to maintain a relatively low cw OPO threshold and high second harmonic conversion efficiency of the signal wavelength within the LBO.

5.5 CW SRO alignment technique and application

5.5.1 Confocal SRO cavity

Employing SRO cavity designs through the course of this work would obviously increase the threshold of the devices to >~few watts requiring very careful cavity design. Initial experiments were performed with the OPO operating in quasi cw regime in order to measure wavelength tuning and to develop a practical alignment technique. For preliminary experiments, a simple confocal two-mirror cavity was adopted as can be seen in figure 5.21:

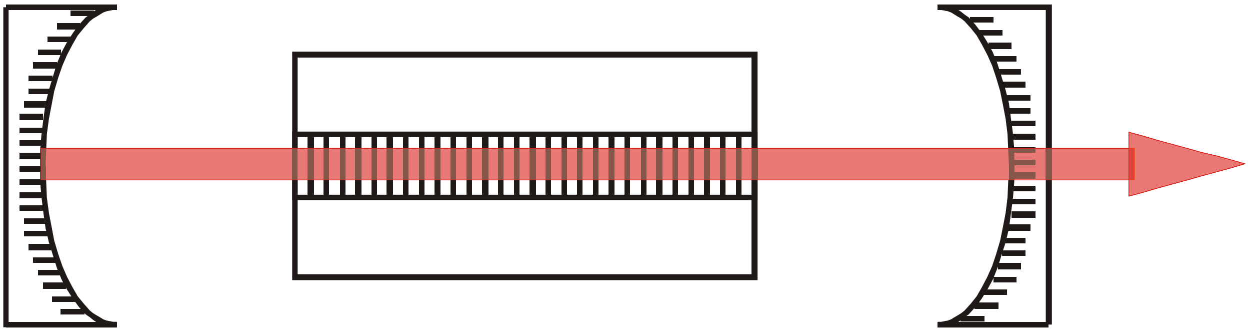

Figure 5.21 Diagram showing the simplified confocal OPO cavity.

The confocal cavity had a pump waist size of 100μm and a signal waist size of 120μm, the cavity comprised of two mirrors, each with a radius of curvature of

50mm, and both HR@1.45-1.5μm, T>85%@3.5-4.5μm and HT@1.053μm. The PPLN sample was 50mm long with a grating period of 28.414μm. The signal spot size as a function of distance through the cavity can be seen in figure 5.22:

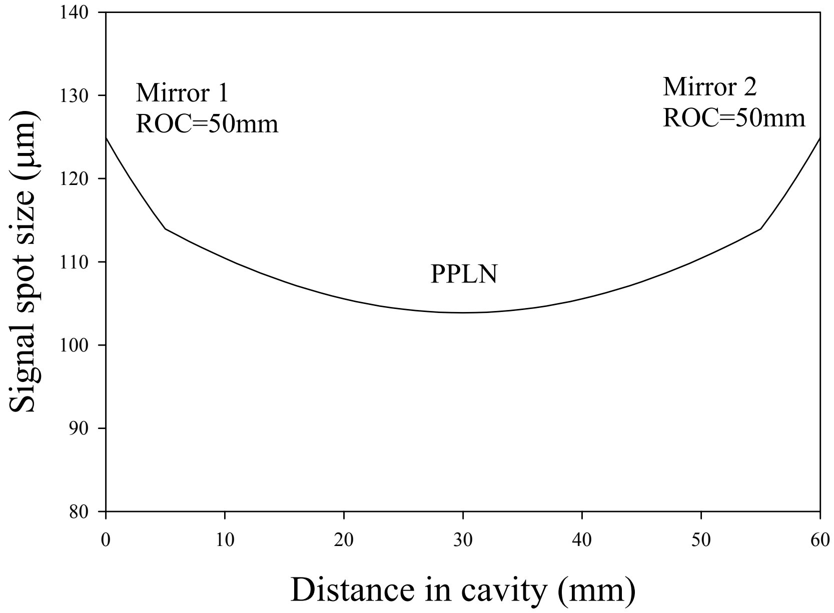

Figure 5.22 Graph showing signal spotsize as a function of cavity length for the confocal OPO cavity.

Using the equation 5.19 the cw threshold for the OPO in this configuration was calculated to be ~12W. This threshold was considered to be far too high for the OPO design to be of any use in a cw regime. However, in a pulsed configuration it was noted in this case, a useful amount of green light was generated via a very small amount of second harmonic generation in the PPLN along the axis of the pump light allowing for accurate alignment of the OPO at a visible wavelength before the pump power was turned up above threshold. The alignment of the PPLN crystal was very sensitive to angular misalignment, this was due to the fact that the PPLN sample itself was 50mm long, however the 28.414μm grating was only 0.5mm wide meaning that the maximum angular displacement in the x-z plane (assuming z is the direction of pump propagation) was ~0.6^0.

5.5.2 Four mirror linear SRO cavity

In order to reduce the threshold further a four-mirror standing wave cavity was then constructed allowing increased control over the signal spot size with the PPLN (figure 5.23), the pump spot waist was reduced to 85µm. In this case, the curved mirrors had an ROC=100mm, and the other mirrors were plane faced, all were HR at the signal wavelength again in order to reduce the cw threshold of the OPO:

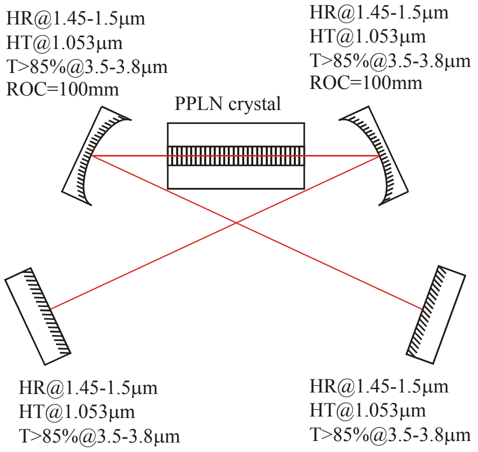

Figure 5.23 Diagram showing the four-mirror standing wave cavity.

Figure 5.24 shows the signal spot size as a function of distance through the cavity.

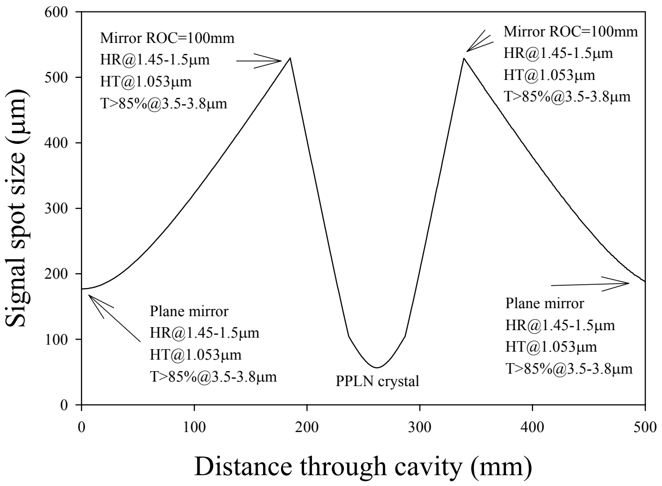

Figure 5.24 Graph showing the signal spot size as a function of cavity length for the four-mirror standing wave cavity.

The four-mirror standing wave cavity gave a calculated threshold value of ~6.0W. Since the cavity at this point was HR (i.e. there was no signal output coupling) at the signal wavelength we observed the idler output at a wavelength of 3.275μm. However, since all the mirrors in the cavity were HT at the idler wavelength each mirror within the cavity displayed a certain amount of idler leakage making it very difficult to measure the total idler output power from the OPO.

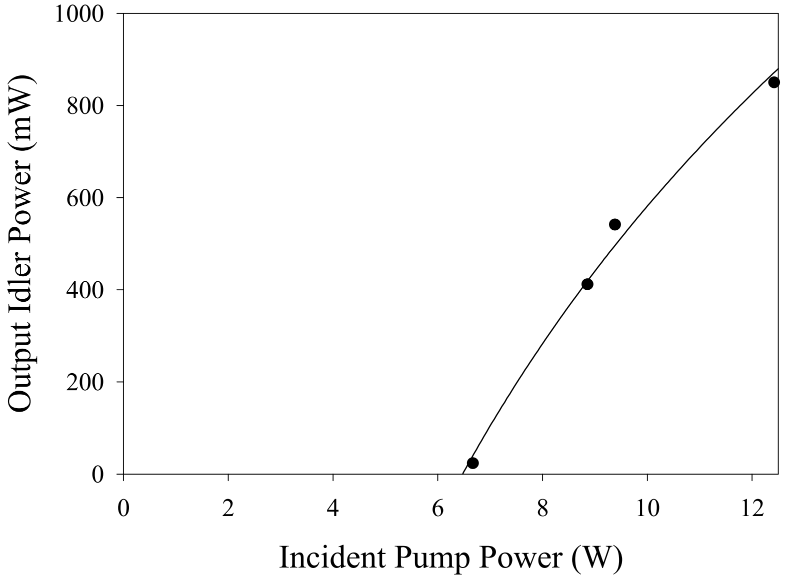

Figure 5.24 Graph showing idler output as a function of incident pump power for the four-mirror standing wave cavity.

Figure 5.24 shows the idler output as a function of incident pump power. Although the values for the actual idler power were inaccurate (due to all the mirrors in the cavity leaking idler light), the graph shows the threshold of the device was ~6W, a result that was in good agreement with our threshold model.

5.5.3 Four-mirror ring SRO cavity

The final stage of OPO development was to build an HR ring oscillator around the PPLN. Figure 5.25 shows the HR cavity and figure 5.26 shows the signal spot size as a function of distance through the cavity.

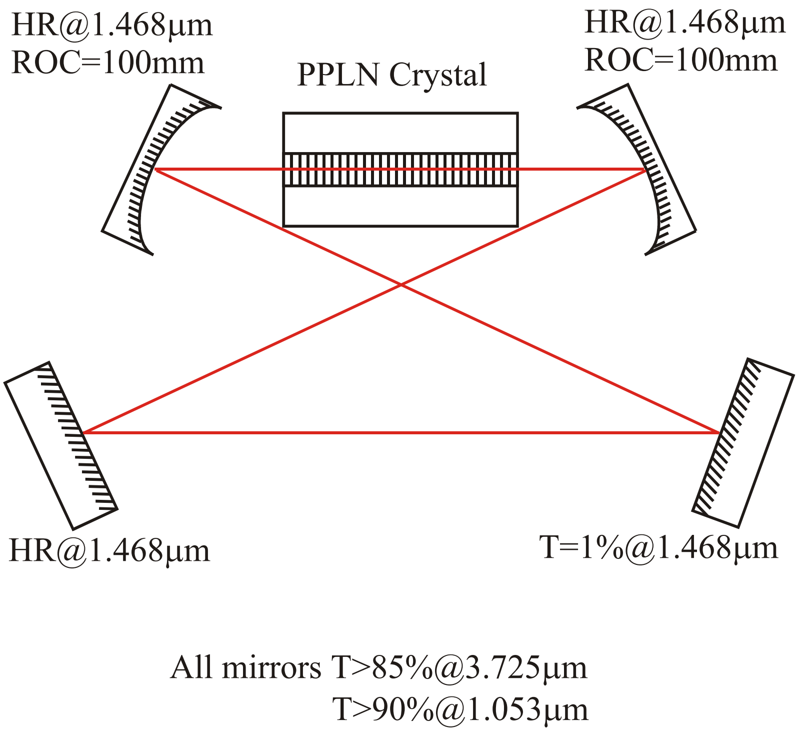

Figure 5.25 HR OPO ring cavity.

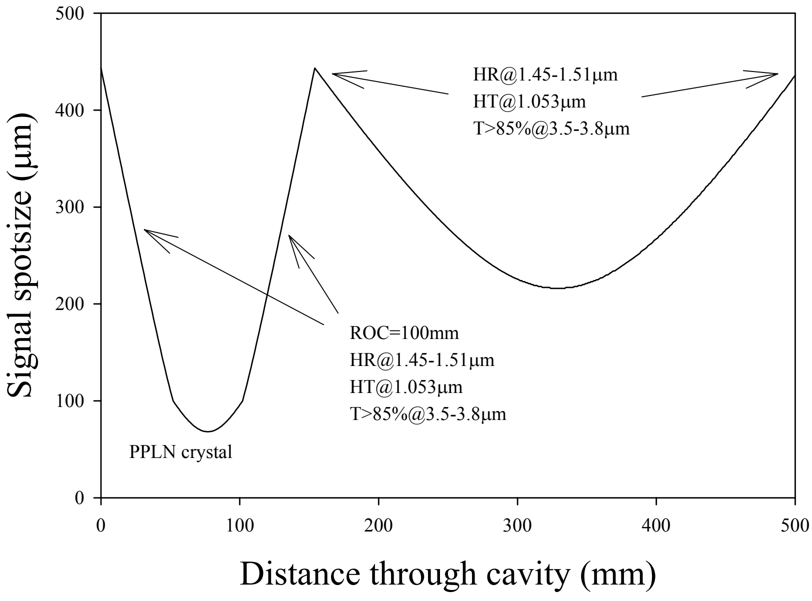

Figure 5.27 Graph showing the signal spot size as a function of distance through the HR four-mirror ring cavity.

In figure 5.27 we can see that the cavity was designed to provide a good pump and signal overlap with w_p=w_s=85µm. Also, due to the ring nature of the cavity the round trip cavity loss seen by the signal (that would always follow the direction of the incident pump light) was halved, reducing the HR cavity threshold to a calculated value of ~3W. The idler wavelength was monitored as a function of incident pump power (figure 5.28):

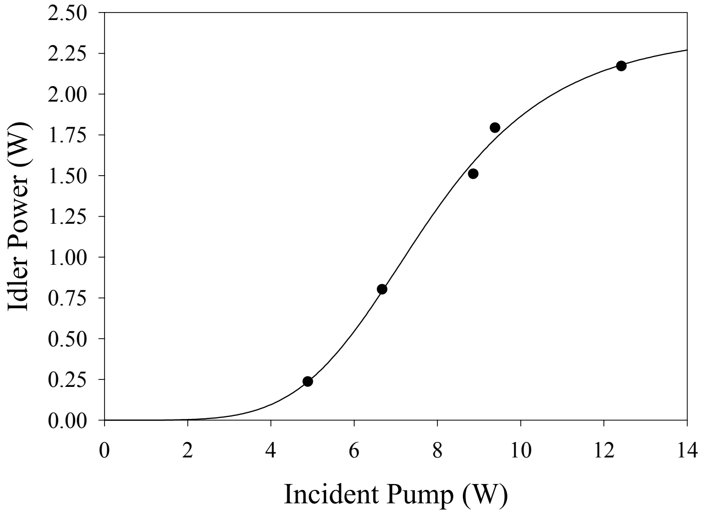

Figure 5.28 Graph showing output idler power as a function of incident pump power for the four mirror HR ring cavity.

Figure 5.28 shows the output idler power as a function of incident pump power. The graph confirmed our theoretical calculation that the threshold of the device was around 3W. The roll-off of the device as we approach maximum incident pump power however indicated that there way some other effect that would limit the output power from the device. This was thought to potentially be thermal lensing within the PPLN leading to mode mismatch of the signal and the pump waists, leading to a decrease in conversion efficiency at higher incident pump powers.

This initial set of results allowed us to fully test the output characteristics of the OPO in term of threshold and temperature tuning. The threshold of each cavity configuration compared well with their calculated value from theory, the idler output wavelength was measured as a function of PPLN temperature using a monochromator (figure 5.29) giving a close match to the theoretical curve produced from the temperature dependent Sellmeier equations:

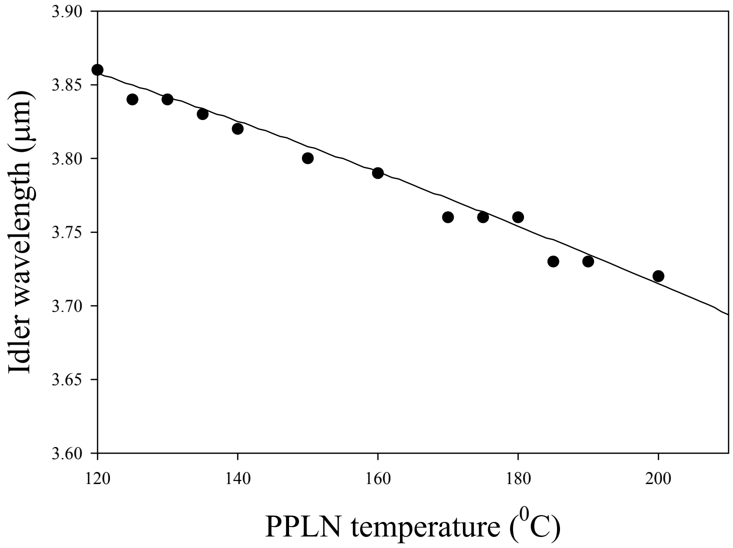

Figure 5.29 Graph showing the idler wavelength from the output from the ring resonator as a function of temperature, measured values (dots), theoretical curve (solid line).

The first three cavity configurations therefore allowed us to monitor the OPO under both pulsed and cw conditions allowing us to firstly test our model for threshold and temperature tuning and, secondly, develop an appropriate alignment technique for aligning ring cavity oscillators.

5.6 Discussion and conclusions

In conclusion to this chapter we have discussed the concept of phase-matching and quasi phase-matching within a nonlinear medium for the purposes of optical parametric generation and oscillation in the cw regime. The principal usages of cw single-frequency OPOs, e.g. spectroscopic applications and LIDAR, require very spectrally stable outputs, and although cw OPOs are inherently single-frequency by nature, the output from these devices suffers detrimentally from mode-hopping, not only due to temperature fluctuations and pressure changes applied to the cavity and thermal expansion of the PPLN, but in the majority due to the movement of the parametric gain curve as a function of temperature. Therefore, although phase-matching can now be readily achieved in nonlinear materials and with the advent of new technologies, the cw singly-resonant threshold of such OPO devices can be lowered to a point whereby they can be operated in a cw regime without the need for added cavity complexity via pump enhancement or doubly-resonant cavity designs, they still suffer detrimentally from mode-hopping. In order to provide robust and reliable single-frequency output expensive and costly cavity additions have been made in some cases, locking the cavity of the OPO to a reference or even extending the mode-hop free tuning range, but without overcoming mode hopping entirely due to the sensitivity of the movement of the parametric gain curve with fluctuations in PPLN temperature. However we suggest a different approach: by including a second harmonic generating crystal within the OPO cavity mode-hop suppression could occur, proportional in range to the nonlinear second harmonic generation of the fundamental signal mode, allowing the OPO to operate single-frequency both robustly and reliably.

Initial results have shown that the OPO in its various cavity configurations has behaved in terms of temperature, wavelength tuning and threshold as our theoretical model predicts, however, in order to more closely observe the spectral characteristics of the signal wavelength, an output coupler at the signal wavelengths needs to be incorporated into the cavity. This will increase the threshold of the device but will allow us to observe the OPO mode hopping with temperature fluctuations over time. The following chapter will record our observations of OPO mode hopping and will follow our attempts to suppress mode hopping by the incorporation of a nonlinear crystal into the OPO cavity in an attempt to utilize our passive technique for mode hop suppression that was outlined in the design and building of the Nd:YLF master oscillator.

5.8 References

1. Batchko, R.G., *Continuous-wave 532-nm-pumped singly resonant optical parametric oscillator based on periodically poled lithium niobate.* Optics Letters, 1998. **23**(3): p. 168-170.
2. Bosenberg, W.R., *2.5-W, continuous-wave, 629-nm solid-state laser source.* Optics Letters, 1998. **23**(3): p. 207-209.
3. Bosenberg, W.R., *Continuous-wave singly resonant optical parametric oscillator based on periodically poled LiNbO3.* Optics Letters, 1996. **21**(10): p. 713-715.
4. Bosenberg, W.R., *93% pump depletion, 3.5-W continuous-wave, singly resonant optical parametric oscillator.* Optics Letters, 1996. **21**(17): p. 1336-1338.
5. Colville, F.G., M.J. Padgett, and M.H. Dunn, *Continuous-Wave, Dual-Cavity, Doubly Resonant, Optical Parametric Oscillator.* Applied Physics Letters, 1994. **64**(12): p. 1490-1492.
6. Edwards, T.J., *Continuous-wave, singly-resonant, optical parametric oscillator based on periodically poled KTiOPO4.* Optics Express, 2000. **6**(3): p. 58-63.
7. Gibson, G.M., *Continuous-wave optical parametric oscillator based on periodically poled KTiOPO4 and its application to spectroscopy.* Optics Letters, 1999. **24**(6): p. 397-399.
8. Myers, L.E., *Cw Diode-Pumped Optical Parametric Oscillator in Bulk Periodically Poled $LiNbO_3$.* Electronics Letters, 1995. **31**(21): p. 1869-1870.
9. Yang, S.T., R.C. Eckardt, and R.L. Byer, *Continuous-Wave Singly Resonant Optical Parametric Oscillator Pumped by a Single-Frequency Resonantly Doubled Nd-Yag Laser.* Optics Letters, 1993. **18**(12): p. 971-973.
10. Miller C., *Tunable coherent parametric oscillation in LiNbO3 at optical frequencies.* Physical Review Letters, 1965. **14**(24): p. 973-976.
11. Marshall, L. *Laser diode-pumped solid-state lasers*. in *CLEO 2001*. 2001.
12. Myers, R.C.E., M.M. Fejer and R.L. Byer, *Quasi-phase-matched optical parametric oscillators in bulk periodically poled $LiNbO_3$.* Journal of the Optical Society of America B-Optical Physics, 1995. **12**(11): p. 2102-2116.

13. Byer, *Optical parametric oscillator threshold and linewidth studies.* Journal of Quantum Electronics, 1979. **QE-15**(6): p. 415-431.

14. Byer, R.L., *Quasi-phasematched nonlinear interactions and devices.* Journal of Nonlinear Optical Physics & Materials, 1997. **6**(4): p. 549-592.

15. Bosenberg, W.R. and R.C. Eckardt, *Optical Parametric Devices - Introduction.* Journal of the Optical Society of America B-Optical Physics, 1995. **12**(11): p. 2084-2084.

16. Butterworth, S.D., V. Pruneri, and D.C. Hanna, *Optical parametric oscillation in periodically poled lithium niobate based on continuous-wave synchronous pumping at 1.047 μm.* Optics Letters, 1996. **21**(17): p. 1345-1347.

17. Eckardt, R.C., *Optical Parametric Oscillator Frequency Tuning and Control.* Journal of the Optical Society of America B-Optical Physics, 1991. **8**(3): p. 646-667.

18. Edwards, T.J., *High-power, continuous-wave, singly resonant, intracavity optical parametric oscillator.* Applied Physics Letters, 1998. **72**(13): p. 1527-1529.

19. Ross, G.W., *Generation of high-power blue light in periodically poled $LiNbO_3$.* Optics Letters, 1998. **23**(3): p. 171-173.

20. Jundt, D.H., *Temperature-dependent Sellmeier equation for the index of refraction, n(e), in congruent lithium niobate.* Optics Letters, 1997. **22**(20): p. 1553-1555.

21. Bamford, D.J., *PPLN Tutorial.* 1998, Gemfire Corporation.

22. Boyd, G.D., *Parametric Interaction of Focused Gaussian Light Beams.* Journal of Applied Physics, 1968. **39**(8): p. 3597-3639.

23. Byer, R.L. and A. Piskarskas, *Optical Parametric Oscillation and Amplification - Introduction.* Journal of the Optical Society of America B-Optical Physics, 1993. **10**(9): p. 1656-1656.

24. McCarthy, M.J. and D.C. Hanna, *All-Solid-State Synchronously Pumped Optical Parametric Oscillator.* Journal of the Optical Society of America B-Optical Physics, 1993. **10**(11): p. 2180-2190.

25. Guha, S., *The effects of Focusing on Parametric Oscillation.* IEEE Journal of Quantum Electronics, 1982. **18**(5): p. 907-912.

26. Guha, S., *Focussing dependence of the efficiency of a singly resonant optical parametric oscillator.* Applied Physics B-Lasers and Optics, 1998. **66**: p. 663-675.

27. Padgett, M.J., PhD *Optical Parametric Oscillators: continuous wave operation*, Universty of St Andrews: Scotland. p. 209-227.

28. Martin, PhD *High power diode pumped single frequency lasers*, in *Optoelectronics Research Centre*. 1996, University of Southampton.

Chapter 6: CW mode-hop-free SROPOs

6.1 Introduction

In chapter 5 we described the operation of cw optical parametric oscillators in terms of threshold and conversion efficiency, pointing out their inherent mode hopping nature due not only to fluctuations in cavity length but also to temperature fluctuations of the PPLN crystal itself, causing movement of the parametric gain curve. To a certain extent, by locking the cavity length of the OPO and accurately stabilising the temperature of the PPLN, a certain extended degree of mode hop free tuning can be realised [1] as described by Turnbull *et al* whereby the use of a dual cavity (to isolate the signal and idler cavity lengths) and pump enhancement (to reduce the threshold of the OPO to 100's mWs) allowed for a certain degree of mode-hop-free. However this sort of active mode-hop-free operation can be both complicated and costly to implement and does not totally overcome mode hopping due to temperature instabilities. In chapter 5 we proposed to use a passive technique for mode-hop-suppression described in chapter 3. As many similarities existed between laser and OPO cavities, the introduction of a nonlinear crystal into the OPO cavity would double the loss seen by the non-oscillating axial modes and hence increase the mode-hop-free tuning range of the OPO considerably. With the emphasis of the OPO output remaining single frequency, we should be able to achieve robust and reliable single-frequency output that is much less sensitive to the temperature fluctuations of the PPLN crystal.

Chapter 6 will therefore describe the design and construction of two OPO cavities both incorporating output coupling at the signal frequency. Once the cw output from these cavities was experimentally recorded, a nonlinear crystal (LBO) was introduced into the cavity in order to attempt to achieve a certain amount of mode-hop-suppression.

6.2 Four-mirror cw OPO cavity

6.2.1 Four-mirror cw OPO without mode-hopping suppression

Initial experiments with a four-mirror cavity proved to be a reasonable success (please see Chapter 5). The idler wavelength was initially observed in order to measure threshold and temperature tuning characteristics based on the temperature dependent Sellmeier equations for lithium niobate. However, our main interest for the purposes of this research was the signal wavelength output and therefore an output coupler was included into the cavity (figure 6.2). The ring oscillator was aligned with the pump laser operating in a pulsed regime. Once the OPO was working (detecting the signal pulses and depletion of the pump pulses), the cavity was optimised and the length of the pulses was increased until the OPO was operating cw. An example long pump pulse can be seen in figure 6.1:

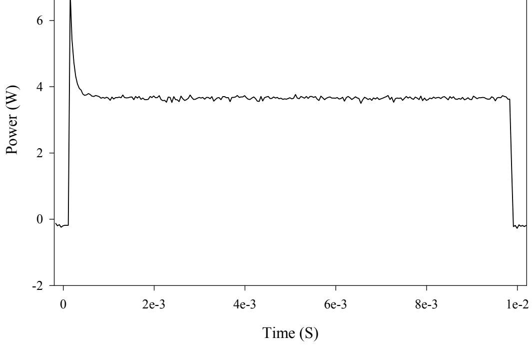

Figure 6.1 Graph showing long duration pump pulse of 9.6ms (100Hz rep rate) .

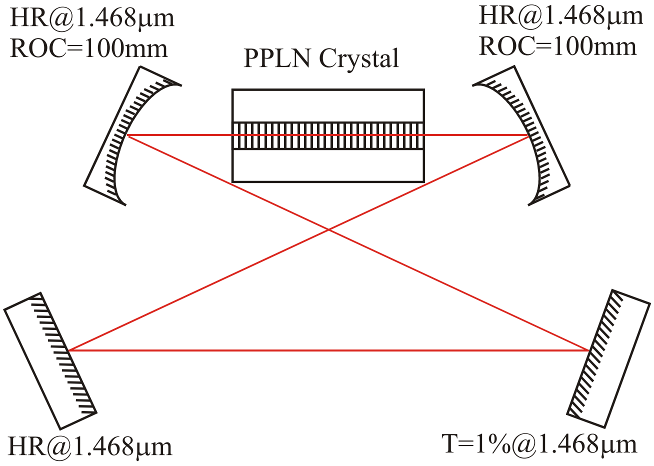

All mirrors T>85%@3.725µm
T>90%@1.053µm

Figure 6.2 Diagram showing the cavity configuration of the four-mirror cw OPO ring cavity with 1% output coupler at the signal wavelength.

The PPLN sample had a grating period of 28.414µm and was held at a temperature of 195^{0}C in order to reduce the effects of photorefractive damage. The mirrors in the cavity were all T>85%@3.5-3.8µm, T>90%@1.053µm. The two curved mirrors were in fact meniscus mirrors designed to minimise any extra focusing effects of the pump light through the PPLN ROC=100mmcc/100mmcx. The two curved mirrors and one plane mirror were also all HR@1.450-1510µm. The output coupler was R=99%@1.450-1510µm. Signal mode size was calculated as a function of position in the cavity using the standard ABCD matrix formulisation (figure 6.3):

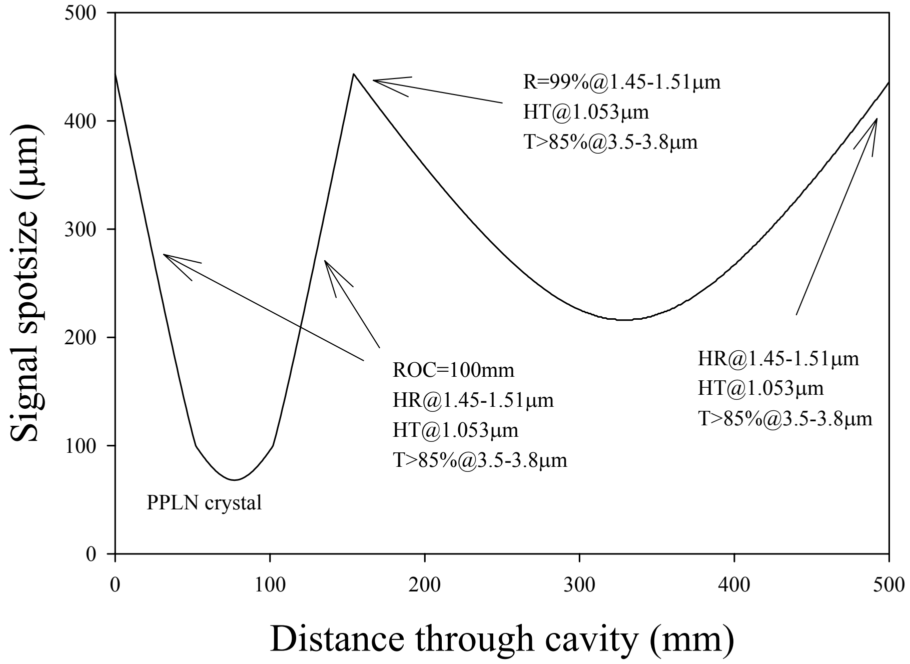

Figure 6.3 Graph showing signal spot size as a function of cavity length for the four mirror cw OPO cavity with 1% output coupler.

The pump focus within the PPLN was measure to be ~85µm radius, with a signal spot size within the PPLN of ~80µm this provided excellent mode overlap within the gain region of the crystal. The influence of the output coupler on the threshold of the device was calculated to be ~4.4W, an increase of 1.4W from the 3W threshold of the equivalent HR cavity in chapter 5. This suggested that the intra cavity loss due to the PPLN was of the order of ~2%.

Once the OPO was optimised for cw operation, the output signal power was measured as a function of incident pump power giving us a direct measurement of threshold and conversion efficiency (figure 6.4):

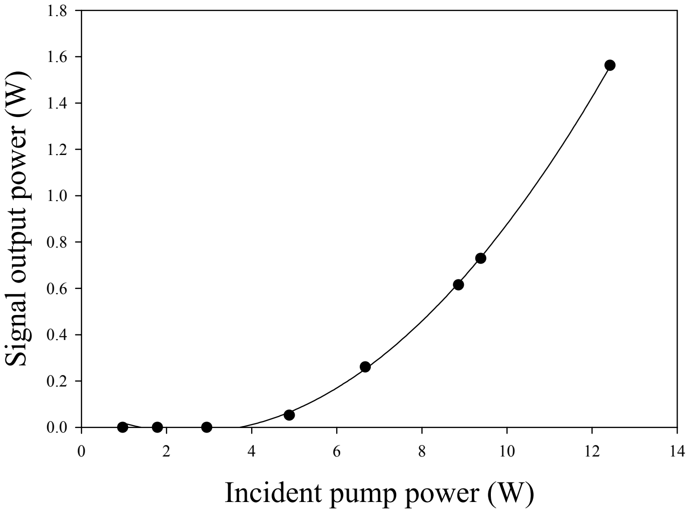

Figure 6.4 Graph showing output signal power as a function incident pump power for the four-mirror cw OPO with 1% output coupling.

The graph in figure 6.4 shows a threshold of ~4.0W, a result in good agreement with the threshold value calculated from theory of 4.4W. The spectral output from the OPO, measure with a plane-plane Fabry-Perot interferometer displayed rapid mode hopping of the fundamental frequency (see figure 6.5) due to the unstable maintenance of the PPLN crystal temperature over time (±0.5^{0}C):

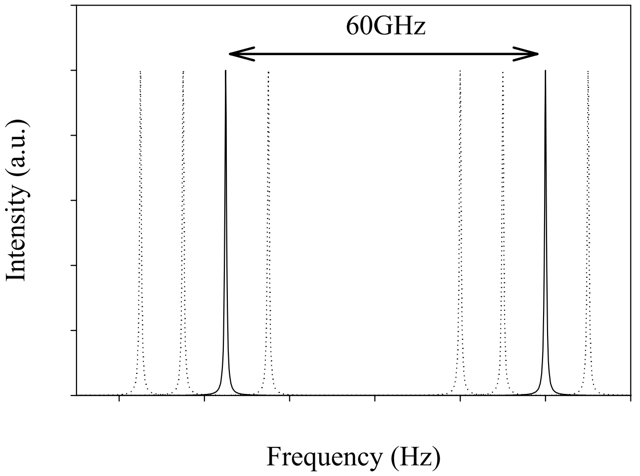

Figure 6.5 Graph showing Fabry-Perot scan of signal output from the OPO over a short period of time. Solid line indicates single-frequency operation of OPO, however, dashed lines indicated mode-hopping due to temperature fluctuations.

Figure 6.5 shows a typical Fabry-Perot scan confirming the OPO is operating single-frequency (single trigger trace on the Fabry-Perot), however the mode-hopping is very frequent (<1s) hence limiting the applicability of the SRO. The next stage of the project therefore was to incorporate a 15mm long LBO crystal into the cavity in order to try our passive technique for mode hop suppression.

6.2.2 Four mirror cw OPO with mode-hopping suppression

The nonlinear crystal was a 15mm long Brewster-cut LBO crystal, type 1 phase-matched to the signal wavelength at 1.468μm. This corresponded to a phase-matching temperature of ~56^{0}C. The nonlinear crystal was placed in the cavity between the two plane mirrors as can be seen in figure 6.6:

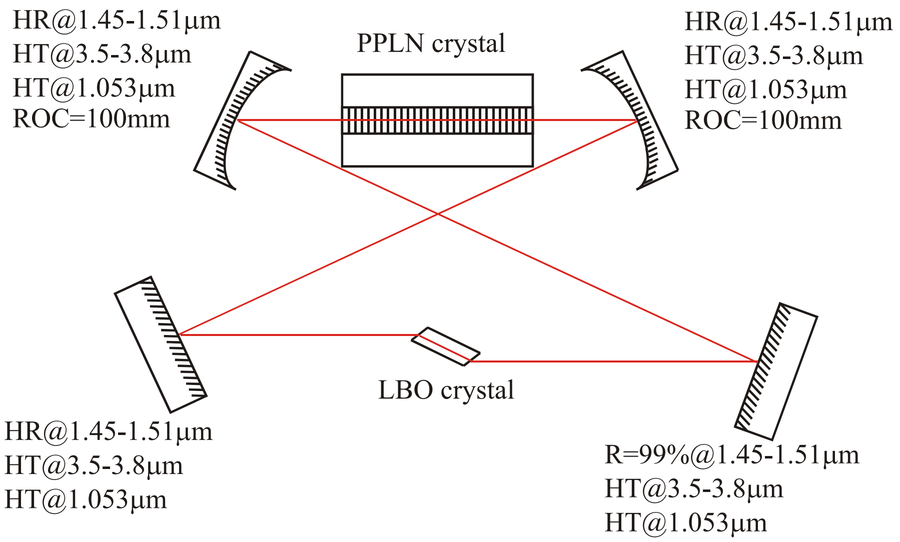

Figure 6.6 Diagram showing the four-mirror cw OPO cavity including LBO crystal for passive mode-hopping-suppression.

The cavity configuration was similar to that of the previous experiment with the inclusion of the LBO crystal. The signal spot size was again calculated as a function of position using ABCD matrices (see figure 6.7):

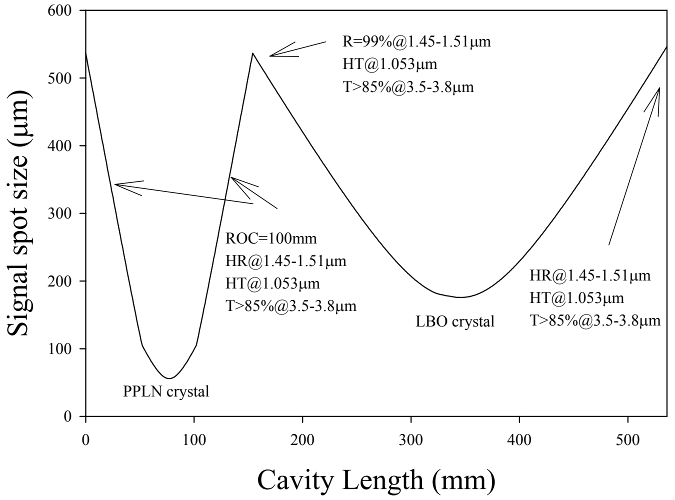

Figure 6.7 Graph showing signal spot size as a function of cavity length for the four-mirror cw OPO including LBO crystal.

Figure 6.7 shows that the overall cavity length of the OPO cavity has increased by 36mm by incorporating the LBO crystal. The insertion loss of the crystal was estimated to be around 0.1% (based on previous experience with the Nd:YLF master-oscillator) and the signal spot size was 85μm within the PPLN, meaning we maintained effective mode overlap with the pump light, while the threshold of the device was calculated to have risen to ~4.6W. The signal output power was measured as a function of incident pump power (figure 6.8):

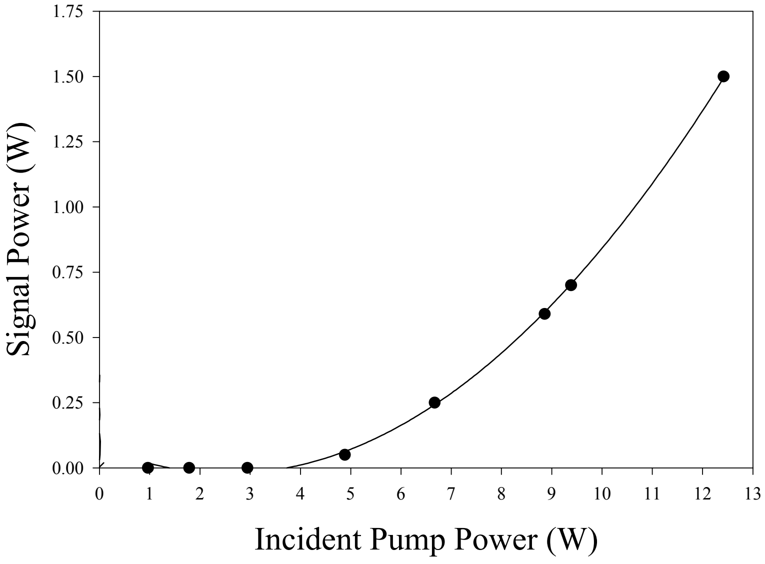

Figure 6.8 Graph showing signal output power as a function of incident pump power for the four-mirror cw OPO cavity incorporating an LBO crystal.

The intracavity signal power based on an output coupling of 1% was then calculated from these results in order to use equation 5.26 from Chapter 5 to calculate the second harmonic conversion efficiency of the four-mirror SRO. The intracavity power as a function of incident pump power can be seen in figure 6.9:

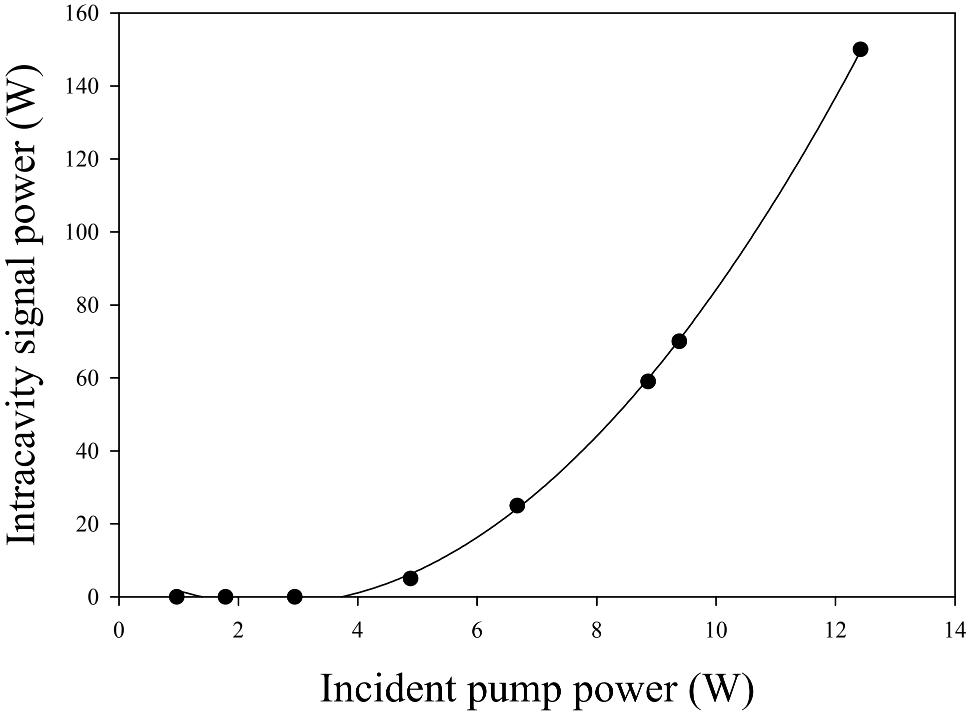

Figure 6.9 Intracavity signal power for the four-mirror SRO with 1% output coupler as a function of incident pump power.

The overall signal output power dropped due to the extracavity losses and due to a few milliwatts of second harmonic generation of the signal wavelength from 1.468μm to 734nm.

Figure 6.10 shows the effective calculated second harmonic conversion efficiency of the intracavity signal power in the LBO for a signal waist of 200μm within the crystal as a function of intracavity signal power.

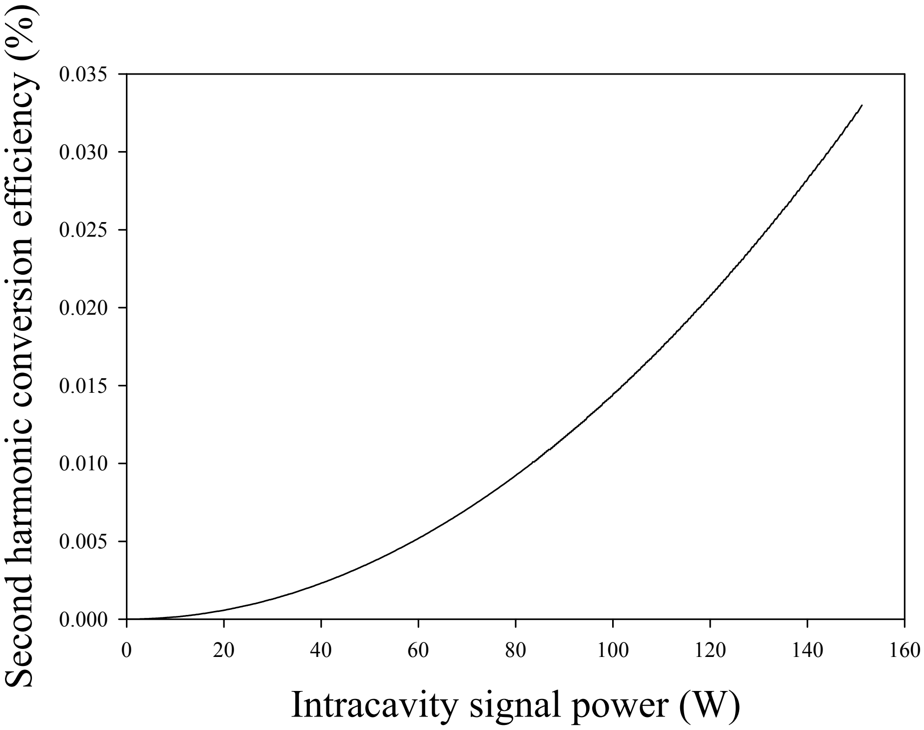

Figure 6.10 Graph showing the second harmonic conversion efficiency of the intracavity signal power for the four-mirror OPO cavity with intracavity LBO.

Using the values for the second harmonic conversion efficiency we can then calculate, using equation 5.19 [2], the maximum mode hop free tuning range for this cavity configuration, the results of which can be seen in figure 6.11:

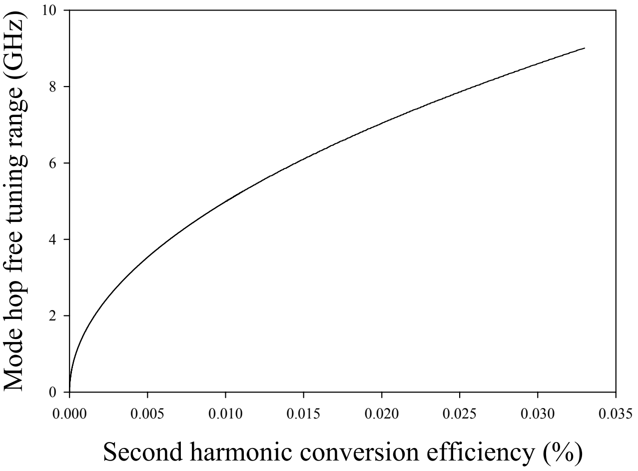

Figure 6.11 Graph showing the mode hop free tuning range of the OPO as a function of second harmonic conversion efficiency of the signal intracavity power.

It can been seen in figure 6.11 that the maximum achievable mode hop free tuning range of the OPO was ~8GHz corresponding to ~20 axial mode spacings under the parametric gain curve. Since the oven keeping the PPLN at a temperature of 195^0C was estimated to be accurate to only ±0.5^0C over the length of the crystal corresponding to the gain bandwidth moving over 60 axial mode spacings, the OPO still suffered from mode-hopping.

In figure 5.14 (Chapter 5) we calculated that for temperature instabilities of as little as ±0.5^0C around the operating temperature of the OPO the gain line centre can move ~40GHz (in comparison with the FWHM of the gain peak of 200GHz for a 50mm PPLN crystal, this corresponds to ~20% of its overall width). Therefore in order to achieve mode hopping suppression within the four-mirror ring OPO the temperature of the PPLN needed to be stabilised to within ~±0.1^0C corresponding to a gain peak movement of ~8GHz, at which point we should have seen the effects of mode hop suppression. However, the difficulties in stabilising the temperature of the PPLN to within this accuracy would have caused many complications to the OPO cavity in terms of thermal isolation and expensive electronic design.

It was therefore decided that more careful cavity design was required, not only allowing us control of the signal spot size within the PPLN in order to keep the threshold of the device as low as possible, but also to allow us control over the signal spot size within the LBO, in order to increase second harmonic conversion efficiency and hence increase the mode hop free tuning range.

6.3 Six-mirror cw OPO cavity

The six-mirror cavity design enabled us to optimise the signal waist position and size both within the PPLN crystal and the LBO crystal in order to reduce threshold and increase the mode hop free tuning range of the device. Figure 6.12 shows the cavity configuration for the six mirror OPO, initially without the LBO crystal in order to reduce alignment complexities in the initial stages of the experiment.

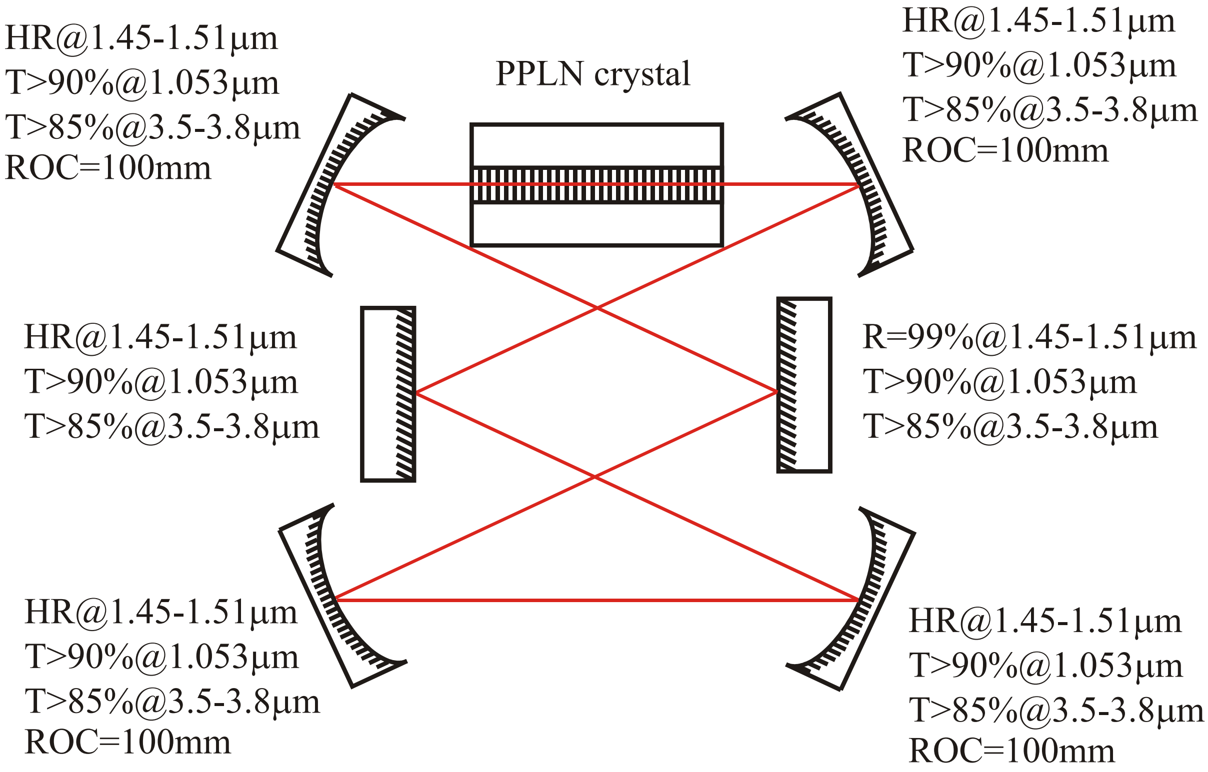

Figure 6.12 Diagram showing the six-mirror OPO ring cavity configuration.

The alignment of the cavity was again carried out under pulsed conditions, optimising for pump pulse depletion. The pump pulses were then increased in length until the OPO was operating in a practically cw regime. Once this alignment was optimise the pump laser was switched to cw and the OPO was closely aligned for maximum cw signal output power.

Signal mode size was calculated as a function of position in the cavity using the standard ABCD matrix formulisation (figure 6.13):

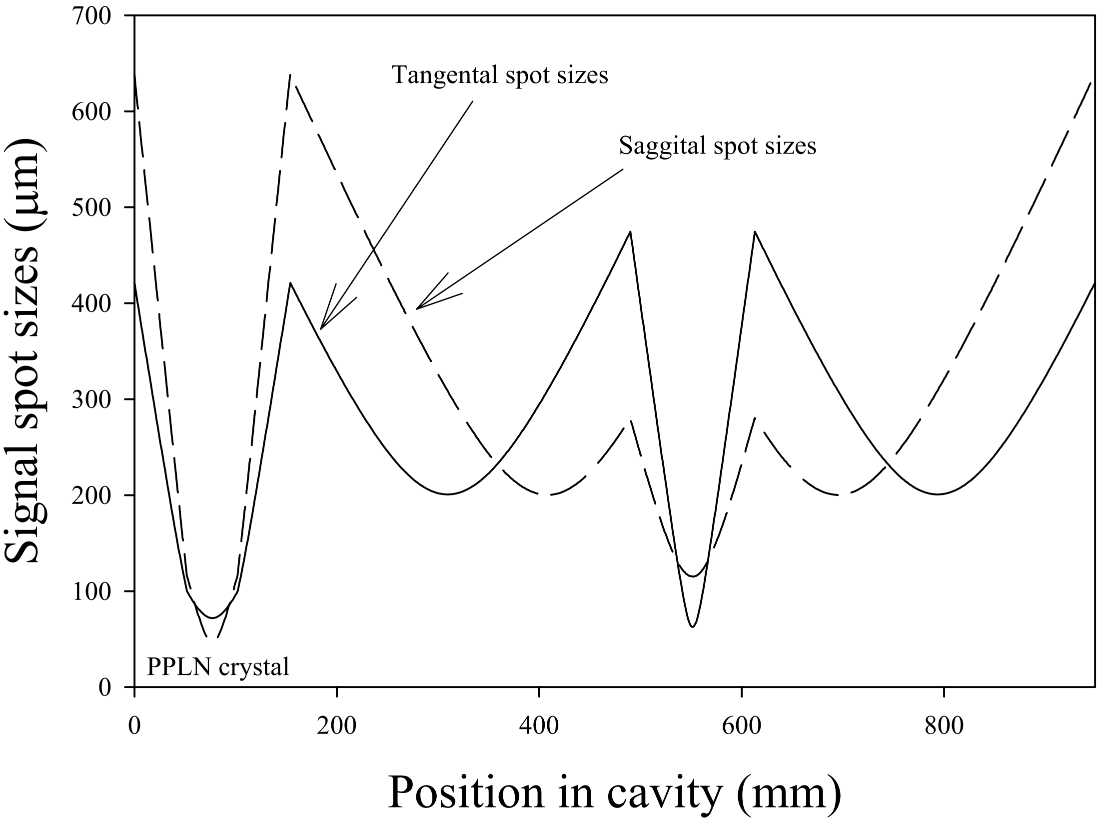

Figure 6.13 Graph showing the signal spot size as a function of cavity length in the saggital and tangential planes of the six-mirror OPO cavity.

Figure 6.13 shows the signal spot sizes for the tangential and saggital planes of the six-mirror cavity. In this instance now we have a waist size of ~80×50µm (in the tangential and saggital planes respectively) in the PPLN crystal and potentially waist size of ~60×100µm in the LBO crystal. The good mode overlap within the PPLN reduced the threshold down to ~3W of incident pump power; however, it can be seen from figure 6.13 that at the output coupler, the beam was very elliptical, to a much greater effect than in the PPLN and LBO positions with dimensions of ~300×500µm. The signal output power in the cw regime was measure as function of incident pump power, the results of which can be seen in figure 6.14:

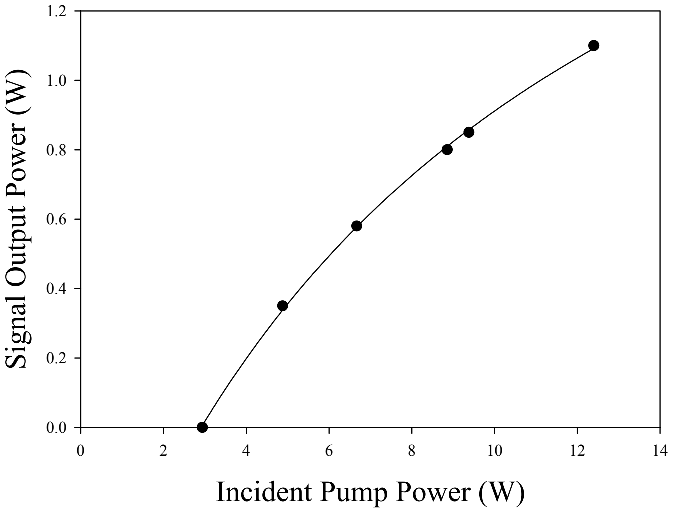

Figure 6.14 Graph showing signal output power as a function of incident pump power for the six-mirror cw OPO cavity without the LBO crystal.

Figure 6.14 shows that the threshold of the device was again in good agreement with the value calculated from theory. The lower output powers at the signal wavelength were attributed to the increased overall cavity losses incurred by the inclusion of more mirrors and an increased difficulty of alignment leading to possible slight misalignment of the signal to the parametric gain region within the PPLN crystal.

The next stage of the research was to incorporate the nonlinear LBO into the cavity as can be seen in figure 6.15:

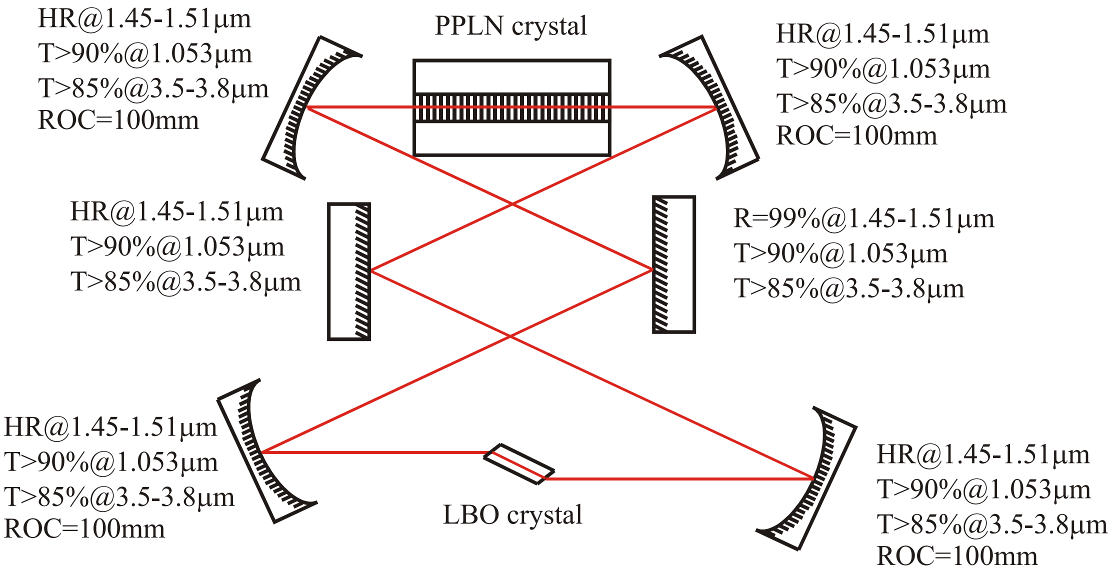

Figure 6.15 Diagram showing the six-mirror OPO cavity with the inclusion of the LBO nonlinear crystal.

Using ABCD matrices, the signal spot size throughout the cavity length could be calculated, the results of which are displayed in figure 6.16:

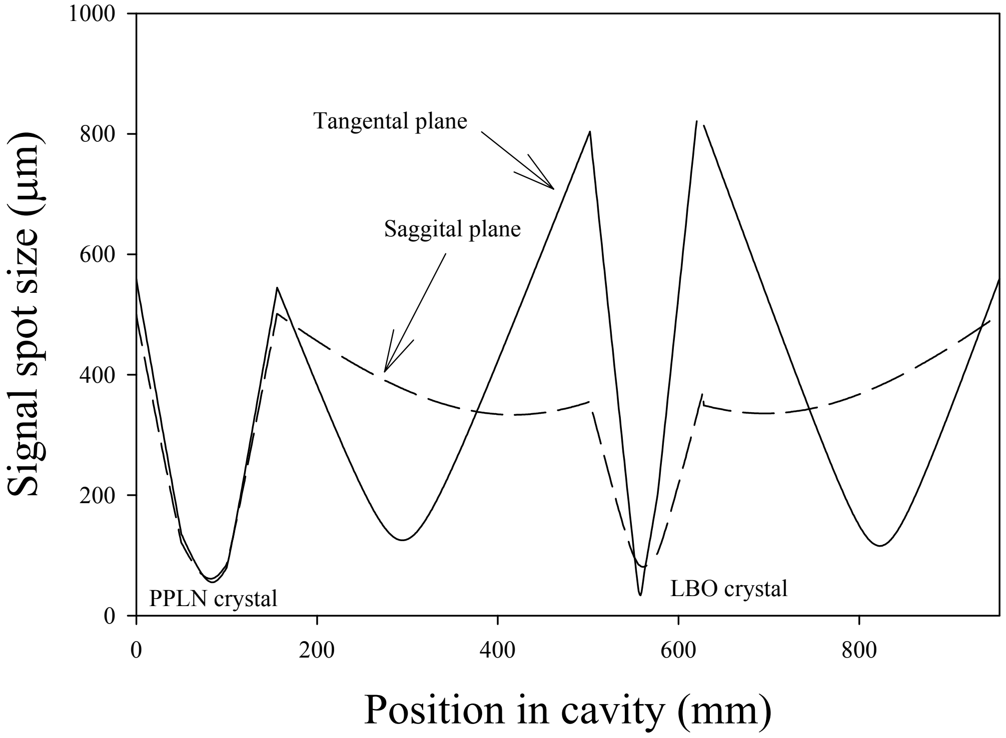

Figure 6.16 Graph showing the signal spot size as a function of cavity length for the six-mirror OPO with intracavity nonlinear crystal for the tangential and saggital planes.

Figure 6.16 shows again that the signal beam in the saggital and tangential planes was very astigmatic at the output coupler, however the astigmatism in the PPLN crystal and LBO crystals was compensated for via careful cavity design. The cavity arrangement was again set-up for output coupling the signal frequency with a small nonlinear loss that would allow mode hop suppression over a certain range.

Pulsed operation was achieved after insertion of LBO into the six mirror cavity, however before cw operation via further cavity alignment could be achieved, catastrophic failure of two of the MOPA diode-bar pump sources meant that that the maximum achievable output power from the MOPA was only ~8.5W cw. Although we still managed to achieve operation of the six-mirror cavity with the LBO incorporated into the design, the added nonlinear loss to the fundamental frequency and the added insertion loss due to the LBO within the cavity meant that it was impossible to achieve robust and reliable cw operation of the OPO and therefore only theoretical analysis of the OPO operation was possible.

The six-mirror OPO incorporating the LBO crystal operated with a cw threshold calculated to be ~4.5W. The theoretical graph of the intracavity signal power as a function of incident pump power can be seen in figure 6.17:

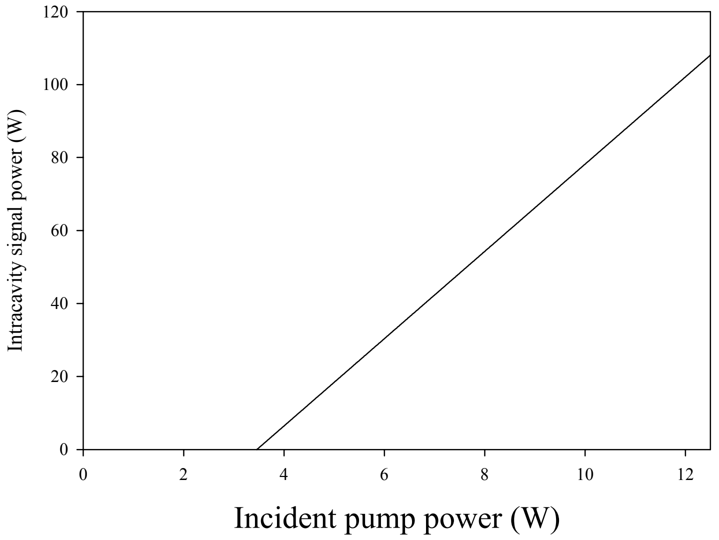

Figure 6.17 Graph showing the theoretical intracavity signal power as a function of incident pump power for the six-mirror OPO incorporating LBO crystal.

The conversion efficiency of the intracavity signal power could now be calculated, assuming a 30µm signal spot size within the LBO crystal, the results of which can be seen in figure 6.18:

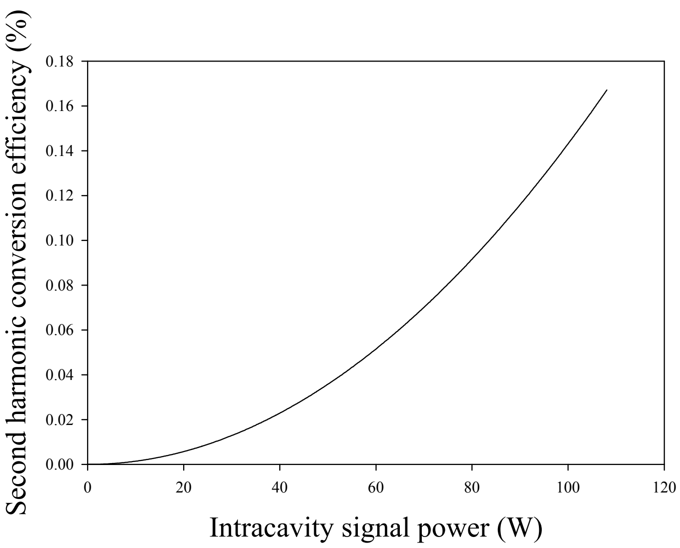

Figure 6.18 Graph showing the theoretical conversion of efficiency of the signal to its second harmonic as a function of intra cavity signal power within the six-mirror OPO.

From the theoretical results in figure 6.18, we can therefore show the potential mode-hop free tuning range of the OPO as a function of second-harmonic conversion efficiency in figure 6.19:

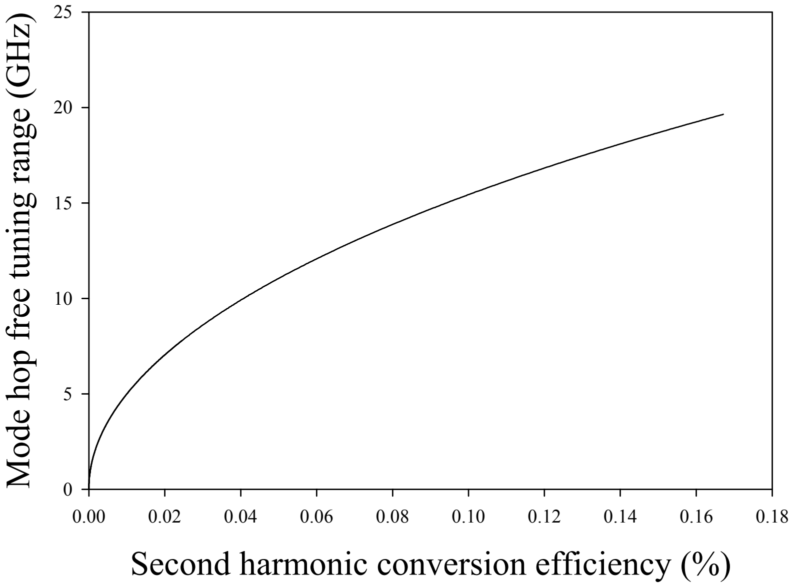

Figure 6.19 Graph showing theoretical mode hop free tuning range as a function of the signal second harmonic conversion efficiency.

From figure 6.19 we can see that the maximum mode hop free tuning range of the six-mirror OPO would have been ~20GHz (~45 axial mode spacings). This would have corresponded to temperature fluctuations of $\pm 0.2^0$C, a result that would have still led to detrimental mode hopping of the OPO signal output due to the inherent temperature fluctuations of the PPLN oven, making the parametric gain cure travel over 40GHz. Therefore only by stabilising the PPLN temperature to better than $\pm 0.2^0$C would we have seen a beneficial effect from our passive technique for mode-hopping-suppression.

6.4 Discussion and conclusion

During the course of this experimental chapter we have demonstrated the operation of various cw singly-resonant OPO configurations based on periodically-poled lithium niobate. Via careful cavity design and alignment procedures, we have reduced the threshold of these devices to levels of power available from the output power provided by the Nd:YLF MOPA, to achieve signal output powers >1W. Although these signal output powers could be used for numerous applications, the output could not be used for any application reliant on reliable and robust single-frequency operation due to mode-hopping. In order to combat this detrimental effect we intended to employ our passive technique for mode-hopping-suppression whereby the inclusion of a nonlinear crystal into the cavity for intracavity second harmonic generation at the signal wavelength, would effectively allow the fundamental frequency to tune of multiple axial mode spacing before a mode hop occurred.

However, it became apparent during the course of the experiments that nomatter how much second harmonic conversion efficiency of the fundamental signal frequency could be achieved, the sensitivity of the OPO to mode-hopping due to temperature fluctuations within the PPLN would always overcome the effects of the nonlinear crystal. Since the second harmonic conversion efficiency of the signal wavelength was directly related to the intracavity power of the OPO at this wavelength, two approaches could be considered in the future to increase the effectiveness of this technique. Firstly, the output power from the Nd:YLF MOPA could be increased to a level (>100W say by the inclusion of a further power amplifier) so that higher amounts of second harmonic conversion efficiency would be achieved leading to mode-hopping-suppression. Secondly, and by far easier, would be to use a crystal with a higher effective nonlinear coefficient, such as another wafer of lithium niobate periodically poled with a grating designed for second harmonic conversion at the signal wavelength. Using this second approach with a six-mirror OPO cavity and assuming that the rest of the parameters stay the same, a 15mm PPLN crystal phase-matched for second harmonic conversion of the signal would allow the following tuning curve (figure 6.20):

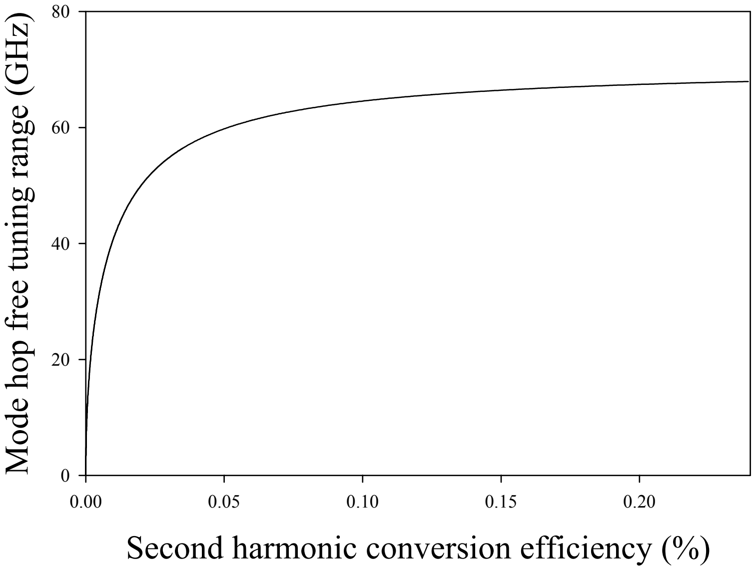

Figure 6.20 Graph showing the theoretical mode hop free tuning curve for the six-mirror OPO with the inclusion of a 15mm long sample of PPLN poled to generate the second harmonic of the signal wavelength.

Figure 6.20 shows the effect of the utilisation of PPLN (d_{eff}=14pm/V) as the second harmonic generating crystal as oppose of LBO (deff=0.7pm/V). Using PPLN as the second nonlinear crystal means that even for the same small amounts of signal generated within the OPO the temperature of the crystal needs only to be stabilised to within ±0.8^{0}C, this was considered achievable with the technology currently in use to maintain the temperature of the PPLN oven at 195^{0}C. With this, if the output power from the MOPA were to be increased via the another amplifier stage, then mode hop suppression of a considerable portion of the OPO gain curve should be easily obtainable, allowing the fundamental frequency to be manually tuned via the alteration of the cavity length or alternatively, without cavity length adjustment, the SRO should operate on a single-longitudinal mode without mode-hopping for long periods of time without active stabilisation.

6.5 References

1. Turnbull, G.A., *Extended mode-hop-free tuning by use of a dual-cavity, pump- enhanced optical parametric oscillator.* Optics Letters, 2000. **25**(5): p. 341-343.
2. Martin, PhD *High power diode pumped single frequency lasers*, in *Optoelectronics Research Centre*. 1996, University of Southampton.

Chapter 7: Conclusions and future work

7.1 Introduction and thesis summary

The work that has taken place during the course of this research has essentially brought together the advantages of numerous technologies in order to design and build a laser system that overcomes the detrimental effects normally associated with power scaling and goes onto to try to utilise the same technology within an optical parametric oscillator. In chapter 1 we outlined the purposes of the research and regarding the current understanding of diode-end-pumped solid-state lasers, aimed to produce a strategy for the rest of the thesis that not only would give the reader a fundamental understanding of the problems associated with the power scaling of DPSSLs would also enable the reader to eventually overcome them.

Chapter 2 outlined a description of a diode-end-pumped solid-state laser in terms of threshold and slope efficiency. Techniques for maintaining single-frequency operation of a laser were described and suitable pump sources and pump delivery schemes were also mentioned in reasonable detail. The common problems of thermally induced stress birefringence, thermal lensing and ultimately thermal stress fracture within commonly used laser materials were then described and their effects on the power scaling limitations of solid-state lasers were also talked about.

Chapter 3 then took our fundamental knowledge further still by describing Nd:YLF in terms of its thermal and spectral properties. The reasons for our design strategy employing Nd:YLF were described outlining the effects of energy-transfer up-conversion and the specific thermal lensing properties that make Nd:YLF and unlikely but wise choice for scaling the output power of a 1μm laser source. The effects of mode hopping were overcome via the use of a passive effect of intra cavity second harmonic generation allowing us to tune the fundamental frequency of the laser over 14 axial mode spacings or alternatively allow the laser to operate mode-hop free for very long periods of time. A design strategy was then described for a single-frequency ring oscillator employing mode-hop-suppression to produce a Nd:YLF oscillator with up to 4.5W of diffraction limited single-frequency output.

In order to de-couple the maintenance of single-frequency operation from scaling the output power of the Nd:YLF oscillator a series of amplifier stages were constructed. Chapter 4 outlined the construction of these devices, describing the effects of ETU on the small signal gain and of thermal lensing on the power scaling limitations. The results from these experiments demonstrated an Nd:YLF master oscillator power-amplifier capable of producing up to 20W of single-frequency output power in a diffraction limited beam with plenty of scope for further power scaling in the future simply via the addition of further amplifier stages.

In Chapter 5 we used the concept of nonlinear frequency conversion in order to extend the tuning range of the Nd:YLF MOPA. The basics of optical parametric generation and oscillation are outline including expressions for threshold and the basic concepts of quasi-phase-matching. The end goal of this chapter was however, to outline the possibility of us being able to employ our passive technique for mode-hopping-suppression within a cw singly-resonant OPO. Chapter 5 also includes a description of cw OPO alignment and operation.

Chapter 6 presents our current results regarding cw single-frequency OPO design and operation. Although numerous cw OPO configurations were constructed, mode-hop-suppression failed to occur due a catastrophic failure of the pump sources for the Nd:YLF MOPA pump source. On analysis of the results however it became apparent that due to thermal fluctuations with the OPO PPLN oven, and due a lack of second harmonic conversion efficiency within the OPO LBO crystal, mode hopping suppression would have failed to occur.

The rest of this chapter therefore will highlight possible improvements for the future that should realise the full potential of Nd:YLF as an easily scaleable solid-state laser material and an increased single-frequency tuning range due to mode-hop-free operation of cw OPOs.

7.2 Nd:YLF master oscillator

Even over the short amount of time this research took to complete, yet further developments of diode pump sources took place via the creation of diode stack devices, whereby, numerous diode-bars were stacked together allowing devices with cw output powers of >2kW available at common pump wavelengths such as 808nm (Nd:YAG). Although the beam quality degradation of these devices scales with their increasing pump power, there has been no doubt that the employment of the two mirror beam shaping scheme would allow us to again equalise the beam quality of such a device to $M^2<200$ in both planes meaning that we have the potential of increasing the incident pump power onto a device by an order of magnitude. Although as far as the master oscillator is concerned, the thermal stress fracture limit of the Nd:YLF rods could only take a fraction of this potential pump power, by upgrading the oscillators pump source to say 40W of incident light (by fibre coupling a 60W device), we should easily be able to scale the output from the master to ~10W leaving greater potential for the amplification process. By increasing the length of the laser rod to 18mm and lowering the dopant concentration to 0.3% we can reduce thermal loading per unit volume thereby negating issues such as thermal lensing and thermal stress facture. Also, by lowering the dopant concentration within the laser rod, the associated effects of ETU within the master oscillator should also be reduced.

By increasing the intra cavity signal power within the master oscillator, we will generate higher amounts of the fundamental frequencies second harmonic, again further extending the mode-hop-free tuning range and therefore making the laser yet more unsusceptible to mode-hopping for longer periods of time at high powers.

This should mean that simply by scaling the incident pump power of the master oscillator, we should be easily able to scale the power to >10W cw single-frequency output without compromising the diffraction limited beam quality or the robust and reliable spectral stability of the output.

7.3 Nd:YLF master oscillator power amplifier

As mentioned in the previous section, the maximum available pump power from a commercially available, single device over the course of the last year has increased by an order of magnitude. To this end the potential for a large stage power amplifier capable of scaling the output power for the master oscillator to >100W of single-frequency, diffraction limited output has increased dramatically. Although it could be possible to use longer laser rods with a lower dopant concentration within a new power amplifier, with pump power provided via a diode stack, a simpler and possibly more attractive route maybe to utilise fibre technology. A fibre amplifier would have better thermal management (since in the past devices have merely been positioned on top of an optical table and required no more further heatsinking) and would also allow for a more compact design of the overall system.

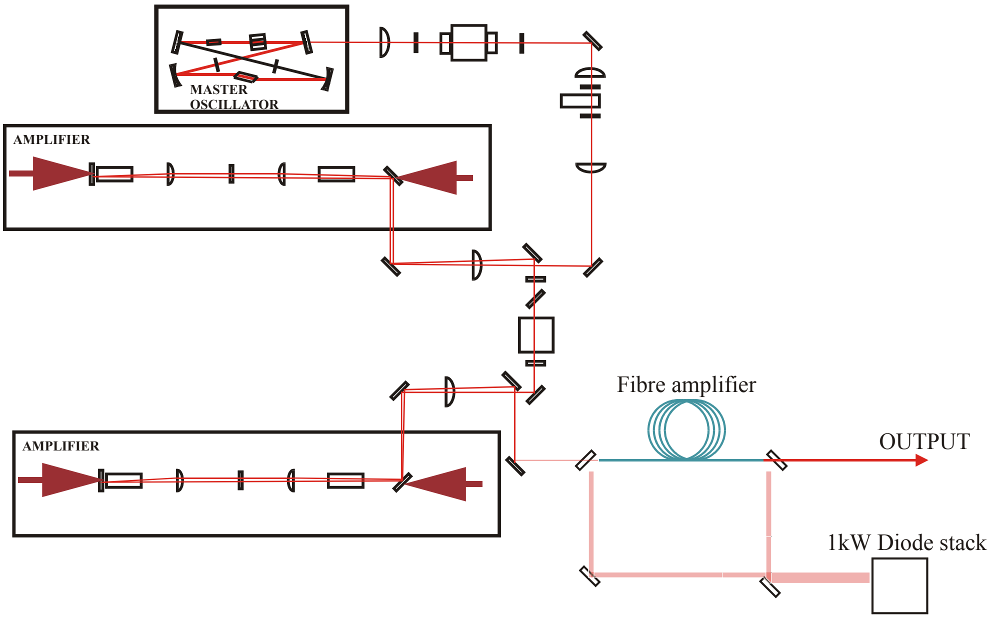

Figure 7.1 Diagram showing one possible implimentaion of a further fibre amplifier stage pumped by a diode stack.

Figure 7.1 demonstrates one possible power amplifier configuration. Without going into any detail, a fibre amplifier stage should enable the output from the master oscillator to be scaled up to 100W, however this may be at the at the expense of the output beam quality.

7.4 cw single-frequency OPOs and mode-hop-suppression

In order to fully realize the overall potential of any laser system, nonlinear frequency conversion will extend the range of output wavelengths over a vast distance. Whether the MOPA is frequency doubled to 526.5nm and then used to pump an OPO to produce tunable signal wavelength around 1μm, or to directly pump an OPO to produce signal wavelengths further into the infra red region of the electromagnetic spectrum, the usefulness of such a laser for applications such as LIDAR and spectroscopy seems endless. We have discussed the concept of phase-matching and hence quasi phase-matching within a nonlinear medium for the purposes of optical parametric generation and oscillation in a cw regime. The principle usages of cw single-frequency OPOS e.g. spectroscopic applications and LIDAR require very spectrally stable outputs, and although cw OPOs are inherently single-frequency by nature, the output from these devices suffers detrimentally from mode-hopping, not only due to temperature fluctuations and pressure changes applied to the cavity and thermal expansion of the PPLN but in the majority due to the movement of the phase-matched gain curve as a function of temperature. Therefore, although phase-matching can now be readily achieved in nonlinear materials and with the advent of new technologies, the cw singly-resonant threshold of such OPO devices can be lowered to a point whereby they can be operated in a cw regime without the need for added cavity complexity via pump enhancement or doubly-resonant cavity designs, they still suffer from mode-hopping so detrimentally that the output from these devices cannot be used for their intended applications. In order to provide robust and reliable single-frequency output expensive and costly cavity additions have been made in some cases, locking the cavity of the OPO to a reference or even extending the mode-hop free tuning range, however we suggest a different approach: By including a second harmonic generating crystal within the OPO cavity mode-hop suppression could occur, proportional in range to the nonlinear second harmonic generation of the fundamental signal mode, allowing the OPO to operate single-frequency both robustly and reliably.

Initial results collected during the course of the research, after observations made of numerous OPO cavity configurations, confirmed the theoretical modeling made of the OPO wavelength-temperature tuning characteristics via observation of the idler wavelengths. Increased cavity loss via inclusion of output coupler allowed close observation of signal mode hopping at expense of higher threshold powers required for oscillation.

Although cw singly-resonant oscillations were demonstrated for various cavity configurations with OPO thresholds as low as 1W, the single-frequency nature of the signal wavelengths were detrimentally affected by mode-hopping due to temperature fluctuations within the PPLN crystal. In order to combat this detrimental effect we intended to employ our passive technique for mode-hopping-suppression whereby the inclusion of a nonlinear crystal into the cavity would effectively allow the fundamental frequency to tune of multiple axial mode spacing before a mode hop occurred.

During the course of applying our passive technique for mode-hopping-suppression however, it became apparent that the amount of second harmonic conversion within the OPO cavity would fail to overcome the sensitivity of the OPO to mode-hopping due to temperature fluctuations. Two approaches to this problem could be immediately suggested based on the reasoning that since the second harmonic conversion efficiency of the signal wavelength was directly related to the intra cavity power of the OPO at this wavelength, two solutions could be considered in the future to increase the effectiveness of this technique: Firstly, the output power from the Nd:YLF MOPA could be increased to level (>100W say by the inclusion of a further power amplifier) so that greater amounts of second harmonic generation lead to successful mode-hopping-suppression. However, by increasing the output power from the laser, we will probably start to experience thermally related problems, similar to those experienced in the power-scaling of a laser, such as thermally induced stress birefringence, thermal lensing within the PPLN crystal and in the case of the OPO increased chance of photorefractive damage due to increased generation of high energy visible wavelengths.

Secondly, and by far easier, would be to use a crystal with a higher effective nonlinear coefficient, such as another wafer of lithium niobate periodically poled with a grating designed for second harmonic conversion of the signal wavelength.

Using this second condition of as a working example for the six mirror OPO cavity and assuming that the rest of the parameters within the cavity stay the same, a 15mm PPLN crystal phase-matched for second harmonic conversion of the signal would allow the following tuning curve (figure 7.2) as taken from the model in Chapter 6:

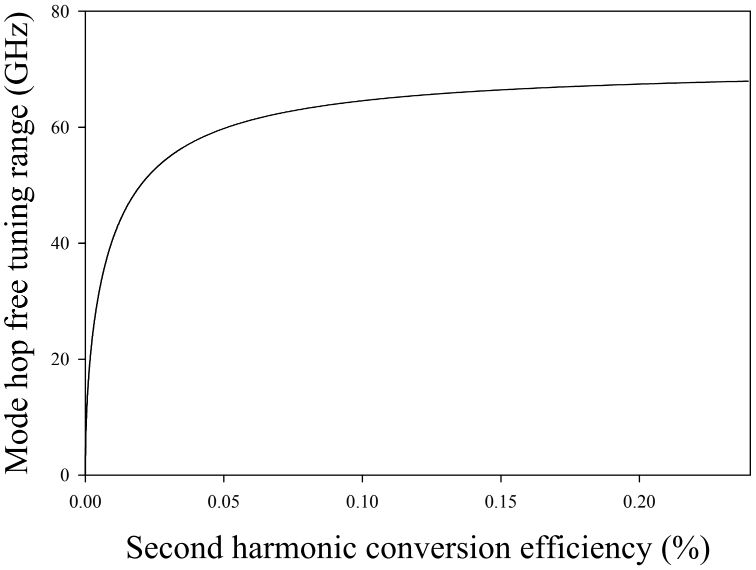

Figure 7.2 Graph showing the theorectical mode hop free tuning curve for the six mirror OPO with the inclusion of a 15mm long sample of PPLN poled to generate the second harmonic of the signal wavelength.

Figure 7.2 shows the effect of the utilisation of PPLN (d_{eff}=14pm/V) as the second harmonic generating crystal as oppose of LBO (deff=0.7pm/V). Using PPLN as the second nonlinear crystal means that even for the same small amounts of signal generated within the OPO the temperature of the crystal needs only to be stabilised to within $\pm 0.8^0$C, a feet easily achievable with simple electronics coupled with a suitably thermally isolated PPLN oven at held at 195^0C. With this, if the output power from the MOPA were to be increased via the another amplifier stage, then mode hop suppression of a considerable portion of the OPO gain curve should be easily obtainable meaning that the fundamental frequency could be manually tuned via the alteration of the cavity length or that the fundamental frequency would remain mode hop free for very long periods of time.

7.5 Summary

The main objective of the work described in this thesis has been the efficient generation of high output power lasers in both the single transverse and longitudinal modes. Using our current understanding of the laser material Nd:YLF we have been able to construct such a source which exhibits relative freedom from the thermal problems usually associated with power scaling diode-end-pumped solid-state lasers allowing us to generate up to 4.5W of single-frequency diffraction-limited output. We have also used the novel phenomenon of mode hop suppression, whereby the nonlinear loss from sum frequency generation provided by an intra cavity frequency doubling crystal can suppress the oscillation of non-lasing modes within the cavity, allowing the laser to be tuned smoothly over many mode spacings, or alternatively, allowing the laser to operate mode hop free for very long periods of time.

The output for the small master oscillator operating on the 1053nm line was then amplified via two amplifier stages to powers around 20W, whilst maintaining the diffraction limited beam quality of the 4.5W signal. The relatively small thermal lens was due to the small negative change in refractive index with temperature on the 1053nm line in Nd:YLF being off-set by the small positive thermal lens generated by the bulging end-faces of the crystal with increasing temperature. The net effect of this was to produce a very weak positive thermal lens that allowed power scaling to high powers without degradation to output beam quality.

In order to increase the output wavelength range of the Nd:YLF MOPA system we successfully demonstrated the operation of numerous cw OPO configurations, generating signal and idler pairs of 1.468μm and 3.275μm respectively. Due to the sensitivity of mode hopping within singly-resonant OPOs, we attempted to employ our passive technique for mode hop suppression by incorporating a nonlinear loss within the cavity. Due to the low intracavity powers of the signal within the OPO and the relatively low nonlinear coefficient of the LBO crystal used, we failed to generate a mode hop suppression range that would overcome the temperature fluctuations of the PPLN oven used. Further analysis of the theory provided us wit the necessary information to employ mode hop suppression within a cw OPO in the future.

Appendices

Appendix 1 Publications and submitted papers

W.A.Clarkson, V.Matera, T.M.J.Kendall, D.C.Hanna, J.Nilsson, P.W.Turner
High-power wavelength-combined cladding-pumped Tm-doped silica fibre lasers
CLEO/QELS 2001 Baltimore 6-11 May 2001 CWM2

T.M.J.Kendall, W.A.Clarkson, P.J.Hardman, D.C.Hanna
Single-frequency Nd:YLF master-oscillator power amplifier with 15W output at 1053nm
QEP-15 Glasgow 3-6 Sep 2001 pp.95

W.A.Clarkson, V.Matera, A.Abdolvand, T.M.J.Kendall, D.C.Hanna, J.Nilsson, P.W.Turner
Spectral beam combining of cladding-pumped Tm-doped fibre lasers
QEP-15 Glasgow 3-6 Sep 2001 pp.13

T.M.J.Kendall, W.A.Clarkson, P.J.Hardman, D.C.Hanna
Efficient Nd:YLF master-oscillator-power-amplifier with 15W single-frequency output at 1053nm
CLEO/Europe-EQEC Munich 18-22 Jun 2001 pp.57

W.A.Clarkson, V.Matera, A.Abdolvand, T.M.J.Kendall, D.C.Hanna, J.Nilsson, P.W.Turner
Power scaling of cladding-pumped Tm-doped silica fibre lasers
CLEO/Europe-EQEC Munich 18-22 Jun 2001 pp.141

T.M.J.Kendall, W.A.Clarkson, P.J.Hardman, D.C.Hanna
High-power Nd:YLF master oscillator power amplifier with 15W single-requency output at 1053nm
CLEO 2001 Baltimore 6-11 May 2001 CTh11

T.M.J.Kendall, W.A.Clarkson, P.J.Hardman, G.W.Ross, D.C.Hanna
Multiline optical parametric oscillators based on periodically-poled lithium niobate
CLEO 2000 San Francisco 7-12 May 2000 CMC7

T.M.J.Kendall, W.A.Clarkson, P.J.Hardman, G.W.Ross, D.C.Hanna
Simultaneous multiple line optical parametric oscillators based on periodically-poled lithium niobate
QE14 Manchester 6-9 Sep 1999 Paper 2-5 pp.41

Journal papers will follow shortly concerning development and results from the Nd:YLF MOPA system with a view to continuing research into SRO mode-hopping-suppression.

Appendix 2 Effect of energy transfer upconversion on diode-end-pumped solid-state laser threshold

The following derivation will modify the analysis of Kubodera and Otsuka and Clarkson *et al* to include terms for ETU in the calculation of diode-end-pumped solid-state laser.

The rate equation of the excited state population can be given by:

$$\frac{dn(x,y,z,t)}{dt}=r(x,y,z,t)-c_n\sigma s(x,y,z,t)n(x,y,z,t)-\frac{n(x,y,z,t)}{\tau_f}-Wn^2(x,y,z,t) \quad (7.1)$$

where σ is the stimulated emission cross-section. The rate equation of the total number of photons in the laser cavity mode can therefore be expressed as:

$$\frac{dS}{dt}=\int_{Cavity} c_n\sigma n(x,y,z,t)s(x,y,z,t)dV-\gamma S(t)$$

where (7.2)

$$S(t)=\int_{Cavity} s(x,y,z,t)dV$$

n(x,y,z,t) is the population inversion density, *r(x,y,z,t)* is the pump-rate per unit volume, *s(x,y,z,t)* is the photon density, c_n is the velocity of light in the laser medium, $\gamma=1/\tau_c$ where τ_c is the cavity photon lifetime and W is the up-conversion parameter of the laser material.

Under steady state conditions

$$\frac{dn}{dt}=\frac{dS}{dt}=0 \quad [7.3]$$

Using equation 7.3 to determine the steady state population inversion using the steady state photon density $s_E(x,y,z,t)$ and the steady-state upper-laser-level population $n_e(x,y,z)$ the saturation intensity defined as:

$$I_0=\frac{1}{c_n\sigma\tau_f}$$

we get

$$W\tau_f n_E^2(x,y,z)+\left(1+\frac{s_E(x,y,z)}{I_0}\right)n_E(x,y,z)-\tau_f r(x,y,z)=0 \tag{7.4}$$

This equation can be solved to determine *$n_E(x,y,z)$* the steady-state population inversion:

$$n_E(x,y,z)=\frac{-\left(1+\frac{s_E(x,y,z)}{I_0}\right)+\sqrt{\left(1+\frac{s_E(x,y,z)}{I_0}\right)^2+4W\tau_f^2 r(x,y,z)}}{2W\tau_f} \tag{7.5}$$

Substituting equation 5.5 into equation 7.2 gives:

$$2W\tau_f^2\gamma I_0=\int\limits_{Cavity}\left[-\left(1+\frac{S_E s_0(x,y,z)}{I_0}\right)+\sqrt{\left(1+\frac{S_E s_0(x,y,z)}{I_0}\right)^2+4W\tau_f^2 R r_0(x,y,z)}\right]s_0(x,y,z)dV \tag{7.6}$$

where *$r_0(x,y,z)$* and *$s_0(x,y,z)$* are normalised distributions given by:

$$\begin{aligned}&s_E(x,y,z)=S_E s_0(x,y,z)\\&r(x,y,z)=Rr_0(x,y,z)\\&\text{and}\\&\int\limits_{Cavity} r_0(x,y,z)dV=\int\limits_{Cavity} s_0(x,y,z)dV=1\end{aligned}$$

where R is the total pump rate. The cavity photon number S_E and the pump rate R may be expressed in terms of output power assuming that the pump causes negligible depletion of the ground state:

$$S_E=\frac{2l_c P_{LO}}{ch\nu_L T} \tag{7.7}$$

$$R=\frac{P_P\eta_q\left[1-\exp\left(-\alpha_P l\right)\right]}{h\nu_P} \tag{7.8}$$

where l_c is the length of the optical cavity, l is the length of the laser crystal, η_q is the pumping quantum efficiency, P_{LO} is the laser output power at threshold ν_L and ν_P are the laser and pump frequencies respectively α_P is the laser materials absorption coefficient and P_P is the incident pump power.

At threshold the output power from the laser is $P_{LO}=0$, therefore inserting equation 7.8 into equation 7.6 gives:

$$2W\tau_f{}^2\gamma I_0 = \int\limits_{Cavity}\left[-1+\sqrt{1+\frac{4W\tau_f{}^2P_{th}\eta_q\left[1-\exp\left(-\alpha_P l\right)\right]}{h\nu_P}r_0(x,y,z)}\right]s_0(x,y,z)dV \qquad [7.9]$$

Assuming a *Top-hat* distribution for the pump profile and a *Gaussian* distribution for the laser cavity mode profile the normalised distributions become:

$$r_0(x,y,z)=\frac{\alpha_P\exp(-\alpha_P z)}{\pi w_P{}^2\left[1-\exp(-\alpha_P l)\right]}\ \text{for}\ r<w_P$$

$$\text{and}\ r_0=0\ \text{for}\ r>w_P$$

[7.10]

$$s_0(r,\theta,z)=\frac{2cf(z)}{c_n\pi w_L{}^2l_c}\exp\left[\frac{-2r^2}{w_L{}^2}\right] \qquad [7.11]$$

where $w_{P,L}$ are the pump and laser spot sizes respectively in the gain medium and *f(z)* is the axial dependence of $s_0(r,z)$. The pump and laser spot sizes are assumed to be constant over the length of the gain medium. For single-longitudinal-mode operation $f(z)=\sin^2 kz$, since *f(z)* varies more rapidly than with variation of the pump rate with distance and $l>\lambda$, then it can be assumed that $f(z)\sim 1$.

Substituting equations 1.10 and 1.11 into equation 1.9 and integrating over θ gives:

$$2\tau_f^2W\gamma I_0=\int\limits_0^l\left(-1+\sqrt{1+\frac{4W\tau_f^2P_{th}\eta_q\alpha_P\exp(-\alpha_P z)}{\pi h\nu_P w_P^2}}\right)\int\limits_0^{w_P}\frac{4c}{c_n w_L^2 l_c}\exp\left(\frac{-2r^2}{w_L^2}\right)rdrdz$$
$$+\int\limits_0^l(-1+\sqrt{1})\int\limits_{W_P}^{\infty}\frac{4c}{c_n w_L^2 l_c}\exp\left(\frac{-2r^2}{w_L^2}\right)rdrdz$$

[7.12]

Simplifying and performing the integration of equation 7.12 over *r* gives the result:

$$2\tau_f^2 W\gamma I_0 = \int_0^l \left(-1 + \sqrt{1 + \frac{4W\tau_f^2 P_{th}\eta_q \alpha_P \exp(-\alpha_P z)}{\pi h\nu_P w_P^2}} \right) \frac{c}{c_n l_c} \left[1 - \exp\left(\frac{-2{w_P}^2}{w_L^2} \right) \right] dz$$

[7.13]

which gives:

$$\frac{2\tau_f^2 W\gamma I_0 c_n l_c}{c} \left[1 - \exp\left(\frac{-2{w_P}^2}{w_L^2} \right) \right]^{-1} = \int_0^l \left(-1 + \sqrt{1 + b\exp(-\alpha_P z)} \right) dz \qquad [7.14]$$

where

$$b = \frac{4W\tau_f^2 P_{th}\eta_q \alpha_P}{\pi h\nu_P w_P^2} \qquad [7.15]$$

If we make the substitution *U=exp(-α*$U=\exp(-\alpha_P l)$ we get the result:

$$\frac{2\tau_f^2 W\gamma I_0 c_n l_c}{c} \left[1 - \exp\left(\frac{-2{w_P}^2}{w_L^2} \right) \right] = -l + \int_{\exp(-\alpha_P l)}^{1} \frac{\sqrt{1+bU}}{\alpha_P U} dU \qquad [7.16]$$

We then make the substitution $V^2=bU$ giving:

$$\frac{2\tau_f^2 W\gamma I_0 c_n l_c}{c} \left[1 - \exp\left(\frac{-2{w_P}^2}{w_L^2} \right) \right] = -l + \int_{\sqrt{b\exp(-\alpha_P l)}}^{\sqrt{b}} \frac{2\sqrt{1+V^2}}{\alpha_P V} dV = I \qquad [7.17]$$

We can now solve this equation using the following identity:

$$\int \frac{\sqrt{x^2+a^2}}{x} dx = \sqrt{x^2+a^2} - a\ln\left[\frac{a+\sqrt{x^2+a^2}}{x} \right] + C \qquad [7.18]$$

Solving for I in equation (7.17) and substituting this expression back into equation (7.18) gives:

$$\frac{2\tau_f^2 W\alpha_P\gamma I_0 c_n l_c}{c}\left[1-\exp\left(\frac{-2w_P{}^2}{w_L^2}\right)\right]^{-1} = \sqrt{b+1}-\sqrt{b\exp(-\alpha_P l)+1}+\ln\left(\frac{1+\sqrt{b\exp(-\alpha_P l)+1}}{1+\sqrt{b+1}}\right)$$

[7.19]

Now we make the assumption that all the pump light is absorbed in the gain medium so that *exp(-*α_P*l)*≈0 so that equation (7.19) becomes:

$$\frac{2\tau_f^2 W\alpha_P\gamma I_0 c_n l_c}{c}\left[1-\exp\left(\frac{-2w_P{}^2}{w_L^2}\right)\right]^{-1} = \sqrt{b+1}-1+\ln\left(\frac{2}{1+\sqrt{b+1}}\right) \qquad [7.20]$$

At low powers, $\ln\left(\frac{2}{1+\sqrt{b+1}}\right)\rightarrow 0$ therefore the expression can be approximated to:

$$\frac{2\tau_f^2 W\alpha_P\gamma I_0 c_n l_c}{c}\left[1-\exp\left(\frac{-2w_P{}^2}{w_L^2}\right)\right]^{-1} \approx \sqrt{b+1}-1 \qquad [7.21]$$

Substituting for *b* and rearranging the expression for threshold pump power we get the expression:

$$P_{th} = \frac{\gamma I_0 c_n l_c \pi h\nu_P w_P^2}{4c\eta_q}\left[1-\exp\left[\frac{-2w_P^2}{w_L^2}\right]\right]^{-1}\left[2+\frac{\tau_f^2 W\alpha_P\gamma I_0 c_n l_c}{c}\left[1-\exp\left[\frac{-2w_P^2}{w_L^2}\right]\right]^{-1}\right]$$

[7.22]

When the up-conversion parameter *W*→0 we get the expression for threshold without ETU:

$$P_{th\alpha 0} = \frac{\gamma I_0 c_n l_c \pi h\nu_P w_P^2}{2c\eta_q}\left[1-\exp\left[\frac{-2w_P^2}{w_L^2}\right]\right]^{-1} \qquad [7.23]$$

substituting for $\gamma = c(L+T)/2l_c$ and I_0 we get:

$$P_{th\alpha 0} = \frac{\pi h\nu_P (L+T) w_P^2}{4\sigma_{SE}\tau_f\eta_q}\left[1-\exp\left[\frac{-2w_P^2}{w_L^2}\right]\right]^{-1} \qquad [7.24]$$

where L is the intracavity loss of the laser not including the output coupler transmission T. So finally we can express the equation for laser threshold including the effects of ETU in terms of the expression for laser threshold without the effects of ETU:

$$P_{th} = P_{th\alpha 0}\left[1 + \frac{\tau_f W \alpha_P (L+T)}{4\sigma_{SE}}\left[1 - \exp\left[\frac{-2w_P^2}{w_L^2}\right]\right]^{-1}\right] \qquad [7.25]$$

.